CORA Cork Open Research Archive
Cartlann Taighde Oscailte Chorcaí

Title	Predictive simulation and design of III-V heterostructures for light emission and detection
Authors	Murphy, Cónal
Publication date	2025
Original Citation	Murphy, C. 2025. Predictive simulation and design of III-V heterostructures for light emission and detection. PhD Thesis, University College Cork.
Type of publication	Doctoral thesis
Rights	© 2025, Cónal Murphy. - https://creativecommons.org/licenses/by/4.0/
Download date	2026-10-31 11:00:22
Item downloaded from	https://hdl.handle.net/10468/17947

UCC
University College Cork, Ireland
Coláiste na hOllscoile Corcaigh

Predictive simulation and design of III-V heterostructures for light emission and detection

Cónal Murphy



Thesis submitted in partial fulfilment of the requirements
of the degree of Doctor of Philosophy

at the
School of Physics,
University College Cork,
National University of Ireland

Supervisor: Prof. Eoin P. O'Reilly
Dr. Christopher A. Broderick
Head of School: Prof. Paul J. Callanan

August 2025

Contents

Declaration of Authorship vii

Dedication viii

Acknowledgements ix

Abstract x

List of Publications xii

1 Introduction and overview 1
- 1.1 Background and motivation . . . 1
- 1.2 Structure of the thesis and overview of primary results . . . 6

2 Theoretical background: the $\mathbf{k}\cdot\mathbf{p}$ and plane wave expansion methods 9
- 2.1 The $\mathbf{k}\cdot\mathbf{p}$ method . . . 10
  - 2.1.1 Outline of the $\mathbf{k}\cdot\mathbf{p}$ method . . . 10
  - 2.1.2 8-band $\mathbf{k}\cdot\mathbf{p}$ Hamiltonian . . . 13
- 2.2 Envelope function approximation and plane wave expansion method . . . 16
  - 2.2.1 Outline of the methods . . . 17
  - 2.2.2 Example: application of the plane wave expansion method to the Kronig-Penney model . . . 20
  - 2.2.3 Application to the 8-band $\mathbf{k}\cdot\mathbf{p}$ Hamiltonian . . . 23
- 2.3 Conclusions . . . 25

3 Theoretical background: density functional theory 27
- 3.1 Kohn-Sham density functional theory . . . 27
- 3.2 Considerations in the implementation of Kohn-Sham density functional theory . . . 30
  - 3.2.1 The local density approximation and Tran-Blaha modified Becke-Johnson exchange potential . . . 31
  - 3.2.2 The Heyd-Scuseria-Ernzerhof hybrid functional for solids . . . 33
  - 3.2.3 Pseudopotentials and the projector augmented-wave method . . . 34
  - 3.2.4 The plane wave formalism . . . 36
- 3.3 Conclusions . . . 38

4 Optimisation of radiative recombination in InAs/GaSb superlattices 41
- 4.1 Overview . . . 41
- 4.2 $\mathbf{k}\cdot\mathbf{p}$ model reparametrisation and benchmarking . . . 43

4.2.1 Spurious solutions and model reparametrisation . . . 44
4.2.2 Emission energy temperature dependence . . . 48
4.3 Electronic properties . . . 50
4.3.1 Carrier localisation . . . 51
4.3.2 Superlattice band structure . . . 53
4.4 Trends in radiative recombination . . . 54
4.4.1 Optical matrix elements and spontaneous emission . . . 55
4.4.2 Quantifying radiative performance via the recombination coefficient B . . . 57
4.4.3 Optimising radiative recombination at fixed emission wavelength . . . 59
4.5 Conclusions . . . 63

5 Optimisation of optical absorption in strain-balanced InAs/InAs$_{1-x}$Sb$_x$ superlattices 65
5.1 Overview . . . 65
5.2 Structural and electronic properties . . . 67
5.2.1 Fixed cut-off wavelength strain-balanced superlattice identification . . . 67
5.2.2 Carrier localisation and band structure . . . 72
5.3 Analysis of optical properties for photodetection . . . 73
5.3.1 Impact of varying Sb composition on optical absorption . . . 74
5.3.2 Optimising optical absorption and internal quantum efficiency . . . 76
5.3.3 Origin of calculated trends in the internal quantum efficiency . . . 79
5.4 Conclusions . . . 82

6 Revised and improved band parameters for III-P semiconductors 85
6.1 Overview . . . 85
6.2 Structural parameters . . . 87
6.2.1 Lattice parameter . . . 88
6.2.2 Elastic parameters . . . 90
6.3 Electronic band structure . . . 92
6.3.1 Fitting to the fundamental energy gap . . . 92
6.3.2 The direct band gap of AlP: reconciling theory and experiment . . . 94
6.4 Unstrained electronic band parameters . . . 98
6.4.1 Direct and indirect band gaps . . . 98
6.4.2 Effective masses and Luttinger parameters . . . 100
6.4.3 Kane parameter and ellipticity . . . 103
6.5 Strained electronic band parameters . . . 105
6.5.1 Band edge deformation potentials . . . 105
6.5.2 Pressure coefficients . . . 108
6.6 Valence band offsets . . . 109
6.7 Conclusions . . . 111

7 Summary, conclusions and outlook 113
7.1 Summary and conclusions . . . 113
7.2 Outlook . . . 115

A Considerations for 8-band k · p plane wave calculations 119
A.1 Presence and mitigation of spurious solutions . . . 119

A.2 Envelope function evolution along minibands in InAs/GaSb superlattices 122

B Interface softening in the plane wave expansion method **125**

Bibliography **129**

Declaration

I, Cónal Murphy (student no. 116301431), hereby declare that, unless otherwise stated, this work is my own, and that it has not been submitted for another degree, either at University College Cork or elsewhere.



Signed: _____

To my Mother

Acknowledgements

Firstly, I would like to thank all of those, both former and current, in the Photonics Theory Group at Tyndall National Institute, University College Cork. Thank you all for your helpful discussions, valuable advice and the welcoming atmosphere that has been present in the office and in our group meetings. I would like to extend my sincere thanks to Dr. Stefan Schulz for all of his help and advice over the last couple of years.

I would like to thank Taighde Éireann - Research Ireland, formerly the Irish Research Council, for the funding that supported my work via a Government of Ireland Postgraduate Scholarship (GOIPG; Grant No. GOIPG/2020/1252).

I would like to thank my family for their support and encouragement throughout both my PhD and undergraduate studies. In particular, I would like to thank my mother, Margaux, for her kindness and ever present motivation. Your determination and resilience will always serve as such a tremendous inspiration to me, and I would not have been able to reach this point if it wasn't for you. I thank all of my friends, your kindness and understanding over the last number of years is something I cannot appropriately thank you for. A special thanks also goes to JJ and James, who have been tremendously understanding and supportive while living with me in the final months of completing my PhD studies.

Finally, I would like to express my sincere gratitude to my supervisors, Prof. Eoin P. O'Reilly and Dr. Christopher A. Broderick, for their patience, advice and support. Thank you both for allowing me the opportunity to carry out research as an undergraduate intern, for supporting my application to undertake my PhD studies, and for the guidance provided throughout and thereafter. I would like to thank Eoin for his guidance and the opportunity to learn from his immense experience and knowledge. I wish you all the best in your retirement, which is most certainly deserved. I would like to thank Chris for his support and guidance. Without his technical and scientific expertise I would not have been able to reach this point. I wish him every success in his future research. I have been extremely fortunate to have such patient, understanding and present supervisors throughout my PhD. I sincerely appreciate all of your advice, both in science and in life.

Abstract

Semiconductor heterostructures have been long established for a variety of applications, particularly in photonic devices such as light-emitting diodes (LEDs) and lasers, in addition to photodetectors and optical amplifiers. Predictive simulations are key to support the development of these technologies. In this Thesis we employ both first-principles and continuum empirical – based respectively on density functional theory (DFT) and the $\mathbf{k} \cdot \mathbf{p}$ method – calculations to analyse and optimise III-V semiconductor heterostructures for light emission and detection.

III-V superlattices (SLs) have attracted significant interest for emission and detection at mid-infrared (mid-IR) wavelengths, for applications relevant to the environmental, industrial, medical, agricultural and defence sectors. We develop a robust framework to rigorously analyse the electronic and optical properties of III-V SLs. We employ a semi-analytical plane wave expansion method in conjunction with an 8-band $\mathbf{k} \cdot \mathbf{p}$ Hamiltonian to compute SL electronic structure, paying careful attention to the identification and mitigation of spurious solutions. The calculated SL eigenstates are then used directly to compute optical emission and absorption spectra, which are in turn used to define figures of merit that allow for in silico optimisation of SL structures for applications as mid-IR emitters and photodetectors.

Firstly, we present a theoretical analysis of mid-IR radiative recombination in InAs/GaSb SLs. The calculated SL eigenstates are used directly to compute spontaneous emission spectra and the radiative recombination coefficient B. We elucidate the origin of the relatively large B coefficients in InAs/GaSb SLs which, despite the presence of spatially indirect (type-II-like) carrier confinement, are close to that of bulk InAs and compare favourably to those calculated for mid-IR type-I pseudomorphic and metamorphic quantum well structures having comparable emission wavelengths. Our analysis explicitly quantifies the roles played by carrier localisation (specifically, partial delocalisation of bound electron states) and miniband formation (specifically, miniband occupation and optical selection rules) in determining the magnitude of B and its temperature dependence. Across the 3.5 - 7 μm wavelength range we use the room temperature B coefficient as a figure of merit. We identify that B is governed by the relative thickness of the electron-confining InAs and hole-confining GaSb layers, with our analysis of B vs. relative thickness providing guidance for the growth of optimised SLs for mid-IR light emitters. These results, combined with the expected low non-radiative Auger recombination rates in structures having spatially indirect electron and hole confinement, corroborate recently observed high output power in prototype InAs/GaSb SL inter-band cascade LEDs.

Secondly, we perform a systematic optimisation of 3 - 5 μm photodetection in strain-balanced InAs/$InAs_{1-x}Sb_x$ SLs, which constitute an emerging platform for the development of efficient mid-IR photodetectors. Growing strain-balanced SLs allows to realise high material quality

in structures containing up to several hundred SL periods, by mitigating defect formation associated with lattice relaxation. For a given target detector cut-off wavelength we employ continuum elasticity theory to identify a strain-balanced SL at each Sb composition x. We then utilise the calculated SL electronic structure to compute the optical absorption spectrum. The SL absorption spectra are used in a model calculation of the internal quantum efficiency (IQE) for photocurrent generation which is employed as a figure of merit to quantify photodetector performance. We demonstrate that increasing the Sb composition to $x \approx 30\%$ can increase the (relative) IQE at fixed cut-off wavelength by $\approx 15\%$, with minimal additional improvement in performance expected at higher Sb compositions.

Thirdly, we then develop an improved set of band parameters for the III-P semiconductors, which we extract from a comprehensive suite of DFT calculations. Despite their relevance to the development of quantum-confined heterostructures for classical and quantum applications, there remains significant uncertainty regarding several key band parameters for the III-P semiconductors AlP, GaP and InP. In literature reports, there is significant uncertainty regarding: (i) the direct band gap in AlP, the magnitude of which varies by approximately 1 eV, and (ii) the reported band edge deformation potentials for III-P compounds. Using hybrid-functional first-principles calculations we demonstrate that the Γ_{6c}-Γ_{8v} band gap of AlP is approximately 1 eV larger than the widely assumed value of 3.63 eV. This prediction is validated by using the predicted inter-band transition energies to reevaluate literature spectroscopic ellipsometry data. Having validated our calculated band structures vs. experimental and theoretical literature data, we compute a comprehensive and consistent set of band parameters for III-P semiconductors, including: direct and indirect band gaps, band edge effective masses, inter-band momentum (Kane) matrix elements, band edge deformation potentials, direct and indirect band gap pressure coefficients, and valence band offsets. Our revised parameter sets reconcile the large spread in reported values for the direct band gap of AlP, and the energy ordering of the AlP conduction band valleys, in addition to providing a consistent set of band edge deformation potentials for GaP and InP. Overall, our DFT calculations enable us to extract a complete and consistent set of 8-band $\mathbf{k} \cdot \mathbf{p}$ parameters for III-P semiconductors, providing an improved basis upon which to develop predictive calculations of the electronic and optical properties of pseudomorphic and metamorphic III-P heterostructures.

Publications

The following is a list of published work in which aspects of the research presented in this Thesis have featured.

1. Refereed journal articles

- "Theory and optimisation of radiative recombination in broken-gap InAs/GaSb superlattices", Cónal Murphy, Eoin P. O'Reilly, and Christopher A. Broderick; *J. Phys. D: Appl. Phys.* **57**, 035103 (2024).
- "Revised direct band gap and band parameters for AlP: hybrid-functional first-principles calculations vs. experiment", Cónal Murphy, Eoin P. O'Reilly, and Christopher A. Broderick; *APL Mater.* **13**, 011110 (2025).
- "In silico optimization of strain-balanced InAs/$InAs_{1-x}Sb_x$ type-II superlattices for mid-infrared photodetectors", Cónal Murphy, George F. Seager, Eoin P. O'Reilly, Andrew R. J. Marshall, and Christopher A. Broderick; *in preparation.*

2. Conference proceedings

- "Efficient multi-band **k**·**p** calculations of superlattice electronic and optical properties using plane waves", Cónal Murphy, Eoin P. O'Reilly, and Christopher A. Broderick; in *Proceedings of 2021 International Conference on Numerical Simulation of Optoelectronic Devices* (NUSOD), Online (2021).

3. Conference talks

During the course of my doctoral research I have personally presented the following conference talks:

- "Theory of radiative recombination in broken-gap InAs/GaSb superlattices", Cónal Murphy, Eoin P. O'Reilly, and Christopher A. Broderick; *Semiconductor Integrated Optoelectronics* (SIOE), Online (2021).
- "Theory of high radiative recombination in broken-gap InAs/GaSb superlattices for mid-infrared emitters", Cónal Murphy, Eoin P. O'Reilly, and Christopher A. Broderick; *Photonics Ireland*, Online (2021).
- "Efficient multi-band $\mathbf{k}\cdot\mathbf{p}$ calculations of superlattice electronic and optical properties using plane waves", Cónal Murphy, Eoin P. O'Reilly, and Christopher A. Broderick; *Numerical Simulation of Optoelectronic Devices* (NUSOD), Online (2021).
- "In silico optimisation of radiative recombination in InAs/GaSb superlattices", Cónal Murphy, Eoin P. O'Reilly, and Christopher A. Broderick; *UK Semiconductors*, Sheffield, U.K., (2023).
- "Quantitative in silico design of strain-balanced InAs/$InAs_{1-x}Sb_x$ type-II superlattices for mid-infrared photodetectors", Cónal Murphy, George F. Seager, Eoin P. O'Reilly, Andrew R. J. Marshall and Christopher A. Broderick; *UK Semiconductors*, Sheffield, U.K., (2024).

4. Conference posters

During the course of my doctoral research I have personally presented the following conference posters:

- "Computationally efficient $\mathbf{k}\cdot\mathbf{p}$ calculations for semiconductor superlattices: plane waves and multi-band Hamiltonians", Cónal Murphy, Eoin P. O'Reilly, and Christopher A. Broderick; *International Workshop on Quantum Antimonides Research and Upscaling* (IQARUS), Donostia-San Sebastián, Spain (2024).

Abbreviations

This list defines some of the commonly used abbreviations which appear throughout this Thesis. For the readers ease these abbreviations are also defined in their instance in each chapter.

DFT Density functional theory – A quantum mechanical method allows to calculate the structural and electronic properties of materials by expressing the total energy as a functional of the electron density.

EFA Envelope function approximation – A quantum mechanical approximation that factorises a wave function into the product of a rapidly oscillating atomic-scale Bloch function, and a slowly varying envelope functions.

HSEsol Heyd-Scuseria-Ernzerhof hybrid functional for solids – A hybrid density functional that includes a fraction of exact (Hartree-Fock) exchange, optimised for solid-state calculations with improved band gap predictions.

LDA Local density approximation – A simple approximation in DFT that treats the exchange-correlation energy as if the electron density were locally uniform.

LED Light-emitting diode – A semiconductor device that converts electrical current into light through radiative recombination of electrons and holes.

MIA Microscopic interface asymmetry – The atomic-scale structural differences between nominally equivalent interfaces that break the assumed mirror symmetry in continuum electronic structure calculations.

Mid-IR Mid-infrared – Electromagnetic radiation having wavelengths 3 - 30 μm, an important spectral range for biological, environmental and industrial applications.

PWEM Plane wave expansion method – A computational technique that expresses electronic envelope functions as linear combinations of plane wave basis functions, exploiting the periodicity of crystalline materials.

QCL Quantum cascade laser – A semiconductor laser that operates through inter-subband transitions within the conduction band, achieving lasing through a cascade of electrons through neighbouring quantum wells.

QW Quantum well – A quantum-confined heterostructure that confines particles (electrons or holes) in one dimension while allowing free motion in the other two dimensions.

SB Spurious band – A non-physical solution of the coupled envelope function (Schrödinger) equations for a heterostructure, that "pollutes" numerical calculations, with potentially deleterious effects on the predicted properties.

SBSL Strain-balanced superlattice – A superlattice design where tensile and compressive strains from different layers admit net zero stress, preventing the accumulation of strain that can drive formation of structural defects.

SE Spontaneous emission – Radiative recombination of an electron-hole pair, emitting a photon without external stimulation.

SL Superlattice – A periodic structure of alternating thin semiconductor layers with different band gaps, creating a one-dimensional artificial crystal with modified electronic properties.

TB-mBJ Tran-Blaha modified Becke-Johnson – An exchange potential that, when combined with the LDA to the electronic correlation, serves as a meta-generalised gradient approximation functional that provides accurate band gaps for semiconductors at low computational cost.

Chapter 1

Introduction and overview

In this introductory chapter we begin by presenting the background and motivation for the research contained in the subsequent chapters. We then provide an outline of the structure of the Thesis, and an overview of the primary results.

1.1 Background and motivation

Semiconductor photonic devices, such as light-emitting diodes (LEDs), laser diodes, and photodetectors, have long been established for a variety of applications. Many important organic and inorganic molecules possess characteristic absorption lines in their vibrational-rotational spectra at mid-infrared (mid-IR) wavelengths [1]. The absorption features associated with a number of biologically, environmentally and industrially important molecules are shown in Fig. 1.1. These absorption spectra admit little overlap in many key absorption features for different molecules, allowing for what is known as "molecular fingerprinting" in mid-IR gas sensors [1]. As a result, mid-IR gas sensing is in demand for a broad range of applications relevant to the environmental, industrial, medical, agricultural and defence sectors [2–7]. The 3 - 5 μm wavelength range is of particular interest for a number of reasons. Firstly, it is the first IR atmospheric window, within which there is minimal absorption of thermal radiation, thereby allowing for robust detection of signals. Secondly, the 3 - 5 μm wavelength range, in particular 3 - 4 μm, has traditionally been a challenging range within which to develop LEDs and diode lasers [8]. For both emitters and detectors, a number of existing technologies operating at these wavelengths pose significant issues for realising the desired efficacy. Mid-IR emission has been achieved with quantum cascade lasers (QCLs). While this technology is well established [4, 9, 10], QCL performance degrades for wavelengths $\lesssim 4$ μm and their deployment presents the dual challenges of complex fabrication and high cost. Mid-IR photodetectors are another established technology, with existing devices based on mercury cadmium telluride, $Hg_{1-x}Cd_xTe$,

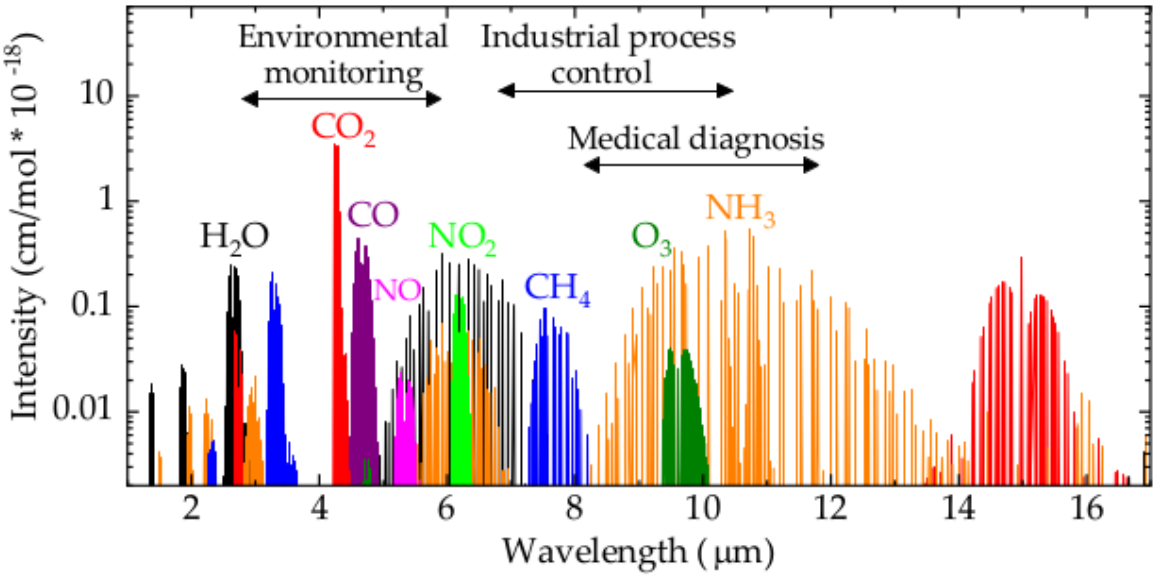


FIGURE 1.1: Mid-infrared absorption spectra of selected molecules with their relative intensities. Water (H_2O), carbon dioxide (CO_2), carbon monoxide (CO), nitric oxide (NO), nitrogen dioxide (NO_2), methane (CH_4), ozone (O_3), ammonia (NH_3). Figure reprinted from Popa et al., *Sensors* **19**, 2076 (2019). Copyright 2019 MDPI.

materials [6, 11]. Their deployment sees limitations including high fabrication cost, required cryogenic cooling, high non-radiative recombination rates, and large dark current due to band-to-band tunneling at high temperature [6, 11]. Additionally, $Hg_{1-x}Cd_xTe$ materials contain dangerous components which pose risks to the environment and human health [6].

An alternative platform for these types of mid-IR applications are III-V superlattices (SLs) [6]. SLs are periodic heterostructures consisting of large numbers of repeats of two, or more, alternating thin layers of III-V semiconductor materials [12]. SLs can be considered as an engineered bulk-like material for which quantum confinement along the growth direction in a QW breaks symmetry, such that the component of the carrier wave vector along the growth direction is no longer a "good" quantum number – i.e. the crystal momentum along the growth direction is not a conserved quantity. Forming a SL restores periodicity along the growth direction, with the quantised QW states acquiring so-called "miniband" energy dispersion, a result of the coupling between QWs. III-V SLs offer flexible engineering of the electronic band structure, including tuning the emission/absorption wavelength via the band gap and offer the potential for high temperature device operation [6]. A number of III-V SL systems have therefore attracted significant and sustained interest. Firstly, research effort on InAs/GaSb SLs and quantum wells (QWs) has been sustained since their initial fabrication in the late-1970s [12]. In the calculation of heterostructure electronic properties, the definition of an absolute reference energy level allows for the alignment of the conduction band (CB) and valence band (VB) offsets between constituent semiconductors [13, 14]. An illustration of the three types of heterojunction band alignment is shown in Fig. 1.2. From left to right we see type-I ("straddling-gap"), type-II ("staggered-gap")

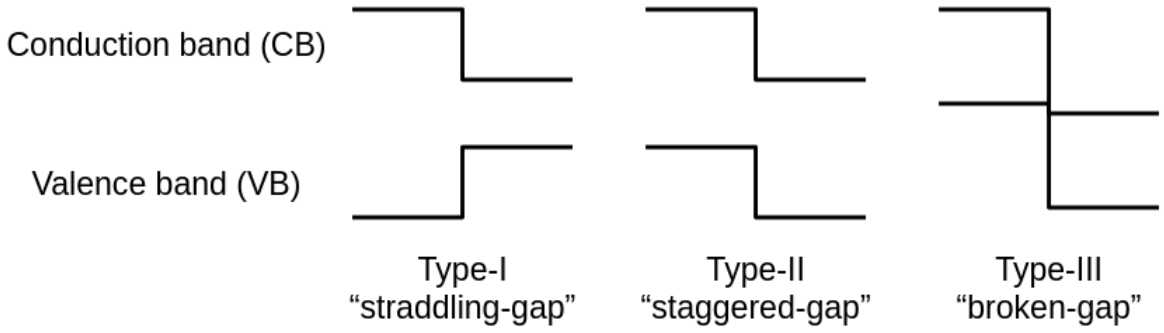


FIGURE 1.2: Illustration of the three types of heterojunction band offsets, in the absence of lattice mismatch. Moving left to right: type-I (“straddling-gap”), type-II (“staggered-gap”) and type-III (“broken-gap”) band alignment.

and type-III (“broken-gap”) band alignment, in the absence of lattice mismatch. Owing to a low lattice mismatch and a large VB offset [15], InAs/GaSb SLs possess type-III (“broken-gap”) band offsets. This means that the VB maximum in GaSb lies higher in energy than the CB minimum in InAs. These broken-gap band offsets produce spatially indirect carrier confinement, akin to that in type-II heterostructures, meaning the electron and hole electronic states are primarily confined in *adjacent* layers of the heterostructure. Prototype inter-band cascade LEDs based on InAs/GaSb SLs have demonstrated promising performance [16]. While there exists previous theoretical studies of this material system, a number of key factors have not been considered. Previous calculations did not examine band filling effects vs. carrier density and temperature via Fermi-Dirac statistics. As such, these factors were not incorporated into rigorous calculations of the spontaneous emission rate and radiative recombination coefficient B. Additionally, previous calculations have not included high-throughput calculations for the in silico optimisation of InAs/GaSb structures to maximise the radiative recombination coefficient B at room temperature for a desired emission wavelength. Our calculations consider these factors in detailed analysis, explicitly accounting for the underlying SL electronic structure.

Secondly, III-V SLs have emerged as an alternative to $Hg_{1-x}Cd_xTe$-based detectors [6]. In particular, InAs/GaSb and InAs/$InAs_{1-x}Sb_x$ based detectors have attracted sustained research effort [6, 11, 17–20]. Over the past 10 - 15 years the Ga-free InAs/$InAs_{1-x}Sb_x$ system, possessing type-II band alignment, has garnered a large amount of interest [6]. This owes, in large part, to the Ga-free design which simplifies growth [6] and mitigates the deleterious impact of chemically inhomogenous interfaces, which can drive performance degradation via the formation of interfacial defects [21–24]. Previous analysis and optimisation has primarily focused on the zone-centre electronic structure [25–29]. While such analysis has provided valuable guidance, the associated consideration of the role of the SL electronic structure in determining the optical properties pertinent to device applications is limited. This research gap emphasises the requirement for further research to support the development of mid-IR photodetectors based on InAs/$InAs_{1-x}Sb_x$ SLs. Our analysis defines an appropriate figure of merit for photodetector

operation, which is then used as the basis of high-throughput calculations to identify optimised structures for device applications.

Visible-wavelength ($\sim$ 380 - 780 nm) photonics is another area of significant interest for a number of practical applications. Technologies including energy-efficient solid-state lighting, display technologies for virtual and augmented reality applications, and visible-wavelength optical communications require efficient and reliable device platforms, such as LEDs and semiconductor lasers. An area of interest is that of heterostructures based on III-P semiconductor materials. These systems are well established as the basis of red LEDs [30] and diode lasers [31–35]. There remains significant interest in these heterostructures for the development of visible-wavelength emitting devices for applications in solid-state lighting and in display technologies [36–38]. Additionally, III-P semiconductor heterostructures continue to attract interest for applications in integrated Si photonics [39–41] and for quantum computing as robust, high-temperature single- and entangled-photon sources [42, 43].

Theoretical work, in support of experimental realisation of these technologies, requires accurately parametrised models of the underlying III-P bulk electronic band structure and its dependence on strain. Accurate material parameters, which are required to parametrise such models, describing the individual constituent compounds of semiconductor alloys are crucial to enable predictive alloy heterostructure calculations. This is key for ensuring accurate predictions, e.g. the indirect to direct band gap transition in III-P alloys. The "fundamental" band gap is the lowest energy band gap that exists between the filled VB and empty CB states in a semiconductor. This fundamental gap can be indirect or direct in nature. If the band gap is direct, the VB maximum and CB minimum reside at the same wave vector $\mathbf{k}$ in the Brillouin zone. The momentum $p = \hbar\omega/c$ carried by an emitted or absorbed photon of energy $\hbar\omega$ is $\sim 10^{-4}$ times the crystal momentum $\hbar\mathbf{k} \sim \hbar\pi/a$ associated with the extent of the Brillouin zone of a semiconductor having lattice parameter a. From the perspective of electron-hole pair generation (recombination) via optical absorption (emission), the change $\hbar\,\Delta\mathbf{k}$ in crystal momentum is negligible with respect to the extent of the Brillouin zone. Optical transitions are thus characterised by $\Delta\mathbf{k} = 0$. This means that radiative recombination involves an electron-hole pair in which both carriers have equal wave vector $\mathbf{k}$. If indirect, the VB maximum and CB minimum reside at different wave vectors $\mathbf{k}$ and $\mathbf{k}'$, rendering electron-hole pair generation optically forbidden. In an indirect-gap semiconductor, optical emission or absorption thus requires simultaneous emission or absorption of a phonon of wave vector $\mathbf{k} - \mathbf{k}'$ to conserve net-zero crystal momentum. The rate of indirect electron-hole pair generation or recombination thus depends on the *product* of (i) an inter-band optical matrix element, and (ii) an electron-phonon matrix element. This most often suppresses the overall generation or recombination rate. The radiative recombination rate in an indirect-gap semiconductor is thus often several orders of magnitude lower than that associated with a direct-gap semiconductor. In Figs. 1.3(a) and 1.3(b) we show the band structure of GaP and InP, respectively. These band structures are

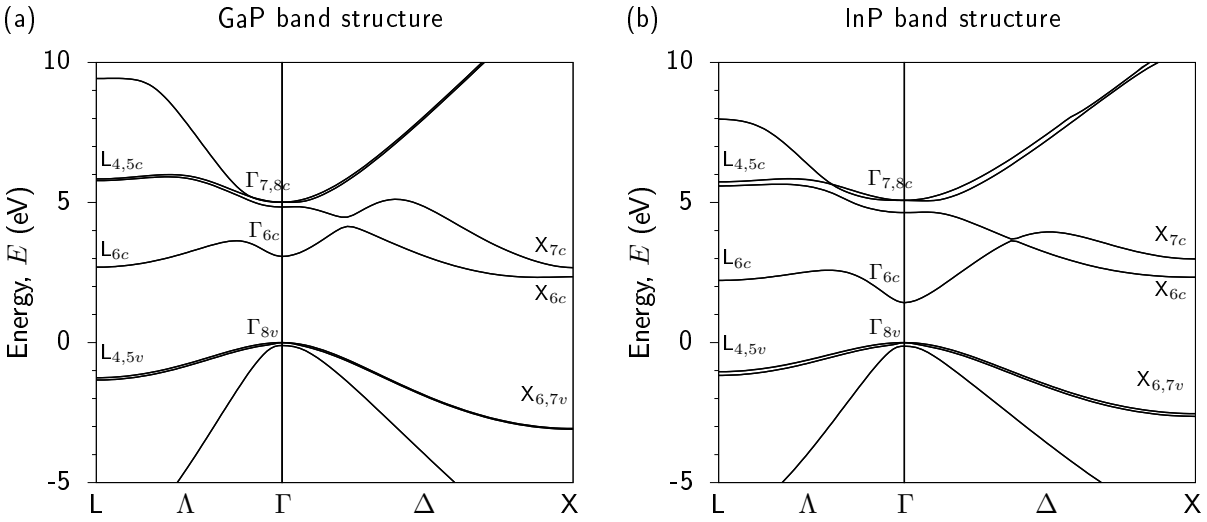


FIGURE 1.3: DFT-calculated band structure for (a) GaP and (b) InP. Calculated using HSEsol exchange-correlation functionals. The exact exchange mixing was adjusted to fit to the experimental zero-temperature fundamental indirect (direct) band gap in GaP (InP), taken from Ref. [44]. The zero of energy is set at the valence band maximum in both (a) and (b). Further details regarding these calculations follow in Chapter 6.

calculated via density functional theory (DFT) (cf. Chapters 3 and 6). GaP possesses an indirect fundamental band gap, with the VB maximum residing at the Γ-point – i.e. the Brillouin zone centre at $\mathbf{k} = 0$, and the CB minimum at the X-point – i.e. at the Brillouin zone edge, close to $\mathbf{k} = (\frac{2\pi}{a}, 0, 0)$ and equivalent $\mathbf{k}$ points. InP possesses a direct fundamental band gap, with both the VB maximum and CB minimum residing at the Γ-point. In a semiconductor alloy, e.g. $In_xGa_{1-x}P$, the determination of the composition at which the fundamental band gap becomes direct is crucial for the design and realisation of photonic devices.

The III-P semiconductor compounds suffer from large uncertainties in key electronic band parameters [44, 45], which limits the ability to perform predictive heterostructure calculations, and hence reliable in silico device design. Notable examples for AlP are the direct band gap, and relative energy and ordering of the CB valley minima. Large uncertainties exist for other III-P electronic band parameters, e.g. the effective masses, and hydrostatic deformation potentials. Additionally, a number of parameters have never been explicitly computed for AlP, GaP and InP, having been inferred based on, e.g., extrapolation of experimental measurements on III-P alloys [44]. Interrogation of the existing literature revealed the necessity for rigorous examination of the electronic structure of AlP, GaP and InP, with the extraction of key electronic band parameters [45]. This will underpin accurate predictive simulations of the application rich III-P alloy heterostructures, enabling the guidance and support of experimental device realisations. We perform a comprehensive set of DFT calculations to produce a complete and acccurate set of band parameters for III-P compounds.

1.2 Structure of the thesis and overview of primary results

This Thesis has two main areas of focus. Firstly, the simulation and in silico optimisation of III-V SLs for applications as emitters and detectors in the 3 - 5 μm mid-IR wavelength range. Secondly, the calculation from first principles of a comprehensive and consistent set of band parameters for III-P semiconductors. We now outline the remaining chapters of this Thesis, and provide an overview of the key results presented therein.

In Chapter 2 we present the multi-band $\mathbf{k} \cdot \mathbf{p}$-based calculational framework that is employed for the analysis of III-V SLs. This framework is used in our analysis of radiative recombination in InAs/GaSb SLs in Chapter 4, and of optical absorption in InAs/$InAs_{1-x}Sb_x$ strain-balanced SLs (SBSLs) in Chapter 5. We outline the 8-band $\mathbf{k} \cdot \mathbf{p}$ Hamiltonian, and describe the semi-analytical plane wave expansion method (PWEM) we employ to solve the coupled multi-band $\mathbf{k} \cdot \mathbf{p}$ envelope function Schrödinger equations and compute the heterostructure electronic and optical properties. To accurately analyse the electronic structure of SLs we must consider the miniband dispersion along the growth direction. This dispersion is encapsulated via the miniband wave vector q, which is neglected in typical plane wave $\mathbf{k} \cdot \mathbf{p}$-based heterostructure calculations. Having outlined the inclusion of this miniband dispersion, we then provide a demonstration of the application of the semi-analytical plane wave expansion method for SLs by computing the miniband dispersion of the textbook Kronig-Penney model. We conclude by describing the computation of the inter-band (optical) momentum matrix elements between pairs of electron and hole eigenstates. The spontaneous emission and optical absorption spectra are determined in large part by these momentum matrix elements, and therefore require rigorous computation to analyse III-V SLs for applications as emitters and photodetectors in the mid-IR spectral range.

In Chapter 3 we present an outline of DFT and considerations for its implementation. This is the basis for our determination of band parameters for III-P semiconductors in Chapter 6. Here we present an overview of the key aspects and considerations relevant to this work. We begin by outlining Kohn-Sham DFT, and how it enables ab initio quantitative predictions of material properties. We then introduce practical elements related to the implementation of DFT calculations. This includes a description of pseudopotentials, the projector-augmented wave method employed in this work, and the plane wave formalism. We finish with a brief description of the DFT code employed in this work, the Vienna Ab-initio Simulation Package (VASP).

In Chapter 4 we present an analysis of radiative recombination in InAs/GaSb SLs, quantifying their optimisation in the context of mid-IR LED applications. We implement and apply the multi-band $\mathbf{k} \cdot \mathbf{p}$-based plane wave calculations described in Chapter 2 to compute the full $\mathbf{k}$-dependent SL band dispersion and eigenstates. Employing a renormalisation of the bulk

inter-band optical matrix element we demonstrate the ability to reliably mitigate the impact of so-called spurious solutions in heterostructure calculations (cf. Appendix A), thereby ensuring the ability to preform reliable SL electronic structure calculations. To our knowledge, previous work has not computed the full SL spontaneous emission (SE) spectra, performed detailed analysis of the contributing factors to the radiative recombination rate, or performed high-throughput calculations to identify optimised structures. We begin by examining the occupation by electrons and holes of miniband states, possessing non-zero wave vector q along the growth direction, to quantify the temperature dependence of the SE peak energy compared to that of the fundamental zone-centre SL band gap. Our analysis, validated via comparison to experimental electroluminescence measurements, shows that this occupation acts to decrease this temperature dependence. We then consider in detail the nature of radiative recombination in exemplar InAs/GaSb SLs having equal InAs and GaSb layer thicknesses. We investigate and quantify the impact of miniband formation on the SE rate and radiative recombination coefficient B. Our calculations predict a high B coefficient, approaching that calculated previously for two novel classes of type-I mid-IR QWs [8, 46] despite the presence of type-II-like (spatially indirect) carrier confinement. Detailed analysis reveals the important roles played by carrier localisation, occupation of miniband states, and wave vector dependence of the inter-band optical matrix elements. Our analysis of the SL electronic structure identifies a significant mismatch in the ranges in q over which the electron and hole states occupy the electron and hole minibands, respectively. This mismatch in miniband occupancy, combined with the requirement to conserve crystal momentum during radiative electron-hole recombination, can – at low temperature – significantly reduce the number of electron-hole pairs that can undergo optical (direct) recombination. Thus, miniband formation decreases both the magnitude of B and its dependence on temperature. This decrease in the magnitude of B is less pronounced at higher temperatures as states at a greater range of q become occupied. We then performed a systematic analysis of SLs having unequal layer thicknesses, for which we performed optimisation of B as a function of emission wavelength at room temperature. Our calculations predict that, for emission between 3 and 7 μm, InAs/GaSb SLs should have InAs layer thickness greater than or equal to that of the GaSb layers, with the ratio of the thickness in the InAs layer to that of the GaSb layer increasing from 1 at 3 μm to 2 at 7 μm to maximise the room temperature radiative recombination coefficient B.

In Chapter 5 we present an analysis of optical absorption in InAs/$InAs_{1-x}Sb_x$ SBSLs for mid-IR photodetectors operating in the 3 - 5 μm wavelength range. This is achieved by extending the computational framework described in Chapter 2, and applied to investigate radiative recombination in Chapter 4, to compute the optical absorption. By enforcing fixed cut-off wavelength λ_{cut} (= 5, 5.5 and 6 μm), in addition to strain-balancing with respect to a GaSb substrate, we systematically identify SBSLs at fixed Sb compositions x = 18 - 40%. In targeting structures compatible with established epitaxial growth, our calculations highlight that for large Sb

composition x the identified SBSLs are challenging, but achievable, to actualise with existing growth techniques. For each identified SBSL we compute the band-to-band optical absorption spectrum, revealing the ability to engineer an increase in optical absorption in the 3 - 5 μm range with increasing Sb composition x. In order to understand the potential for optimised photodetection and provide an appropriate figure of merit, the calculated SBSL absorption spectra were employed in a model calculation of the internal quantum efficiency (IQE). Our calculations identify target Sb compositions for optimised photodetection in the 3 - 5 μm spectral range, for all of the targeted cut-off wavelengths. Our calculations reveal the competing factors in the electronic structure which drive the behaviour of the IQE. Additionally, our calculations reveal the extent to which the IQE can be enhanced by designing structures to have longer cut-off wavelength, where we see sizable increase in the IQE at fixed Sb composition x moving from $\lambda_{\text{cut}} = 5$ μm to $\lambda_{\text{cut}} = 5.5$ μm. We predict minimal additional enhancement for photodetection in the 3 - 5 μm window beyond $\lambda_{\text{cut}} = 5.5$ μm.

In Chapter 6 we present an analysis of the electronic band parameters of the III-P semiconductors AlP, GaP and InP. Interrogation of theoretical and experimental data from literature revealed significant uncertainties in key electronic band parameters for III-P semiconductors. To address this uncertainty, we carry out a comprehensive set of DFT calculations of the electronic structure of AlP, GaP and InP. We demonstrate that by carrying out appropriate empirical fitting of DFT input parameters we can produce a reliable description of the band edge electronic structure. Where available, our DFT calculations are in good quantitative agreement with literature experimental and theoretical data. For AlP, we identify large uncertainties in several key band parameters, notably the value of the direct band gap, for which a value with large uncertainty has proliferated in the literature over the past several decades. For AlP, using our DFT-calculated electronic structure we undertake a critical assessment of literature spectroscopic ellipsometry data. Our investigation revises a number of key band parameters, most notably the direct band gap in AlP. Additionally, a number of the parameters we present are computed explicitly here for the first time. In order to underpin accurate predictive heterostructure calculations, we extract a robust and consistent set of electronic band parameters for AlP, GaP and InP.

In Chapter 7 we conclude and summarise our results. This is followed by an outlook, in which we discuss potential next steps to build upon the results developed in this Thesis.

Chapter 2

Theoretical background: the $\mathbf{k} \cdot \mathbf{p}$ and plane wave expansion methods

In this Chapter we outline the theoretical methods used in our analysis of radiative recombination in InAs/GaSb superlattices (SLs) in Chapter 4, and of optical absorption in InAs/$InAs_{1-x}Sb_x$ strain-balanced SLs in Chapter 5. We begin in Sec. 2.1 by providing general background on the $\mathbf{k}\cdot\mathbf{p}$ method, and describe the 8-band $\mathbf{k}\cdot\mathbf{p}$ Hamiltonian employed in this Thesis. In Sec. 2.1.1 we introduce the $\mathbf{k}\cdot\mathbf{p}$ method for an electron in a periodic solid using time-independent (Rayleigh-Schrödinger) perturbation theory, which allows us to treat the $\mathbf{k}\cdot\mathbf{p}$ coupling as a small perturbation. In Sec. 2.1.1 we also present the form of this technique for the description of degenerate energy bands in a semiconductor, using the Löwdin renormalisation approach to time-independent perturbation theory. This approach partitions the material eigenstates into two sets: (A) the bands we wish to incorporate in our $\mathbf{k} \cdot \mathbf{p}$ Hamiltonian, and (B) other "energetically remote" bands. Löwdin renormalisation block diagonalises the resulting Hamiltonian, incorporating the impact of states B in a perturbative Hamiltonian that explicitly treats states A. In Sec. 2.1.2 we present the 8-band $\mathbf{k} \cdot \mathbf{p}$ Hamiltonian that underpins our SL calculations in Chapters 4 and 5. In Sec. 2.2, we introduce the techniques employed in our implementation of the 8-band $\mathbf{k} \cdot \mathbf{p}$ Hamiltonian described in Sec. 2.1.2. In Sec. 2.2.1 we outline the plane wave expansion method (PWEM) in the envelope function approximation (EFA) for the calculation of heterostructure electronic properties. This includes treatment of the SL miniband dispersion. In Sec. 2.2.2, we provide an example of the application of this approach, by considering a 1-band (Schrödinger) model of the Kronig-Penney model of a periodic SL potential. Next, in Sec. 2.2.3 we outline of the application of the PWEM in conjunction with the 8-band $\mathbf{k} \cdot \mathbf{p}$ Hamiltonian, and detail our procedure for the calculation of inter-band (optical) momentum matrix elements, which enable the calculation of optical properties, including the spontaneous emission and optical absorption spectra. Finally, in Sec. 2.3 we summarise and conclude.

2.1 The k · p method

In this Section we will outline the $\mathbf{k}\cdot\mathbf{p}$ method. This method employs the eigenstates of the crystal Hamiltonian at a given wave vector $\mathbf{k}_0$ as a basis, and allows to calculate the eigenstates at nearby wave vectors $\mathbf{k}$ via time-independent perturbation theory. In practice, the $\mathbf{k}\cdot\mathbf{p}$ interaction is treated as a small perturbation that couples different band states at a reference wave vector $\mathbf{k}_0$. With this general form outlined, we then present the 8-band $\mathbf{k}\cdot\mathbf{p}$ Hamiltonian employed in the calculations described in Chapters 4 and 5.

2.1.1 Outline of the k · p method

The time-independent Schrödinger equation for an electron in a periodic crystal, and associated Hamiltonian $\widehat{H}_0$, at wave vector $\mathbf{k}$, is [13, 45, 47]

$$\widehat{H}_0\psi_n(\mathbf{k},\mathbf{r}) = E_n(\mathbf{k})\psi_n(\mathbf{k},\mathbf{r})\,, \tag{2.1}$$

$$\widehat{H}_0 = -\frac{\hbar^2}{2m_0}\nabla^2 + V_0(\mathbf{r})\,, \tag{2.2}$$

where V_0 is the periodic potential of the crystal with periodicity $V_0(\mathbf{r}) = V_0(\mathbf{r}+\mathbf{R})$, with $\mathbf{R} = n_1\mathbf{a}_1 + n_2\mathbf{a}_2 + n_3\mathbf{a}_3$ a Bravais lattice vector described by the lattice vectors $\mathbf{a}_1$, $\mathbf{a}_2$ and $\mathbf{a}_3$, with $n_i \in \mathbb{Z}$. Using Bloch's theorem the electron wave function, having energy dispersion $E_n(\mathbf{k})$ described by the Bloch wave vector $\mathbf{k}$, can be written in the form [48]

$$\psi_n(\mathbf{k}) = e^{i\mathbf{k}\cdot\mathbf{r}}u_n(\mathbf{k},\mathbf{r})\,, \tag{2.3}$$

where $u_n(\mathbf{k},\mathbf{r})$ is a cell-periodic function, $u_n(\mathbf{k},\mathbf{r}) = u_n(\mathbf{k},\mathbf{r}+\mathbf{R})$. Wanting to compute the band energies $E_n(\mathbf{k})$ at a given wave vector $\mathbf{k}$, close to the wave vector $\mathbf{k}_0$ at which we know the solutions of Eq. (2.1), we can use Eqs. (2.1) and (2.3). Substituting $\mathbf{k}\to\mathbf{k}-\mathbf{k}_0$, which shifts the origin of the wave vector expansion to $\mathbf{k}_0$, we can write

$$\left[-\frac{\hbar^2}{2m_0}\nabla^2 + V_0(\mathbf{r})\right]\left[e^{i(\mathbf{k}-\mathbf{k}_0)\cdot\mathbf{r}}u_n(\mathbf{k}-\mathbf{k}_0,\mathbf{r})\right] = E_n(\mathbf{k}-\mathbf{k}_0)e^{i(\mathbf{k}-\mathbf{k}_0)\cdot\mathbf{r}}u_n(\mathbf{k}-\mathbf{k}_0,\mathbf{r})\,. \tag{2.4}$$

Applying the Laplacian, we can write the $\mathbf{k}$-dependent Schrödinger equation, and $\mathbf{k}$-dependent contribution to the Hamiltonian $\widehat{H}'$, for the periodic function $u_n(\mathbf{k}-\mathbf{k}_0,\mathbf{r})$ as

$$\left(\widehat{H}_0+\widehat{H}'\right)u_n(\mathbf{k}-\mathbf{k}_0,\mathbf{r}) = E_n(\mathbf{k}-\mathbf{k}_0)u_n(\mathbf{k}-\mathbf{k}_0,\mathbf{r})\,, \tag{2.5}$$

$$\widehat{H}' = \frac{\hbar^2}{2m_0}|\mathbf{k}-\mathbf{k}_0|^2+\frac{\hbar}{m_0}(\mathbf{k}-\mathbf{k}_0)\cdot\mathbf{p}\,, \tag{2.6}$$

where $\mathbf{p}=-i\hbar\nabla$ is the momentum operator. The $\mathbf{k}\cdot\mathbf{p}$ method seeks to solve Eq. (2.5), which includes the $\mathbf{k}$-dependent Hamiltonian $\widehat{H}'$ of Eq. (2.6), otherwise referred to as the $\mathbf{k}\cdot\mathbf{p}$ Hamiltonian. For a known value of $E_n(\mathbf{k}_0)$, and assuming a known periodic function $u_n(0,\mathbf{r})$ at $\mathbf{k}=\mathbf{k}_0$, the band structure $E_n(\mathbf{k}-\mathbf{k}_0)$ can then be evaluated in the vicinity of $\mathbf{k}_0$ by applying time-independent perturbation theory. To second-order in $\mathbf{k}-\mathbf{k}_0$, and writing $u_n(\mathbf{r},\mathbf{k}_0)=\langle\mathbf{r}|u_n(\mathbf{k}_0)\rangle$, $E_n(\mathbf{k}-\mathbf{k}_0)$ can be written as

$$\begin{aligned} E_n(\mathbf{k}-\mathbf{k}_0) &= \langle u_n(\mathbf{k}_0)|\,\widehat{H}_0+\widehat{H}'\,|u_n(\mathbf{k}_0)\rangle \\ &= E_n(\mathbf{k}_0)+\frac{\hbar^2|\mathbf{k}-\mathbf{k}_0|^2}{2m_0}\langle u_n(\mathbf{k}_0)|u_n(\mathbf{k}_0)\rangle+\frac{\hbar(\mathbf{k}-\mathbf{k}_0)}{m_0}\langle u_n(\mathbf{k}_0)|\,\mathbf{p}\,|u_n(\mathbf{k}_0)\rangle \end{aligned} \tag{2.7}$$

Operating with the momentum $\mathbf{k}=-i\nabla$ introduces a change in parity of the periodic functions, $u_n(\mathbf{r},\mathbf{k}_0)$ such that the term linear in $\mathbf{k}$ in Eq. (2.7) vanishes, leaving terms of second-order in $\mathbf{k}$, i.e. $\sim\mathcal{O}(\mathbf{k}^2)$. Due to the orthonormality of the periodic functions $|u_n(\mathbf{k}_0)\rangle$, we can write $\langle u_m(\mathbf{k}_0)|u_n(\mathbf{k}_0)\rangle=\delta_{mn}$. We can therefore write Eq. (2.7) as

$$E_n(\mathbf{k}-\mathbf{k}_0)=E_n(\mathbf{k}_0)+\frac{\hbar^2|\mathbf{k}-\mathbf{k}_0|^2}{2m_0}\,. \tag{2.8}$$

This description of the band structure has not taken into account spin-orbit coupling or the interaction between multiple bands, which are required to produce an accurate description of the band structure of a real semiconductor using the $\mathbf{k}\cdot\mathbf{p}$ method. Typical multi-band $\mathbf{k}\cdot\mathbf{p}$ methods aim to describe the band structure within a narrow range of wave vector $\mathbf{k}$. The perturbative nature of the method allows for an accurate quantitative description in a small range of wave vectors close to $\mathbf{k}_0$ [45].

To account for the interaction between bands we must now introduce an inter-band coupling correction to Eq. (2.8). Using Löwdin renormalisation [13, 49], we can divide the eigenstates at wave vector $\mathbf{k}_0$ into two classes, A and B. Our chosen basis states are those in class A, the interaction between which will be included explicitly in the Hamiltonian. Class B consists of all other bands outside of class A, which are typically energetically remote from class A. The $\mathbf{k}\cdot\mathbf{p}$ Hamiltonian, using second-order perturbation theory for degenerate bands, is then given as [13, 47]

$$H_{mn}(\mathbf{k}) = E_n(\mathbf{k}_0)\delta_{mn} + H'_{mn}(\mathbf{k}) + \sum_{l\in \mathrm{A}\neq n} \frac{H'_{ml}(\mathbf{k})H'_{ln}(\mathbf{k})}{E_n(\mathbf{k}_0) - E_l(\mathbf{k}_0)} + \sum_{\gamma\in \mathrm{B}} \frac{H'_{m\gamma}(\mathbf{k})H'_{\gamma n}(\mathbf{k})}{E_{\mathrm{A}}(\mathbf{k}_0) - E_\gamma(\mathbf{k}_0)}\,, \tag{2.9}$$

where interactions between states in class A, and the impact of coupling to class B states, are described by the first and second sum respectively. In practice, class B states are assumed to be energetically remote from class A states. This means the quantity $E_{\mathrm{A}}(\mathbf{k}_0)$ in the second sum denotes some appropriate average energy of class A states. Further detail regarding the derivation of Eq. (2.9) can be found in Appendix B of Ref. [45].

Using Eq. (2.9), the band structure $E_n(\mathbf{k})$ at wave vector $\mathbf{k}$ can be calculated knowing (i) the periodic basis functions $u_n(\mathbf{k}_0)$ for the bands in class A, (ii) the band edge energies of the basis states (class A) at the reference wave vector $\mathbf{k}_0$, and (iii) the perturbation sums describing electronic coupling between the class A and B states. This approach is typically applied for electronic structure calculations near high symmetry points in the Brillouin zone (BZ), close in energy to the conduction and/or valence band edges. These symmetry-distinct perturbation sums are then assigned values, that we treat as empirical parameters to parametrise the band structure, the latter being computed by diagonalising the Hamiltonian matrix derived in the basis of class A states. An example of such a parametrisation comes from the so-called effective mass approximation. In the effective mass approximation the energy dispersion $E_n(\mathbf{k})$ can be written in terms of the (inverse) effective mass tensor, which, in units of free electron mass m_0, is expressed as [45, 50]

$$\frac{1}{m^*_{ij}} = \delta_{ij} + \frac{1}{m_0}\sum_{m\in \mathrm{A}\neq n} \frac{p^{(i)}_{nm}p^{(j)}_{mn} + p^{(j)}_{nm}p^{(i)}_{mn}}{E_n(0) - E_m(0)} + \frac{1}{m_0}\sum_{m\in \mathrm{B}} \frac{p^{(i)}_{nm}p^{(j)}_{mn} + p^{(j)}_{nm}p^{(i)}_{mn}}{E_{\mathrm{A}}(0) - E_{\mathrm{B}}(0)}\,. \tag{2.10}$$

where $p^{(i)}_{mn}$ is the momentum matrix element describing the coupling between states m and n (cf. Sec. 2.2.3).

In choosing basis functions for the $\mathbf{k}\cdot\mathbf{p}$ Hamiltonian, we note that in III-V semiconductors eigenstates close to the valence band (VB) and conduction band (CB) edges can be well described as sp^3 hybridised linear combinations of atomic orbitals [45]. Therefore, we work with a basis of Bloch states that are linear combinations of atomic s-, p_x-, p_y- and p_z-like orbitals. The subscript m (n), and superscript i (j), for $p^{(i)}_{mn}$ in Eq. (2.10) correspond to the m (n) functions and the i (j) component of the momentum matrix, respectively.

The zone-centre effective mass tensor for the VBs is defined using the Luttinger parameters γ_i^L for cubic crystals [44]. The assumption of p_x-, p_y- and p_z-like basis states produces three symmetry-distinct perturbation sums (cf. Eq. (2.10)), which define the parameters K, M and N [13, 45]

$$K = \frac{\hbar^2}{2m_0}\left(1+\frac{2}{m_0}\sum_{m\in B}\frac{p_{xm}^{(x)}p_{mx}^{(x)}}{E_A(0)-E_m(0)}\right), \tag{2.11}$$

$$M = \frac{\hbar^2}{2m_0}\left(1+\frac{2}{m_0}\sum_{m\in B}\frac{p_{xm}^{(y)}p_{mx}^{(y)}}{E_A(0)-E_m(0)}\right), \tag{2.12}$$

$$N = \frac{\hbar^2}{m_0^2}\sum_{m\in B}\frac{p_{xm}^{(x)}p_{my}^{(y)}+p_{xm}^{(y)}p_{my}^{(x)}}{E_A(0)-E_m(0)}. \tag{2.13}$$

The parameters K, M and N define the Luttinger parameters as [13, 45]

$$\gamma_1^L = -\frac{2m_0}{3\hbar^2}(K+2M), \tag{2.14}$$

$$\gamma_2^L = -\frac{m_0}{3\hbar^2}(K-M), \tag{2.15}$$

$$\gamma_3^L = -\frac{m_0}{3\hbar^2}N. \tag{2.16}$$

These quantities are typically parametrised based on data obtained from experimental measurements or first-principles calculations (cf. Chapter 6). In particular, the Luttinger parameters, which are mathematically defined based on symmetry constraints, are treated as empirical parameters that determine the VB edge effective masses.

2.1.2 8-band $\mathbf{k}\cdot\mathbf{p}$ Hamiltonian

Having outlined the procedure for constructing a general N-band $\mathbf{k}\cdot\mathbf{p}$ Hamiltonian (cf. Sec. 2.1.1), we now present the 8-band $\mathbf{k}\cdot\mathbf{p}$ Hamiltonian for zinc-blende, including spin-orbit coupling [45, 51, 52], that underpins our analysis of the optoelectronic structure of semiconductor SLs in Chapters 4 and 5.

We work in a Cartesian coordinate system in which the x, y and z axes respectively align with the [100], [010] and [001] cubic crystal principal axes. The 8-band $\mathbf{k}\cdot\mathbf{p}$ Hamiltonian employed in this work is constructed using a basis of spin-degenerate Γ-point Bloch functions $|u_b\rangle$ ($b = 1, 2, \ldots, 8$) associated with the lowest energy CB, as well as the heavy-hole (HH), light-hole (LH) and spin-split-off (SO) VBs [53]. These basis states, constructed as a linear combination of s- and p-like atomic orbitals, are written as [45, 53]

$$
\begin{aligned}
|u_1\rangle &= |s;\uparrow\rangle\,, && (2.17)\\
|u_2\rangle &= \frac{i}{\sqrt{2}}[|x;\uparrow\rangle + i|y;\uparrow\rangle]\,, && (2.18)\\
|u_3\rangle &= \frac{i}{\sqrt{6}}[|x;\downarrow\rangle + i|y;\downarrow\rangle - 2|z;\uparrow\rangle]\,, && (2.19)\\
|u_4\rangle &= \frac{i}{\sqrt{3}}[|x;\downarrow\rangle + i|y;\downarrow\rangle + |z;\uparrow\rangle]\,, && (2.20)\\
|u_5\rangle &= -|s;\downarrow\rangle\,, && (2.21)\\
|u_6\rangle &= -\frac{i}{\sqrt{2}}[|x;\downarrow\rangle - i|y;\downarrow\rangle]\,, && (2.22)\\
|u_7\rangle &= \frac{i}{\sqrt{6}}[|x;\uparrow\rangle - i|y;\uparrow\rangle + 2|z;\downarrow\rangle]\,, && (2.23)\\
|u_8\rangle &= \frac{i}{\sqrt{3}}[|x;\uparrow\rangle - i|y;\uparrow\rangle - |z;\downarrow\rangle]\,. && (2.24)
\end{aligned}
$$

These basis states $|u_b\rangle$ diagonalise the spin-orbit Hamiltonian, i.e. at $\mathbf{k}=0$ the Hamiltonian is diagonal, with the diagonals then being the $\mathbf{k}=0$ band energies [53]. These basis states come as Kramer's pairs $|u_{b+4}\rangle = \widehat{T}|u_b\rangle$, where $\widehat{T}$ is the time-reversal operator, which relates states of opposite spin [53]. Using these basis functions we can construct the 8-band $\mathbf{k}\cdot\mathbf{p}$ Hamiltonian as [45, 53]

$$
\widehat{H} = \begin{pmatrix}
E_{\mathrm{CB}} & -\sqrt{3}T_+ & \sqrt{2}U & -U & 0 & 0 & -T_- & -\sqrt{2}T_- \\
 & E_{\mathrm{HH}} & \sqrt{2}S & -S & 0 & 0 & -R & -\sqrt{2}R \\
 & & E_{\mathrm{LH}} & Q & T_+^* & R & 0 & \sqrt{3}S \\
 & & & E_{\mathrm{SO}} & \sqrt{2}T_+^* & \sqrt{2}R & -\sqrt{3}S & 0 \\
 & & & & E_{\mathrm{CB}} & -\sqrt{3}T_- & \sqrt{2}U & -U \\
 & & & & & E_{\mathrm{HH}} & \sqrt{2}S^* & -S^* \\
 & & & & & & E_{\mathrm{LH}} & Q \\
 & & & & & & & E_{\mathrm{SO}}
\end{pmatrix}, \qquad (2.25)
$$

where Eq. (2.25) is a Hermitian matrix so the below-diagonal terms are the complex conjugates of the corresponding above-diagonal terms: $H_{nm}(\mathbf{k}) = H_{mn}^*(\mathbf{k})$. The functions that define the matrix elements of Eq. (2.25) are given by

$$E_{\mathrm{CB}}(\mathbf{k}) = E_{\mathrm{CB}_0} + \frac{\hbar^2}{2m_0} s_c \left(k_\parallel^2 + k_z^2\right) , \tag{2.26}$$

$$E_{\mathrm{HH}}(\mathbf{k}) = E_{\mathrm{VB}_0} - \frac{\hbar^2}{2m_0} \left(\gamma_1 + \gamma_2\right) k_\parallel^2 - \frac{\hbar^2}{2m_0} \left(\gamma_1 - 2\gamma_2\right) k_z^2 , \tag{2.27}$$

$$E_{\mathrm{LH}}(\mathbf{k}) = E_{\mathrm{VB}_0} - \frac{\hbar^2}{2m_0} \left(\gamma_1 - \gamma_2\right) k_\parallel^2 - \frac{\hbar^2}{2m_0} \left(\gamma_1 + 2\gamma_2\right) k_z^2 , \tag{2.28}$$

$$E_{\mathrm{SO}}(\mathbf{k}) = E_{\mathrm{VB}_0} - \Delta_{\mathrm{SO}} - \frac{\hbar^2}{2m_0} \gamma_1 \left(k_\parallel^2 + k_z^2\right) , \tag{2.29}$$

$$T_\pm(\mathbf{k}) = \frac{1}{\sqrt{6}} P \left(k_x \pm i k_y\right) , \tag{2.30}$$

$$U(\mathbf{k}) = \frac{1}{\sqrt{3}} P k_z , \tag{2.31}$$

$$S(\mathbf{k}) = \sqrt{\frac{3}{2}} \frac{\hbar^2}{m_0} \gamma_3 k_z \left(k_x - i k_y\right) , \tag{2.32}$$

$$R(\mathbf{k}) = \frac{\sqrt{3}}{2} \frac{\hbar^2}{2m_0} \left[\left(\gamma_2 + \gamma_3\right) \left(k_x - i k_y\right)^2 - \left(\gamma_3 - \gamma_2\right) \left(k_x + i k_y\right)^2\right] , \tag{2.33}$$

$$Q(\mathbf{k}) = -\frac{1}{\sqrt{2}} \frac{\hbar^2}{m_0} \gamma_2 k_\parallel^2 + \sqrt{2} \frac{\hbar^2}{m_0} \gamma_2 k_z^2 , \tag{2.34}$$

where Δ_{SO} is the VB spin-orbit splitting energy, which describes the separation between the SO VB and the LH and HH VBs at $\mathbf{k} = 0$. s_c is the renormalised inverse zone-centre CB effective mass accounting for remote band contributions. Precise definition for s_c is provided in Chapter 4. γ_i are the modified VB Luttinger parameters, defined as $\gamma_1 = \gamma_1^L - \frac{E_P}{3E_g}$ and $\gamma_{2,3} = \gamma_{2,3}^L - \frac{E_P}{6E_g}$, where γ_i^L are the bare VB Luttinger parameters (cf. Eqs.(2.14) - (2.16)), E_g is the Γ-point band gap, E_P is the Kane parameter (cf. Secs. 4.2.1 and 6.4.3) and P is the Kane matrix element (cf. Eq. (2.63)). As shown in Sec. 2.1.1, the Luttinger parameters γ_i can be used to define the VB edge effective masses [13, 45]. The Luttinger parameters specify the zone-centre HH and LH VB (inverse) effective masses along different crystal directions as [44]

$$\left(\frac{1}{m^*_{\mathrm{HH}}}\right)^{[001]} = \gamma_1 - 2\gamma_2\,, \tag{2.35}$$

$$\left(\frac{1}{m^*_{\mathrm{HH}}}\right)^{[110]} = \frac{1}{2}\left(2\gamma_1 - \gamma_2 - 3\gamma_3\right)\,, \tag{2.36}$$

$$\left(\frac{1}{m^*_{\mathrm{HH}}}\right)^{[111]} = \gamma_1 - 2\gamma_3\,, \tag{2.37}$$

$$\left(\frac{1}{m^*_{\mathrm{LH}}}\right)^{[001]} = \gamma_1 + 2\gamma_2\,, \tag{2.38}$$

$$\left(\frac{1}{m^*_{\mathrm{LH}}}\right)^{[110]} = \frac{1}{2}\left(2\gamma_1 + \gamma_2 + 3\gamma_3\right)\,, \tag{2.39}$$

$$\left(\frac{1}{m^*_{\mathrm{LH}}}\right)^{[111]} = \gamma_1 + 2\gamma_3\,, \tag{2.40}$$

and the SO VB edge (inverse) effective mass as [44]

$$\frac{1}{m^*_{\mathrm{SO}}} = \gamma_1 - \frac{E_P\,\Delta_{\mathrm{SO}}}{3E_g\left(E_g + \Delta_{\mathrm{SO}}\right)}\,. \tag{2.41}$$

We implement Eq. (2.25) using the axial approximation, which neglects the warping of the valence bands in the x-y plane [45, 54]. This approximation eliminates the anisotropic non-parabolicity of the band structure obtained by diagonalising Eq. (2.25), and imposes axial symmetry about k_z. In the axial approximation, the band dispersion in the (001)-plane depends only on the magnitude $k_{\parallel} = |\mathbf{k}_{\parallel}|$ of the in-plane wave vector. This is achieved by neglecting the $(\gamma_3 - \gamma_2)$ term in the function $R(\mathbf{k})$ (cf. Eq. (2.33)).

2.2 Envelope function approximation and plane wave expansion method

In this Section we outline the techniques employed in applying the 8-band $\mathbf{k}\cdot\mathbf{p}$ Hamiltonian presented in Sec. 2.1.2 to compute the electronic properties of SL heterostructures. We begin by outlining the EFA and PWEM, through which we are able to express a general envelope function Hamiltonian in a plane wave basis. Next, in Sec. 2.2.2 we provide a demonstration of the technique outlined in Sec. 2.2.1 for a 1-band PWEM using a computational supercell of a single SL period, explicitly including the miniband dispersion. We demonstrate the computational efficiency of this approach, owing largely to the relatively small size of the plane wave basis set required to achieve convergence of the calculated electronic properties. In Sec. 2.2.3, we outline the application of this approach to the 8-band $\mathbf{k}\cdot\mathbf{p}$ Hamiltonian used in this Thesis,

including the calculation of properties such as the inter-band matrix elements. We also describe the inclusion of the miniband dispersion in the calculation of spectral properties, which will be employed in our calculation of spontaneous emission in Chapter 4 and optical absorption in Chapter 5.

2.2.1 Outline of the methods

We begin with a brief outline of the EFA, which begins using Bloch's theorem, as in Eq. (2.3). Using Bloch's theorem, it is convenient to write the eigenstates $|\psi_n(\mathbf{k},\mathbf{r})\rangle$ as linear combinations of the Bloch states of the associated Hamiltonian [55]

$$|\psi_n(\mathbf{k},\mathbf{r})\rangle = \sum_{\mathbf{G}} a_{n\mathbf{G}}(\mathbf{k}) e^{i(\mathbf{q}+\mathbf{G})\cdot\mathbf{r}} |u(\mathbf{k})\rangle \ , \tag{2.42}$$

where $\mathbf{G}$ are the reciprocal lattice vectors. In the EFA and expanding the wave function at wave vector $\mathbf{k}$, it is assumed that the periodic Bloch function $|u(\mathbf{k})\rangle$ weakly depend on the wave vector $\mathbf{q} = \mathbf{k} - \mathbf{k}_0$ in the vicinity of $\mathbf{k}_0$. As such, Eq. (2.42) can be approximated as

$$\begin{aligned} |\psi_n(\mathbf{k},\mathbf{r})\rangle &\approx \left(\sum_{\mathbf{G}} a_{n\mathbf{G}}(\mathbf{k})\, e^{i(\mathbf{q}+\mathbf{G})\cdot\mathbf{r}}\right) |u(\mathbf{k}_0)\rangle \ , \\ &\equiv F_n(\mathbf{k},\mathbf{r})\ |u(\mathbf{k}_0)\rangle \ , \end{aligned} \tag{2.43}$$

where $\mathbf{k}_0$ is the band edge wave vector, and $F_n(\mathbf{k},\mathbf{r})$ is a slowly-varying envelope function defined as a linear combination of the Bloch components of the eigenstates $|\psi_n(\mathbf{k},\mathbf{r})\rangle$. Equation (2.43) defines the EFA, where the probability densities associated with $|u(\mathbf{k}_0)\rangle$ and $F_n(\mathbf{k},\mathbf{r})$ are assumed to be normalised over the unit cell and crystal volume, respectively. In this Thesis we consider SL heterostructures in which carrier eigenstates are localised along the growth direction z via quantum confinement arising from the periodic SL potential, which for an N-band $\mathbf{k}\cdot\mathbf{p}$ Hamiltonian means we can write Eq. (2.43) as

$$|\psi_n(\mathbf{k},z)\rangle = \sum_{b=1}^{N} F_{nb}(\mathbf{k},z)\ |u_b\rangle \ , \tag{2.44}$$

where $F_{nb}(\mathbf{k},z)$ is the component of the carrier envelope function in subband n associated with bulk band b, and $|u_b\rangle$ is the zone-centre Bloch state associated with bulk band b. For the 8-band $\mathbf{k}\cdot\mathbf{p}$ Hamiltonian employed in this Thesis, the corresponding Bloch states are given in Eqs. (2.17) - (2.24). In our analysis of SL heterostructures we also consider wave vector $\mathbf{k}$

to not only consist of the in-plane wave vector $\mathbf{k}_{\parallel}$, but also the wave vector associated with the miniband dispersion due to periodicity along the growth (z) direction. We denote the miniband wave vector along the growth direction as q, which gives $\mathbf{k} = \left(\mathbf{k}_{\parallel}, q\right)$. As described in Chapter 1, the inclusion of the miniband dispersion is crucial in accurate description of the SL optoelectronic properties, and is typically neglected in $\mathbf{k}\cdot\mathbf{p}$-based methods. The choice of neglecting the miniband dispersion is typically made since (i) thick surrounding barrier layers in QW structures make the SL period L large, and hence q small, and (ii) electronic coupling between QW eigenstates localised in neighbouring SL periods can generally be neglected. As we will describe in Chapters 4 and 5, the SLs considered in this Thesis possess narrow barrier layers. This means that the contributions associated with q cannot be neglected. The multi-band envelope function equation can be expressed as

$$\sum_{b=1}^{N} \widehat{H}_{b'b}(\mathbf{k})\, F_{nb}(\mathbf{k}, z) = E_n(\mathbf{k})\, F_{nb'}(\mathbf{k}, z)\,, \tag{2.45}$$

where $E_n(\mathbf{k})$ is the SL band structure, and Eq. (2.45) is obtained using the orthonormality of the Bloch basis states, which gives $\langle u_{b'}|u_b\rangle = \delta_{b'b}$. We note, the operator $\widehat{H}_{b'b}(\mathbf{k}) = \langle u_{b'}|\,\widehat{H}(\mathbf{k})\,|u_b\rangle$ is obtained by substituting $k_z \to -i\frac{\mathrm{d}}{\mathrm{d}z}$ in the $\mathbf{k}\cdot\mathbf{p}$ matrix element $H_{b'b}(\mathbf{k})$, and the resulting differential operators are ordered with respect to the position-dependent material parameters to ensure that the envelope functions $F_{nb}(\mathbf{k}, z)$ are continuous across the SL interfaces. Equation (2.45) then represents a set of coupled differential equations, which can be solved to obtain the SL band structure $E_n(\mathbf{k}) = E_n(\mathbf{k}_{\parallel}, q)$ and envelope functions $F_{nb}(\mathbf{k}, z)$. We will now outline the PWEM, which can be used to solve Eq. (2.45).

The "semi-analytical" PWEM approach we employ in this work allows to write the quantised matrix elements of a general N-band $\mathbf{k}\cdot\mathbf{p}$ Hamiltonian as analytical expressions. The evaluation of these matrix elements does not rely on numerical differentiation or integration unlike, e.g., finite difference methods [55]. The resulting matrix representation of the heterostructure Hamiltonian can then be diagonalised to solve Eq. (2.45). We will begin our description of the PWEM with the example of a 1-band (Schrödinger) model for the Kronig-Penney SL.

The 1-band Schrödinger equation in the EFA is

$$\widehat{H}\, F_n(z) = E_n\, F_n(z)\,, \tag{2.46}$$

with the envelope function Hamiltonian $\widehat{H}$ is given as

$$\widehat{H} = -\frac{\hbar^2}{2m_0}\frac{\mathrm{d}}{\mathrm{d}z}\left(\frac{1}{m^*(z)}\frac{\mathrm{d}}{\mathrm{d}z}\right) + V(z)\,, \tag{2.47}$$

where $m^*(z)$ and $V(z)$ are the position-dependent relative effective mass and potential, respectively. The PWEM consists of expanding the envelope function in a Fourier series as

$$F_n(z) = \frac{1}{\sqrt{L}} \sum_{m=-M}^{M} a_{nm}\, e^{i(G_m+q)z}\,, \tag{2.48}$$

where $G_m = \frac{2m\pi}{L}$, and $m \in [-M, \ldots, M] \in \mathbb{Z}$. As in our outline of the EFA, here we have included the miniband wave vector q. Equation (2.48) indicates that each eigenstate of Eq. (2.47) is described as a linear combination of a set of $2M+1$ plane wave basis functions, given as $\frac{1}{\sqrt{L}}e^{i(G_m+q)z}$. These basis functions are periodic along the growth direction z such that, the envelope functions $F_n(z)$, which represent the eigenstates of $\widehat{H}$, are periodic on the closed interval $z \in \left[-\frac{L}{2}, \frac{L}{2}\right]$. Here L is the period of this interval, or the SL period. describe this interval as our calculational "supercell", the miniband dispersion associated with which is described by the wave vector $-\frac{\pi}{L} \leq q \leq +\frac{\pi}{L}$. Substituting Eq. (2.48) in Eq. (2.46) leads to a reciprocal space eigenvalue equation, which is the plane wave representation of the Schrödinger equation. In this equation, the eigenvectors are comprised of the Fourier coefficients a_{nm} of the envelope function $F_n(z)$.

We now conclude this section by outlining the derivation of the general form of the envelope function equation in the plane wave representation. The reciprocal space equivalent of Eq. (2.46), substituting in Eq. (2.47), is expressed as [55]

$$\sum_{m=-M}^{M} \left(\frac{1}{L} \int_{-\frac{L}{2}}^{\frac{L}{2}} e^{-i(G_{m'}+q)z}\, \widehat{H}\, e^{i(G_m+q)z}\, \mathrm{d}z \right) a_{nm} = E_n\, a_{nm'}\,, \tag{2.49}$$

where we have also multiplied across by $e^{-i(G_{m'}+q)z}$ and integrated over the supercell. We note, the orthonormality of the plane wave basis functions over the supercell gives

$$\frac{1}{L} \int_{-L/2}^{L/2} e^{i(G_m - G_{m'})z} \mathrm{d}z = \delta_{mm'}\,. \tag{2.50}$$

Rewriting the left side of Eq. (2.49) by defining the matrix elements $H_{m'm}$ as

$$H_{m'm} = \frac{1}{L} \int_{-\frac{L}{2}}^{\frac{L}{2}} e^{-i(G_{m'}+q)z}\, \widehat{H}\, e^{i(G_m+q)z}\, \mathrm{d}z\,. \tag{2.51}$$

so that Eq. (2.49) becomes

$$\sum_{m=-M}^{M} H_{m'm}a_{nm} = E_n a_{nm'}\,, \tag{2.52}$$

which is the plane wave representation of Eq. (2.46). The plane wave basis states of Eq. (2.48) have therefore been used to generate the matrix representation presented in Eq. (2.51) for the envelope function Hamiltonian $\widehat{H}$, for which $H_{m'm}$ has dimensions $(2M+1)\times(2M+1)$ and is Hermitian. The PWEM can be summarised in Eqs. (2.51) and (2.48), which can be respectively used to calculate the matrix representation of a given envelope function Hamiltonian, and to construct the corresponding eigenstates of the system in real space. We note that Eq. (2.48) becomes exact in the limit $M \to \infty$. The PWEM possesses significant advantages over real space techniques, e.g. the finite difference method, since the number of components in Fourier space required to represent $F_n(z)$ is typically significantly less than the number of grid points required to obtain the equivalent accuracy in a real space calculation [55].

2.2.2 Example: application of the plane wave expansion method to the Kronig-Penney model

To demonstrate the accuracy and efficiency of the PWEM, we now apply the method to the Kronig-Penney (K-P) model. The K-P superlattice corresponds to a 1-band model of an idealised infinite SL [47]. As in Sec. 2.2.1 we assume that the calculational supercell, having period L, lies along the z-direction in the range $z \in \left[-\frac{L}{2}, \frac{L}{2}\right]$. In this example we choose our QW to have thickness a and lie in the range $z \in \left[-\frac{a}{2}, \frac{a}{2}\right]$, with barrier thickness b, such that the SL has period $L = a + b$. The potential profile is given as

$$V(z) = \begin{cases} 0, & |z| < \frac{a}{2} \\ V_0, & \text{otherwise} \end{cases} \tag{2.53}$$

and the effective mass in these regions is described piecewise continuously as

$$m^*(z) = \begin{cases} m_w^*, & |z| < \frac{a}{2} \\ m_b^*, & \text{otherwise} \end{cases} \tag{2.54}$$

where V_0 is the QW potential depth, and m_w^* (m_b^*) is the effective mass in the well (barrier) region.

To solve the K-P superlattice described by Eqs. (2.53) and (2.54), we begin by outlining the derivation of the 1-band PWEM. Using Eqs. (2.47) and (2.51) we obtain

$$H_{m'm} = -\frac{i\hbar^2(G_m+q)}{2m_0 L}\int_{-\frac{L}{2}}^{\frac{L}{2}} e^{-i(G_{m'}+q)z}\,\frac{\mathrm{d}}{\mathrm{d}z}\left(\frac{e^{i(G_m+q)z}}{m^*(z)}\right)\mathrm{d}z + \frac{1}{L}\int_{-\frac{L}{2}}^{\frac{L}{2}} V(z)\,e^{i(G_m-G_{m'})z}\,\mathrm{d}z\,. \tag{2.55}$$

The Fourier transform of a supercell-periodic function $f(z)$ in terms of the wave vector G is defined as [55]

$$\widetilde{f}(G) = \frac{1}{L}\int_{-\frac{L}{2}}^{\frac{L}{2}} f(z)\,e^{-iGz}\,\mathrm{d}z \tag{2.56}$$

and we define the "characteristic function" $\chi(z)$ for a QW of thickness a lying in the range $z \in \left[-\frac{a}{2}, \frac{a}{2}\right]$ by [55]

$$\chi(z) = \begin{cases} 1, & |z| < \frac{a}{2} \\ 0, & \text{otherwise} \end{cases} \tag{2.57}$$

which takes a value of one within the QW only. Using Eqs. (2.53) and (2.54) we obtain

$$\begin{aligned} H_{m'm} &= \left(\frac{\hbar^2}{2m_0}\frac{(G_{m'}+q)(G_m+q)}{m_b^*} + V_0\right)\delta_{m'm} \\ &+ \widetilde{\chi}(G_m - G_{m'})\left(\frac{\hbar^2}{2m_0}(G_{m'}+q)(G_{m'}+q)\left(\frac{1}{m_w^*}-\frac{1}{m_b^*}\right) - V_0\right), \end{aligned} \tag{2.58}$$

where $\widetilde{\chi}(G_m - G_{m'}) = \frac{a}{L}\mathrm{sinc}\left(\frac{a}{2}(G_m - G_{m'})\right)$ is the Fourier transform of the characteristic function $\chi(z)$, with $\delta_{m'm} = \mathrm{sinc}\left(\frac{L}{2}(G_m - G_{m'})\right)$. Equation (2.58) is an explicit expression for the matrix representation of the 1-band envelope function Hamiltonian described in Eq. (2.47), in the plane wave basis defined in Eq. (2.48). We obtain bound state energies E_n by diagonalising Eq. (2.58).

In order to benchmark the solutions for the 1-band PWEM we obtain via Eq. (2.58), we now present the solutions of the K-P model. The K-P model can be used to obtain the solutions, via Bloch's theorem, for a periodic SL potential [47]. For a SL with well thickness a and barrier thickness b, we apply boundary conditions requiring continuity of the envelope function and its derivative with respect to z across the well/barrier interfaces, combined with the use of Bloch's theorem to enforce periodicity. Under the application of these boundary conditions the energy dispersion as a function of wave vector q can be found as the solutions of the equation [47]

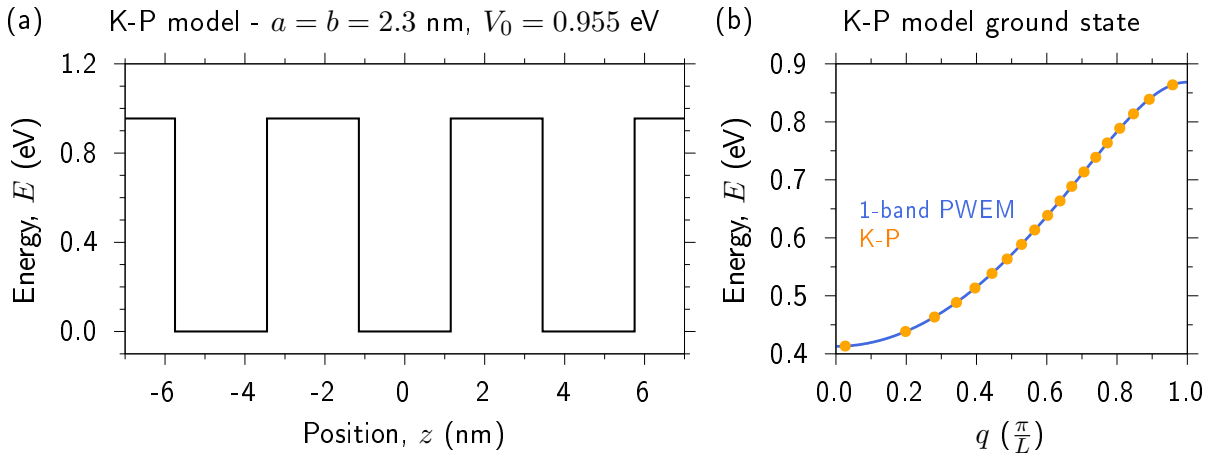


FIGURE 2.1: (a) Potential profile for a Kronig-Penney superlattice having equal well and barrier thicknesses ($a = b = 2.3$ nm), and barrier potential energy depth $V_0 = 0.955$ eV. (b) Solution for the energy dispersion (band structure) of the lowest energy bound states in the superlattice of (a) as a function of wave vector q – obtained using the Kronig-Penney model (filled orange circles) and the 1-band plane wave expansion method (solid blue line).

$$\cos\left(q(a+b)\right) = \cos(ka)\cosh(\kappa b) + \frac{1}{2}\left(\frac{\kappa}{k} - \frac{k}{\kappa}\right)\sin(ka)\sinh(\kappa b)\,, \tag{2.59}$$

where $k = \sqrt{\frac{2m_w^*}{\hbar^2}E_n}$ and $\kappa = \sqrt{\frac{2m_b^*}{\hbar^2}(V_0 - E_n)}$. Equation (2.59) is a transcendental equation in wave vector q, for which the solutions can be found via any standard root finding algorithm to obtain the miniband dispersion $E_n(q)$.

We now compare the 1-band PWEM, including the miniband wave vector q, and the K-P model for an exemplar periodic SL potential, with $V_0 = 0.955$ eV and equal well and barrier thicknesses, such that $a = b = 2.3$ nm ($L = a + b = 4.6$ nm). We also take the effective mass in the well and the barrier to be equal $m_w^* = m_b^* = 0.025\ m_0$. This periodic potential is shown in Fig. 2.1(a) for three supercell periods. The miniband dispersion $E(q)$ associated with the lowest energy bound state of the periodic potential in Fig. 2.1(a) is shown in Fig. 2.1(b). The solutions of Eq. (2.59) for the Kronig-Penney model are shown using filled orange circles, and the solutions for the 1-band PWEM, obtained via the diagonalisation of the Hamiltonian matrix constructed using Eq. (2.58), are shown using a solid blue line. We note the strong agreement between the results obtained via the K-P model and the 1-band PWEM, demonstrating the ability of the PWEM to accurately describe SL bound states numerically and reproduce the K-P model miniband dispersion. In our calculations using the 1-band PWEM, the results were found to be sufficiently converged by $M = 9$, corresponding to a Hamiltonian matrix of size 19×19 ($= (2M+1)\times(2M+1)$). This framework therefore provides a computationally efficient method with which to compute SL electronic structure. As we will see in Sec. 2.2.3, the PWEM allows for semi-analytical computation of SL properties having computed the energy dispersion and corresponding eigenstates, and here using a calculational supercell of a single SL period.

2.2.3 Application to the 8-band k · p Hamiltonian

Having, in Sec. 2.2.2, demonstrated the PWEM for a 1-band model, we now describe the application of this approach to the 8-band $\mathbf{k}\cdot\mathbf{p}$ Hamiltonian presented in Sec. 2.1.2. We also outline the calculation of key SL properties, such as the inter-band matrix elements, and describe the calculation of SL spectral properties with explicit inclusion of the miniband dispersion.

Application to the 8-band $\boldsymbol{k}\cdot\boldsymbol{p}$ Hamiltonian for SL heterostructure calculations:

We now apply the PWEM to the 8-band $\mathbf{k}\cdot\mathbf{p}$ Hamiltonian (cf. Eq. (2.25)) to compute the electronic structure of [001]-orientated quantum-confined SL heterostructures. We consider a SL in which the growth direction aligns with z axis of a Cartesian coordinate system. As demonstrated in Sec. 2.2.1, the PWEM consists of expanding the envelope functions $F_{nb\mathbf{k}}(z)$ as a truncated Fourier series, such that a general SL eigenstate $|\psi_{n\mathbf{k}}(z)\rangle$ having energy $E_{n\mathbf{k}}$ at wave vector $\mathbf{k} = (\mathbf{k}_{\parallel}, q)$ is given by [56–58]

$$|\psi_{n\mathbf{k}}(z)\rangle = \sum_{b=1}^{N_b}\left(\frac{1}{\sqrt{L}}\sum_{m=-M}^{+M} a_{nbm\mathbf{k}}\, e^{i(G_m+q)z}\right)|u_b\rangle\,, \tag{2.60}$$

where $N_b = 8$ is the number of Bloch basis states of the underlying bulk $\mathbf{k}\cdot\mathbf{p}$ Hamiltonian (cf. Sec. 2.1.2), $\mathbf{k}_{\parallel}$ is the component of the wave vector in the plane perpendicular to the growth direction, and q is the component of the wave vector along the growth direction describing the miniband dispersion. We now have one envelope function component for each Bloch basis state, for which we employ a plane wave expansion akin to that in Eq. (2.48). Generating the plane wave representation of the associated multi-band EFA Schrödinger equation $\widehat{H}_{\mathbf{k}}|\psi_{n\mathbf{k}}(z)\rangle = E_{n\mathbf{k}}|\psi_{n\mathbf{k}}(z)\rangle$ proceeds via the same procedure that led to Eq. (2.52). This yields the reciprocal space matrix representation in the plane wave basis of the element $\widehat{H}_{b'b,\mathbf{k}}$ of the heterostructure Hamiltonian $\widehat{H}_{\mathbf{k}}$ [55, 59]

$$\left(\widetilde{H}_{b'b,\mathbf{k}}\right)_{m'm} = \frac{1}{L}\int_{-\frac{L}{2}}^{+\frac{L}{2}} e^{-i(G_{m'}+q)z}\,\widehat{H}_{b'b,\mathbf{k}}(z)\,e^{i(G_m+q)z}\,\mathrm{d}z\,, \tag{2.61}$$

which is a complex-valued $(2M+1)\times(2M+1)$ matrix. In Eq. (2.61), the operators $\widehat{H}_{b'b,\mathbf{k}}(z)$ must be derived from the bulk $\mathbf{k}\cdot\mathbf{p}$ matrix elements (cf. Eq. (2.25)).

In the 1-band model, the Hamiltonian gets quantised to become an operator, which generates a $(2M+1)\times(2M+1)$ matrix representation using a set of plane wave basis states. For an N-band model, the same procedure is applied, but is applied to each element of the bulk $N\times N$ Hamiltonian matrix. Each bulk Hamiltonian matrix element is then assigned a $(2M+1)\times(2M+1)$ matrix representation, such that the matrix representation of the N-band Hamiltonian is of size

$N(2M+1)\times N(2M+1)$. Previous comparative analysis between these boundary conditions and the "exact" Burt-Foreman EFA boundary conditions, demonstrated that asymmetric contributions in the latter play a minimal role in determining the character of eigenstates computed using an 8-band $\mathbf{k}\cdot\mathbf{p}$ Hamiltonian [60]. Symmetrising, quantising and evaluating Eq. (2.61) for all matrix elements of the underlying bulk $\mathbf{k}\cdot\mathbf{p}$ Hamiltonian yields the reciprocal space representation $\widetilde{H}_{\mathbf{k}}$ of $\widehat{H}_{\mathbf{k}}$, which is a $N_b(2M+1)\times N_b(2M+1)$ Hermitian matrix. The eigenvalues of $\widetilde{H}_{\mathbf{k}}$ are the band energies $E_{n\mathbf{k}}$, while its eigenvectors are given by the Fourier coefficients $a_{nbm\mathbf{k}}$ of the envelope functions $F_{nb\mathbf{k}}(z)$. Having included the miniband dispersion in Eq. (2.61), we note that the operators $\widehat{H}_{b'b,\mathbf{k}}(z)$ are in general differential operators, with their matrix representation via Eq. (2.61) being q-dependent. A detailed derivation of the matrix elements Eq. (2.61) for the 8-band $\mathbf{k}\cdot\mathbf{p}$ Hamiltonian employed in this work can be found in Ref. [55].

Bloch character:

Having computed our 8-band $\mathbf{k}\cdot\mathbf{p}$ eigenstates using Eqs. (2.60) and (2.61), we note that we can compute the "Bloch character" of these eigenstates. Having eigenstates that are linear combinations of the basis states $|u_b\rangle$ $(b=1,2,\ldots,8)$, the Bloch character describes the hybridisation between the states in the 8-band description of the electronic structure, and the degree to which each heterostructure eigenstate can be associated with each basis state $|u_b\rangle$. For our choice of basis functions (cf. Sec. 2.1.2), this would be CB, HH, LH, or SO character which they possess. The calculation of the Bloch character faciliates analysis of SL electronic structure in Chapters 4 and 5, e.g. the identification of whether a given bound hole state is predominately HH- or LH-like. For the heterostructure eigenstate Eq. (2.60), the Bloch character associated with the bulk basis state $|u_b\rangle$ is given by

$$c_{nb\mathbf{k}} \equiv \int_{-L/2}^{+L/2} \langle F_{nb\mathbf{k}}(z)|\psi_{nb\mathbf{k}}(z)\rangle \,\mathrm{d}z = \sum_m |a_{nbm}|^2 \tag{2.62}$$

where Eq. (2.62) can be evaluated directly using the Fourier coefficients of the envelope function $F_{nb\mathbf{k}}(z)$, which we obtain via the eigenvectors of the plane wave matrix representation of the heterostructure Hamiltonian.

Inter-band optical (momentum) matrix elements:

To analyse and optimise SL structures for optical emission and absorption (cf. Chapters 4 and 5), we respectively compute the spontaneous emission (cf. Sec. 4.2.2) and optical absorption (cf. Sec. 5.3.1). This requires accurate evaluation of the inter-band optical (momentum) matrix elements $\mathbf{p}_{n_c n_v \mathbf{k}}$ between an electron eigenstate $|\psi_{n_c\mathbf{k}}(z)\rangle$ in conduction subband n_c and a hole eigenstate $|\psi_{n_v\mathbf{k}}(z)\rangle$ in valence subband n_v, at wave vector $\mathbf{k}$. We recall from Chapter 1, that optical emission or absorption follows strict $\mathbf{k}$-selection, $\Delta\mathbf{k}=0$ for optical transitions, imposing

that the electron and hole states have equal wave vector. We compute $\mathbf{p}_{n_c n_v \mathbf{k}}$ via the Hellmann-Feynman theorem [61], using the SL Hamiltonian and eigenstates explicitly at each wave vector $\mathbf{k}$

$$p^{(e)}_{n_v n_c \mathbf{k}} \equiv \widehat{e} \cdot \mathbf{p}_{n_v n_c \mathbf{k}} = \frac{m_0}{\hbar} \langle \psi_{n_v \mathbf{k}} | \, \widehat{e} \cdot \nabla_{\mathbf{k}} \widehat{H}_{\mathbf{k}} \, | \psi_{n_c \mathbf{k}} \rangle \,, \tag{2.63}$$

where $\widehat{e}$ is a unit vector denoting the polarisation of the emitted or absorbed photon, with $\widehat{e} \cdot \nabla_{\mathbf{k}} \widehat{H}$ then denoting the directional derivative of the supercell Hamiltonian with respect to the component of $\mathbf{k}$ parallel to the photon polarisation. Evaluation of Eq. (2.63) requires calculation of the reciprocal space matrix representation of $\widehat{e} \cdot \nabla_{\mathbf{k}} \widehat{H}_{\mathbf{k}}$, which can be evaluated analytically by replacing $\widehat{H}_{b'b,\mathbf{k}}(z)$ by $\widehat{e} \cdot \nabla_{\mathbf{k}} \widehat{H}_{b'b,\mathbf{k}}(z)$ in Eq. (2.61). The simple analytical form of the plane wave basis states of complex exponentials allows the matrix representation of $\widehat{e} \cdot \nabla_{\mathbf{k}} \widehat{H}_{\mathbf{k}}$ to be computed analytically in the same manner as for the Hamiltonian matrix elements (cf. Eq. (2.61)). This analytical evaluation is possible as, the solution of the multi-band envelope function expansion is in reciprocal space (cf. Sec. 2.2.1) and the plane wave basis functions possess a simple form in real space, leading to the spatial integrations associated with the calculation of matrix elements between states being analytical. As a result, the PWEM has the additional advantage of removing the need to perform the costly numerical quadrature associated with real space implementations of such calculations. By explicitly employing the SL eigenstates and Hamiltonian, we take all effects such as carrier localisation, partial reflection of wave functions at layer interfaces, and band hybridisation, explicitly into account.

Accounting for the miniband dispersion in the calculation of spectral properties:

To compute energy-dependent properties in a QW, e.g., density of states, spontaneous emission and optical absorption, it is necessary to integrate over the in-plane degrees of freedom – i.e. the in-plane wave vector $\mathbf{k}_{\|}$. For a SL this is modified to incorporate q-dependent miniband dispersion and eigenstates as

$$\int \frac{\mathrm{d}\mathbf{k}_{\|}}{(2\pi)^2} \longrightarrow \left(\frac{2\pi}{L}\right)^{-1} \int_{-\frac{\pi}{L}}^{+\frac{\pi}{L}} \mathrm{d}q \int \frac{\mathrm{d}\mathbf{k}_{\|}}{(2\pi)^2} \,, \tag{2.64}$$

where $\frac{2\pi}{L}$ is the SL BZ extent along z. As our calculations employ the axial approximation (cf. Sec. 2.1.2), the in-plane integration is reduced to a one-dimensional integral, i.e. $\int d\mathbf{k}_{\|} \rightarrow 2\pi \int k_{\|} dk_{\|}$. Thus, instead of calculating the SL electronic structure on a grid with order of N^2 points $\mathbf{k}_{\|} = (k_x, k_y)$ this allows for calculation of the electronic structure on a grid of N points along $k_{\|} = |\mathbf{k}_{\|}|$, substantially reducing computational expense. Therefore, in the axial approximation, we perform two-dimensional integrals over $k_{\|}$ and q to compute spectral properties.

2.3 Conclusions

In this Chapter we have presented the theoretical methods employed in our calculations of SL electronic and optical properties. This theoretical framework is employed in the analysis of radiative recombination in InAs/GaSb SLs in Chapter 4, and of optical absorption in strain-balanced InAs/$InAs_{1-x}Sb_x$ SLs in Chapter 5. In Sec. 2.1, we began by outlining the $\mathbf{k}\cdot\mathbf{p}$ method for an electron in a periodic solid, using time-independent (Rayleigh-Schrödinger) perturbation theory. We then presented the form of the multi-band $\mathbf{k}\cdot\mathbf{p}$ Hamiltonian employing Löwdin renormalisation, which partitions the eigenstates of a periodic potential into two classes, class A and B. Class A states are those that we choose as the basis within which to generate the $\mathbf{k}\cdot\mathbf{p}$ Hamiltonian. Class B states are the remaining, energetically remote states, whose impact on the states in class A is important in determining the semiconductor electronic structure, notably the effective masses. The use of Löwdin renormalisation to paritition these eigenstates allows us to focus on a subset (class A), while treating their coupling to other bands (class B) perturbatively. We then introduced the 8-band $\mathbf{k}\cdot\mathbf{p}$ Hamiltonian, including spin-orbit splitting, for zinc blende semiconductors that will underpin our work on SL structures in Chapters 4 and 5. This Hamiltonian is constructed using zone-centre (Γ-point) Bloch basis functions $|u_b\rangle$, consisting of one conduction and three valence spin degenerate states. This 8-band $\mathbf{k}\cdot\mathbf{p}$ Hamiltonian allows to compute the band structure in the vicinity of the Γ-point. Following this, we described aspects of our implementation of this multi-band $\mathbf{k}\cdot\mathbf{p}$ Hamiltonian for quantum-confined heterostructures. In Sec. 2.2 we presented our implementation of the PWEM in the EFA, and the application of this approach in conjunction with the 8-band $\mathbf{k}\cdot\mathbf{p}$ Hamiltonian. In Sec. 2.2.1, we provided an outline of this approach, including the miniband dispersion via the wave vector q and, in Sec. 2.2.2, demonstrated how this approach allows for efficient computation of SL electronic properties using analytical expressions for the matrix elements of the $\mathbf{k}\cdot\mathbf{p}$ Hamiltonian, using a 1-band PWEM to recover the K-P miniband dispersion. This demonstrated the accuracy and efficiency of the description of the miniband dispersion for SL heterostructure calculations prescribed by inclusion of q, which can be obtained using a small number of plane waves in a 1-band PWEM calculation. Next, in Sec. 2.2.3 we described the application of the PWEM to the 8-band $\mathbf{k}\cdot\mathbf{p}$ Hamiltonian, which includes the description of the miniband dispersion along the growth direction z. As discussed in Chapter 1, typical $\mathbf{k}\cdot\mathbf{p}$-based calculations neglect the miniband dispersion, which is required in accurate predictive calculations. Finally, in Sec. 2.2.3 we also described the analytical calculation of momentum matrix elements in the PWEM using our computed SL eigenstates. The theoretical methods we have detailed in this Chapter underpin the accurate and computationally efficient calculations of SL heterostructures in this Thesis. These methods are employed in the analysis of radiative recombination in InAs/GaSb SLs in Chapter 4, and of optical absorption in InAs/$InAs_{1-x}Sb_x$ strain-balanced SLs in Chapter 5.

Chapter 3

Theoretical background: density functional theory

In this Chapter we outline the theoretical methods used in our analysis of the structural, elastic and electronic properties of the III-P compounds AlP, GaP and InP in Chapter 6. We begin in Sec. 3.1 by describing the Kohn-Sham formalism of density functional theory (DFT). In Sec. 3.2, we provide an outline of key considerations and approximations employed in the implementation of Kohn-Sham DFT calculations. In Sec. 3.2.1, we begin by discussing schemes for the determination of the exchange-correlation (XC) energy in Kohn-Sham DFT, such as the local density approximation (LDA), generalised gradient approximations (GGAs) and the Tran-Blaha modified Becke-Johnson (TB-mBJ) exchange potential. In Sec. 3.2.2, we outline another approach for the determination of the XC energy, the hybrid Heyd-Scuseria-Ernzerhof functional for solids (HSEsol). In Sec. 3.2.3, we overview the use of pseudopotentials for the description of the Kohn-Sham effective potential, and the projector augmented-wave (PAW) method for the description of all-electron wave functions. In Sec. 3.2.4, we describe the plane wave formalism for Kohn-Sham DFT calculations. Finally, in Sec. 3.3 we summarise and conclude.

We note that our analysis of III-P band parameters by means of DFT calculations in Chapter 6, using the methods outlined in this Chapter, are implemented using the Vienna Ab-initio Software Package (VASP) [62, 63].

3.1 Kohn-Sham density functional theory

In this Section we present an outline of the Kohn-Sham formulation of DFT, comprehensive detail of which is provided by Martin [64]. The Hohenberg-Kohn theorems outlined that the electron density $n(\mathbf{r})$ can be considered as a "basic variable", such that any system of many

interacting particles can be viewed as a functional of the ground state density $n_0(\mathbf{r})$ [65]. As such, this density determines all the information in the many-body wave function of the ground state. Kohn and Sham proposed an independent-particle approach for the determination of the density [66]. This approach, building upon the Hohenberg-Kohn theorems, approximates the density $n(\mathbf{r})$ via a set of independent wave functions $\psi_n(\mathbf{r}) = \langle \mathbf{r}|\psi_n\rangle$ as

$$n(\mathbf{r}) = \sum_{n\in \mathrm{occ}} |\psi_n(\mathbf{r})|^2 \,, \tag{3.1}$$

where n runs over all occupied states. In the Kohn-Sham formalism, all many-body effects are assumed to be encapsulated by an XC functional, however no exact functionals are known for any system of more than one electron [64]. We now outline the evaluation of the total energy of the a many-body system using the Kohn-Sham formalism.

In calculating the electronic ground state, the total energy of the system must be evaluated. The Hamiltonian operator for a system consisting of an arbitrary number of interacting electrons and nuclei can be written as [64]

$$\widehat{H} = \widehat{T} + \widehat{V}_{\mathrm{ext}} + \widehat{V}_{\mathrm{int}} + \widehat{T}_{\mathrm{nuc}} + E_{\mathrm{II}} \,, \tag{3.2}$$

where $\widehat{T}$ is the kinetic operator for the electrons, $\widehat{V}_{\mathrm{ext}}$ is the attractive electrostratic potential acting on the electrons due to the nuclei, $\widehat{V}_{\mathrm{int}}$ describes the repulsive electron-electron electrostatic interactions, $\widehat{T}_{\mathrm{nuc}}$ is the kinetic operator for the nuclei, and E_{II} describes the repulsive nucleus-nucleus interactions. The total energy of the system is given by the expectation value of Eq. (3.2)

$$E = \langle\psi|\, \widehat{H}\, |\psi\rangle \equiv \langle \widehat{H}\rangle \,, \tag{3.3}$$

where $\psi(\mathbf{r}) = \langle \mathbf{r}|\psi\rangle$ is the normalised wave function characterising the state of the many-electron system.

When providing an explicit form of Eq. (3.2), approximations can be made in order to simplify computation [64, 67]. The first of these is the Born-Oppenheimer approximation [68]. This approximation considers the movement of electrons and nuclei separately, and assumes that the nuclear positions are fixed. This approximation is made as the more massive nuclei move slowly compared with the motion of electrons. This allows for the separation of the wave function into parts containing the nuclear and electronic degrees of freedom independently as

$$|\psi\rangle = |\psi\rangle_e \times |\psi\rangle_I \,, \tag{3.4}$$

where $|\psi\rangle_e$ ($|\psi\rangle_I$) is the electron (nuclei) wavefunction. In the Born-Oppenheimer approximation, we focus on $|\psi\rangle_e$, which for simplicity we denote as $|\psi\rangle_e \equiv |\psi\rangle$. As such, in Eq. (3.2) we neglect $\widehat{T}_{\text{nuc}}$, the nuclei kinetic operator. This imposes that the nucleus-nucleus interactions E_{II} become constant [67] – i.e. simply a reference energy – with the nuclear positions becoming parameters. The total energy can then be written as

$$E = \langle \widehat{T} \rangle + \int V_{\text{ext}}(\mathbf{r})\, n(\mathbf{r})\, \mathrm{d}\mathbf{r} + \langle \widehat{V}_{\text{int}} \rangle \,. \tag{3.5}$$

The calculation of the expectation value of $\widehat{V}_{\text{int}}$, $\langle \widehat{V}_{\text{int}} \rangle$, is one of the main difficulties in DFT calculations [67]. As an approximation, $\langle \widehat{V}_{\text{int}} \rangle$ can be expressed as the sum of the classical electrostatic energy and the XC energy E_{XC}

$$\langle \widehat{V}_{\text{int}} \rangle = E_{\text{XC}} + \frac{1}{8\pi\epsilon_0} \int\int \frac{n(\mathbf{r})n(\mathbf{r}')}{|\mathbf{r}-\mathbf{r}'|}\, \mathrm{d}\mathbf{r}\, \mathrm{d}\mathbf{r}' \,, \tag{3.6}$$

where E_{XC} is the difference between the energy of the quantum-mechanical electron-electron interaction and that corresponding to the classical electrostatic electron-electron interaction, or Hartree energy E_{Hartree} [67]. Initial attempts to solve Eq. (3.5) by Thomas [69] and Fermi [70], leading to the Thomas-Fermi model, produced large errors compared to calculations that neglect E_{XC} [67]. To overcome the limitations of the Thomas-Fermi model, Kohn and Sham presented their formalism, as described in Eq. (3.1), where the density is constructed via a set of independent single-electron wave functions (the so-called Kohn-Sham orbitals). Using Eq. (3.1), the electron kinetic energy can be expressed as

$$T_{\text{KS}} = -\frac{\hbar^2}{2m_0} \sum_{n\in\text{occ}} \langle \psi_n | \nabla_n^2 | \psi_n \rangle \,, \tag{3.7}$$

so that the total energy can be written as

$$\begin{aligned} E_{\text{KS}} = \; & -\frac{\hbar^2}{2m_0} \sum_{n\in\text{occ}} \langle \psi_n | \nabla_n^2 | \psi_n \rangle + \int V_{\text{ext}}(\mathbf{r})\, n(\mathbf{r})\, \mathrm{d}\mathbf{r} + \frac{1}{8\pi\epsilon_0} \int\int \frac{n(\mathbf{r})n(\mathbf{r}')}{|\mathbf{r}-\mathbf{r}'|}\, \mathrm{d}\mathbf{r}\, \mathrm{d}\mathbf{r}' \\ & + E_{\text{XC}}[n(\mathbf{r})] + E_{\text{II}} \,. \end{aligned} \tag{3.8}$$

Having now expressed the total energy in the Kohn-Sham formalism, what remains is to determine the XC energy. Following from above, the XC energy can be written as

$$E_{\text{XC}} = \langle \widehat{T} \rangle - T_{\text{KS}} + \langle \widehat{V}_{\text{int}} \rangle - E_{\text{Hartree}} \,, \tag{3.9}$$

which expresses E_{XC} as the difference between the energy of the exact many-body interacting system and its energy calculated in the independent-electron approximation. Under application of the variational principle and treating the energy as a functional of the electron density, $E[n(\mathbf{r})]$, the Kohn-Sham eigenvalue equation, Hamiltonian $\widehat{H}_{\mathrm{KS}}$, and effective potential $\widehat{V}_{\mathrm{KS}}$ are given as [64]

$$\widehat{H}_{\mathrm{KS}}\psi_i(\mathbf{r}) = \epsilon_i\psi_i\,, \tag{3.10}$$

$$\widehat{H}_{\mathrm{KS}} = -\frac{\hbar^2}{2m_0}\nabla^2 + \widehat{V}_{\mathrm{KS}}(\mathbf{r})\,, \tag{3.11}$$

$$\widehat{V}_{\mathrm{KS}} = \widehat{V}_{\mathrm{ext}}(\mathbf{r}) + \frac{\delta E_{\mathrm{Hartree}}}{\delta n(\mathbf{r})} + \frac{\delta E_{\mathrm{XC}}}{\delta n(\mathbf{r})}\,, \tag{3.12}$$

where δ denotes the functional derivative. From Eq. (3.9), we see that the accuracy of the electronic ground state obtained from the implementation of the Kohn-Sham formulation of DFT relies heavily on the choice of XC functional $E_{\mathrm{XC}}[n(\mathbf{r})]$, the choice of which is non-trivial. Information regarding the choice of XC functionals employed in this work are provided in Sec. 3.2.

3.2 Considerations in the implementation of Kohn-Sham density functional theory

In this Section we provide a basic outline of the considerations and techniques employed in our implementation of the Kohn-Sham formalism of DFT, outlined in Sec. 3.1. We begin in Sec. 3.2.1 by describing the LDA. In Sec. 3.2.1 we also outline the TB-mBJ exchange potential, which with the LDA correlation can be combined to perform DFT calculations in the meta-GGA. Next, in Sec. 3.2.2 we detail hybrid functionals, specifically the HSEsol hybrid functional, as a generalisation of the Kohn-Sham approach. Following this, in Sec. 3.2.3 we describe the PAW method, which is a robust approach allowing for the computation of the many-electron ground state via DFT. Finally, in Sec. 3.2.4 we outline the plane wave formalism for implementing DFT calculations.

3.2.1 The local density approximation and Tran-Blaha modified Becke-Johnson exchange potential

As discussed in Sec. 3.1, the choice of XC functional is key in determining the accuracy of Kohn-Sham DFT calculations. One approach for determining the XC energy is the LDA, which builds on analysis of a uniform electron gas (UEG), where the system is completely specified by a constant density [64, 67, 71]

$$n = \frac{3}{4\pi r_s^3}\,, \tag{3.13}$$

where r_s is the Wigner-Seitz radius which defines a sphere containing one electron on average. Thus r_s measures the average distance between electrons in a UEG. In the LDA the XC energy is treated as an integral of the product of the electron density and the XC energy density over all space. In the LDA the XC energy density at each point is assumed to be equal to that in a UEG with density equal to the local density, $n(\mathbf{r})$. The LDA exchange energy $E_{\mathrm{X}}^{\mathrm{LDA}}$ is then given as a functional of the local charge density $n(\mathbf{r})$ as [64, 67]

$$E_{\mathrm{X}}^{\mathrm{LDA}}\left[n(\mathbf{r})\right] = \int n(\mathbf{r})\epsilon_{\mathrm{X}}^{\mathrm{UEG}}\left[n(\mathbf{r})\right]\mathrm{d}\mathbf{r}\,, \tag{3.14}$$

where $\epsilon_{\mathrm{X}}^{\mathrm{UEG}} = E_{\mathrm{X}}^{\mathrm{UEG}}/N_e$ is the exchange energy of the UEG per electron, with N_e being the total number of electrons, and $\epsilon_{\mathrm{X}}^{\mathrm{UEG}} \propto r_s^{-1}$. The remaining aspect of the LDA implementation is then to parametrise $\epsilon_{\mathrm{XC}}^{\mathrm{UEG}}$, which can be separated into exchange and correlation contributions, $\epsilon_{\mathrm{XC}}^{\mathrm{UEG}} = \epsilon_{\mathrm{X}}^{\mathrm{UEG}} + \epsilon_{\mathrm{C}}^{\mathrm{UEG}}$. The exchange contribution $\epsilon_{\mathrm{X}}^{\mathrm{UEG}}$ takes an analytical form [64, 67], while the correlation contribution $\epsilon_{\mathrm{C}}^{\mathrm{UEG}}$ must be numerically parametrised [64, 67]. There exist several approaches to parametrise $\epsilon_{\mathrm{C}}^{\mathrm{UEG}}$, one key example being that of Perdew and Zunger, where they fit to quantum Monte Carlo data for the energy of the UEG [72].

A key limitation of LDA DFT calculations is that they significantly underestimate the band gap of semiconductors and insulators [73]. While the approach of Perdew and Zunger [72] gives the exact XC energy for an idealised UEG with constant charge density, in real systems the charge density is position dependent [67], where $\epsilon_{\mathrm{XC}}(\mathbf{r})$ is dependent not only on the local density $n(\mathbf{r})$, but also semi-local contributions encapsulated by $\nabla n(\mathrm{r})$ and higher-order spatial derivatives. As such, we now examine methods beyond the LDA for the determination of the XC energy, which allow to address the band gap underestimation problem. In the GGA it is assumed that $\epsilon_{\mathrm{XC}}(\mathbf{r})$ is a functional of $n(\mathbf{r})$ and $\nabla n(\mathbf{r})$, which gives [64, 67, 74]

$$E_{\mathrm{XC}}^{\mathrm{GGA}}\left[n(\mathbf{r})\right] = \int n(\mathbf{r})\,\epsilon_{\mathrm{XC}}^{\mathrm{GGA}}\left[n(\mathbf{r}), \nabla n(\mathbf{r})\right]\,\mathrm{d}\mathbf{r}\,. \tag{3.15}$$

There exist a number of GGAs, such as the parametrisation of Perdew, Burke and Ernzerhof, the PBE functional [74]. Another approach is the meta-GGA, where an appropriate exchange potential is employed which takes into account the local kinetic energy density $\tau(\mathbf{r}) \propto \nabla^2 n(\mathbf{r})$. In the meta-GGA the XC functional is therefore given by

$$E_{\mathrm{XC}}^{\mathrm{mGGA}}\left[n(\mathbf{r})\right] = \int n(\mathbf{r})\, \epsilon_{\mathrm{XC}}^{\mathrm{mGGA}}\left[n(\mathbf{r}), \nabla n(\mathbf{r}), \nabla^2 n(\mathbf{r})\right]\, \mathrm{d}\mathbf{r}\,. \tag{3.16}$$

The TB-mBJ exchange potential proposed by Tran and Blaha [73], building on the work of Becke and Johnson [75], is an example of a meta-GGA approach to DFT. The TB-mBJ exchange potential yields calculated band gaps that achieve accuracy comparable to more computationally expensive approaches [73], making it an increasingly popular approach to analyse the electronic structure of semiconductor materials. The TB-mBJ exchange potential is [73]

$$V_{\mathrm{X}}^{\mathrm{mBJ}}(\mathbf{r}) = c\, V_{\mathrm{X}}^{\mathrm{BR}}(\mathbf{r}) + (3c-2)\frac{1}{\pi}\sqrt{\frac{5}{12}}\sqrt{\frac{2\tau(\mathbf{r})}{n(\mathbf{r})}}\,, \tag{3.17}$$

where $V^{\mathrm{BR}}(\mathbf{r})$ is the Becke-Roussel (BR) potential [76]

$$V^{\mathrm{BR}}(\mathbf{r}) = -\frac{1}{b(\mathbf{r})}\left(1 - e^{-x(\mathbf{r})} - \frac{1}{2}x(\mathbf{r})e^{-x(\mathbf{r})}\right)\,, \tag{3.18}$$

where $b(\mathbf{r}) = \left[x(\mathbf{r})e^{-x(\mathbf{r})}/\left(8\pi n(\mathbf{r})\right)\right]^{1/3}$. The function $x(\mathbf{r})$ is determined via the solutions of a position dependent non-linear equation which determines the exchange hole, exchange energy and corresponding exchange energy density [73, 76]. $x(\mathbf{r})$ is determined via $\tau(\mathbf{r})$, $n(\mathbf{r})$, $\nabla n(\mathbf{r})$, and $\nabla^2 n(\mathbf{r})$. The inclusion of this BR potential is weighted by the BR "mixing" parameter c, which Tran and Blaha chose to depend linearly on the square root of the average of $|\nabla n(\mathbf{r})|/n(\mathbf{r})$ as [73]

$$c = \alpha + \beta\left(\frac{1}{\Omega}\int_{\Omega}\frac{|\nabla n(\mathbf{r}')|}{n(\mathbf{r}')}\mathrm{d}\mathbf{r}'\right)^{1/2}\,, \tag{3.19}$$

where α and β are adjustable parameters, and Ω is the unit cell volume. We note that c can be treated as an empirical parameter through which to fit to an experimental band gap, an approach we will employ and analyse in Chapter 6. Tran and Blaha included the BR potential in their modifications to the Becke-Johnson potential, in order to model the Coulomb potential generated by the exchange hole, replacing the Slater potential proposed for this purpose by Becke and Johnson [75]. The TB-mBJ exchange potential recovers the LDA for a constant electron density and effectively mimics the behaviour of orbital-dependent potentials [73]. Therefore, the use of the TB-mBJ exchange potential, which is employed in conjunction with the LDA

correlation, is a computationally inexpensive approach for determining the XC potential in Kohn-Sham DFT. We note that the TB-mBJ is a "potential only" functional, meaning it has no associated XC energy, and is hence not self-consistent with respect to the total energy. The use of the TB-mBJ exchange potential improves the description of band gaps vs. the LDA alone [73]. However, a key issue with the TB-mBJ XC potential is its tendency to overestimate band edge effective masses [77, 78]. As a result, to describe the electronic structure with even greater accuracy, below we will examine hybrid functional approaches for the determination of the XC energy. Finally, we note that since TB-mBJ is a "potential only" functional, it is not possible to employ TB-mBJ to compute Hellmann-Feynmann ionic forces, thus meaning that it is not possible to perform structural relaxation using this method. In Chapter 6, we therefore combine LDA calculations of structural properties with TB-mBJ calculations to analyse the electronic structure at the meta-GGA level.

3.2.2 The Heyd-Scuseria-Ernzerhof hybrid functional for solids

In Sec. 3.2.1, we described the determination of the XC functional using (i) the LDA, (ii) the PBE GGA, and (iii) the TB-mBJ meta-GGA. These approximations to the XC energy retain limitations and can produce systematic errors in the calculation of several key material properties [79]. For example, the LDA (PBE) XC functional typically underestimates (overestimates) the lattice parameter by 1 - 2%, and the error in PBE-calculated lattice parameters systematically increases with increasing ionic mass [79]. To address limitations of this type, so-called generalised, or "hybrid", Kohn-Sham approaches have emerged [80]. This generalised formalism involves introducing a portion of exact Hartree-Fock exchange into the XC energy. The HSE screened hybrid functional, introduced by Heyd, Scuseria and Ernzerhof [81], is one such approach. In general, hybrid XC functionals describe a number of chemical properties accurately but, typically, with the trade-off that the calculation of the Hartree-Fock exchange term is highly computationally expensive [81]. The HSE functional is based on a screened Coulomb potential for the exchange interaction which partially mitigates this issue. In the HSE approach, the Coulomb kernel for the exchange energy is separated into short-range (SR) and long-range (LR) contributions following [67]

$$\frac{1}{|\mathbf{r}-\mathbf{r}'|} = \underbrace{\frac{\operatorname{erfc}(\mu|\mathbf{r}-\mathbf{r}'|)}{|\mathbf{r}-\mathbf{r}'|}}_{\text{SR}} + \underbrace{\frac{\operatorname{erf}(\mu|\mathbf{r}-\mathbf{r}'|)}{|\mathbf{r}-\mathbf{r}'|}}_{\text{LR}}, \tag{3.20}$$

where erf and erfc are the error and complementary error functions, respectively, and μ^{-1} is the distance at which the range separation is imposed. In the HSE approximation, only a portion of the SR exchange is Hartree-Fock (HF), the remainder of the exchange energy is determined via the PBE functional [67]. The HSE XC energy is expressed as [81]

$$E_{\mathrm{XC}}^{\mathrm{HSE}} = \alpha E_{\mathrm{X}}^{\mathrm{HF,SR}}(\mu) + (1-\alpha)E_{\mathrm{X}}^{\mathrm{PBE,SR}}(\mu) + E_{\mathrm{X}}^{\mathrm{PBE,LR}}(\mu) + E_{\mathrm{C}}^{\mathrm{PBE}}\,, \tag{3.21}$$

where α is the exact-exchange mixing parameter determining how much exact-exchange is included in the calculation. We employ the typical value $\mu = 0.2$ Å^{-1} [67]. This approach yields an improved description of many chemical properties, particularly in comparison to the pure PBE functional [79]. Notably, the HSE description of the XC energy effectively addresses the band gap underestimation problem that limits the applicability of the LDA, as well as many GGA and meta-GGA approaches (cf. Sec. 3.2.1). However, the tendency of the PBE functional to overestimate lattice parameters and incorrectly describe atomisation energies is retained [79]. To address these issues, the HSE functional for solids (HSEsol) was introduced by Schimka et al. [79]. The HSEsol XC functional takes the same form as the HSE functional in Eq. (3.21), but is based on the PBEsol functional for the semi-local exchange and correlation terms, where PBEsol is the revised PBE functional for solids [82]. The use of the PBEsol XC functional provides an improved description of equilibrium properties of solids and surfaces [82, 83]. The use of the HSEsol hybrid functional has demonstrated an improved description of the chemical properties of solids vs. other XC functionals, including the lattice parameters and enthalpies of formation [79], and notably the accurate description of band edge effective masses [78]. Crucially, the HSEsol functional provides an improved description of these material properties while producing accurate band gaps [79]. Like the BR mixing c in the TB-mBJ exchange potential, the exact exchange mixing α in the HSE(sol) XC functional can be treated as an empirical parameter to fit to a target band gap. Therefore, in employing the HSEsol XC functional in our analysis of III-P band parameters in Chapter 6, we apply this procedure and undertake a critical analysis of its performance vs. experiment.

3.2.3 Pseudopotentials and the projector augmented-wave method

A pseudopotential is an effective potential constructed to replace the strong Coulomb potential of the nucleus and the effects of the tightly bound core electrons by an effective ionic potential acting on the valence electrons beyond a certain cut-off distance from the nucleus, or ionic core [64, 84]. This pseudopotential can then be substituted for the all-electron potential of Eq. (3.2). In a psuedopotential calculation, the "core" consists of the nucleus and electrons occupying orbitals in filled shells, which are strongly localised around the nucleus [67]. Beyond the cut-off distance, outside the core region, the potential is that of the Coulomb interaction between the core and each of the valence electrons. Inside the core region the true potential, which is characterised by rapid spatial oscillations, is challenging to describe numerically, mandating very fine grid point spacing in real space calculations, or very high plane wave cut-off energy in reciprocal space calculations. Numerically, this true potential is replaced by a smooth function. Pseudopotentials are constructed so that the valence electron wave functions outside the core region

are the same as those of an all-electron calculation. The use of pseudopotentials is strongly motivated by the fact that most chemical properties can be modelled accurately in calculations which only account for valence states. As outlined above, pseudopotentials additionally offer a numerically efficient platform to perform such calculations. The valence states typically have minimal interaction with the core states, a result of tightly bound core states possessing significantly lower energies. Notable exceptions to this are elements possessing "shallow core" or "semi-core" states, which possess energies large enough to influence chemical properties [67, 85].

The PAW method, originally introduced by Blöchl [84], has gained popularity for the description of psuedopotentials. The PAW method offers computational advantages compared to other approaches, such as norm-conserving and ultra-soft pseudopotentials [86]. The PAW method considers a linear transformation $\widehat{\mathcal{T}}$ relating the all-electron valence wave function $|\psi\rangle$ and the smooth pseudo wave function $|\psi_{\mathrm{PS}}\rangle$. $\widehat{\mathcal{T}}$ is equal to the identity operator $\widehat{I}$ outside of the core region, i.e. $|\psi\rangle$ and $|\psi_{\mathrm{PS}}\rangle$ are set equal outside of the core region, with $\widehat{\mathcal{T}} = \widehat{I} + \widehat{\mathcal{T}}_R$ defining the transformation operator $\widehat{\mathcal{T}}_R$ acting within the core region. $\widehat{\mathcal{T}}_R$ is specified by two sets of partial waves, the all-electron partial waves $|\phi_k\rangle$ and the pseudo partial waves $|\phi_k^{\mathrm{PS}}\rangle$ which, within the core region, give

$$|\psi\rangle = \sum_k c_k \, |\phi_k\rangle \ , \tag{3.22}$$

$$|\psi_{\mathrm{PS}}\rangle = \sum_k c_k \, |\phi_k^{\mathrm{PS}}\rangle \ , \tag{3.23}$$

where the expansion coefficients $c_k = \langle p_k | \phi_k^{\mathrm{PS}} \rangle$ are determined by the projector $\langle p_k|$, which resolves the identity via $\sum_k |\phi_k^{\mathrm{PS}}\rangle \langle p_k| = \widehat{I}$ within the core region. It follows that the transformation $\widehat{\mathcal{T}}$ can be written as

$$\widehat{\mathcal{T}} = \widehat{I} + \sum_k \left(|\phi_k\rangle - |\phi_k^{\mathrm{PS}}\rangle \right) \langle p_k| \ . \tag{3.24}$$

In the PAW method, the all-electron wave function $|\psi\rangle$ can then be obtained from the pseudo wave function $|\psi^{\mathrm{PS}}\rangle$ as

$$|\psi\rangle = |\psi^{\mathrm{PS}}\rangle + \sum_k \left(|\phi_k\rangle - |\phi_k^{\mathrm{PS}}\rangle \right) \langle p_k | \psi^{\mathrm{PS}} \rangle \ . \tag{3.25}$$

Guidelines for the implementation of the all-electron operators as pseudo operators, and expressions for the charge density and total energy, are given by Blöchl in Ref. [84]. Further technical

details regarding the implementation of the PAW method are given by Kresse and Joubert in Ref. [86].

3.2.4 The plane wave formalism

As shown in Sec. 2.2, formulating electronic structure calculations using plane waves is effective as a result of the periodic nature of crystalline materials. Expanding the Kohn-Sham wave functions in a plane wave basis is an approach employed by a number of DFT codes, including the VASP code employed in this work. The plane-wave expansion is expressed in three-dimensions as

$$\psi_{n\mathbf{k}}(\mathbf{r}) = \frac{1}{\sqrt{\Omega}} \sum_{\mathbf{G}} a_{n\mathbf{k}\mathbf{G}}\, e^{i(\mathbf{k}+\mathbf{G})\cdot\mathbf{r}}\,, \tag{3.26}$$

where $a_{n,\mathbf{G}}(\mathbf{k})$ are the Fourier expansion coefficients of the single-particle eigenstates, for which there is one eigenvalue $\epsilon_n(\mathbf{k})$ per $\mathbf{k}$-point per band n, we are operating in the momentum basis $|\mathbf{q}\rangle = |\mathbf{k}+\mathbf{G}\rangle$, and note that $\langle\mathbf{r}|\mathbf{k}+\mathbf{G}\rangle = \frac{e^{i(\mathbf{k}+\mathbf{G})\cdot\mathbf{r}}}{\sqrt{\Omega}}$, denoting the real-space representation of the plane wave basis states. In plane wave DFT calculations, the cut-off wave vector G_{cut} determines the cut-off energy $E_{\text{cut}} = \frac{\hbar^2}{2m}G_{\text{cut}}^2$, which specifies the basis set via $|\mathbf{G}+\mathbf{k}| < G_{\text{cut}}$. As such, all plane waves with a kinetic energy smaller than E_{cut} are included in the basis set. The choice of cut-off energy is analogous to the choice of the total number of plane waves in the plane wave expansion method (cf. Sec. 2.2). For any function $f(\mathbf{r})$ sharing the same periodicity as the lattice, $f(\mathbf{r}) = f(\mathbf{r}+\mathbf{R})$ (cf. Sec. 2.1.1), the Fourier transform $\widetilde{f}(\mathbf{G})$ of $f(\mathbf{r})$ is non-zero only when $\mathbf{G}$ is a reciprocal lattice vector. The Fourier transform of the function $f(\mathbf{r})$ is defined as

$$\tilde{f}(\mathbf{G}) = \frac{1}{\Omega}\int_{\Omega} f(\mathbf{r}) e^{-i\mathbf{G}\cdot\mathbf{r}} \mathrm{d}\mathbf{r}\,, \tag{3.27}$$

where $\Omega = \mathbf{a}_1\cdot(\mathbf{a}_2\times\mathbf{a}_3)$ is the unit cell volume (cf. Sec. 6.2.1). If the single-electron (Kohn-Sham) Hamiltonian $\widehat{H}$ is given by the sum of the kinetic energy operator and an effective potential $V_{\text{eff}}(\mathbf{r})$, the Kohn-Sham equation can be written as [64]

$$\sum_{\mathbf{G}'} H_{\mathbf{G},\mathbf{G}'}(\mathbf{k}) a_{n,\mathbf{G}'}(\mathbf{k}) = \epsilon_n(\mathbf{k}) a_{n,\mathbf{G}}(\mathbf{k})\,. \tag{3.28}$$

We note that the Fourier transform applied in obtaining Eq. (3.28), mirrors the plane wave expansion method introduced in the context of $\mathbf{k}\cdot\mathbf{p}$-based heterostructure calculations in Sec. 2.2. These approaches to solving the relevant Schrödinger equations – i.e. the coupled multi-band

envelope function Schrödinger equations in $\mathbf{k}\cdot\mathbf{p}$ calculations, or the Kohn-Sham equations in DFT – are formally equivalent, and lead to a reciprocal space representation of Schrödinger's equation. The matrix elements $H_{\mathbf{G},\mathbf{G}'}$ of the Kohn-Sham Hamiltonian are given by

$$H_{\mathbf{G},\mathbf{G}'}(\mathbf{k}) = \frac{\hbar^2}{2m_0}|\mathbf{k}+\mathbf{G}|^2\delta_{\mathbf{G},\mathbf{G}'} + \widetilde{V}_{\text{eff}}(\mathbf{G}-\mathbf{G}')\,, \tag{3.29}$$

where $\widetilde{V}_{\text{eff}}(\mathbf{G}-\mathbf{G}')$ is the Fourier transform of the effective potential (cf. Sec. 3.1). Convergence in plane wave DFT calculations is determined, in part, by the size of the corresponding basis set [67]. Computing the electronic contribution to the total energy mandates including all contributions from filled (valence) bands at all wave vectors $\mathbf{k}$ in the Brillouin zone. The Kohn-Sham equations must be solved at wave vectors $\mathbf{k}$ throughout the Brillouin zone and an integral with respect to $\mathbf{k}$ must then be performed. Therefore, as Eq. (3.28) must be solved at each $\mathbf{k}$-point, the evaluation of any function accurately becomes computationally expensive in realistic calculations with large numbers of $\mathbf{k}$-points. Given a $\mathbf{k}$-dependent function $\eta_n(\mathbf{k})$, the integral, where the summation takes place over energy bands n, is

$$\begin{aligned}\int \eta_n \,\mathrm{d}\mathbf{k} &= \frac{1}{(2\pi)^3}\sum_n \int_{\mathrm{BZ}} \eta_n(\mathbf{k}) f_{n,\mathbf{k}} \mathrm{d}\mathbf{k}\,, \\ &\to \frac{1}{(2\pi)^3}\frac{1}{\Omega}\sum_{\mathbf{k}} w_{\mathbf{k}}\,\eta_n(\mathbf{k})\,f_{n,\mathbf{k}}\,,\end{aligned} \tag{3.30}$$

where the occupancy $f_{n,\mathbf{k}}$, in the zero-temperature limit, is given by 1 (occupied) or 0 (unoccupied), and $w_{\mathbf{k}}$ is a weighting factor related to the distribution of $\mathbf{k}$ states chosen. In the finite-temperature case, the occupancies can vary continuously between 0 and 1. The accuracy of calculating any function following Eq. (3.30) is determined by the density and choice of the weighted sum over $\mathbf{k}$-points.

As the number of $\mathbf{k}$-points included in a calculation increases, the accuracy of the numerical approximation to the integral in Eq. (3.30) will improve [67]. However, calculations using large numbers of $\mathbf{k}$-points quickly become computationally prohibitive, meaning that there must be careful consideration of the $\mathbf{k}$-points employed in DFT calculations. For energies near the Fermi level, the occupancies will, in general, vary for the same band at different $\mathbf{k}$-points. For narrow-gap semiconductors and metals, a large number of $\mathbf{k}$-points may be required to reconstruct the Fermi surface [87]. This is not an issue for the relatively wide gap semiconductors considered in this Thesis, but can pose computational challenges for convergence vs. the number of $\mathbf{k}$-points employed in the BZ integration in other cases. The smearing method, originally introduced by Fu and Ho [87], is one technique to accelerate this convergence with $\mathbf{k}$-points. This approach "smears" the energies of each of the eigenstates using, e.g., a Gaussian distribution. The Fermi

energy is then calculated from the density of states given by the smeared energies. Then, the partial occupancy of each band equals the portion of its smeared value lying below the calculated Fermi energy [87]. This mandates the total energy E being replaced by a generalised free energy F, that latter containing an extra term that depends on the partial occupancies [63], resembling the entropy of the finite-temperature case [67].

We note that, in numerical Kohn-Sham DFT calculations, the Schrödinger equation is solved self-consistently via an iterative procedure. Beginning from an initial charge density and iteratively optimising towards convergence, the Kohn-Sham Hamiltonian is specified and the single-particle eigenstates computed, with these eigenstates then employed to construct an updated charge density (cf. Eq. (3.1)). This updated charge density then serves as the input for the next iteration, and the procedure is iterated until the difference in total energy between two consecutive iterations has converged to a desired precision – i.e. achieving so-called charge self-consistency. Upon the completion of this self-consistent cycle the final single-particle eigenstates (Kohn-Sham orbitals) define a converged charge density which, due to the Hohenberg-Kohn theorems, uniquely determines the electronic ground state [65].

3.3 Conclusions

In this Chapter we have presented the theoretical methods employed in our analysis of the electronic band parameters of the III-P compounds AlP, GaP and InP in Chapter 6. We began in Sec. 3.1 by presenting an overview of the Kohn-Sham formalism of DFT. We described the approach to compute the total energy of a many-electron system in this formalism, where having used the Born-Oppenheimer approximation to freeze the nuclei and separate the electrons and nuclei, and their interactions, the many-electron problem is tackled using the single-electron Kohn-Sham approach. We described how, under the application of appropriate approximations, the accuracy of the implementation of the Kohn-Sham formalism can be largely determined by the XC energy. The XC energy is defined as the energy difference between the exact many-body interacting system and the non-interacting electron density, described by a set of independent wave functions. In Secs. 3.2.1 and 3.2.2, we then provided detail on the treatment of the XC energy as a functional of the electron density. In Sec. 3.2.1, we began with the description of the LDA, an XC functional corresponding to a UEG where the electron density is treated as constant. We then described the GGA and meta-GGA, which go beyond the LDA by including semi-local effects via spatial derivatives of the electron density. We described the TB-mBJ exchange potential in which the Coulomb potential created by the exchange hole is modelled via the BR potential. The TB-mBJ scheme is a potential only approach and must therefore be employed in conjunction with the LDA correlation, but delivers improved description of the electronic structure vs. LDA alone. Notably the TB-mBJ approach overcomes the band gap underestimation problem present in the LDA. In Sec. 3.2.2, we outlined the

hybrid HSEsol XC functional, a hybrid XC functional that combines the PBEsol functional with a fraction α of the exact Hartree-Fock exchange energy. In Sec. 3.2.2, we described that the HSEsol functional provides an accurate description of the chemical properties of solids in Kohn-Sham formalised DFT, including providing an accurate description of the band edge effective masses and the band gaps of semiconductors and insulators. Next, in Sec. 3.2.3 we described pseudopotentials, and the PAW method, which is a robust and efficient approach to compute the all-electron wave function, that represents an extension of the commonly employed pseudopotential approach. In Sec. 3.2.4, we then outline the plane wave formalism for DFT calculations, and how this technique offers a computationally efficient basis for DFT calculations, akin to benefits offered by the plane wave expansion method seen in Chapter 2. The theoretical methods and technical details outlined in this Chapter will underpin our analysis of III-P band parameters in Chapter 6.

Chapter 4

Optimisation of radiative recombination in InAs/GaSb superlattices

4.1 Overview

The narrow-gap semiconductors InAs and GaSb, members of the so-called "6.1 Å family" of III-V compounds [15], combine low lattice mismatch, $\sim 0.6\%$, with a large valence band (VB) offset that produces an unusual type-III ("broken-gap") band alignment. Type-III band alignment means that the VB maximum in the hole confining layers lies higher in energy than the conduction band (CB) minimum in the electron confining layers (cf. Sec. 1.1). This low lattice mismatch allows for growth of high-quality superlattices (SLs) consisting of alternating InAs and GaSb layers, and has established InAs/GaSb SLs as the archetypal broken-gap SL system. Research effort on InAs/GaSb SLs and quantum wells (QWs) has been sustained since their initial fabrication in the late-1970s [12] by the vast possibilities offered by their highly tunable electronic structure, which continues to attract interest from both fundamental and applied perspectives. From a fundamental perspective InAs/GaSb SLs are an established reference system for electronic structure methodologies, including empirical atomistic [88–93] and continuum ($\mathbf{k}\cdot\mathbf{p}$-based) [94–97] models and, more recently, first principles calculations [98–102]. In addition to sustained interest from the perspective of mid-infrared (mid-IR) photonics, InAs/GaSb heterostructures have over the past 15 years also attracted significant interest for the engineering of topologically non-trivial electronic states [103–105]. This includes the pursuit of Majorana fermions as a platform for fault-tolerant topological quantum computation [106].

From a practical perspective, there exists a strong imperative to develop efficient and cost-effective mid-IR light sources for a broad range of sensing applications relevant to the environmental, industrial, medical, agricultural and defence sectors [2–5]. While quantum cascade laser (QCL) technology is well-established [4, 9, 10], QCL performance degrades for wavelengths $\lesssim 4$ μm and their deployment presents the dual challenges of complex fabrication and high cost. This represents a significant opportunity for the development of mid-IR light-emitting diodes (LEDs) and diode lasers based on III-V semiconductor heterostructures. Such devices have the potential to deliver simplified fabrication, lower cost and reduced power consumption compared to QCL technologies, and to significantly improve performance compared to existing incandescent light sources [107]. Mid-infrared emitters based on QWs having type-I band offsets experience performance degradation with increasing wavelength, due to a combination of thermal carrier leakage and high non-radiative Auger recombination rates [108, 109]. Heterostructures having type-II (staggered-gap) band offsets have attracted significant attention for the development of mid-IR emitters [20, 110–113]. Compared to QWs or SLs having type-I (spatially direct) band offsets, they offer a combination of enhanced electrical confinement and intrinsically low Auger recombination rates [114]. This can enhance internal quantum efficiency by respectively mitigating carrier leakage and reducing non-radiative losses [115, 116]. InAs/GaSb SLs, already the basis of demonstrated mid-IR photodetectors [17–19], have continued to attract interest as a candidate platform for the development of mid-IR LEDs. Progress on light-emitting InAs/-GaSb SLs has included fabrication of prototype inter-band cascade LEDs (IC-LEDs) by several groups [117–119]. These prototypes have demonstrated promising characteristics such as low turn-on voltage, low series resistance, and room temperature radiance approaching 1 W cm^{-2} sr^{-1} [16].

We undertake a detailed analysis of the electronic structure of, and radiative recombination in, InAs/GaSb SLs. Recombination processes in these structures have been the subject of previous theoretical analysis [120]. However, to our knowledge, there has been no detailed discussion of the explicit role played by various aspects of the underlying electronic structure in determining the radiative recombination rate and its temperature dependence. Additionally, no systematic in silico optimisation of the radiative recombination rate as a function of emission wavelength has been carried out. It is to these two issues that we dedicate our attention. In our calculations we employ a Cartesian coordinate system in which the x, y and z axes respectively align with the [100], [010] and [001] principal crystal axes. We consider InAs/GaSb SLs grown on an [001]-orientated InAs substrate, with k_z then being quantised in the [001]-orientated SL calculations. As detailed in Chapter 2, we recapitulate the calculation of SL electronic structure using a multi-band $\mathbf{k}\cdot\mathbf{p}$ Hamiltonian, employing here a reciprocal space plane wave expansion method (PWEM). This numerically efficient approach allows the miniband dispersion to be computed explicitly using a calculational supercell consisting of a single SL period. We highlight that analysis of the bulk *complex* band structure is essential to identify

and inform mitigation of spurious solutions in $\mathbf{k}\cdot\mathbf{p}$-based heterostructure calculations. By reassessing the fundamentals of the InAs/GaSb SL electronic structure we identify and quantify the role played by miniband formation in determining the radiative recombination rate, which we quantify via the radiative recombination coefficient B. By comparing the results of our full SL calculations to test calculations for an equivalent QW - i.e. by neglecting miniband dispersion - we highlight the importance of the mismatch in electron and hole miniband dispersion in influencing the magnitude of B and its temperature dependence. We demonstrate that the formation of minibands acts to reduce the magnitude of B, while simultaneously reducing the rate at which B decreases with increasing temperature, and identify that this behaviour has originates from the mismatch in dispersion between the highly (minimally) dispersive electron (hole) minibands. This analysis quantifies the potential enhancement in radiative recombination rate that could be achieved by engineering SL band structure to better match electron and hole miniband dispersion, in a manner akin to that achieved by exploiting the impact of strain on the VB dispersion in QW lasers [121, 122]. This provides guidance to inform structural optimisation to enhance the internal quantum efficiency of SL-based emitters. Finally, we perform high-throughput calculations in which the relative thickness of the InAs and GaSb layers that constitute each period of the SL are varied, identifying combinations of layer thickness that maximise B at room temperature for emission wavelengths spanning the 3.5 – 7 μm range.

The rest of this chapter is organised as follows. In Sec. 4.2 we describe the reparametrisation (cf. Sec. 4.2.1) and benchmarking (cf. Sec. 4.2.2) of the 8-band $\mathbf{k}\cdot\mathbf{p}$ model, to mitigate the impact of spurious solutions in electronic structure calculations. In Sec. 4.3 we present our analysis of the electronic properties of InAs/GaSb SLs. In Sec. 4.3.1 we describe the impact of the spatially indirect type-III band offsets and narrow layer thicknesses on the optoelectronic properties, and as a result the radiative performance, in InAs/GaSb SLs. In Sec. 4.3.2 we describe the associated electronic band structure. In Sec. 4.4 we investigate trends in the optical properties of InAs/GaSb SLs. In Sec. 4.4.1 we analyse trends in the inter-band optical (momentum) matrix elements and spontaneous emission (SE). In Sec. 4.4.2 we quantify and analyse the radiative performance of an exemplar InAs/GaSb SL, and in Sec. 4.4.3 we investigate the potential for optimisation of InAs/GaSb SLs to establish guidelines for epitaxial growth. In Sec. 4.5 we summarise our analysis and conclude.

4.2 $\mathbf{k}\cdot\mathbf{p}$ model reparametrisation and benchmarking

In this section we present our analysis and key considerations for the application of the 8-band $\mathbf{k}\cdot\mathbf{p}$ method in conjunction with the PWEM, outlined in Chapter 2, to enable investigation of the electronic structure of type-III ("broken gap") InAs/GaSb SLs. Accurate and reliable electronic structure is required to analyse these SLs. In order to achieve this description accurately we investigate the presence of spurious solutions, which can "pollute" electronic structure

calculations and hence those of optical properties. This investigation includes a reparametrisation of the 8-band Hamlitonian which we benchmark via comparison to literature theoretical calculations and experimental measurements.

4.2.1 Spurious solutions and model reparametrisation

The 8-band $\mathbf{k} \cdot \mathbf{p}$ Hamiltonian for zinc blende is known to provide an incomplete description of the electronic structure of tetrahedrally-bonded ("pyramid-like") semiconductors – i.e. semiconductors in which each atom is polar covalent bonded to four nearest neighbours, with these nearest neighbours residing at the vertices of a tetrahedron. The incompleteness of this description can lead to the introduction of spurious solutions in the bulk band dispersion [123]. These spurious solutions can manifest as states having energies lying within the band gap and/or possessing complex-valued wave vectors. When performing heterostructure calculations, the presence of such solutions must be carefully considered and mitigated to obtain reliable electronic properties.

We begin our analysis by using the InAs and GaSb bulk band parameters, including the Varshni parameters for the bulk band gap temperature dependence and the InAs/GaSb VB offset (= 0.56 eV), recommended by Vurgaftman et al [44]. We note that the reduction of the band gap of a semiconductor with increasing temperature has two contributions: lattice thermal expansion and electron-phonon coupling [124, 125]. The Varshni relation is parametrised by fitting to the experimentally measured temperature-dependent band gap, and therefore implicitly contains both contributions. In principle, lattice thermal expansion could be considered by employing temperature-dependent lattice parameters to compute the strain in each layer of the heterostructure. We therefore restrict the temperature dependence of our band parameters to the bulk InAs and GaSb band gaps only. Test calculations verify that, since we keep the Kane parameter E_P fixed vs. temperature, the reduction in bulk band gap with increasing temperature leads to a reduction in band edge effective mass in line with experimental measurements [126]. As we will describe below, some of the bulk band parameters recommended in Ref. [44] require modification to mitigate the deleterious impact of unphysical spurious solutions on the calculated SL eigenstates. Following Ref. [127] we neglect the impact of strain on the SL band structure, due to the small lattice mismatch between InAs and GaSb. This is consistent with the x-ray diffraction measurements of Ref. [16], which demonstrated lattice mismatch $\sim 10^{-5}$ with respect to the InAs substrate for the InAs/GaSb SLs against whose experimental characterisation we will benchmark our calculations in Sec. 4.2.2.

In the 8-band $\mathbf{k} \cdot \mathbf{p}$ Hamiltonian the CB dispersion is described in part by the parameter s_c, alternatively denoted by A_c in the literature [128, 129],

$$s_c = \frac{1}{m_c^*} - \frac{E_P}{3}\left(\frac{2}{E_g} + \frac{1}{E_g + \Delta_0}\right), \tag{4.1}$$

where the first and second terms respectively describe the free-electron and remote-band contributions to the CB edge effective mass m_c^*, where E_g and Δ_0 are the Γ-point band gap and VB spin-orbit splitting, and E_P is the Kane parameter. This parameter appears in the Hamiltonian as $\frac{\hbar^2 k^2}{2m_0}\, s_c$ and, since $s_c < 0$ for most conventional semiconductors [44], this can lead to unphysical downward bending of the CB dispersion into the band gap at large $k = |\mathbf{k}|$. This is of particular importance for the simulation of short-period SL structures using the PWEM. Since $G_m \propto L^{-1}$, the plane wave basis set can readily sample wave vectors corresponding to large real values of the bulk k_z in short-period SL heterostructures. This can therefore pollute the heterostructure eigenstates by sampling spurious large-k_z bulk states. Additionally, InAs/-GaSb SLs demonstrate type-II-like (spatially indirect) carrier confinement, so that the Bloch character of a given eigenstate can abruptly change from being, e.g., predominantly CB-like to predominantly VB-like across an InAs/GaSb interface for a bound electron state. These factors mandate careful selection of the (i) band parameters, and (ii) plane wave basis set, in numerical calculations.

We work with the 8-band $\mathbf{k}\cdot\mathbf{p}$ Hamiltonian in the total angular momentum basis $|J; m_J\rangle$ of zone-centre Bloch states that diagonalise the spin-orbit interaction [51, 52]. With $k_x = k_y = 0$ the Hamiltonian block diagonalises such that the heavy-hole (HH) VB is decoupled, with the dispersion of the light-hole (LH) and spin-split-off (SO) VBs and the lowest energy CB along [001] then described by the 3×3 Hamiltonian

$$H_{3\times3}(k_z) = \begin{pmatrix} E_g + \frac{\hbar^2}{2m_0}\, s_c\, k_z^2 & \sqrt{\frac{2}{3}} P k_z & -\frac{1}{\sqrt{3}} P k_z \\ \sqrt{\frac{2}{3}} P k_z & -\frac{\hbar^2}{2m_0}\left(\gamma_1 + 2\gamma_2\right) k_z^2 & \sqrt{2}\frac{\hbar^2}{m_0}\gamma_2\, k_z^2 \\ -\frac{1}{\sqrt{3}} P k_z & \sqrt{2}\frac{\hbar^2}{m_0}\gamma_2\, k_z^2 & -\Delta_0 - \frac{\hbar^2}{2m_0}\gamma_1\, k_z^2 \end{pmatrix} \begin{matrix} |\frac{1}{2}; \pm\frac{1}{2}\rangle \\ |\frac{3}{2}; \pm\frac{1}{2}\rangle \\ |\frac{1}{2}; \pm\frac{1}{2}\rangle \end{matrix}, \tag{4.2}$$

where P is the inter-band (Kane) momentum matrix element, related to the Kane parameter via $E_P = \frac{2m_0 P^2}{\hbar^2}$.

We compute the complex band structure admitted by Eq. (4.2) using the eigenvalue method described in Ref. [130]. We write Eq. (4.2) as $H_{3\times3}(k_z) = H^{(0)} + H^{(1)}k_z + H^{(2)}k_z^2$, where $H^{(0)}$, $H^{(1)}$ and $H^{(2)}$ are the 3×3 coefficient matrices for terms in Eq. (4.2) that are respectively independent of k_z, linear in k_z and quadratic in k_z. Using these coefficient matrices we construct the 6×6 "companion" matrix to $H_{3\times3}(k_z)$

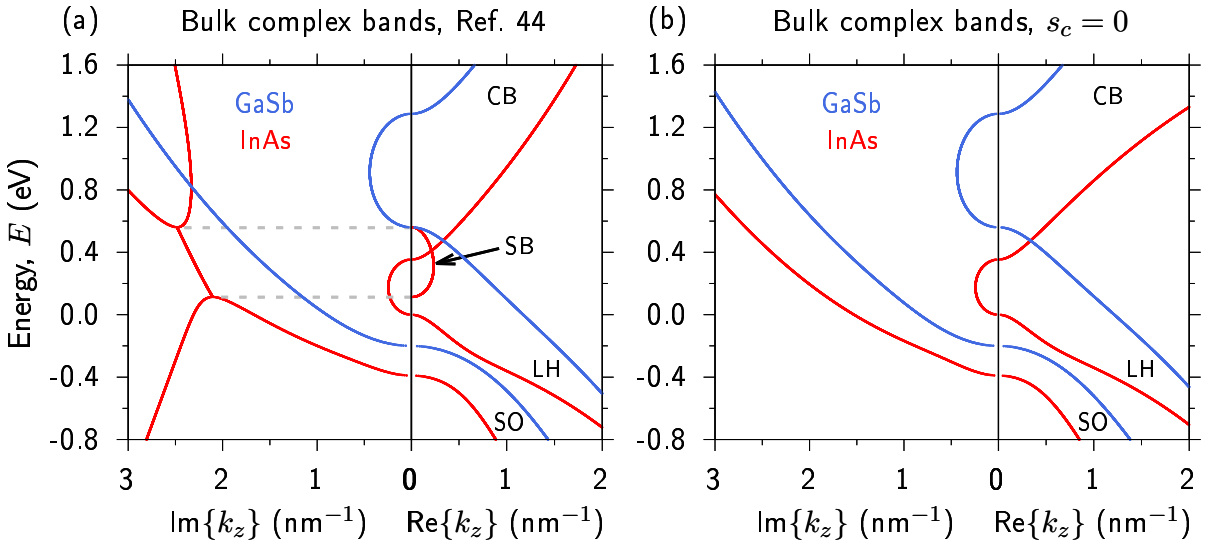


FIGURE 4.1: (a) Complex band structure of bulk InAs (solid red lines) and GaSb (solid blue lines) along [001], using an 8-band $\mathbf{k}\cdot\mathbf{p}$ Hamiltonian with the parameters of Ref. [44]. The arrow highlights the real k_z component of a spurious band (SB) lying close in energy to the InAs CB edge, with the imaginary component of the SB lying in the same energy range in the left-hand panel. (b) As in (a), but using renormalised parameters in which $s_c = 0$.

$$C(E) = \begin{pmatrix} 0 & I \\ -(H^{(2)})^{-1}(H^{(0)} - EI) & -(H^{(2)})^{-1}H^{(1)} \end{pmatrix}, \tag{4.3}$$

where I is the 3×3 identity matrix. Diagonalising Eq. (4.3) as a function of energy E then yields the, in general, complex-valued wave vectors $k_{z,n}(E, k_x = 0, k_y = 0)$.

Solid red and blue lines in Fig. 4.1(a) respectively show the bulk complex band structure, at temperature $T = 300$ K, computed along k_z for InAs and GaSb, with $\mathbf{k}_{\|} = 0$. This is done using the 8-band $\mathbf{k}\cdot\mathbf{p}$ Hamiltonian parameterised following Ref. [44]. The zero of energy is set at the InAs VB maximum. The left- and right-hand panels of Fig. 4.1(a) respectively show the imaginary and real parts of k_z associated with each bulk state at energy E. Note that we have omitted HH bands from Figs. 4.1(a) and 4.1(b) for simplicity, since the HH band decouples from the CB, LH and SO bands along [001] and is hence not relevant to this discussion.

The InAs complex band dispersion in Fig. 4.1(a) reveals the presence of a spurious band (SB), which has complex-valued k_z and straddles the CB minimum in the energy range 0.11 – 0.55 eV (highlighted by horizontal dashed grey lines). This SB originates due to the presence of a large negative value $s_c \approx -11.7$, and occurs in an energy range in which a purely imaginary (evanescent) band having Im$\{k_z\} \approx 2.5$ nm^{-1} across the full plotted energy range intersects the evanescent band originating from the SO VB. As described above, large negative values of s_c most often give rise to a SB at large real k_z, due to unphysical downward dispersion of the CB. Such unphysical CB dispersion is *not* observed in the real band dispersion of the 8-band model parameterised following Ref. [44]. However, the combination of s_c and the LH and SO effective

masses of Ref. [44] (determined by the modified VB Luttinger parameters γ_1 and γ_2) produce a SB having complex-valued k_z that is not visible in the computed real bulk band dispersion, but which nonetheless pollutes the results of heterostructure calculations. Test calculations for InAs/GaSb SLs using this parameter set demonstrated the introduction of spurious solutions lying close in energy to the CB edge for plane wave basis sets containing as few as $2M + 1 = 7$ plane waves – a consequence of the appearance of the SB at small real k_z – with these spurious solutions moving downwards in energy into the band gap, and subsequently into the VB, with increasing M.

Our analysis using Eq. (4.2) demonstrates that, as s_c approaches zero, this SB evolves from having complex-valued wave vector with small real k_z, towards being an evanescent state having purely imaginary k_z with $|\mathrm{Im}\{k_z\}| \to \infty$ as $s_c \to 0$. To mitigate the impact of this SB we set $s_c = 0$, following the approach suggested in Ref. [128] by Foreman. We achieve this by decreasing the Kane parameter E_P to fix $s_c = 0$ in both InAs and GaSb, leaving the value of the bulk CB edge effective mass unchanged in each case. This parameter renormalisation is consistent with the analysis of Veprek et al. [129], who demonstrated that reducing E_P – which, in turn, adjusts the modified VB Luttinger parameters in addition to s_c – is an effective approach to eliminate spurious solutions by enforcing ellipticity of the 8-band $\mathbf{k} \cdot \mathbf{p}$ Hamiltonian. Solid red and blue lines in Fig. 4.1(b) respectively show the calculated InAs and GaSb bulk complex band dispersion using a renormalised parameter set in which $s_c = 0$. The complex band dispersion of InAs close in energy to the band gap is now in very good agreement with that obtained from full-band atomistic tight-binding calculations [131, 132]. We therefore retain these renormalised parameters for our analysis of the InAs/GaSb SL electronic and optical properties.

Enforcing $s_c = 0$ removes a complex-valued SB from close to the zone centre in InAs. However, we note that this SB is replaced by an evanescent state having large imaginary wave vector (cf. Appendix A). Calculation of bound heterostructure eigenstates, which are formally equivalent to a linear combination of bulk states having complex-valued wave vectors, typically requires matching of envelope function amplitudes and (appropriately weighted) spatial derivatives at material interfaces [133]. Given that our choice of renormalised band parameters replaces a SB by an evanescent state in InAs, we might then expect that this will impact the character of the computed eigenstates. As described by Foreman in Ref. [128], setting $s_c = 0$ removes the requirement that the CB Bloch component of the envelope function be continuous across an interface. We will observe, and discuss, below that this is indeed the case for our calculated InAs/GaSb SL bound electron states.

An appropriately parametrised 8-band $\mathbf{k} \cdot \mathbf{p}$ Hamiltonian provides a robust approach to compute SL electronic properties. However, the resulting artificially high symmetry neglects the impact of microscopic interface asymmetry (MIA) associated with InAs/GaSb layer interfaces [59]. To overcome this limitation, previous 8-band $\mathbf{k} \cdot \mathbf{p}$ calculations for InAs/GaSb SLs have treated

MIA via inclusion of a localised potential at each interface, the magnitude of which was treated as an empirical parameter and adjusted to fit to the measured variation with layer thickness of the SL band gap [127, 134]. The primary impact of this symmetry-breaking potential is to induce hybridisation of HH- and LH-like eigenstates [135], which can induce strong in-plane anisotropy in the inter-band optical matrix elements. Here, we are concerned with computing the SE rate, and quantities derived therefrom, which are polarisation-averaged. We therefore neglect MIA in the present analysis, and further employ the axial approximation such that the computed in-plane band dispersion and eigenstates depend only on the magnitude $k_{\|} = |\mathbf{k}_{\|}|$ of the in-plane wave vector [54].

4.2.2 Emission energy temperature dependence

Motivated by the structures considered in Ref. [16], we begin our analysis by considering InAs/-GaSb SLs having equal InAs and GaSb layer thicknesses ($t_{\mathrm{InAs}} = t_{\mathrm{GaSb}} \equiv t$). The corresponding length of our calculational supercell – i.e. the SL period – is $L = 2t$. Firstly, in order to establish an appropriate choice of plane wave basis set, we take exemplar structures and compute the $\mathbf{k} = 0$ bound state energies as a function of the number of plane waves – i.e. by varying M (cf. Chapter 2). A basis set containing $2M + 1 = 51$ plane waves was found to be sufficient to converge all calculated bound state energies to within 0.1 meV, with respect to further increases in the size of the basis set. We therefore set $M = 25$ for all of our calculations. This choice of plane wave basis set generates a reciprocal space plane wave Hamiltonian matrix $\widetilde{H}_{\mathbf{k}}$ of size $8(2M+1) \times 8(2M+1) = 408 \times 408$ at each wave vector $\mathbf{k}$. Having established an appropriate choice of plane wave basis set we proceed by performing benchmark calculations in comparison to the temperature-dependent electroluminescence (EL) measurements of Ref. [16]. To do this we begin by noting that the SL band gap is the energy gap between the lowest energy bound electron state ($e1$) and the highest energy bound hole state ($h1$) at $\mathbf{k} = 0$. This energy gap can then be referred to as the $e1$-$h1$ band gap. However, in EL measurements the emission peak can be expected to be slightly blueshifted vs. the SL band gap due to the band filling, or Burstein-Moss, effect [136, 137]. As such, both the in-plane ($\mathbf{k}_{\|}$) and miniband (q) dispersion play important roles in determining not only the EL/SE peak energy, but also its temperature dependence. For this reason, rather than compare the calculated $e1$-$h1$ band gap to experiment, we compute the SE spectrum under carrier injection and extract the peak energy of the SE spectrum vs. temperature for comparison.

The results of our benchmark calculations are summarised in Fig. 4.2, where closed black circles depict the EL data of Ref. [16]. We present two sets of theoretical data in Fig. 4.2. Firstly, we compute the emission energy as the peak energy of the full SL SE spectrum. We compute the SE rate spectrum in the quasi-equilibrium approximation as [138–140]

$$r_{\rm sp}(\hbar\omega) = \frac{e^2 n_r \hbar\omega}{\pi\epsilon_0 m_0^2 \hbar^2 c^3} \sum_{n_c,n_v} \left(\frac{2\pi}{L}\right)^{-1} \int_{-\frac{\pi}{L}}^{+\frac{\pi}{L}} \mathrm{d}q \int \frac{\mathrm{d}\mathbf{k}_\parallel}{(2\pi)^2} |\widetilde{p}_{n_c n_v \mathbf{k}}|^2 \times f_e(E_{n_c\mathbf{k}}, F_e)\,[1 - f_h(E_{n_v\mathbf{k}}, F_h)]\,\delta\left(E_{n_c\mathbf{k}} - E_{n_v\mathbf{k}} - \hbar\omega\right), \quad (4.4)$$

where $E_{n_c(n_v)\mathbf{k}}$ is the dispersion of conduction subband n_c (valence subband n_v), $f_{e(h)}$ is the electron (hole) Fermi-Dirac distribution function at temperature T, $F_{e(h)}$ is the associated electron (hole) quasi-Fermi level corresponding to an injected electron (hole) carrier density n (p), and the Dirac distribution δ imposes conservation of energy for photon emission. As described in Sec. 2.2, Eq. (4.4) explicitly includes the miniband dispersion and q-dependence of the interband optical matrix elements (cf. Eq. (2.64)). The calculation of the matrix elements $\mathbf{p}_{n_c n_v \mathbf{k}}$ employs the full $\mathbf{k}$-dependent SL Hamiltonian and eigenstates (cf. Sec. 2.2.3). In order to numerically evaluate Eq. (4.4) the Dirac distribution $\delta\left(E_{n_c\mathbf{k}} - E_{n_v\mathbf{k}} - \hbar\omega\right)$ must be replaced by a normalised, finite-width lineshape. In our calculations we employ a hyperbolic secant lineshape [141], the spectral width (= 4 meV) of which was chosen based on qualitative comparison between our calculated SE spectra and the measured EL spectra of Ref. [16] (cf. Fig. 4.2).

The SE peak energy is expected to correspond closely to the experimentally measured EL peak energy. We therefore proceed by taking the measured $T = 300$ K EL peak energy (= 0.283 eV

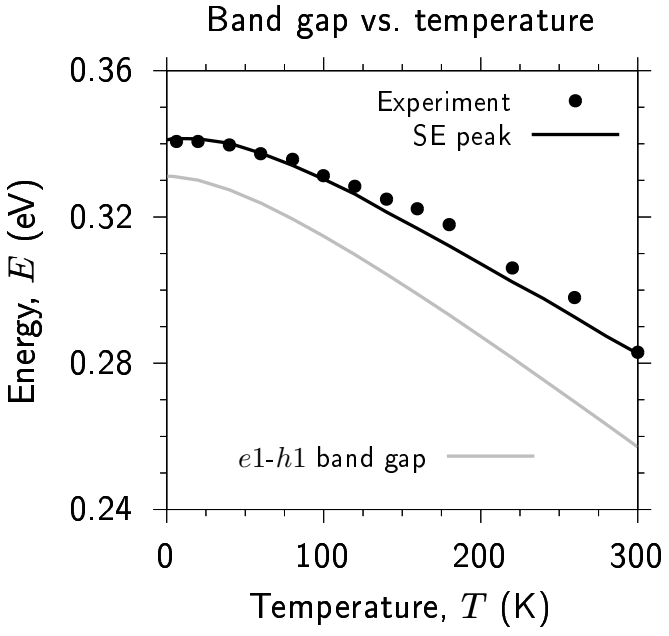


FIGURE 4.2: Theory vs. experiment comparison of the dependence of the emission energy vs. temperature T for an InAs/GaSb SL having equal InAs and GaSb layer thicknesses $t = 2.14$ nm (SL period $L = 2t = 4.28$ nm). The solid black line shows the calculated SE peak energy vs. T at injected electron and hole carrier densities $n = p = 10^{17}$ cm^{-3}. The solid grey line shows the calculated SL ($e1$-$h1$) band gap at $\mathbf{k} = 0$. Experimental data (closed black circles) are from Ref. [16].

= 4.38 μm) as a reference, and adjust the layer thickness t to match our calculated $T = 300$ K SE peak energy to this reference. This yields $t = 2.14$ nm ($L = 4.28$ nm), which corresponds well to the nominal $t = 2.3$ nm of Ref. [16]. This minor discrepancy between the nominal and best-fit layer thicknesses in our calculations vs. the device structures investigated in Ref. [16] is expected due to (i) the incorporation of a small fraction ($\lesssim 10\%$) of As in the GaSb layers in that work, to minimise lattice mismatch with respect to InAs, and (ii) the fact that the SL regions of the devices were lightly n-doped, which is not considered in our calculations. Keeping this value of t fixed we then compute the T-dependent SE peak energy, shown by the solid black line in Fig. 4.2. We note good quantitative agreement with the measurements of Ref. [16] (closed black circles). For comparison the solid grey line in Fig. 4.2 shows the calculated T-dependent $\mathbf{k} = 0$ $e1$-$h1$ SL band gap for the same structure. Due to the Burstein-Moss effect, the fundamental $e1$-$h1$ SL band gap is lower in energy than the peak energies extracted from the SE calculations. To quantify the T-dependence of these two sets of calculated energies for InAs/GaSb SLs, we fit to the empirical Varshni relation [44, 142]

$$E_{\mathrm{gap/peak}}(T) = E_{\mathrm{gap/peak}}(0) - \frac{\alpha\, T^2}{T + \beta}\,, \tag{4.5}$$

where $E_{\mathrm{gap/peak}}(0)$ is the zero-temperature SL band gap or SE peak energy.

To facilitate comparison to literature experimental data, we follow Ref. [143] by fixing $\beta = 270$ K when fitting the theoretical data of Fig. 4.1 via Eq. (4.5). We recall that our analysis employs only the bulk InAs and GaSb Varshni parameters as input to the SL electronic structure calculations, with the subsequent Varshni fits to the temperature-dependent $e1$-$h1$ band gap and SE peak energies computed for the SL heterostructure then being predictions of the full SL calculations. The respective best-fit values of the Varshni parameter α are 0.383 and 0.493 meV K^{-1} for the calculated full SE peak energy (solid black line) and $\mathbf{k} = 0$ SL band gap (solid grey line). We note the Varshni parameter $\alpha = 0.383$ meV K^{-1} for the full SE calculation – i.e. including the full $\mathbf{k}$-dependent in-plane and miniband dispersion, and optical matrix elements – is in close quantitative agreement with the range $\alpha = 0.30$ – 0.37 meV K^{-1} of experimental values given in Ref. [143].

4.3 Electronic properties

Having established an appropriate set of band parameters, and having benchmarked our calculations against experimental data, we now turn our attention to analysing the electronic properties of InAs/GaSb SLs. Specifically, we investigate the impact of the type-III ("broken-gap") band alignment on carrier localisation and the resulting electronic band structure, including the

miniband dispersion. We outline the impact we expect the carrier localisation and miniband formation to have on the optical properties.

4.3.1 Carrier localisation

Despite the fact that the T-dependence of the bulk InAs and GaSb band gaps used as input to our calculations – by applying Eq. (4.5) in conjunction with the parameters of Ref. [44] – are treated identically for both sets of calculations shown in Fig. 4.2, we note that the best-fit values of the Varshni parameter α for the SL band gap and SE peak energy vary by close to 30%. This describes that, relative to the SL band gap, filling of in-plane bands and minibands by injected carriers acts not only to blueshift the SE peak energy at fixed T, but also to decrease its T dependence compared to that of the bulk band gaps of the SL's constituent materials. Having demonstrated the ability of our model to quantitatively capture the experimentally measured T-dependence of the SL emission energy, we now turn our attention to a detailed interpretation of radiative recombination in this equal layer thickness SL ($t = 2.14$ nm, $L = 2t$) based on its calculated electronic structure. Unless otherwise stated, all calculations below are performed at $T = 300$ K.

We begin by considering the electron and hole localisation, summarised in Fig. 4.3. Solid red and blue lines respectively show the computed CB and VB offsets (demonstrating the type-III band alignment), and also the probability densities associated respectively with the $e1$ and $h1$ $\mathbf{k} = 0$ bound states. Dash-dotted red and blue lines respectively denote the computed $e1$ and $h1$ bound state energies at $\mathbf{k} = 0$, which in each case serves as the zero of the plotted probability density (in units of nm^{-1}). We note that the probability density for each SL eigenstate ($n = e1$, $h1$) is computed at each position z by summing over $|F_{nb\mathbf{k}}(z)|^2$ with respect to the bulk Bloch band index $b = 1, 2, \ldots, 8$ at $\mathbf{k} = 0$. The $e1$ probability density therefore contains CB, LH and SO – i.e. $|J; m_J\rangle = |\frac{1}{2}; \pm\frac{1}{2}\rangle$, $|\frac{3}{2}; \pm\frac{1}{2}\rangle$ and $|\frac{1}{2}; \pm\frac{1}{2}\rangle$ – contributions, while the $h1$ probability density contains only HH – i.e. $|J; m_J\rangle = |\frac{3}{2}; \pm\frac{3}{2}\rangle$ – contributions. While our electronic structure calculations are performed for supercells consisting of a single SL period we have, for clarity, exploited the periodic boundary conditions to plot the band offsets and probability densities in Fig. 4.3 over three SL periods.

We note that the $h1$ state is tightly confined within GaSb layers in the structure, with its probability density dropping rapidly to near-zero values at the centre of InAs layers as a consequence of the large VB offset and large HH VB edge effective mass in GaSb. Conversely, we note that the $e1$ state is, while primarily localised in InAs layers, significantly less localised than $h1$. The $e1$ probability density retains significant non-zero values throughout GaSb layers. This partial delocalisation of the $e1$ state is a consequence of the combination of low InAs CB edge effective mass and low GaSb layer thickness, and reflects strong electronic coupling between electrons bound in neighbouring SL periods. As we will describe below, this leads to (i) strong dispersion

of the $e1$ miniband along q, and (ii) significant electron-hole spatial overlap, leading to optical matrix elements that can be considered high for a structure possessing spatially indirect electron and hole confinement.

Before proceeding, we note a technical consideration relevant to the calculation of the carrier envelope functions. Our preliminary calculations of the $e1$ probability density demonstrated oscillations [57], suggesting the potential presence of a spurious contribution to the probability density, despite the choice of renormalised parameters having $s_c = 0$. Detailed analysis confirms that these oscillations are *not* a consequence of a spurious contribution to the $e1$ eigenstate. Rather, they are a consequence of the use of a plane wave basis set in conjunction with $s_c = 0$ [128]. In this case, oscillations in the $e1$ probability density arise in the presence of spatially abrupt InAs/GaSb interfaces, due to an accompanying discontinuity in the $e1$ envelope function (cf. Appendix A). Mathematically, these oscillations arise due to the description of the envelope function discontinuity in the PWEM – i.e. via a truncated Fourier series (cf. Chapter 2) – as a manifestation of the Gibbs phenomenon, which produces oscillatory behaviour near discontinuities [144]. To eliminate this behaviour we have softened the InAs/GaSb interfaces by convoluting the initial piecewise continuous real space band offset profile with a Gaussian distribution of standard deviation $\sigma = 7.5 \times 10^{-2}$ nm. This emulates intermixing between the InAs and GaSb layers, generated the continuous band offset profile shown in Fig. 4.3, while still allowing for analytical evaluation of the matrix elements of $\widetilde{H}_{\mathbf{k}}$ via the convolution theorem (cf. Appendix B). With this applied InAs/GaSb intermixing we observe in Fig. 4.3 that the

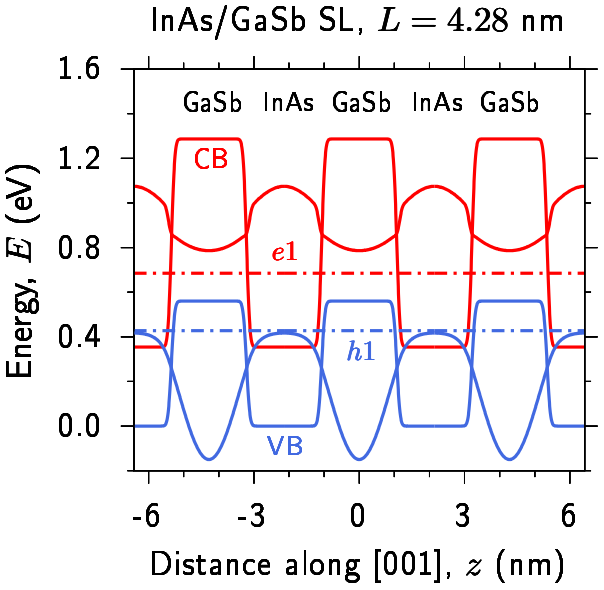


FIGURE 4.3: Calculated CB (solid red line) and VB (solid blue line) offsets, illustrated for three periods of a InAs/GaSb SL having equal InAs and GaSb layer thickness $t = 2.14$ nm (SL period $L = 4.28$ nm). The dash-dotted red (blue) line denotes the energy of the lowest energy bound electron state $e1$ (highest energy bound hole state $h1$). The $e1$ ($h1$) probability density is shown using a solid red (blue) line, shifted so that the zero of probability density lies at the $e1$ ($h1$) energy.

magnitude of the $e1$ probability density changes abruptly across InAs/GaSb interfaces. This is expected based on Foreman's analysis of the behaviour of a CB envelope function when $s_c = 0$ [128], and is also consistent with recent atomistic calculations of the $e1$ probability density based on the tight-binding method [92].

4.3.2 Superlattice band structure

We now turn our attention to the calculated SL band structure and DOS, shown in Figs. 4.4(a) and 4.4(b) for $T = 4$ and 300 K respectively. In Figs. 4.4(a) and 4.4(b) the left-hand and centre panels respectively show the calculated miniband and in-plane band dispersion, while the right-hand panel shows the calculated DOS. In each case the calculated CB DOS, which is significantly lower than the VB DOS, has been multiplied by 10 for improved visibility. Line colours denote the Fermi-Dirac band occupancy, which ranges from 1 (purple) to $\leq 10^{-4}$ (yellow), using the electron and hole quasi-Fermi levels computed for injected carrier densities $n = p = 10^{17}$ cm^{-3}. We note that there is minimal qualitative difference between the calculated $T = 4$ and 300 K SL band structures, with the only significant quantitative difference being a 74 meV reduction in SL band gap (cf. Fig. 4.2). Examining the computed miniband structures we firstly note that, as described above, the partial $e1$ delocalisation is reflected by the presence of highly dispersive $e1$ minibands. As a consequence, electrons only occupy states over a limited range of q. At low temperature $T = 4$ K, the range of q across which $e1$ miniband states are occupied is strongly limited by the step-like nature of the Fermi-Dirac distribution function, with only states lying

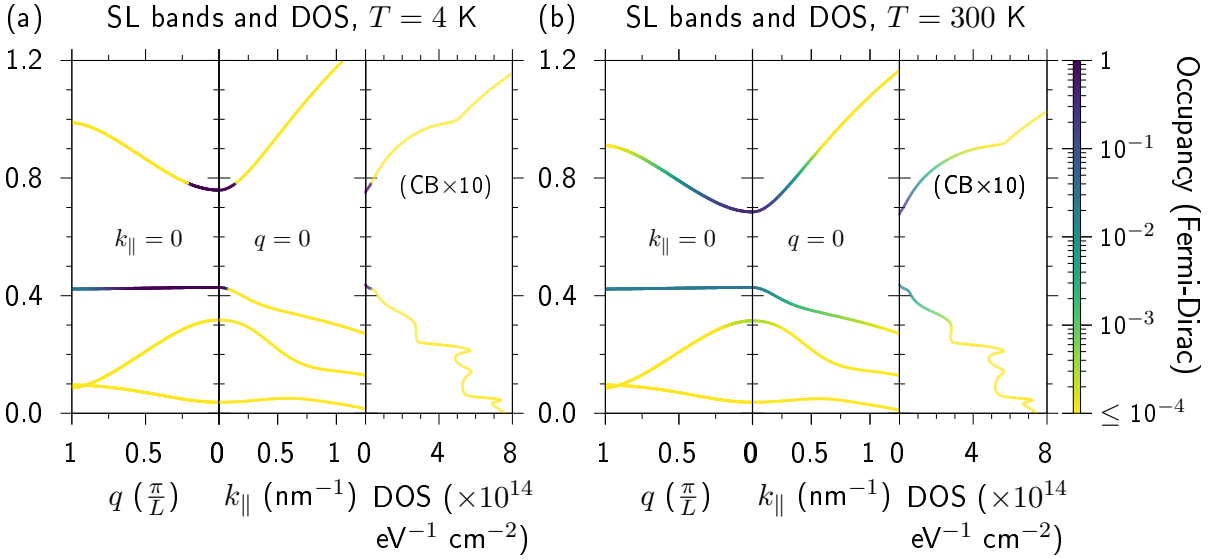


FIGURE 4.4: (a) and (b) Calculated band structure and DOS at temperature (a) $T = 4$ K, and (b) $T = 300$ K, for the equal layer thickness SL of Fig. 4.3. The left-hand, centre and right-hand panels in (a) and (b) respectively show the calculated miniband dispersion, in-plane band dispersion and DOS. The CB DOS is scaled ×10 to enhance visibility. The line colour is weighted by the Fermi-Dirac occupancy, for injected electron and hole carrier densities $n = p = 10^{17}$ cm^{-3}.

within the first $\approx 20\%$ of the SL BZ being occupied – i.e. $|q| \lesssim \frac{\pi}{5L}$. Conversely, the strong $h1$ localisation suppresses electronic coupling of VB edge hole states in neighbouring SL periods, which is reflected by nearly dispersionless $h1$ minibands. Holes therefore occupy $h1$ miniband states throughout the entirety of the SL BZ, $|q| \leq \frac{\pi}{L}$, even at low T.

This mismatch in the dispersion of the $e1$ and $h1$ minibands, when combined with strict ($\Delta\mathbf{k} = 0$) $\mathbf{k}$-selection for optical transitions (cf. Chapter 2), will act to reduce the radiative recombination rate. Specifically, holes occupying $h1$ miniband states at large $|q|$ are without electrons having matching wave vector, and hence have no available electrons with which to recombine. We therefore expect, and will demonstrate below, that the presence of this mismatched $e1$ and $h1$ miniband dispersion leads to a reduction of B at fixed temperature and carrier density vs. an equivalent QW structure (i.e. the same heterostructure considered without miniband dispersion). We note that this behaviour mirrors that associated with the mismatch of the in-plane CB and VB edge DOS in conventional QW structures, which served as a key motivation for the development of strain-engineered QW structures to improve the performance of LEDs and diode lasers [121, 145, 146]. While the mismatch in the range of q over which electrons and holes occupy miniband states is exacerbated at low temperature, we note that this behaviour is partially mitigated at $T = 300$ K. As T is increased to 300 K the emergence of a high-energy tail above the quasi-Fermi level in the electron Fermi-Dirac distribution allows electrons to occupy $e1$ miniband states over a significantly larger fraction of the SL BZ (cf. Fig. 4.4(b) vs. Fig. 4.4(a)), thereby providing a radiative recombination pathway for holes having larger $|q|$. The impact of this behaviour on the magnitude of B and its temperature dependence will be quantified below.

4.4 Trends in radiative recombination

In this section we present our analysis of trends in radiative recombination in InAs/GaSb SLs. We quantify the behaviour in optical matrix elements and SE, which highlight the importance of considering the miniband dispersion in calculating SL optoelectronic properties. We demonstrate that the miniband dispersion acts to reduce the SE rate, which leads in turn to a reduction in the radiative recombination rate. We quantify the radiative performance (recombination rate) via the radiative recombination coefficient B. Having carried out analysis for an exemplar InAs/GaSb SL having equal InAs and GaSb layer thickness we investigate pathways to maximising B at fixed SE peak emission wavelength λ_{peak}, providing guidelines for epitaxial growth for the development of optimised mid-IR LEDs.

4.4.1 Optical matrix elements and spontaneous emission

Using the SL Hamiltonian $\widetilde{H}_{\mathbf{k}}$ and eigenstates $|\psi_{n\mathbf{k}}\rangle$ we explicitly compute the TE- and TM-polarised $(\mathbf{k}, q)$-dependent optical matrix elements for $e1$-$h1$ transitions (cf. Sec. 2.2.3), corresponding to $\widehat{e} = \widehat{x}$ and $\widehat{e} = \widehat{z}$ respectively. The results of these calculations are summarised in Fig. 4.5(a), where the left- and right-hand panels respectively show the optical matrix elements vs. q for $k_{\|} = 0$, and vs. $k_{\|}$ for $q = 0$. TE- and TM-polarised matrix elements are respectively denoted by solid blue and dashed red lines. We present the squared optical matrix elements as $\frac{2}{m_0}|p^{(e)}_{n_c n_v \mathbf{k}}|^2$ – i.e. having units of energy, so that a natural reference is provided by the bulk Kane parameters E_P. The in-plane matrix elements obey conventional selection rules. At $k_{\|} = 0$ the $h1$ state is purely HH-like, possessing no p_z-like orbital component, so that the TM-polarised transition is symmetry forbidden. Away from $k_{\|} = 0$ the $h1$ band begins to hybridise with other bands and acquire LH-like Bloch character – and, to a lesser extent, SO- and CB-like character – thereby acquiring a p_z-like orbital component such that the TM-polarised matrix element initially grows with increasing $k_{\|}$ before again reducing as $k_{\|}$ increases further (due in part to the growth in the $E_{e1,k_{\|}} - E_{h1,k_{\|}}$ energy gap). The TE-polarised matrix element is non-zero across the full range of $k_{\|}$ for which $e1$ and $h1$ band states are occupied reflecting that, despite strong band hybridisation away from $k_{\|} = 0$, the $e1$ and $h1$ states respectively retain significant CB- and HH-like Bloch character. We note that the calculated TE-polarised optical matrix element at $\mathbf{k} = 0$ achieves a value that is 64.0% of the renormalised bulk InAs Kane parameter $E_P = 16.49$ eV employed in the electronic structure calculation. This value, which we note is quite large given the spatially indirect carrier confinement, is a consequence of the partial $e1$ delocalisation described above, which allows for large $e1$-$h1$ spatial overlap.

At $k_{\|} = 0$ the TE-polarised matrix element decreases with increasing $|q|$, becoming zero at $|q| = \frac{\pi}{L}$, as has been observed in some previous calculations (see, e.g., Fig. 6(a) of Ref. [127]). We identify that this behaviour traces its origin to an interplay between the evolution of the $e1$ and $h1$ envelope functions with increasing $|q|$, combined with the spatially indirect carrier confinement in the SL. As a consequence of the spatially indirect carrier confinement, the peaks of the $e1$ and $h1$ probability densities in this exemplar equal layer thickness structure are offset by a distance $\Delta z = t = \frac{L}{2}$. As such, traversing the $e1$ and $h1$ minibands – i.e. varying q from 0 to $\frac{\pi}{L}$ while maintaining $k_{\|} = 0$ – imparts a phase factor of $\exp(iq\Delta z) = \exp(i\frac{qL}{2})$ between the $e1$ and $h1$ envelope functions. This phase attains a value of $\frac{\pi}{2}$ at $q = \frac{\pi}{L}$, with the corresponding phase factor $\exp(i\frac{\pi}{2}) = i$ then being tantamount to introducing opposite parity between the $e1$ and $h1$ envelope functions (vs. their having equal parity at $\mathbf{k} = 0$). By plotting the envelope functions at $q = 0$ and $q = \frac{\pi}{L}$, we demonstrate this evolution of the envelope functions along the minibands in Appendix A. As a result, the TE-polarised optical matrix element between the $e1$ and $h1$ states vanishes at $|q| = \frac{\pi}{L}$. We note that this $q = \pm\frac{\pi}{L}$ "selection rule" arises due to the imposed symmetry in our calculations, a consequence of neglecting MIA in our

continuum $\mathbf{k}\cdot\mathbf{p}$ Hamiltonian. Inclusion of MIA – either implicitly in atomistic calculations, or via an empirical potential in continuum calculations – lowers the symmetry of the calculated SL eigenstates, so that the $e1$-$h1$ transition attains a much reduced but formally non-zero matrix element at $|q| = \frac{\pi}{L}$ [127, 131]. From the perspective of the present analysis we emphasise that electrons do not occupy $e1$ miniband states at large $|q|$, so that this slight underestimation of the TE-polarised optical matrix element at large $|q|$ will not appreciably impact the calculated SE spectra or values of B derived therefrom. We find the calculated optical matrix elements of Fig. 4.5(a) to be in good overall agreement with previous work.

Using the computed SL electronic structure and optical matrix elements for this exemplar equal layer thickness InAs/GaSb SL, we evaluate the SE spectrum for injected carrier density $n = p = 10^{17}$ cm^{-3} via Eq. (4.4). For comparative purposes, we show the results of two calculations in Fig. 4.5(b). The solid blue line shows the full calculated SL SE spectrum, which explicitly accounts for the q dependence of the SL electronic structure and optical matrix elements. The dashed red line shows the results of a simplified calculation in which we fix $q = 0$ and neglect q dependence – i.e. treating a single SL period as a conventional QW by omitting miniband dispersion. Comparison of these two sets of SE calculations elucidates the impact of SL miniband formation on radiative recombination. Firstly, the strong dispersion of the $e1$ miniband in a short-period SL results in electrons occupying CB states at higher energy (cf. Fig. 4.4(a) and 4.4(b)), leading in turn to a slight blueshift of the SL peak energy compared to an equivalent isolated QW. Secondly, the aforementioned mismatch in the occupancy of $e1$

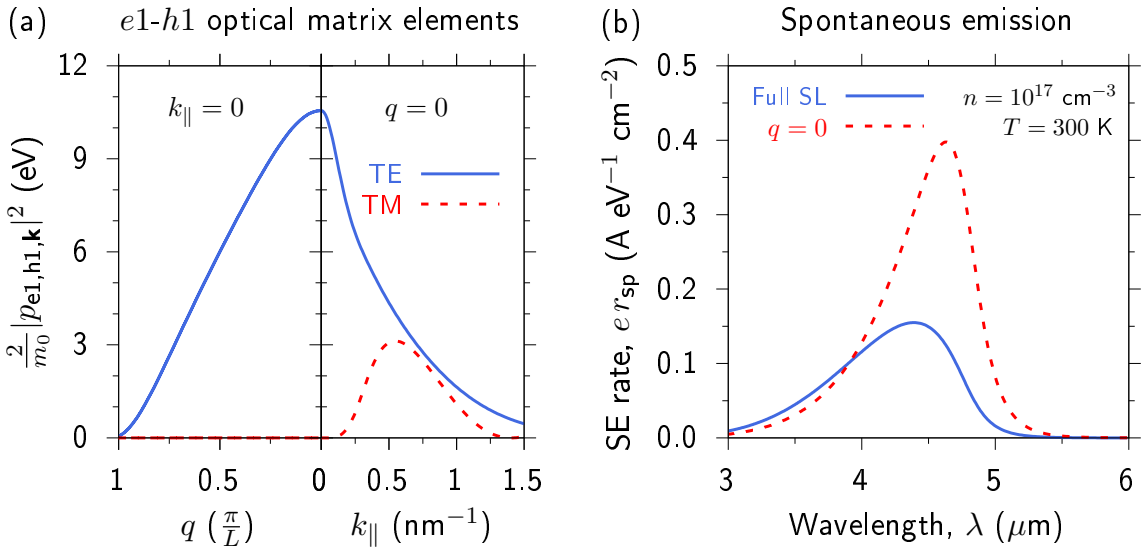


FIGURE 4.5: (a) Calculated TE-polarised (solid blue line) and TM-polarised (dashed red line) squared optical (momentum) matrix elements between the $e1$ and $h1$ subbands, as a function of the SL wave vector q (left-hand panel) and in-plane wave vector $k_{\parallel}$ (right-hand panel). (b) Comparison of SE spectra for an InAs/GaSb SL having equal InAs and GaSb layer thicknesses $t = 2.14$ nm (SL period $L = 2t = 4.28$ nm), calculated at temperature $T = 300$ K and injected carrier density $n = 10^{17}$ cm^{-3}, directly using Eq. (4.4) (solid blue line) and via a simplified calculation neglecting miniband dispersion by fixing $q = 0$ (dashed red line).

and $h1$ minibands at large $|q|$ reduces the number of electron-hole pairs that can recombine radiatively via $\Delta\mathbf{k} = 0$ (optical) transitions thereby reducing the peak SE rate. This reduction of the radiative recombination rate in response to miniband formation highlights the requirement for careful band structure engineering – potentially exploiting alloying and strain in addition to adjusting the thickness of electron- and hole-confining layers – to optimise the performance of SL-based emitters.

For $n = p = 10^{17}$ cm^{-3} we compute at $T = 300$ K that 100% of injected electrons occupy $e1$ band states, while $> 99.6\%$ of injected holes occupy $h1$ band states. The SE spectrum is therefore determined almost entirely by radiative recombination of $e1$ electrons and $h1$ holes. For our high-throughput calculations of B below, we reduce the computational cost of computing the SE spectra by restricting the evaluation of Eq. (4.4) to include only the $n_c = e1$ conduction and $n_v = h1$ valence subbands. Further test calculations reveal that the SE is dominated by TE-polarised $e1$-$h1$ transitions. For example, integrating over the $T = 300$ K SE spectrum obtained from a calculation that omits the TM-polarised contribution to $|\widetilde{p}_{n_c n_v \mathbf{k}}|^2$ (cf. Sec. 2.2.3) yields a radiative recombination rate that is 96.4% of that obtained from the full calculation including both TE- and TM-polarised transitions. That this is the case is expected based on our calculated band occupancies and optical matrix elements: at $T = 300$ K the $e1$ and $h1$ bands only have significant occupancies $\gtrsim 10^{-2}$ for in-plane wave vectors $k_\parallel \lesssim 0.25$ nm^{-1} (cf. Fig. 4.4(a)), in which range the TE-polarised $e1$-$h1$ optical matrix element significantly exceeds its TM-polarised counterpart (cf. Fig. 4.5(a)).

4.4.2 Quantifying radiative performance via the recombination coefficient B

We quantify radiative performance via the radiative recombination coefficient B. Integrating the SE rate $r_{\mathrm{sp}}(\hbar\omega)$, described by Eq. (4.4), with respect to photon energy $\hbar\omega$ yields J_{rad}/e, where J_{rad} is the radiative current density, which is given in the Boltzmann approximation by $J_{\mathrm{rad}} = eBnp$, where B is the radiative recombination coefficient [138–140] and n and p are the injected 3D electron and hole carrier densities respecitvely. B can therefore be computed as

$$B = \frac{1}{np} \int r_{\mathrm{sp}}(\hbar\omega)\, \mathrm{d}(\hbar\omega)\,. \tag{4.6}$$

The results of our calculations of the T-dependent B coefficient for this equal layer thickness SL structure are summarised in Fig. 4.6. Closed blue circles denote the B coefficients obtained from full SL calculations, while open red circles summarise the B coefficients obtained from simplified $q = 0$ "QW" calculations. In line with our calculated peak SE rates (cf. Fig. 4.5(b)), we firstly note that the SL demonstrates reduced B coefficient at fixed temperature compared to an equivalent QW structure. We secondly note that the degree to which the SL B coefficient is reduced in the SL is strongly dependent on temperature. Miniband formation drives strong

reduction of B at low T, with the calculated SL radiative recombination coefficient $B = 6.16 \times 10^{-10}$ cm^3 s^{-1} at $T = 4$ K being only 32.5% of that obtained from the equivalent $q = 0$ calculation. This disparity is reduced at $T = 300$ K, with $B = 1.81 \times 10^{-11}$ cm^3 s^{-1} being 60.0% of that obtained from the equivalent "$q = 0$" calculation. This behaviour can be understood in light of the T-dependent $e1$ miniband occupancy (cf. Fig. 4.4(a) and 4.4(b)). In a conventional QW, the large difference in CB and VB edge effective masses leads to electrons (holes) occupying $e1$ ($h1$) subband states over a larger range of energy (in-plane wave vector $\mathbf{k}_{\|}$) than holes (electrons) [121, 122]. At fixed carrier density this mismatch in occupancy is exacerbated with increasing T, as the electron (hole) quasi-Fermi level moves upwards (downwards) in energy, such that the B coefficient of a QW decreases strongly with increasing T. In the SL structures under consideration, the mismatch in $e1$ and $h1$ subband occupancy at fixed T is exacerbated by miniband formation. However, the reduction in the $e1$ and $h1$ occupancy mismatch along q with increasing T constitutes a competing effect, acting to mitigate the degree to which the number of electron-hole pairs available to undergo radiative recombination is reduced. We therefore expect that the T-dependence of B should be reduced in the SL compared to the equivalent QW.

The T dependence of B is summarised in the inset to Fig. 4.6, where closed blue (open red) circles display a log-log plot of B vs. T in the range $T = 200$ – 300 K for the full SL ($q = 0$) calculations. Here, we take $B \propto T^s$ and obtain s as the slope of a linear fit – shown using a solid blue or dashed red line – to the log-log data. In the standard analytical treatment of B – which makes the simplifying assumptions of CB and VB parabolicity, temperature-independent band

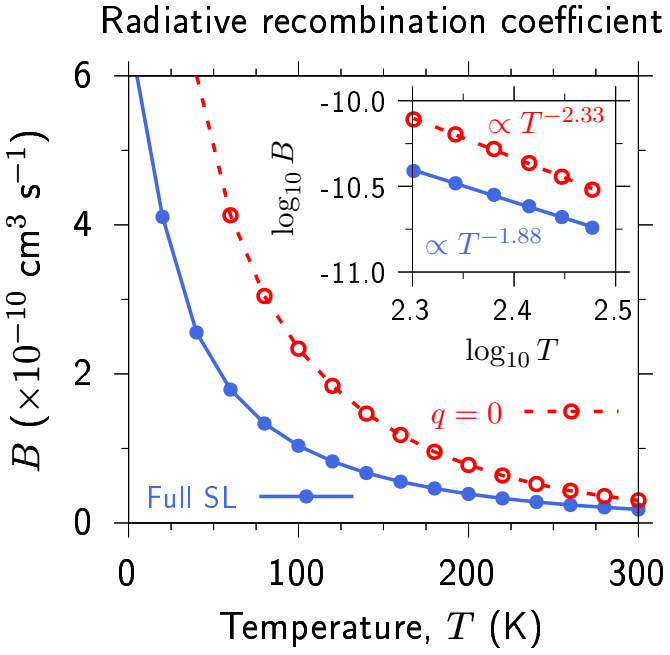


FIGURE 4.6: Comparison of the T-dependent radiative recombination coefficient B obtained from the $q = 0$ (open red circles) and full SE calculations (closed blue circles). Inset: $\log_{10} B$ vs. $\log_{10} T$ for $T = 200$ – 300 K, where $B \propto T^s$ with s equal to the log-log slope.

gap, and non-degenerate (Maxwell-Boltzmann) carrier statistics – this results in $B \propto E_g\, T^{-D/2}$ in a semiconductor having band gap E_g and D-dimensional band dispersion [138, 147]. For our exemplar SL ($D = 3$) we verify this expected behaviour by performing a test calculation in which we omit the T dependence of the InAs and GaSb band gaps, and reduce the carrier density to 10^{15} cm^{-3} so that the tails of the electron and hole Fermi-Dirac distribution functions that enter into the conduction and valence bands mimic the non-degenerate (Boltzmann) regime. The T dependence of B then originates solely from that of the carrier distribution functions (cf. Eq. (4.4)). This test calculation yields $s = -1.49$, in line with the expected analytical result $B \propto T^{-3/2}$, with minor deviation expected based on the nonparabolicity of the energy bands in our numerical calculations. The enhanced temperature sensitivity $B \propto T^{-1.88}$ obtained from the full T-dependent SL calculation is therefore attributed to the reduction of the SL band gap with increasing T (cf. Fig. 4.2). The equivalent $q = 0$ "QW" calculation demonstrates higher sensitivity of B on T, with $s = -2.33$, confirming our expectation that miniband formation can act to reduce the dependence of B on T in a SL in which there exists a significant mismatch in the dispersion of the $e1$ and $h1$ minibands.

We note that our calculated values of B are, for structures having spatially indirect (type-II-like) carrier confinement, relatively high. At $T = 300$ K and $n = p = 10^{17}$ cm^{-3} our full SL calculation – i.e. including miniband dispersion and q-dependent optical matrix elements – yields $B = 1.81 \times 10^{-11}$ cm^3 s^{-1} for an InAs/GaSb SL having $t_{\mathrm{InAs}} = t_{\mathrm{GaSb}} = 2.14$ nm. This value is close to B computed for bulk InAs from first principles [148], and compares favourably with previous calculations for novel GaAs-based metamorphic $\mathrm{InAs}_{1-x}\mathrm{Sb}_x/\mathrm{Al}_x\mathrm{In}_{1-x}\mathrm{As}$ and InP-based pseudomorphic $\mathrm{In}_y\mathrm{Ga}_{1-y}\mathrm{As}_{1-x}\mathrm{Bi}_x/\mathrm{In}_{0.53}\mathrm{Ga}_{0.47}\mathrm{As}$ mid-IR QWs having spatially direct (type-I) carrier confinement [8, 46]. For example, this calculated value of B is $\approx 31\%$ of the value $B = 5.88 \times 10^{-11}$ cm^3 s^{-1} previously computed for a type-I $\mathrm{InAs}/\mathrm{Al}_{0.125}\mathrm{In}_{0.875}\mathrm{As}$ metamorphic QW at the same temperature and carrier density [46]. Despite having significantly reduced electron-hole spatial overlap compared to structures possessing spatially direct (type-I) carrier confinement, we conclude that partial delocalisation of near-zone-centre CB electrons in broken-gap InAs/GaSb SLs can produce a high radiative recombination rate suitable for applications in mid-IR light-emitting devices. Our analysis therefore corroborates the experimental observation in Ref. [16] of high optical output power in prototype InAs/GaSb SL IC-LEDs.

4.4.3 Optimising radiative recombination at fixed emission wavelength

Having elucidated the nature of the electronic structure and radiative recombination for an exemplar SL having equal InAs and GaSb layer thicknesses t_{InAs} and t_{GaSb}, we now turn our attention to the maximisation of B in InAs/GaSb SLs having unequal InAs and GaSb layer thicknesses, $t_{\mathrm{InAs}} \neq t_{\mathrm{GaSb}}$. For a chosen emission wavelength λ_{peak} – corresponding, as above, to the peak of the calculated SE spectrum at temperature $T = 300$ K for carrier density

$n = p = 10^{17}$ cm^{-3} – we identify SLs that maintain fixed λ_{peak} by systematically varying the relative thickness $r = t_{\text{InAs}}/t_{\text{GaSb}}$ of the InAs and GaSb layers. In the PWEM, a basis set consisting of $2M+1$ plane waves possesses a minimum wavelength of L/M (cf. Chapter 2). Since the SL period $L = t_{\text{InAs}} + t_{\text{GaSb}}$ can vary significantly to achieve a given emission wavelength, and in fixed-wavelength structures having $t_{\text{InAs}} \neq t_{\text{GaSb}}$, we treat SLs having different L on an equal footing by varying M so as to maintain L/M as close as possible to the value 4.28/25 nm = 0.1712 nm employed to analyse the equal layer thickness ($r = 1$) SL of Sec. 4.4.2 above. This ensures that the plane wave basis sets employed in the electronic structure calculations maintain equivalent real space resolution for the different structures considered. The results of this high-throughput structure search are summarised in Fig. 4.7(a), which shows contours of constant peak SE wavelength $\lambda_{\text{peak}}(t_{\text{InAs}}, t_{\text{GaSb}})$ for emission wavelengths ranging from 3.5 μm (blue) to 7 μm (red).

Having identified these sets of fixed emission wavelength SLs, we then compute B as a function of relative layer thickness $r = t_{\text{InAs}}/t_{\text{GaSb}}$ for each value of λ_{peak} – i.e. moving along the constant wavelength contours of Fig. 4.7(a). The results of these calculations are summarised in Fig. 4.7(b) for $\lambda_{\text{peak}} = 4.5$ μm (closed blue circles), 5.5 μm (closed green squares), and 6.5 μm (closed red triangles) at $T = 300$ K. To highlight relative changes in B and associated trends as a function of emission wavelength, each set of B coefficients in Fig. 4.7(b) is normalised to the B coefficient calculated for an equal layer thickness ($r = 1$) SL at the corresponding value of λ_{peak} – i.e. $B = 1$ for $r = 1$ at each fixed λ_{peak}. Figure 4.7(b) therefore summarises the relative increase in B that can in principle be achieved by varying the InAs and GaSb layer thicknesses in each period of an ideal InAs/GaSb SL. We note that quantitative values of layer thicknesses and B coefficients are provided in Figs. 4.7(a) and 4.8, respectively.

Across the investigated wavelength range, our analysis predicts a strong reduction in B for SLs having $r < 1$ (i.e. $t_{\text{InAs}} < t_{\text{GaSb}}$). At $\lambda_{\text{peak}} = 4.5$ μm we find that B is reduced by $\approx 15\%$ when the relative thickness is reduced from 1 to 0.8, and that this reduction in B is exacerbated with increasing emission wavelength (e.g. decreasing by $\approx 40\%$ when r is reduced from 1 to 0.8 at $\lambda_{\text{peak}} = 6.5$ μm). The origin of this behaviour is straightforwardly understood: SLs in which the thickness of the hole-confining GaSb layers exceeds that of the electron-confining InAs layers reduce the ability of the $e1$ probability density to penetrate towards the centre of the GaSb CB barrier. This enhanced electron localisation strongly reduces the $e1$-$h1$ spatial overlap, and hence the optical matrix element, leading in turn to a reduction of the radiative recombination rate. Our analysis therefore suggests that to maximise the radiative recombination rate, regardless of the choice of emission wavelength, priority should be given during growth to ensuring that the thickness of the electron-confining InAs layers is equal to or greater than that of the hole-confining GaSb layers. More generally, these results emphasise the importance of enhancing electron-hole spatial overlap in heterostructures having spatially indirect carrier confinement: the thickness of electron-confining layers, and the CB

offset between those layers and the hole-confining layers, should be chosen to enhance electron delocalisation into the centre of the hole-confining layers in order to maximise B (since such delocalisation is typically more readily achieved for low effective mass electrons than for high effective mass holes).

For SLs having $r > 1$ we find that the optimum relative layer thickness r depends strongly on the chosen emission wavelength. Beginning with the $\lambda_{\text{peak}} = 4.5$ μm results, we note that an equal layer thickness ($r = 1$) SL already presents a near-maximised B coefficient. The maximum computed value of B at $\lambda_{\text{peak}} = 4.5$ μm occurs for relative thickness $r = 1.15$, and is only 2% larger than that calculated for the $r = 1$ SL. However, moving to longer wavelengths, our calculations identify significant potential to enhance B by increasing the relative layer thickness r. Achieving longer emission wavelengths requires increased t_{InAs}, which in turn mandates a significant reduction in t_{GaSb} to maintain fixed λ_{peak} (cf. Fig. 4.7(a)). The resulting increase in r allows for further penetration of the $e1$ probability density into GaSb layers, thereby increasing the $e1$-$h1$ spatial overlap and hence the $e1$-$h1$ optical matrix element. This indicates that, for target emission wavelengths > 5 μm, the radiative recombination rate can be maximised by growing structures having relative layer thickness $r \approx 1.5 - 2$. Our analysis confirms that the evolution of the $e1$-$h1$ spatial overlap plays the dominant role in driving the calculated trends in B. This is summarised by the inset to Fig. 4.7(b), which highlights that the relative increase of the squared $\mathbf{k} = 0$ TE-polarised $e1$-$h1$ optical matrix element, $|p^{(x,y)}_{e1\text{-}h1}|^2$, with r – for $\lambda_{\text{peak}} =$

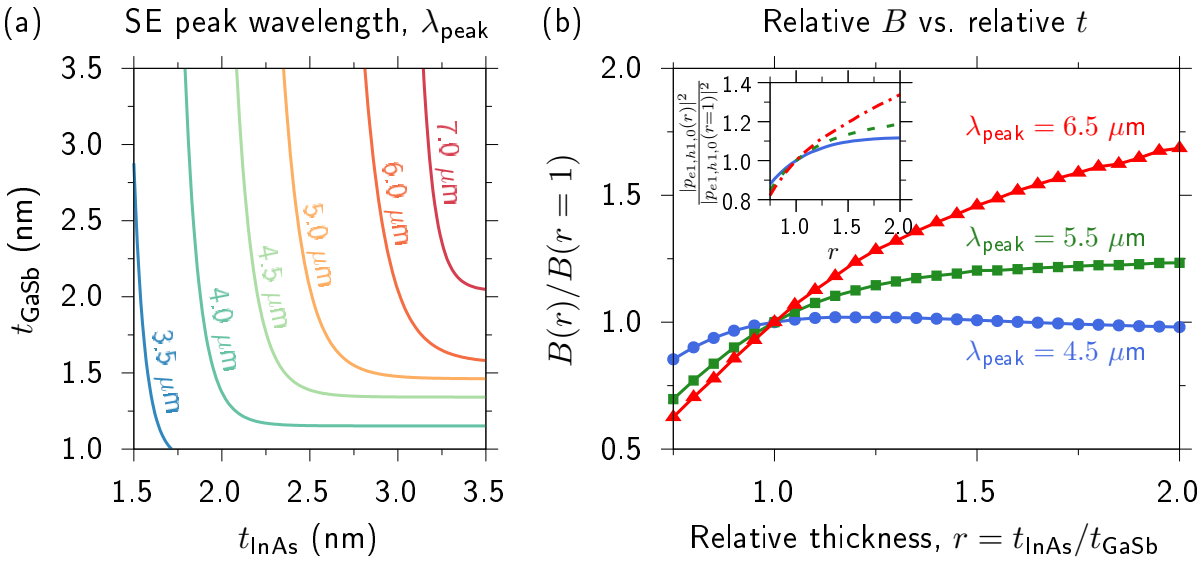


FIGURE 4.7: (a) Contour map denoting combinations of InAs and GaSb layer thicknesses t_{InAs} and t_{GaSb} that maintain fixed peak SE wavelengths λ_{peak} ranging from 3.5 μm (blue) to 7 μm (red), at temperature $T = 300$ K and carrier density $n = p = 10^{17}$ cm^{-3}. (b) Calculated variation of the radiative recombination coefficient B as a function of the relative InAs and GaSb layer thickness $r = t_{\text{InAs}}/t_{\text{GaSb}}$, for $\lambda_{\text{peak}} = 4.5$ μm (closed blue circles), 5.5 μm (closed green squares), and 6.5 μm (closed red triangles). For a given λ_{peak}, B values are shown relative to their calculated value in an equal thickness structure having $r = 1$. Inset: relative squared TE-polarised optical matrix element vs. r for the same λ_{peak} as in the main figure.

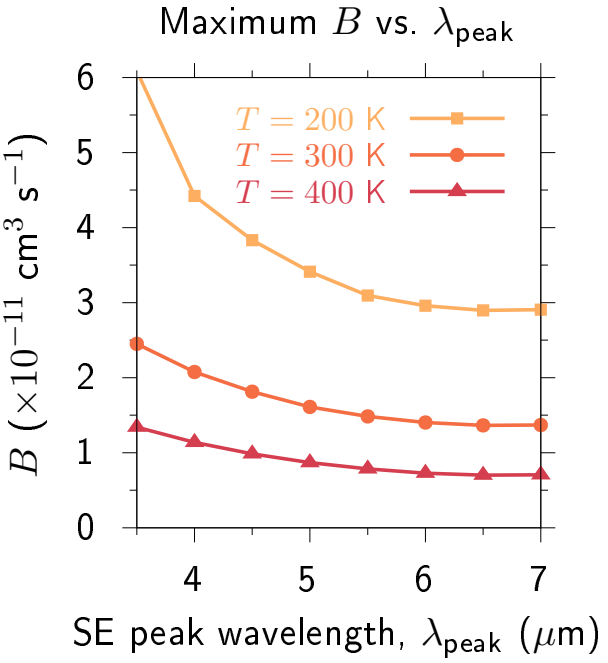


FIGURE 4.8: Maximised radiative recombination coefficient B as a function of emission wavelength λ_{peak}, for temperature T = 200 K (closed orange squares), 300 K (closed dark orange circles), and 400 K (closed red triangles).

4.5 μm (solid blue line), 5.5 μm (dashed green line), and 6.5 μm (dash-dotted red line) – closely tracks the calculated relative B values. While this enhancement of $|p_{e1\text{-}h1}^{(x,y)}|^2$ accounts for the majority of the increase in B, we note that the reduction in t_{GaSb} required to maintain fixed λ_{peak} with increasing r simultaneously acts to reduce the in-plane DOS close in energy to the VB maximum, which further contributes to enhancing the SE rate at fixed T and carrier density [121, 122, 149].

Finally, Fig. 4.8 shows the calculated maximum $B(r)$ as a function of λ_{peak} for temperatures T = 200 K (closed orange squares), 300 K (closed dark orange circles), and 400 K (closed red triangles). Here, having engineered the layer thicknesses to maximise the $e1$-$h1$ spatial overlap at each value of λ_{peak}, we note that the calculated values of B track closely the idealised $B \propto E_g$ scaling expected for a bulk semiconductor (e.g. reducing by close to a factor of 2 as the emission wavelength doubles from 3.5 to 7 μm) [138, 147]. Overall, our calculations suggest the potential to enhance the radiative recombination rate in InAs/GaSb SLs, through band structure engineering enabled by structural optimisation. This suggests that it may be possible to further improve on the optical output power and wallplug efficiency demonstrated in Ref. [16], to produce high-performance light-emitters at technologically important mid-IR wavelengths.

4.5 Conclusions

We have presented a theoretical analysis of radiative recombination in broken-gap InAs/GaSb SLs, based on multi-band $\mathbf{k} \cdot \mathbf{p}$ calculations of the SL electronic and optical properties. Exploiting the periodicity of a plane wave basis set we established full $\mathbf{k}$-dependent calculations of SL band dispersion and eigenstates, with these quantities then used explicitly to compute the inter-band optical matrix elements, SE rate and radiative recombination coefficient B. Systematic optimisation of B via high-throughput calculations provided guidelines for the growth of optimised SLs that maximise the radiative recombination rate across the application rich 3.5 – 7 μm mid-IR wavelength range.

The presence of spurious solutions in the calculated SL electronic properties was elucidated semi-analytically via the bulk complex band structure (cf. Appendix A), and it was confirmed that the prescription of Ref. [128] is sufficient to mitigate their impact in heterostructure calculations. The resultant renormalised InAs and GaSb band parameters were employed in full SL calculations, where it was demonstrated that the calculated temperature-dependent SE peak energy is in quantitative agreement with experimental EL measurements. Detailed analysis confirmed that miniband filling acts to decrease the temperature dependence of the SE peak energy compared to that of the fundamental zone-centre SL band gap. Extracted Varshni parameters for the temperature dependence of the SL SE peak energy were also found to be in quantitative agreement with experimental measurements.

Next, we considered InAs/GaSb SLs having equal InAs and GaSb layer thicknesses, and quantified the impact of miniband formation on the SE rate and B. Here, our calculations revealed the important roles played by (i) electron and hole localisation, (ii) carrier occupation of miniband states, and (iii) optical selection rules vs. SL wave vector q along a given pair of minibands. Firstly, it was shown that a combination of low InAs CB edge effective mass and GaSb layer thickness leads to partial electron delocalisation, allowing for high spatial overlap with hole states that are strongly localised in GaSb layers. This allows for high optical matrix elements, and hence for B values that are large relative to other structures admitting spatially indirect carrier localisation. Secondly, the SL band structure was found to be characterised primarily by a mismatch between the dispersion of the lowest energy electron and highest energy hole minibands. The calculated electron minibands were found to be strongly dispersive such that, in the structure considered, only states out to $|q| \lesssim \frac{\pi}{2L}$ have appreciable occupancy at room temperature. Conversely, the calculated hole minibands were found to be almost dispersionless, with holes then occupying miniband states throughout the entire SL BZ, $|q| \leq \frac{\pi}{L}$, at all temperatures. This mismatch in miniband dispersion prevents holes close to the SL BZ edge from undergoing radiative recombination, so that miniband formation decreases both the magnitude of B and its dependence on temperature. Finally, we undertook a systematic analysis of SLs having unequal InAs and GaSb layer thicknesses. We demonstrated that, at fixed emission

wavelength: (i) for shorter wavelengths close to 3.5 μm B is maximised in structures in which the InAs layer thickness is close to equal to the GaSb layer thickness, (ii) for longer wavelengths approaching 7 μm B is maximised for InAs layer thickness $\approx 1.5 - 2 \times$ the GaSb layer thickness, and (iii) B decreases rapidly if the InAs layer thickness is reduced below that of GaSb.

Strategies to increase the radiative recombination rate in SLs should aim to incorporate reduction of the mismatch between the dispersion of the occupied electron and hole minibands, an approach akin to that deployed in the design of strained-layer QW lasers. Since the q-dependent optical matrix elements decrease strongly in magnitude with increasing $|q|$, our analysis suggests that it is beneficial to engineer the band structure such that the hole miniband dispersion is increased, so that fewer holes occupy states close to the SL BZ edge. Therefore, the ability to increase B at fixed emission wavelength in SL structures beyond InAs/GaSb will rely in part upon the ability to match the electron and hole effective mass along the growth direction. This can potentially be achieved by exploiting layer thickness and/or strain engineering (enabled, e.g., via alloying and/or metamorphic growth).

Overall, our results emphasise the importance of considering the full $\mathbf{k}$-dependent miniband dispersion and eigenstates when analysing SL electronic and optical properties, and indicate that explicit calculations of this nature are essential to enable predictive interpretation of experimental data and quantitative SL design for device applications. While we have focused in this paper on InAs/GaSb as an archetypal mid-IR SL system, we note that the established calculational framework is generally applicable to systems whose constituent material bulk band structures can be well described via a multi-band $\mathbf{k} \cdot \mathbf{p}$ Hamiltonian. This provides an accurate and computationally inexpensive approach to compute SL electronic and optical properties, providing a suitable platform for high-throughput calculations to support device design. Further analysis will be required to enable rigorous in silico optimisation of SL internal quantum efficiency, mandating accurate high-throughput calculation of the Auger-Meitner recombination coefficient C due to the importance of this non-radiative recombination process as a loss mechanism in narrow-gap heterostructures.

Chapter 5

Optimisation of optical absorption in strain-balanced InAs/$InAs_{1-x}Sb_x$ superlattices

5.1 Overview

In this Chapter we present a systematic optimisation of InAs/$InAs_{1-x}Sb_x$ strain-balanced superlattices (SBSLs) for 3 - 5 μm photodetection, based on rigorous calculations of the optoelectronic properties using the plane wave **k·p** computational framework outlined in Chapter 2. There exists significant demand to develop inexpensive and efficient emitters and photodetectors in the mid-infrared (mid-IR) spectral range for sensing applications in environmental, medical, agricultural, industrial and defence domains [5–7]. Existing technologies for these applications are largely based on II-VI $Hg_{1-x}Cd_xTe$ materials which possess several limitations including high fabrication cost, required cooling to cryogenic temperatures, high non-radiative recombination rates, and large dark current due to band-to-band tunneling at high temperature [6, 11, 150, 151]. Beyond these limitations $Hg_{1-x}Cd_xTe$ materials also pose significant problems for the environment as their constituent materials are toxic, posing challenges for safe disposal [6]. Type-II III-V SLs are an emerging platform for applications as mid-IR detectors and emitters since they offer, via their highly tunable electronic structure, the opportunity to deliver high-performance devices with simplified fabrication and lower cost [6, 11, 20, 150–152]. SBSLs are desirable for these applications, since strain compensation facilitates growth of thick (several μm) SL absorber layers possessing low defect densities due to the suppression of dislocations associated with strain relaxation [25]. InAs/$InAs_{1-x}Sb_x$ SBSLs have attracted significant interest for several reasons. Firstly, a Ga-free design simplifies growth [6] and mitigates the deleterious impact of chemically inhomogeneous interfaces between material layers, which can impede performance

via the formation of localised electronic defect states [21–24, 151]. Secondly, in addition to having a highly tunable band gap, InAs/InAs$_{1-x}$Sb$_x$ SLs possess type-II band offsets which reduces the non-radiative (Auger-Meitner) recombination rate [114, 153]. Additionally, integration of InAs/InAs$_{1-x}$Sb$_x$ SLs on Si has been achieved via growth on GaSb-on-Si buffer layers [11, 20], and high performance has been demonstrated in prototype photodetectors [154, 155].

Previous analysis of InAs/InAs$_{1-x}$Sb$_x$ SBSLs has often focused on the zone-centre electron-hole spatial overlap associated with the SL band gap as a figure of merit [25–29]. While such analysis has provided valuable guidance, the associated consideration of the electronic and optical properties is limited. Considering a single transition at a single energy neglects that photodetection generally encompasses a range of wavelengths, within which the in-plane ($\mathbf{k}_\parallel$) band dispersion, miniband (q) dispersion and ($\mathbf{k}_\parallel, q$)-dependent optical matrix elements all play important roles in determining the optical absorption [156, 157]. For a defined cut-off wavelength we uniquely identify a SBSL at each Sb composition x by imposing strain balancing to constrain the InAs and InAs$_{1-x}$Sb$_x$ layer thicknesses. Following this procedure there are two primary design regimes: (i) thicker layers at lower Sb composition, and (ii) thinner layers at higher Sb composition. We extend the formalism described in Chapter 4, including the renormalisation of the Kane parameter to mitigate spurious solutions, and compute the optical absorption spectrum. The SL absorption spectra are used in a model calculation of the internal quantum efficiency (IQE), which is employed as a figure of merit to quantify photodetector performance. This constitutes a detailed interrogation of the InAs/InAs$_{1-x}$Sb$_x$ SBSL design space, quantitatively comparing the endpoints (i) thicker layers at lower Sb composition, and (ii) thinner layers at higher Sb composition for SBSL design. We demonstrate that increasing the Sb composition to $x \approx 30\%$ can increase the (relative) IQE at fixed cut-off wavelength by $\approx 15\%$, with minimal additional improvement in performance expected at higher Sb compositions.

The rest of this Chapter is organised as follows. In Sec. 5.2 we identify and analyse InAs/InAs$_{1-x}$Sb$_x$ SBSLs at fixed cut-off wavelength and describe their associated electronic properties. In Sec. 5.2.1 we describe the procedure we applied to identify InAs/InAs$_{1-x}$Sb$_x$ SBSLs having fixed target cut-off wavelength. We also quantify properties relevant to the epitaxial growth of InAs/InAs$_{1-x}$Sb$_x$ SBSLS, including the in-plane strain, strain-balanced layer thicknesses, and critical thickness. In Sec. 5.2.2 we describe the electronic properties of InAs/InAs$_{1-x}$Sb$_x$ SBSLs and outline the impact of carrier localisation and the electronic band structure on the optical (momentum) matrix elements, and their implictions for the optical absorption. In Sec. 5.3 we describe the trends in optical properties of InAs/InAs$_{1-x}$Sb$_x$ SBSLs pertinent to mid-IR photodetection. In Sec. 5.3.1 we investigate the trends in the optical absorption spectra of InAs/InAs$_{1-x}$Sb$_x$ SBSLs as a function of Sb composition x. In Sec. 5.3.2 we quantify the potential to optimise the photodetector performance in the 3 - 5 μm wavelength range by computing the IQE, and offer guidelines for epitaxial growth based on our calculations. In Sec. 5.3.3 we analyse contributions to the optical absorption at the level of the electronic

structure to quantify the origin of the observed trends in the calculated IQE. Finally, in Sec. 5.4 summarise our analysis, and guidelines for material growth, and conclude.

5.2 Structural and electronic properties

In this section we present our framework for the identification of InAs/InAs$_{1-x}$Sb$_x$ SBSLs having fixed target cut-off wavelength λ_{cut}. Having established this framework we analyse the trends in the identified SBSLs and consider structural and elastic properties pertinent to the viability of epitaxial growth. Then, we investigate the electronic band structure and trends in carrier localisation and outline their expected impact on optical properties.

5.2.1 Fixed cut-off wavelength strain-balanced superlattice identification

We consider InAs/InAs$_{1-x}$Sb$_x$ SLs to be grown on a GaSb substrate. When grown pseudomorphically on a [001]-oriented GaSb substrate, InAs is under 0.62% tensile strain in the (001) plane. We employ linear interpolation to compute the InAs$_{1-x}$Sb$_x$ lattice parameter, meaning we calculate that pseudomorphic InAs$_{1-x}$Sb$_x$ is lattice-matched to GaSb for $x = 8.9\%$, and is under tensile (compressive) strain for $x < 8.9\%$ ($x > 8.9\%$). To obtain strain-balancing we therefore consider compressively strained InAs$_{1-x}$Sb$_x$ layers with Sb composition $x > 8.9\%$ chosen to balance the tensile strain in the InAs layers. Formally, strain-balancing between two adjacent pseudomorphic layers occurs when they admit zero net stress in the plane perpendicular to the growth direction [158]. We denote via subscripts "0" and "x" properties associated respectively with the electron-confining InAs ($x = 0$) and hole-confining InAs$_{1-x}$Sb$_x$ layers. Using elastic continuum theory we construct strain-balanced SLs by enforcing strain-balancing between a tensile strained InAs layer thickness t_0 and a compressively strained InAs$_{1-x}$Sb$_x$ layer of thickness t_x, such that each two-layer SL period is strain-balanced.

The in-plane biaxial strain is defined as $\epsilon_{\parallel} = (a(\text{GaSb}) - a(\text{InAs}_{1-x}\text{Sb}_x))/a(\text{InAs}_{1-x}\text{Sb}_x)$, where a is the unstrained lattice parameter. For a pseudomorphic strained layer under biaxial stress in the (001)-plane this then gives the stress along the (001) direction as $\sigma_{zz} = C_{12}(\epsilon_{xx} + \epsilon_{yy}) + C_{11}\epsilon_{zz} = 2C_{12}\epsilon_{\parallel} + C_{11}\epsilon_{\perp}$. Setting $\sigma_{zz} = 0$ yields $\epsilon_{\perp} \equiv \epsilon_{zz} = -2C_{12}\epsilon_{\parallel}/C_{11}$, where C_{ij} denote the material elastic constants. We can then express the elastic energy per unit volume U as [158–160]

$$U = \frac{C_{11}^2 + C_{11}C_{12} - 2C_{12}^2}{C_{11}}\,\epsilon_{\parallel}^2\,. \tag{5.1}$$

For two strained layers, the average strain energy density – for a pair of strained layers of thickness t_0 and t_x with SL period $L = t_0 + t_x$ – is given by [158]

$$U_{\text{av}} = \frac{U_0 t_0 + U_x t_x}{t_0 + t_x} = \frac{A_0 \epsilon_{\parallel,0}^2 t_0 + A_x \epsilon_{\parallel,x}^2 t_x}{t_0 + t_x}\,, \tag{5.2}$$

where $A = C_{11} + C_{12} - 2C_{11}^{-1}C_{12}^2$. We can derive the average in-plane stress from the derivative of the average energy density with respect to the strain in a given layer. The strain-balancing condition mandates that this quantity vanishes – i.e. $\frac{\partial U_{\text{av}}}{\partial \epsilon_{\parallel,x}} = \frac{\partial U_{\text{av}}}{\partial \epsilon_{\parallel,0}} = 0$. Applying this condition to Eq. (5.2) gives, for each individual SL period, the strain-balancing condition such that there is zero net stress in the (001) plane as [158, 161]

$$\frac{t_x}{t_0} = -\frac{A_0\, \epsilon_{\parallel,0}\, a_x}{A_x\, \epsilon_{\parallel,x}\, a_0}\,. \tag{5.3}$$

Given a target optical absorption cut-off wavelength λ_{cut}, which we treat as being equal to the SBSL zone-centre ($\mathbf{k}_\parallel = q = 0$) band gap [29], we identify candidate SBSLs as follows. For a given Sb composition x we choose an InAs layer thickness t_0 and solve Eq. (5.3) to obtain the InAs$_{1-x}$Sb$_x$ layer thickness t_x that imposes strain balancing. This combination of x, t_0 and t_x then fully specifies a candidate SBSL, for which we calculate the zone-centre band gap between the lowest-energy bound electron state $e1$ and highest-energy bound hole state, the latter possessing purely heavy-hole (HH) Bloch character at $\mathbf{k}_\parallel = q = 0$ and which we therefore label as $hh1$. To determine the Bloch band character of a given SL eigenstate we note that the calculated SL eigenstates posess eight envelope function components, each associated with one of the zone-centre Bloch basis states employed in the underlying bulk $\mathbf{k}\cdot\mathbf{p}$ Hamiltonian (cf. Chapter 2). The Bloch character can then be evaluated by projecting the SL eigenstate $|\psi_{n\mathbf{k}}(z)\rangle$ onto the bulk basis states $|u_b\rangle$ (cf. Eq. (2.62)).

Repeating this procedure as a function of t_0 at fixed x yields the zone-centre $e1$-$hh1$ band gap vs. t_0, from which we identify the SBSL having band gap E_g corresponding to the desired λ_{cut} – i.e. $E_g = hc/\lambda_{\text{cut}}$. As an example of this procedure, we present in Fig. 5.1 the results of these calculations for a single Sb composition $x = 18\%$ – i.e. the full set of candidate InAs/InAs$_{0.82}$Sb$_{0.18}$ SBSLs. In Fig. 5.1(a) we present the identified InAs$_{0.82}$Sb$_{0.18}$ thicknesses t_x as a function of InAs thickness t_0, calculated using Eq. (5.3). In Fig. 5.1(b) we show the calculated $e1$-$hh1$ energy gap E_g as a function of SL period L for the candidate SBSLs detailed in Fig. 5.1(a).

The design space for InAs/InAs$_{1-x}$Sb$_x$ SLs is expansive, consisting of structures having varying InAs and InAs$_{1-x}$Sb$_x$ layer thicknesses t_0 and t_x and Sb composition x. Imposing (i) fixed λ_{cut}, and (ii) strain balancing, significantly reduces the extent of this space by reducing a 3D optimisation problem in (x, t_0, t_x) to a 1D optimisation problem in x. Applying constraints (i) and (ii) allows us to identify a unique SBSL – defined by x, $t_0(x)$ and $t_x(x)$ – at each Sb composition x. In the first instance, we carry out analysis of SBSLs having $\lambda_{\text{cut}} = 5$ μm,

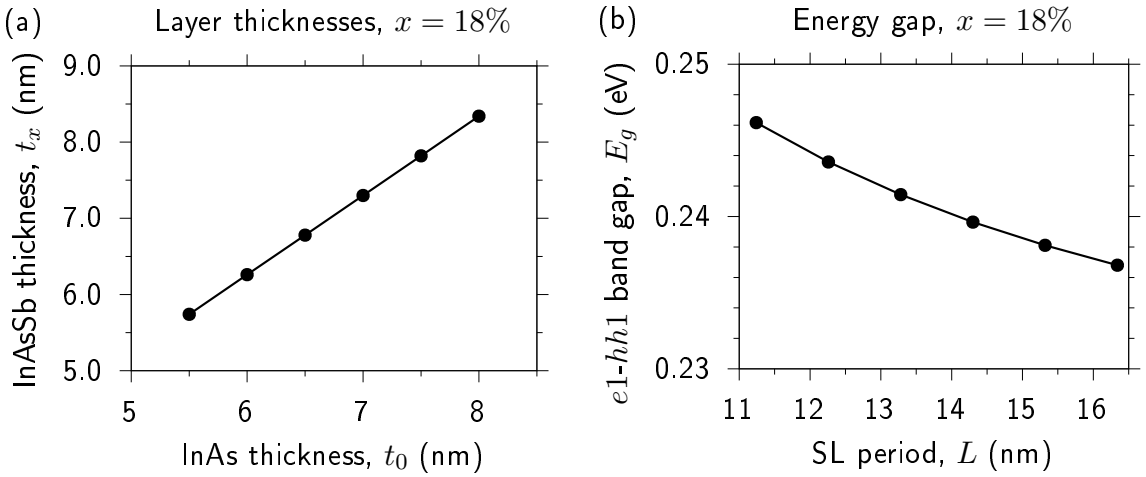


FIGURE 5.1: (a) Computed InAs$_{0.82}$Sb$_{0.18}$ layer thicknesses t_x as a function of InAs layer thicknesses t_0, specifying identified InAs/InAs$_{0.82}$Sb$_{0.18}$ ($x = 18\%$) SBSLs computed via Eq. (5.3). (b) Calculated $e1$-$hh1$ energy gap E_g as a function of SL period L of the SBSLs detailed in (a).

calculated at a representative detector operating temperature $T_D = 150$ K. This choice of λ_{cut} reflects the upper limit of the mid-IR atmospheric transmission window [152, 162]. Moving λ_{cut} to longer wavelengths beyond 5 μm is one approach employed to enhance photodetection in the mid-IR spectral range [163]. For this reason we also carry out analysis of InAs/InAs$_{1-x}$Sb$_x$ SBSLs having $\lambda_{cut} = 5.5$ and 6 μm. For operation at $T_D = 150$ K, test calculations indicate that it is not possible to achieve $\lambda_{cut} = 5$ μm for Sb composition $x < 18\%$, $\lambda_{cut} = 5.5$ μm for Sb composition $x < 20\%$, or $\lambda_{cut} = 6$ μm for Sb composition $x < 22\%$. We therefore restrict our attention to SBSLs having $x = 18$ - 40%, $x = 20$ - 40% and $x = 22$ - 40% for $\lambda_{cut} = 5$, 5.5 and 6 μm respectively.

Following this procedure we systematically identify layer thicknesses for InAs/InAs$_{1-x}$Sb$_x$ SBSLs having $\lambda_{cut} = 5$, 5.5 and 6 μm ($e1$-$hh1$ band gap = 0.248, 0.225 and 0.207 eV). The resulting structures are summarised in Figs. 5.2(a), 5.2(b) and 5.2(c) respectively. The upper limit of the investigated Sb composition range, $x = 40\%$, was selected based on the fact that the (001) in-plane compressive strain $|\epsilon_{\parallel,x}|$ reaches a high value of 2.1% at $x = 40\%$ (cf. Fig. 5.2(d)). As the Sb composition increases the layer thicknesses t_0 and t_x required to maintain λ_{cut} decrease, with the higher $e1$ and $hh1$ confinement energies in the thinner layers compensating for the reduced InAs$_{1-x}$Sb$_x$ bulk band gap. These results highlight the two primary design regimes: requiring thicker layers to reach the target λ_{cut} at lower x, changing to thinner layers with increasing x to retain both fixed λ_{cut} and strain-balancing. Higher Sb compositions can pose challenges for epitaxial growth. For larger Sb composition x strain-balancing mandates thin highly-strained layers, which make the optoelectronic properties susceptible to factors including minor variations in layer thickness and Sb intermixing at the interfaces [164]. For $\lambda_{cut} = 5$ μm, at $x = 40\%$ we find SBSLs requiring InAs$_{1-x}$Sb$_x$ layers having $t_x < 1$ nm ($\lesssim 4$ monolayers). These concerns are lessened moving to longer λ_{cut} since, at fixed Sb composition, thicker InAs and InAs$_{1-x}$Sb$_x$ layers are sufficient to maintain fixed λ_{cut}. At $x = 40\%$ we find

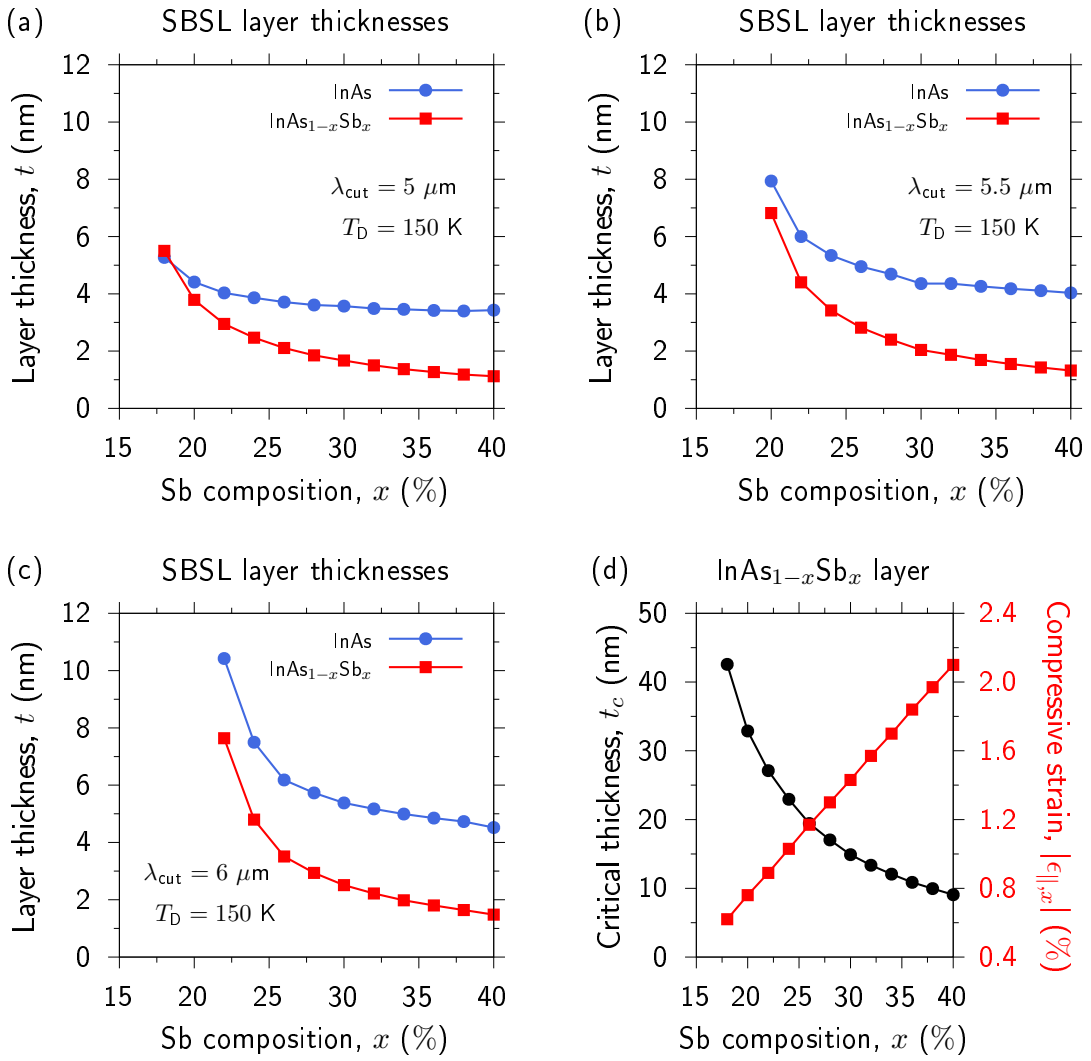


FIGURE 5.2: (a) Calculated InAs (closed blue circles) and InAs$_{1-x}$Sb$_x$ (closed red squares) layer thicknesses for SBSLs having fixed cut-off wavelength $\lambda_{\text{cut}} = 5$ μm as a function of Sb composition x. (b) Equivalent to (a) for SBSLs having $\lambda_{\text{cut}} = 5.5$ μm. (c) Equivalent to (a) for SBSLs having $\lambda_{\text{cut}} = 6$ μm. (d) Calculated critical thickness t_c (closed black circles and left-hand vertical axis) and compressive in-plane strain $\epsilon_{\parallel,x}$ (closed red squares and right-hand vertical axis) as a function of Sb composition x.

that InAs$_{1-x}$Sb$_x$ layer thicknesses $t_x = 1.32$ and 1.48 nm are respectively required to achieve $\lambda_{\text{cut}} = 5.5$ and 6 μm. These low layer thicknesses still likely pose challenges for expitaxial growth since the InAs$_{1-x}$Sb$_x$ layer thickness t_x is less than several monolayers. Nonetheless, the work of Ref. [152] has demonstrated that the types of structures which we identify in this work are compatible with recently demonstrated epitaxial growth. The challenge for epitaxial growth will now become the reproducible growth of many SL periods with uniform low layer thickness and high Sb composition.

When considering epitaxial layer design to guide materials growth and inform device fabrication, it is important to consider the strain-thickness limits of the constituent materials. To ensure that these limits are not exceeded during epitaxial growth of InAs/InAs$_{1-x}$Sb$_x$ SBSLs, we

calculate the critical thickness t_c associated with our InAs and InAs$_{1-x}$Sb$_x$ layers. This is motivated by noting that our identified SBSLs include highly strained InAs$_{1-x}$Sb$_x$ layers, it is therefore pertinent to assess their compatibility with strain-thickness limits for growth on [001]-orientated GaSb. If an epitaxial layer is grown with thickness exceeding its critical thickness, it becomes energetically favourable to relieve strain via the formation of a dislocation (plastic lattice relaxation), rendering the strained layer thermodynamically unstable [165]. To obtain an expression for this critical thickness we begin by considering the elastic energy density E_{st} of a dislocation-free pseudomorphically strained layer. We define the shear modulus as $G = \frac{1}{2}(C_{11} - C_{12})$ and Poisson's ratio as $\sigma = \frac{C_{12}}{C_{11}+C_{12}}$. We then multiply Eq. (5.1), the bulk elastic energy density, by the layer thickness t to obtain the elastic energy per unit area stored in a [001]-orientated pseudomorphically strained layer of thickness t, which gives [160, 165, 166]

$$E_{\mathrm{st}} = 2G\left(\frac{1+\sigma}{1-\sigma}\right)\epsilon_{\parallel,x}^2\, t\,. \tag{5.4}$$

Following the approach of Voisin [167], the energy per unit length associated with a plastic dislocation E_{dis} can be evaluated as

$$E_{\mathrm{dis}} = \frac{G}{16\pi}\left(\frac{a}{\sqrt{2}}\right)^2\left(\frac{4-\sigma}{1-\sigma}\right)\left(1+\ln\left(\frac{\sqrt{2}\,t}{a}\right)\right)\,, \tag{5.5}$$

where a is the substrate lattice constant. The critical thickness occurs when Eqs. (5.4) and (5.5) are equal, with scaling of the former with the average spacing between dislocations $s = a/\left(\sqrt{2}\,|\epsilon_{\parallel,x}|\right)$ [168]. The critical thickness of a strained layer can then be determined as [160, 161, 165, 167, 169]

$$t_c = \frac{a}{8\sqrt{2}\pi\,|\epsilon_{\parallel,x}|}\left(\frac{4-\sigma}{1+\sigma}\right)\left(1+\ln\left(\frac{\sqrt{2}\,t_c}{a}\right)\right)\,. \tag{5.6}$$

For tetrahedral semiconductors $C_{12} \approx C_{11}/2$, and so the Poisson ratio is $\sigma \approx 1/3$, this is the value we use in our calculations of t_c [165]. A number of approaches exist for computing t_c, however the results from the method that we have outlined above are in good agreement with experimental measurements for a number of semiconductor materials [160, 161, 165, 167, 169]. Equation (5.6) is an implicit equation in t_c, from which t_c can be computed numerically via any standard root-finding algorithm. To assess the practical viability of our identified InAs/InAs$_{1-x}$Sb$_x$ SBSLs we calculate the InAs$_{1-x}$Sb$_x$/GaSb critical thickness by solving Eq. (5.6). The calculated InAs/GaSb critical thickness is 41.94 nm, corresponding to a strain-thickness limit $t_c|\epsilon_{\parallel}| = 41.94$ nm $\times\, 0.62\% = 26$ nm %. For the InAs$_{1-x}$Sb$_x$ layers the critical thickness is a function of the Sb composition x, since the composition determines the values of the lattice parameters, in-plane

strain and elastic moduli that enter Eq. (5.6). The calculated $t_c(x)$ for InAs$_{1-x}$Sb$_x$/GaSb is shown in Fig. 5.2(d), alongside the composition dependent in-plane compressive strain $\epsilon_{\parallel,x}$. The identified InAs SBSL layer thicknesses t_0 for $\lambda_{\text{cut}} = 5$, 5.5 and 6 μm are $\leq 25\%$ of the InAs critical thickness, a result of the low tensile strain in InAs/GaSb. The identified InAs$_{1-x}$Sb$_x$ SBSL layer thicknesses t_x for $\lambda_{\text{cut}} = 5$, 5.5 and 6 μm at $x = 40\%$ are $\leq$ 38, 44 and 50% of the corresponding critical thickness respectively. We therefore expect the identified SBSLs to lie safely within the expected strain-thickness limits across the investigated composition range, and hence to be compatible with established epitaxial growth [170].

5.2.2 Carrier localisation and band structure

In Fig. 5.3(a) we show the calculated conduction band (CB) and HH valence band (VB) offsets, and the $e1$ and $hh1$ probability densities at $\mathbf{k}_{\parallel} = q = 0$, for the identified InAs/InAs$_{0.70}$Sb$_{0.30}$ ($x = 30\%$) SBSL having $\lambda_{\text{cut}} = 5$ μm. The zero of energy is set at the VB maximum of unstrained InAs. Our calculations employ the unstrained InSb/InAs VB offset recommended by Vurgaftman et al. [44] of 0.59 eV. Our calculations predict a smaller strained, with respect to an [001]-orientated GaSb substrate, InSb/InAs VB offset of 0.49 eV. We note, consistent with literature reports [11, 152, 170], that our model solid theory calculation predicts type-II band alignment, which generates spatially indirect confinement of the electron and hole envelope functions. As x increases we see the type-II band alignment begin to approach type-III (broken-gap) alignment, however this transition takes place beyond the Sb composition range investigated in this work. Our model solid theory calculations predict a type-II to type-III band alignment transition at $x \approx 43\%$. While we observe the $hh1$ state to be strongly localised in the InAs$_{1-x}$Sb$_x$ layers, we note that the weakly bound $e1$ state is significantly delocalised. This delocalisation of the $e1$ state is a result of the shallow CB offset, low InAs CB edge effective mass, and the low InAs$_{1-x}$Sb$_x$ layer thickness. This behaviour holds for all the identified SBSLs across the investigated range of Sb composition and cut-off wavelengths. We note that as x increases, and the corresponding layer thicknesses decrease (cf. Fig. 5.2), we expect increasing spatial overlap of the zone-centre $e1$ and $hh1$ envelope functions. This increasing spatial overlap will act to enhance the inter-band momentum matrix elements, and hence increase the optical absorption close in energy to the band edge.

In Fig. 5.3(b) we present the calculated SL electronic structure, consisting of the miniband dispersion (q) at $\mathbf{k} = 0$ and the in-plane dispersion ($\mathbf{k}_{\parallel}$) at $q = 0$, in addition to the density of states (DOS) for the SBSL of Fig. 5.3(a). The zero of energy is as in Fig. 5.3(a). In the miniband dispersion we note a highly dispersive $e1$ and nearly dispersionless $hh1$ miniband. The nature of the strongly delocalised $e1$ and strongly localised $hh1$ states are responsible for this behaviour with, e.g., the weakly bound $e1$ state possessing strong spatial overlap with its periodic image in other SL periods, leading to strong $e1$ miniband dispersion [58]. For the full suite of identified

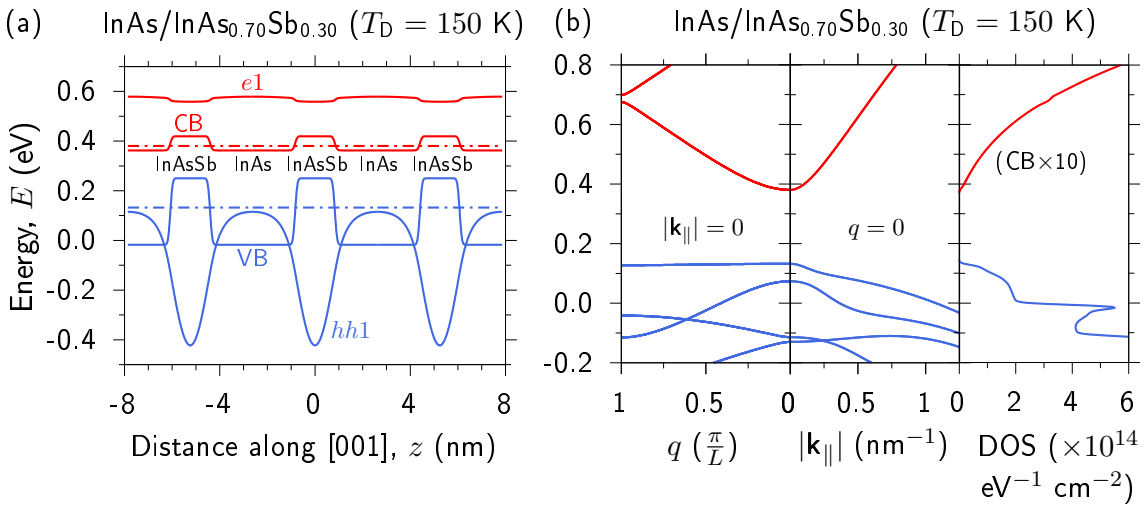


FIGURE 5.3: (a) Calculated CB (red) and VB (blue) offsets, illustrated for three periods of an InAs/InAs$_{0.70}$Sb$_{0.30}$ ($x = 30\%$) SBSL with $\lambda_{\text{cut}} = 5$ μm having respective InAs and InAs$_{1-x}$Sb$_x$ layer thicknesses $t_0 = 3.57$ nm and $t_x = 1.67$ nm (SL period $L = t_0 + t_x = 5.24$ nm). The dash-dotted red (blue) line denotes the energy of the lowest energy bound electron state $e1$ (highest bound hole state $hh1$). The corresponding $e1$ ($hh1$) probability density at $\mathbf{k}_{\parallel} = q = 0$ is shown using a solid red (blue) line, shifted so that the zero of probability density lies at the $e1$ ($hh1$) energy. (b) Calculated band structure and density of states (DOS) at temperature $T_{\text{D}} = 150$ K for the SBSL of (a). The left-hand, centre and right-hand panels respectively show the calculated miniband (q) dispersion, in-plane ($\mathbf{k}_{\parallel}$) band dispersion and DOS.

SBSLs (cf. Fig. 5.2), our calculations show that for increasing λ_{cut} CB (VB) states move closer in energy to the CB (VB) edge. This is a result of the increasing layer thicknesses, and hence SL period, which act to confine a greater number of states (cf. Sec. 5.3.3) while also reducing the confinement energy of each bound state. Our calculated in-plane and miniband dispersion are in quantitative agreement with similar calculations performed for comparable InAs/InAs$_{1-x}$Sb$_x$ SLs [170, 171].

5.3 Analysis of optical properties for photodetection

In this section we present our calculated optical absorption spectra for the InAs/InAs$_{1-x}$Sb$_x$ SBSLs described in Sec. 5.2. In analysing the trends in optical absorption we identify the potential for optimisation of photodetector performance as a function of Sb composition x. Then, for the 3 - 5 μm mid-IR window, we compute the IQE to determine to what extent photodetection can be optimised, and in which Sb composition range it is then predicted to be favourable to target growth. Finally, we analyse the SL electronic structure to elucidate the factors that to and dominate the calculated trends in IQE.

5.3.1 Impact of varying Sb composition on optical absorption

Following the same procedure previously outlined to calculate the spontaneous emission spectrum including the contribution of the miniband dispersion (cf. Chapter 4), we calculate the band-to-band optical absorption spectrum including q dependence in the same manner. Using our calculated SL eigenstates we compute the band-to-band optical absorption spectrum as [13, 127]

$$\alpha^{(\widehat{e})}(\hbar\omega) = \frac{\pi e^2}{\epsilon_0 m_0^2 c n_r \omega L} \sum_{n_c,n_v} \left(\frac{2\pi}{L}\right)^{-1} \int_{-\frac{\pi}{L}}^{+\frac{\pi}{L}} \mathrm{d}q \int \frac{\mathrm{d}\mathbf{k}_{\|}}{(2\pi)^2} |\widehat{e}\cdot\mathbf{p}_{n_c n_v \mathbf{k}}|^2 \, \delta(E_{n_c\mathbf{k}} - E_{n_v\mathbf{k}} - \hbar\omega)\,, \quad (5.7)$$

where $\hbar\omega$ is the photon energy, L is the SL period, $E_{n_c(n_v)\mathbf{k}}$ is the energy of conduction subband n_c (valence subband n_v) at wave vector $\mathbf{k} = (\mathbf{k}_{\|}, q)$, and $\mathbf{p}_{n_c n_v \mathbf{k}}$ is the inter-band momentum matrix element between subbands n_c and n_v at wave vector $\mathbf{k}$ (cf. Eq. (2.63)). $\mathbf{k}_{\|}$ is the wave vector in the (001) plane, while q describes the miniband dispersion along [001] (cf. Sec. 4.2.2) [58]. The unit vector $\widehat{e}$ denotes the photon polarisation, which we consider to be transverse electric (TE; $\widehat{e} = \widehat{x}$), i.e. incident normal to the growth plane of the SBSL. The calculation of the inter-band momentum matrix elements $\mathbf{p}_{n_c n_v \mathbf{k}}$ follows the procedure outlined in Secs. 4.2.2 and 2.2.3. As done in Sec. 4.2.2 (cf. Eq. 4.4), for numerical evaluation we replace the Dirac delta distribution in Eq. (5.7) by a hyperbolic secant lineshape [141] of width $\delta = 4$ meV [58].

In Fig. 5.4 we show the calculated TE-polarised ($\widehat{e} = \widehat{x}$) optical absorption in the 3 - 6.5 μm range for a selection of the $\lambda_{\text{cut}} = 5$, 5.5 and 6 μm SBSLs of Figs. 5.2(a), 5.2(b) and 5.2(c). We note excellent quantitative agreement with the measured absorption of Ref. [170] for an InAs/InAs$_{0.65}$Sb$_{0.35}$ SL having equivalent layer thicknesses and $\lambda_{\text{cut}} = 5$ μm. Our calculations across the investigated range of λ_{cut} predict an increase in the optical absorption with increasing x. For $\lambda_{\text{cut}} = 5$ μm, beginning at $x = 18\%$ we see an increase in optical absorption up to $x \approx 30\%$, beyond which there is minimal additional increase up to $x = 40\%$. In the 3 - 5 μm wavelength range, for SBSLs designed to have longer λ_{cut} ($= 5.5, 6$ μm) our calculations indicate enhanced scope to the increase the optical absorption for Sb compositions $x > 30\%$. However, for these longer wavelength SBSLs we note that the rate at which the magnitude of the optical absorption increases with increasing x still begins to reduce for $x > 30\%$. These results suggest the possibility to optimise photodetector performance in a given target wavelength range. It is to that optimisation that we now turn our attention.

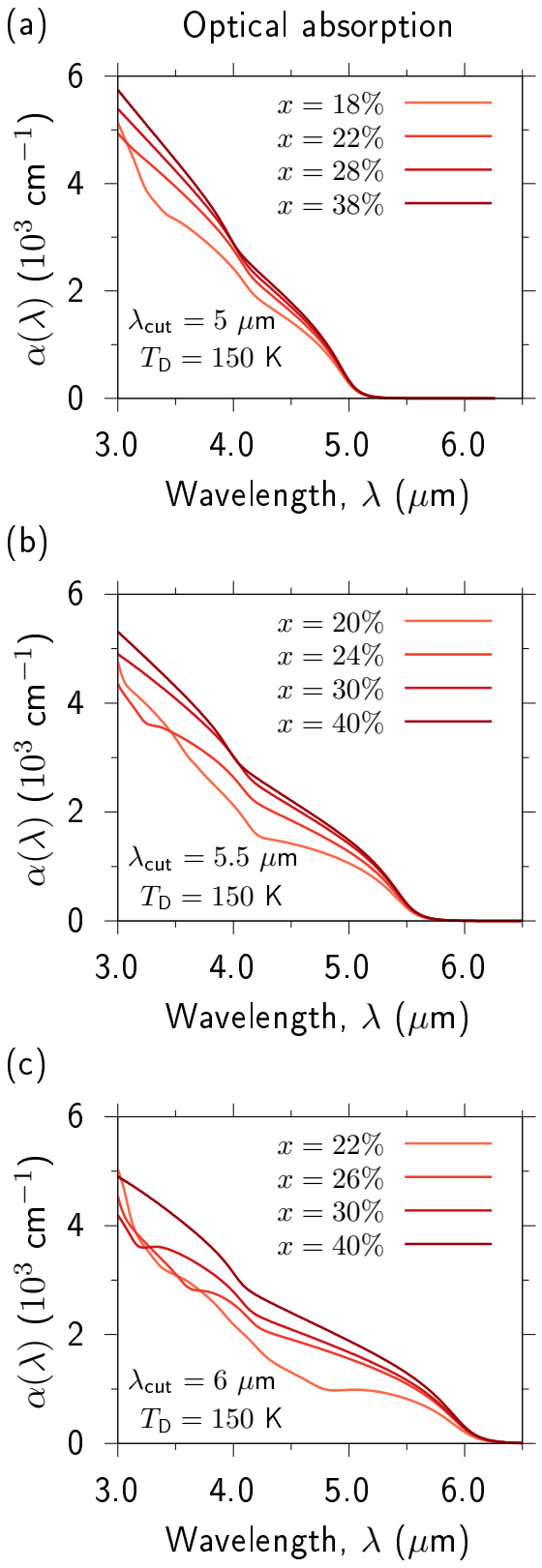


FIGURE 5.4: (a) Calculated optical absorption spectra $\alpha(\lambda)$ for InAs/InAs$_{1-x}$Sb$_x$ SBSLs with $\lambda_{\text{cut}} = 5$ μm having Sb compositions $x = 18$, 22, 28 and 38% (darkening red lines), at temperature $T_{\text{D}} = 150$ K. (b) and (c) are as in (a), but for respective cut-off wavelengths $\lambda_{\text{cut}} = 5.5$ and 6 μm, and for Sb compositions $x = 20$, 24, 30 and 40% and $x = 22$, 26, 30 and 40%.

5.3.2 Optimising optical absorption and internal quantum efficiency

When assessing photodetector performance there are several figures of merit that can be employed. These metrics are, in general, device-based and include, e.g. responsivity, normalised or specific detectivity, and noise-equivalent power [172]. Such figures of merit typically assess full device performance, with their calculation requiring definition of a full device structure and knowledge of parameters including the root mean square detector noise and signal bandwidth [172]. Our aim in this theoretical analysis is to provide general guidance by quantifying the performance of an InAs/InAs$_{1-x}$Sb$_x$ SBSL photodetector in a generic manner that is independent of the surrounding device structure. As such, we choose a figure of merit that quantifies the performance of the SL absorber region in isolation. For this purpose, we compute and analyse the IQE. Our evaluation of the IQE is based on using the calculated absorption spectrum for a given SL structure to compute the photocurrent generated by the absorption of photons in an an energy range $[\hbar\omega_{\mathrm{min}}, \hbar\omega_{\mathrm{max}}]$. This model calculation does not consider transport of photo-generated carriers within a device structure and, as such, corresponds to the idealised limit of long carrier diffusion lengths.

The spectral photocurrent density generated by absorption of photons of energy $\hbar\omega$, incident normal to the growth plane of the SBSL absorber from a radiating blackbody source, is [173]

$$\frac{\mathrm{d}J}{\mathrm{d}(\hbar\omega)} = e\,[1 - R(\hbar\omega)]\,a(\hbar\omega, T_{\mathrm{D}})\,b(\hbar\omega, T_{\mathrm{S}})\,, \tag{5.8}$$

where R is the surface reflectivity, a is the SBSL (photodetector) absorptivity, and b is the spectral photon flux of a radiating blackbody source at temperature T_{S}, with

$$a(\hbar\omega, T_{\mathrm{D}}) = 1 - \exp\left(-\alpha(\hbar\omega)d\right)\,, \tag{5.9}$$

$$b(\hbar\omega, T_{\mathrm{S}}) = \frac{2\pi}{h^3c^2}\,\frac{(\hbar\omega)^2}{\exp\left(\hbar\omega/k_{\mathrm{B}}T_{\mathrm{S}}\right) - 1}\,, \tag{5.10}$$

where $\alpha(\hbar\omega)$ is the calculated SBSL absorption at photon energy $\hbar\omega$ and detector operating temperature T_{D} (cf. Eq. (5.7)), and d is the total thickness of the SBSL absorber (which, in practice, typically consists of several hundred SL periods). Assuming zero reflection of photons impinging on the SBSL, $R(\hbar\omega) = 0$, integrating Eq. (5.8) yields the photocurrent density J generated by absorbing photons having energies between $\hbar\omega_{\mathrm{min}}$ and $\hbar\omega_{\mathrm{max}}$ in an absorber of thickness d as

$$J(d) = \frac{2\pi e}{h^3c^2}\int_{\hbar\omega_{\mathrm{min}}}^{\hbar\omega_{\mathrm{max}}} \frac{(\hbar\omega)^2\,\left[1 - \exp\left(-\alpha(\hbar\omega)d\right)\right]}{\exp\left(\hbar\omega/k_{\mathrm{B}}T_{\mathrm{S}}\right) - 1}\,\mathrm{d}(\hbar\omega)\,. \tag{5.11}$$

We assume a typical photodetector operating temperature $T_{\mathrm{D}} = 150$ K – employed in the electronic structure calculations whose eigenstates are used to evaluate Eq. (5.7) – for the detection of photons emitted by a blackbody at ambient temperature $T_{\mathrm{S}} = 300$ K. Using our calculated SBSL absorption spectra $\alpha(\hbar\omega)$ as input to Eq. (5.11), we compute $J(d)$ for $\lambda_{\mathrm{cut}} = 5$, 5.5 and 6 μm and absorber thickness up to $d = 5$ μm (corresponding to SBSLs containing $\approx$ 170 - 1,100 periods), for absorption between 3 and 5 μm. As we are targeting photodetection in the 3 - 5 μm window, we apply this as the integration range of Eq. (5.11), i.e. $\hbar\omega_{\mathrm{min}} = 0.248$ eV and $\hbar\omega_{\mathrm{max}} = 0.413$ eV. We note that the 3 - 5 μm range encompasses 0.32% of the photon flux obtained by integrating Eq. (5.10).

Finally, we compute the IQE as

$$\eta(d) = \frac{J(d)}{J(\infty)}\,, \tag{5.12}$$

where $J(\infty)$ is the photocurrent density at unit absorptivity, corresponding to absorption of all incident photons (cf. Eq. (5.9)). We note that the 3 - 5 μm wavelength (0.248 - 0.413 eV energy) integration range is applied to all calculations of IQE that follow, independent of λ_{cut}.

In Fig. 5.5(a) we present the calculated IQE vs. absorber thickness d for $\lambda_{\mathrm{cut}} = 5$ μm SBSLs having Sb compositions $x = 18$, 28 and 38%. At fixed d we note a relative increase in IQE of up to 17.5% with increasing Sb composition. The majority of this enhancement is achieved between $x = 18$ and 28%, with minimal further increase between $x = 28$ and 38%. This mirrors the behaviour observed for the optical absorption in Fig. 5.4(a), as described in Sec. 5.3.1. Equivalent calculations for SBSLs with $\lambda_{\mathrm{cut}} = 5.5$ and 6 μm reveal similar trends, where we note that the rate of enhancement of the IQE with increasing x is reduced beyond $x \approx 30$%. However, as in the optical absorption (cf. Figs. 5.4(b) and 5.4(c)), at longer λ_{cut} we do not observe the same saturation of the IQE as the cut-off wavelength moves further beyond the upper bound (5 μm) of the wavelength range investigated in our IQE calculations. This is consistent with our calculated absorption spectra since, for $\lambda_{\mathrm{cut}} > 5$ μm, the absorption does not tend towards zero in the 3 - 5 μm range. For $x = 30$% and $d = 5$ μm, we see in Fig. 5.5 a 23% and 24% increase in IQE moving from $\lambda_{\mathrm{cut}} = 5$ μm to $\lambda_{\mathrm{cut}} = 5.5$ and 6 μm, respectively. As detailed in Sec. 5.2.1, for increasing λ_{cut} the required layer thicknesses remain safely within our calculated critical thickness limits. Therefore, we conclude that increasing λ_{cut} to 5.5 μm for the SBSLs investigated in this work is a viable approach to increase IQE in the 3 - 5 μm wavelength range, but little further benefit is expected when increasing λ_{cut} to 6 μm. As expected, based on Eq. (5.11), at fixed x, we also note an overall increase of the IQE with increasing d. This is expected based on the absorptivity, Eq. (5.9), which increases with increasing d.

In Figs. 5.5(b), 5.5(c) and 5.5(d) we show the calculated IQE as a function of Sb composition x for SBSL absorber thicknesses $d = 3$, 4 and 5 μm, at cut-off wavelengths $\lambda_{\mathrm{cut}} = 5$, 5.5 and

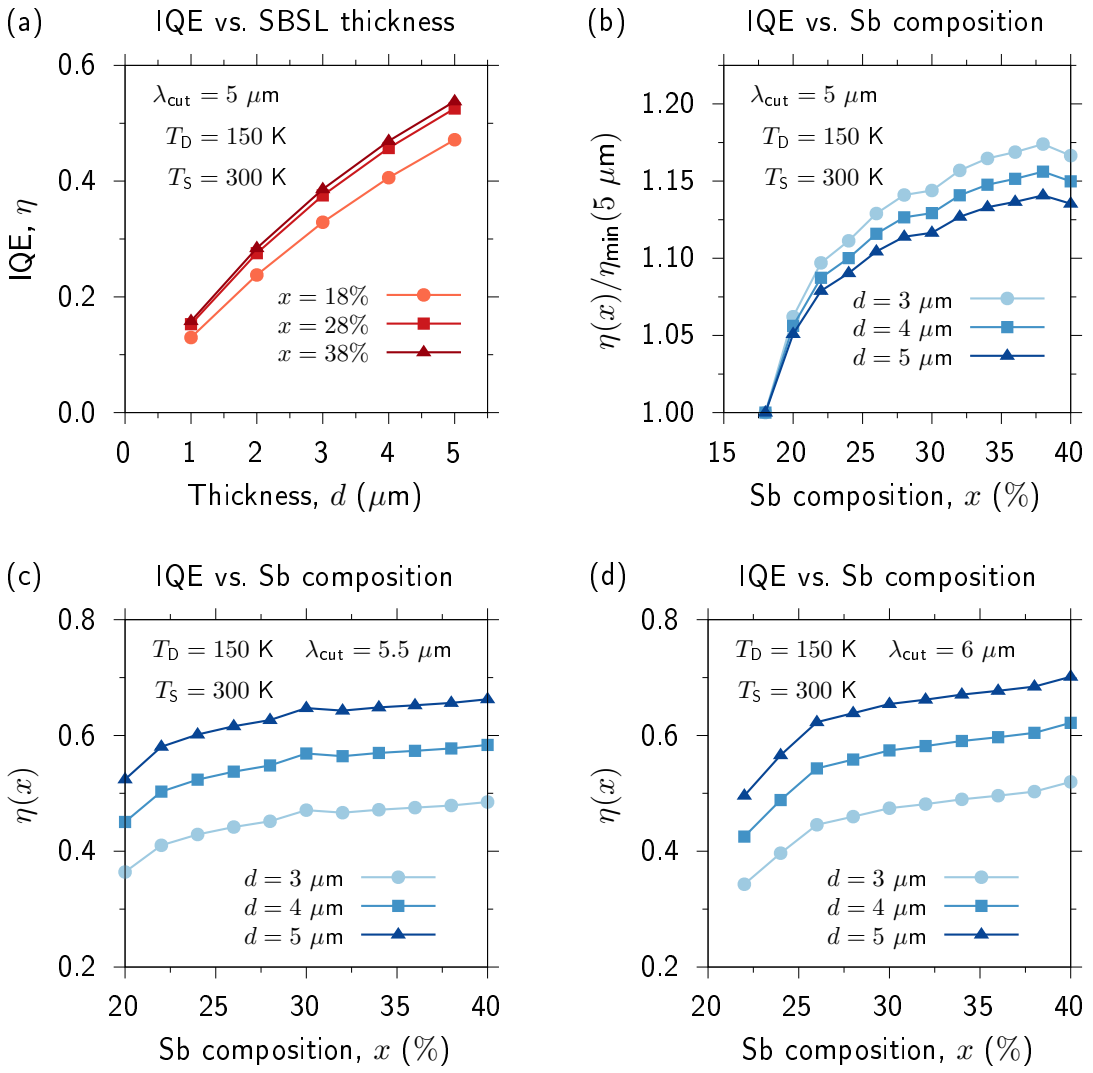


FIGURE 5.5: (a) Calculated IQE η vs. total SBSL absorber thickness d for InAs/InAs$_{1-x}$Sb$_x$ SBSLs having $\lambda_{cut} = 5$ μm, for Sb compositions $x = 18\%$ (closed orange circles), 28% (closed red squares) and 38% (closed dark red triangles), calculated assuming detector operating temperature $T_D = 150$ K for the absorption of 3 - 5 μm wavelength radiation emitted by a blackbody source at temperature $T_S = 300$ K. (b) Calculated IQE η vs. Sb composition x for SBSLs having $\lambda_{cut} = 5$ μm for absorber thicknesses $d = 3$ μm (closed light blue circles), 4 μm (closed blue squares) and 5 μm (closed dark blue triangles), with $T_D = 150$ K and $T_S = 300$ K. In each case the IQE is shown relative to its calculated value at $x = 18\%$. (c) Calculated IQE η vs. Sb composition x for SBSLs having $\lambda_{cut} = 5.5$ μm for absorber thicknesses $d = 3$ μm (closed light blue circles), 4 μm (closed blue squares) and 5 μm (closed dark blue triangles), with $T_D = 150$ K and $T_S = 300$ K. (d) Equivalent to (c) for SBSLs having $\lambda_{cut} = 6$ μm. In each case the IQE is calculated with $\hbar\omega_{min} = 0.248$ eV and $\hbar\omega_{max} = 0.413$ eV

6 μm respectively. In Fig. 5.5(b), to quantify trends across different absorber thicknesses for $\lambda_{cut} = 5$ μm, for each value of d we normalise the IQE relative to the minimum IQE calculated for a given cut-off wavelength, $\eta_{min}(\lambda_{cut})$, which for $\lambda_{cut} = 5$ μm is at $x = 18\%$. As detailed in Sec. 5.2.1, increasing λ_{cut} increases the lowest Sb composition for which that cut-off wavelength can be reached in a SBSL. In Figs. 5.5(c) and 5.5(d), for $\lambda_{cut} = 5.5$ and 6 μm we show the IQE for absorption between 3 and 5 μm on an absolute scale. Firstly, we examine the predicted

trends for $\lambda_{\text{cut}} = 5$ μm. Independent of d we observe a consistent trend: the IQE initially increases rapidly up to $x = 30\%$, demonstrating a relative increase of up to $\approx 15\%$. Beyond $x = 30\%$ we see minimal additional enhancement of the IQE up to $x = 40\%$. This trend is strongly mirrored for $\lambda_{\text{cut}} = 5.5$ μm, with a larger rate of increase of the IQE with increasing x for $x < 30\%$. We compute a relative increase of up to $\approx 30\%$ at $x = 30\%$. For SBSLs having $\lambda_{\text{cut}} = 6$ μm, for $x < 26\%$ we see IQE lower than that of SBSLs having $\lambda_{\text{cut}} = 5.5$ μm. For $\lambda_{\text{cut}} = 6$ μm we predict a larger rate at which the IQE increases with increasing Sb composition for $x < 30\%$. However, this larger rate of increase only allows for minimal further enhancement in the IQE compared to SBSLs having $\lambda_{\text{cut}} = 5.5$ μm for $x > 30\%$.

These results, in conjunction with the results of Sec. 5.2, suggest that growth of InAs/InAs$_{1-x}$Sb$_x$ SBSLs for mid-IR photodetectors should not exclusively target structures having either lower Sb composition with thicker layers, or higher Sb composition with thinner layers. Instead, our calculations predict that device development should target intermediate Sb compositions close to $x = 30\%$. We have reached this general conclusion based on consideration of three key factors: (i) for $x > 30\%$ we generally observe a rapid saturation of the calculated IQE, particularly for shorter λ_{cut}, (ii) approaching $x = 40\%$ we predict large in-plane compressive strains in excess of 2% which, while within estimated strain-thickness limits, nonetheless increase the chance that deleterious strain-related defects form in the lattice, and (iii) approaching $x = 40\%$ we also observe layer thicknesses corresponding to a small number of material monolayers where, in such thin layers, the SBSL electronic and optical properties will be strongly sensitive to sub-nm variations in layer thicknesses, in addition to Sb composition profiles due to unintentional intermixing [174–176]. The latter two factors represent key challenges for epitaxial growth and device development.

5.3.3 Origin of calculated trends in the internal quantum efficiency

Having described trends in the calculated SBSL IQE vs. both cut-off wavelength and Sb composition, we now turn our attention to elucidating and quantifying the origin of these trends. In practice, there are two key contributions to the optical absorption described by Eq. (5.7): the joint density of states (JDOS) and the $(\mathbf{k}_{\parallel}, q)$-dependent momentum matrix elements, with the latter weighting the individual $(\mathbf{k}_{\parallel}, q)$-resolved pairwise subband contributions to the JDOS. We therefore analyse in detail the interplay of these two quantities, which allows to identify the consequences of their evolution and competition with increasing Sb composition as the underlying driver of the calculated trends in IQE discussed above.

Using the calculated electronic structure for each SBSL, we evaluate the JDOS per unit volume as [13]

$$\mathrm{JDOS}(E) = \frac{1}{L}\sum_{n_c,n_v}\left(\frac{2\pi}{L}\right)^{-1}\int_{-\pi/L}^{+\pi/L}\mathrm{d}q\int\frac{\mathrm{d}\mathbf{k}_\parallel}{(2\pi)^2}\delta\left(E_{n_c\mathbf{k}} - E_{n_v\mathbf{k}} - E\right). \tag{5.13}$$

The leading factor of $1/L$ matches that in the optical absorption, thereby removing the explicit dependence on the SL period and allowing comparison between structures having different L on equal footing. For consistency with our calculated optical absorption spectra (cf. Eq. (5.7)) in our evaluation of the JDOS we replace the Dirac delta distribution in Eq. (5.13) by a hyperbolic secant lineshape [141] of width $\delta = 4$ meV [58]. In Figs. 5.6(a) and 5.6(b) we show the calculated JDOS for InAs/InAs$_{1-x}$Sb$_x$ SBSLs with $\lambda_{\mathrm{cut}} = 5$ μm having $x = 18$ and 30% respectively, for the 0.248 - 0.413 eV energy (3 - 5 μm wavelength) range considered in the IQE calculations. We show the calculated full JDOS which includes contributions from all conduction and valence subband pairs n_c and n_v. Firstly, at $x = 18\%$ we note the presence of a larger number of individual subband pairs in the investigated energy range, with the thicker SBSL structures at lower Sb composition supporting a larger number of bound states. For example, the $x = 38\%$ SBSL supports only two bound hole states: the HH-like $hh1$ and a predominantly light-hole-like $lh1$, the latter identified via its calculated Bloch band character [170, 171]. Secondly, we note that the overall JDOS is decreased by a factor of approximately two at $x = 38\%$, but the $e1$-$hh1$ contribution to the JDOS is little changed between $x = 18$ and 38%. This reduction in JDOS between $x = 18$ and 38% is out of step with the calculated increase in optical absorption in this energy range (cf. Fig. 5.4(a)). This indicates that an increase in optical matrix elements must dominate over the reduction in JDOS and account for the enhanced optical absorption.

The full $(\mathbf{k}_\parallel, q)$-dependent momentum matrix elements between subband pairs are not readily visualised. To corroborate that increasing Sb composition at fixed λ_{cut} can strongly increase individual optical matrix elements, we show in Fig. 5.6(c) the calculated $\mathbf{k}_\parallel = q = 0$ squared momentum matrix elements $|\hat{x}\cdot\mathbf{p}_0|^2$ for SBSLs having $\lambda_{\mathrm{cut}} = 5$ μm and Sb compositions $x = 18$ - 38% in steps of 4%. These results are presented as the dimensionless oscillator strength f, calculated via the Kane parameter E_P as [177]

$$f = \frac{E_P}{E_g} = \frac{2|\hat{x}\cdot\mathbf{p}_0|^2}{m_0 E_g}, \tag{5.14}$$

where E_g is the transition energy between a subband pair. Using Eq. (5.14) to calculate the dimensionless oscillator strength f allows comparison of the strength of transitions with different energies. The inset of Fig. 5.6(c) displays the calculated $e1$-$hh1$ momentum matrix elements vs. Sb composition x, shown relative to the calculated value at $x = 18\%$. The 3 - 5 μm range employed in our IQE calculations is shown as a grey shaded region. We note the additional dipole-allowed $e1$-$hh3$ optical transitions seen for $x = 18$ and 22%, which respectively lie within and outside the IQE calculation range. As with the additional bound subband contributions to

the JDOS for lower Sb compositions, the thicker InAs and InAs$_{1-x}$Sb$_x$ layers required to maintain λ_{cut} for lower Sb composition x drive this behaviour. As the $e1$-$hh3$ inter-band transitions do not lie within the 3 - 5 μm range for the majority of the $x = 18$ - 40% composition range, we restrict our analysis to the $e1$-$hh1$ and $e1$-$lh1$ transitions. For $x = 18\%$ we note that the $e1$-$lh1$ (squared) optical matrix element is 55% of that associated with the $e1$-$hh1$ transition. The $e1$-$hh1$ optical matrix element increases by 21% up to $x = 30\%$, beyond which it increases by

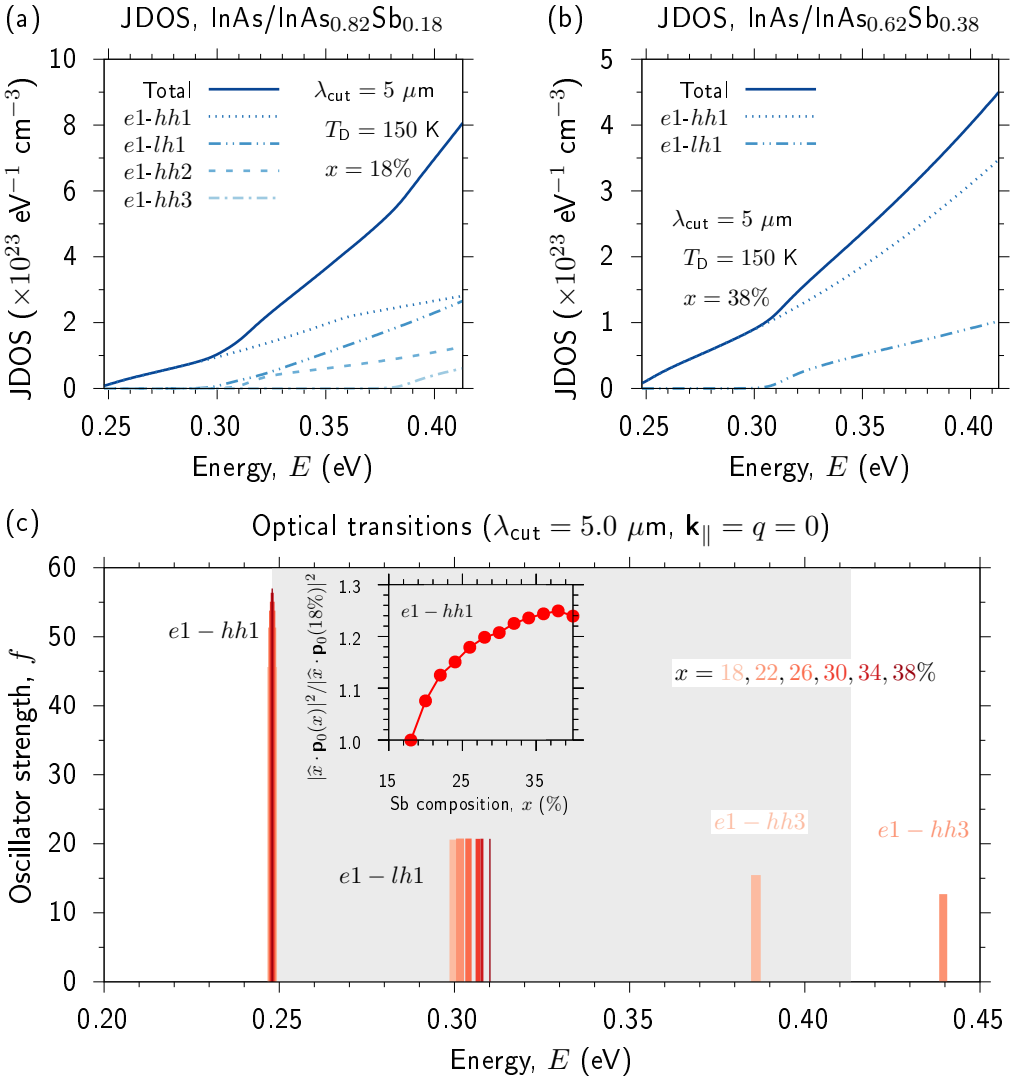


FIGURE 5.6: (a) Calculated JDOS of an InAs/InAs$_{0.82}$Sb$_{0.18}$ ($x = 18\%$) SBSL with $\lambda_{\text{cut}} = 5$ μm, including contributions from all conduction and valence subband pairs (solid blue line). Dotted, dashed and dash-dotted lines show contributions to the JDOS from individual subband pairs, which in this SBSL corresponds to one bound electron state $e1$ and four bound hole states $hh1$, $lh1$, $hh2$ and $hh3$ (in order of decreasing energy at $\mathbf{k}_{\parallel} = q = 0$). (b) As in (a), but for an InAs/InAs$_{0.62}$Sb$_{0.38}$ SBSL supporting two bound hole states $hh1$ and $lh1$. (c) Calculated $\mathbf{k}_{\parallel} = q = 0$ squared optical (momentum) matrix elements $|\hat{x} \cdot \mathbf{p}_0|^2$, scaled as the oscillator strength f vs. inter-band transition energy E for a selection of SBSLs having $\lambda_{\text{cut}} = 5$ μm and Sb compositions $x = 18$, 22, 26, 30, 34 and 38% (darkening red). Shaded region highlights the $\hbar\omega = 0.248$ - 0.413 eV photon energy ($\lambda = 3$ - 5 μm wavelength) range used in evaluation of the IQE. Inset: $\mathbf{k}_{\parallel} = q = 0$ $e1$-$hh1$ squared optical matrix elements vs. x for $\lambda_{\text{cut}} = 5$ μm. The squared optical matrix elements are shown relative to their calculated value at $x = 18\%$.

a maximum of 25% at $x = 38\%$. This increase is significantly larger than that associated with $e1$-$lh1$, which increases by only 4% between $x = 18$ and 38%. When examined independently, the trend in the $e1$-$hh1$ optical matrix elements strongly mirror that of the IQE (cf. Figs. 5.5(b) and 5.6(c)). This explicitly validates the $e1$-$hh1$ momentum matrix element – which is largely determined by the $e1$-$hh1$ spatial overlap – as a useful heuristic for high-level analysis. As x increases the layer thicknesses decrease to maintain $\lambda_{\text{cut}} = 5$ μm, resulting in a larger $e1$-$hh1$ spatial overlap that in turn increases the optical matrix element. Our analysis therefore indicates that the increase in IQE with increasing x is driven and dominated by a strong increase in the strength of the zone-centre $e1$-$hh1$ transitions with increasing Sb composition.

5.4 Conclusions

In summary, the methodology developed to investigate radiative recombination in unstrained InAs/GaSb SLs in Chapter 4 has been extended here to treat optical absorption in strained, and strain-balanced, InAs/InAs$_{1-x}$Sb$_x$ SLs for applications in mid-IR photodetectors operating in the 3 - 5 μm wavelength range. By enforcing fixed cut-off wavelength λ_{cut}, in addition to mandating strain balancing with respect to a GaSb substrate, we systematically identified mid-IR SBSLs having Sb compositions $x = 18$ - 40%. For $\lambda_{\text{cut}} = 5$, 5.5 and 6 μm we identified that SBSLs can reach the desired λ_{cut} for Sb compositions $x \geq 18$, 20 and 22% respectively. At $x = 40\%$ the InAs$_{1-x}$Sb$_x$ layers have in-plane compressive strain $> 2\%$, with strain balancing mandating small layer thickness approaching $\lesssim$ five monolayers. The high Sb composition regime thus poses challenges for epitaxial growth. Based on rigorous SL electronic structure calculations we computed $(\mathbf{k}_{\parallel}, q)$-dependent optical matrix elements and absorption spectra. These calculations predict an increase in optical absorption in the 3 - 5 μm range with increasing x. The calculated SBSL absorption spectra were employed in a model calculation of the IQE for 3 - 5 μm photodetection of radiation from an ambient blackbody source. At fixed Sb composition x and SBSL absorber thickness d, we demonstrated the potential to increase the IQE in the 3 - 5 μm window by targeting longer cut-off wavelength λ_{cut}. For $x = 30\%$ and $d = 5$ μm, we see a 23% and 24% increase in IQE moving from $\lambda_{\text{cut}} = 5$ μm to $\lambda_{\text{cut}} = 5.5$ and 6 μm, respectively. For $\lambda_{\text{cut}} = 5$ μm, the calculated IQE vs. x demonstrated a (relative) enhancement of $\approx 15\%$ between $x = 18$ and 30%, with minimal subsequent increase at higher Sb composition. For $\lambda_{\text{cut}} = 5.5$ and 6 μm, we predict a greater rate of increase in IQE up to $x = 30\%$ and increased enhancement of the IQE beyond $x = 30\%$. Moving from $\lambda_{\text{cut}} = 5.5$ to 6 μm sees a reduction in the IQE for $x < 26\%$. Also, while the rate of increase of IQE is larger for $\lambda_{\text{cut}} = 6$ μm, minimal additional enhancement of the IQE is observed for $x > 30\%$. We also note that interrogation of the electronic structure vs. x elucidated that this trend derives from a competition between the JDOS and optical matrix elements, which respectively decrease and increase in SBSLs with increasing x. The increase of the latter being sufficient to drive a net increase of the IQE.

The results of our analysis suggest targeting growth of InAs/InAs$_{1-x}$Sb$_x$ SBSLs having Sb compositions $x \approx 25$ - 30%. SBSLs in this composition range are predicted to deliver appreciable enhancement of the IQE, while avoiding the large in-plane strain and narrow layer thicknesses required to maintain strain-balancing at higher Sb composition ($x \approx 40\%$). The optimum SBSLs identified by our analysis are compatible with recently demonstrated epitaxial growth, suggesting a promising route for device design to guide the development of III-V SL photodetectors for real-world applications.

Chapter 6

Revised and improved band parameters for III-P semiconductors

6.1 Overview

In this Chapter we examine the band parameters of III-P semiconductors.[1] III-P semiconductors are well established as the basis of red light emitting diodes [30] and diode lasers [31–35], and there remains significant interest in III-P heterostructures for the development of visible-wavelength light emitters for applications in solid-state lighting and in display technologies for virtual and augmented reality [36–38], in addition to applications of III-P quantum wells and dots in integrated Si photonics [39–41], and as hosts of Wigner crystallisation for quantum computing [42, 43]. Accurate knowledge of the electronic band parameters is essential to facilitate predictive theory and design of the physical properties of these nanostructures. Despite its relevance to practical applications, limited detailed investigation of the electronic structure of AlGaInP alloys and, in particular, the properties of AlP has been undertaken.

Notably, there remains large uncertainty surrounding several key band structure parameters for AlP. Several sets of published parameters for AlP have been inferred based on extrapolation of parameters for $Al_x(Ga,In)_{1-x}P$ alloys [44, 178, 179]. Key examples include the relative energy and ordering of the Γ- and L-point conduction band (CB) valley minima above the indirect X-point CB minimum, and the magnitude of the direct Γ_{6c}-Γ_{8v} band gap. Literature reports differ on the presence of X-L-Γ vs. X-Γ-L CB valley energy ordering [180–182], and reported values of the direct Γ_{6c}-Γ_{8v} band gap vary by > 1 eV [44, 178–180, 183–185]. While less uncertainty exists for (Ga,In)P, there are key uncertainties that, while smaller than in AlP, can still significantly impact the results of electronic structure calculations for quantum-confined heterostructures

[1] The calculations in this Chapter were performed in collaboration with my Co-Supervisor, Dr. Christopher A. Broderick, who performed fitting to spectroscopic ellipsometry data in Sec. 6.3.2, calculation of effective masses and Luttinger parameters in Sec. 6.4.2, and the valence band offset calculations in Sec. 6.6.

[45]. This includes a number of CB minima energy splittings between the Γ, X and L CB valleys in InP [44]. For GaP, there exists a large spread in reported effective masses [44]. Additionally, the band edge deformation potentials for III-P compounds have not been subject to rigorous examination and, in many cases, have yet to be explicitly investigated [44, 45]. A number of commonly employed parameter values have been taken from the extrapolation of results measured from $Ga_{1-x}In_xP$ lattice-matched to GaAs [44, 45, 186, 187].

Systematic review of literature parameters for III-P compounds highlights the challenges disparate parameter values present for predictive simulations [45]. The spread in reported values of key material parameters for III-P compounds – and specifically for AlP [44] – are sufficiently large to qualitatively change the nature (direct or indirect) of the predicted band gap in III-P heterostructures [45]. Improved knowledge of the band parameters and band edge deformation potentials is thus critical to underpin accurate and predictive analysis of III-P heterostructures.

We present a detailed analysis of the band structure of AlP, GaP and InP, which hereafter we refer to as (Al,Ga,In)P, using first-principles calculations based on density functional theory (DFT) employing a hybrid exchange-correlation (XC) functionals. Our calculations follow the method outlined in Chapter 3, meaning DFT calculations were performed using the projector augmented-wave (PAW) method as implemented in VASP. We use a combination of XC functionals to compute structural, elastic and electronic band parameters. For the calculation of structural parameters and elastic moduli we use the local density approximation (LDA) and revised Heyd-Scuseria-Ernzerhof for solids (HSEsol) XC functionals [79]. Bulk electronic band structure calculations are carried out using the HSEsol XC functional, and also in the meta-generalised gradient approximation (meta-GGA) by combining the Tran-Blaha modified Becke-Johnson (TB-mBJ) exchange potential with the LDA to the electronic correlation [73, 77]. The potential-only TB-mBJ functional possesses no associated exchange-correlation energy, meaning that it is not possible to compute forces, thereby precluding TB-mBJ-based structural relaxation. We use LDA-calculated structural parameters in our TB-mBJ calculations. The TB-mBJ exchange potential, combined with the LDA to the electronic correlation, has become a popular approach to analyse semiconductor band structure, due to its resolution of the band gap underestimation problem at low (near-LDA) computational expense. This work does not perform a direct comparison between meta-GGA and hybrid functional band structure calculations. Such benchmark calculations have been performed by several other groups [78, 188]. Therefore we employ two independent frameworks: (i) computationally expensive HSEsol hybrid functional calculations, and (ii) comparatively computationally inexpensive LDA + TB-mBJ calculations. In the context of DFT, approach (i) provides state-of-the-art accuracy, while approach (ii) has gained popularity for high-throughput calculations (e.g. composition-dependent alloy supercells [189–191]). The HSEsol (TB-mBJ) calculations employed a plane wave cutoff energy of at least 400 eV (500 eV), and Γ-centred grids containing at least $11 \times 11 \times 11$ **k**-points for Brillouin zone (BZ) integration. A key initial observation is an apparent inconsistency between reported

values of the direct band gap in AlP. Here, detailed analysis of literature data highlights the inadequacy of the interpretation of experimental measurements, motivating us to re-evaluate literature ellipsometry data. Careful re-evaluation of experimental data in light of our DFT calculations allows to revise the magnitude of the direct Γ_{6c}-Γ_{8v} band gap upwards by ≈ 1 eV vs. the previously accepted value. This reconciles theory and experiment for this critical material parameter. Then, with a revised set of parameters in place for AlP, we also compute parameters for GaP and InP to reduce the systematic uncertainties present in the literature. Specifically, we compute revised values of the band edge effective masses, band edge deformation potentials and direct and indirect band gap pressure coefficients. While previous III-P parameter sets have generally been assembled piecewise from the experimental and theoretical literature [44], our calculations provide a consistent set of material parameters for III-P semiconductors. This resolves a significant and decades-old inconsistency for the direct band gap in AlP. This provides an improved basis from which to establish predictive calculations of the optoelectronic properties of III-P heterostructures for classical and quantum photonic applications.

The remainder of this chapter is organised as follows. In Sec. 6.2 we present our calculated structural parameters for zinc-blende III-P materials. In Sec. 6.2.1 we calculate and analyse the equilibrium lattice parameters for (Al,Ga,In)P. In Sec. 6.2.2 we present our analysis of the elastic moduli for (Al,Ga,In)P. In Sec. 6.3 we present our analysis of the electronic structure of (Al,Ga,In)P. In Sec. 6.3.1 we describe our approach to fitting the exact exchange (Becke-Roussel) mixing in the HSEsol (TB-mBJ) calculations, to reproduce the experimentally known fundamental band gap. With this procedure outlined, in Sec. 6.3.2 we validate this approach via detailed comparison to experimental results for AlP. Having validated our electronic structure calculations, in Sec. 6.4 we compute unstrained electronic band parameters, with comparison to existing literature. In Sec. 6.4.1 we analyse the calculated direct and indirect band gaps, and key band edge energy splittings. In Sec. 6.4.2 we discuss the calculated effective masses and Luttinger parameters. In Sec. 6.4.3 we detail calculated Kane parameters E_P, and demonstrate of the ellipticity of the extracted parameters set for application in 8-band $\mathbf{k}\cdot\mathbf{p}$ Hamiltonians. In Sec. 6.5 we analyse the computed deformation potentials and hydrostatic pressure coefficients. In Sec. 6.6 we analyse the predicted natural (unstrained) valence band offsets (VBOs). Finally, in Sec. 6.7 we summarise and conclude.

6.2 Structural parameters

In this Section we describe and present our calculations of the equilibrium lattice parameters and elastic moduli of (Al,Ga,In)P. We begin with a brief recapitulation of linear elasticity theory, which we then apply to obtain equilibrium lattice parameters a for zinc-blende (Al,Ga,In)P. Our calculation of the lattice parameters is required for the calculation of the unstrained and

strained electronic band parameters, analysis of these parameters follows this Section, beginning from Sec. 6.3. We then describe our calculation of and present our results for the elastic moduli C_{ij}, bulk modulus B_0 and internal strain (Kleinman) parameter ζ.

6.2.1 Lattice parameter

We consider materials with zinc-blende crystal structure, this being the equilibrium crystal structure of (Al,Ga,In)P. The face-centred cubic lattice vectors of the zinc-blende primitive unit cell are given in Cartesian coordinates by

$$\mathbf{a}_1 = \left(0, \frac{a}{2}, \frac{a}{2}\right), \tag{6.1}$$
$$\mathbf{a}_2 = \left(\frac{a}{2}, 0, \frac{a}{2}\right), \tag{6.2}$$
$$\mathbf{a}_3 = \left(\frac{a}{2}, \frac{a}{2}, 0\right), \tag{6.3}$$

where a is the equilibrium lattice parameter, and the x, y and z axes are respectively chosen to align with the [100], [010] and [001] principal crystal axes, having corresponding Cartesian unit vectors $\widehat{x}$, $\widehat{y}$ and $\widehat{z}$. The equilibrium positions of the atoms in the zinc-blende primitive unit cell, a basis of two atoms, are therefore given by

$$\mathbf{r}_1 = \mathbf{0}, \tag{6.4}$$
$$\mathbf{r}_2 = \left(\frac{a}{4}, \frac{a}{4}, \frac{a}{4}\right). \tag{6.5}$$

We then apply an arbitrary deformation to this primitive unit cell, described by the macroscopic strain tensor ϵ. The positions of the atoms in the unit cell then become

$$\mathbf{r}_1 = \mathbf{0}, \tag{6.6}$$
$$\mathbf{r}_2 = (I + \epsilon)\left(\frac{a}{4}, \frac{a}{4}, \frac{a}{4}\right) + \mathbf{t}, \tag{6.7}$$

where I is the 3×3 identity matrix, and $\mathbf{t}$ is the internal strain vector. The internal strain vector is given by [192]

$$\mathbf{t} = \left(-\frac{a}{2}\zeta\epsilon_{yz}, -\frac{a}{2}\zeta\epsilon_{xz}, -\frac{a}{2}\zeta\epsilon_{xy}\right), \tag{6.8}$$

where ζ is the internal strain, or Kleinman, parameter [193]. When the crystal is in equilibrium when the internal strain is minimised, i.e. $\mathbf{t} = 0$. When a strain having non-zero shear components is applied, the crystal develops a non-zero internal strain – i.e. a relative displacement of the two interpenetrating face-centred cubic lattices that make up the zinc-blende structure – in order to minimise the lattice energy.

At equilibrium the total energy, and the magnitude of the components of the macroscopic stress experienced by the unit cell, will be minimised, indicating that the structure has reached its most stable geometric configuration. To determine the equilibrium lattice parameter we vary the lattice parameter, performing an internal relaxation of the ionic positions $\mathbf{r}_1$ and $\mathbf{r}_2$, and calculate the stress on the unit cell. In a small range near equilibrium, the lattice parameter vs. stress relationship will behave approximately linearly. In this approximately linear regime, in which we seek zero stress to compute the equilbrium lattice parameter, we

TABLE 6.1: DFT-calculated equilibrium lattice parameter a, elastic moduli C_{ij}, bulk modulus B_0 and Kleinman parameter ζ for AlP, GaP and InP. HSEsol- and LDA-calculated results are respectively denoted by a dagger (†) and an asterisk ($*$). The HSEsol calculations used $\alpha = 0.25$.

	AlP		GaP		InP	
Parameter	This work	Reference	This work	Reference	This work	Reference
a (Å)	$5.449^{\dagger}$	5.467^{a}	$5.427^{\dagger}$	5.451^{a}	$5.879^{\dagger}$	5.870^{a}
	5.435^{*}	5.471^{b}	5.426^{*}	5.456^{f}	5.878^{*}	5.886^{f}
		5.417^{c}		5.451^{h}		5.86^{h}
		5.460^{d}		5.443^{i}		5.861^{i}
C_{11} (GPa)	$139.7^{\dagger}$	133.0^{a}	$152.29^{\dagger}$	140.5^{a}	$107.74^{\dagger}$	101.1^{a}
	132.5^{*}	138.3^{b}	141.29^{*}	150.0^{f}	99.60^{*}	105.9^{f}
		150.0^{e}		143.9^{i}		104.2^{i}
		133.6^{f}				
C_{12} (GPa)	$70.8^{\dagger}$	63.0^{a}	$70.15^{\dagger}$	62.03^{a}	$61.75^{\dagger}$	56.1^{a}
	68.9^{*}	67.7^{b}	66.97^{*}	64.3^{f}	58.72^{*}	56.4^{f}
		64.2^{e}		65.2^{i}		60.5^{i}
		65.1^{f}				
C_{44} (GPa)	$65.8^{\dagger}$	61.5^{a}	$73.51^{\dagger}$	70.33^{a}	$46.99^{\dagger}$	45.6^{a}
	61.7^{*}	66.5^{b}	67.80^{*}	78.4^{f}	42.65^{*}	49.3^{f}
		61.1^{e}				
		64.1^{e}				
B_0 (GPa)	$93.91^{\dagger}$	86.3^{a}	$97.72^{\dagger}$	88.2^{a}	$77.25^{\dagger}$	71.1^{a}
	90.25^{*}	92.8^{e}	92.15^{*}	91.4^{i}	72.69^{*}	75.1^{i}
		86.0^{g}		89.6^{g}		71.0^{g}
		90.3^{g}		88.2^{g}		71.6^{g}
ζ	$0.631^{\dagger}$	0.576^{j}	$0.568^{\dagger}$	0.533^{j}	$0.686^{\dagger}$	0.652^{j}
	0.619^{*}		0.583^{*}		0.703^{*}	

[a]Recommended by Vurgaftman et al., see Ref. [44] for details
Theory: [b]Ref. [194], [c]Ref. [195], [f]Ref. [185], [g]Ref. [196], [h]Ref. [180], [j]Ref. [197]
Experiment: [d]Ref. [198], [e]Ref. [199], [i]Ref. [200]

extract the lattice parameter as the zero stress intercept of a linear fit of the lattice parameter and stress. This means we can then determine the equilibrium lattice parameter a by computing the value of a that produces zero stress on the unit cell. Our HSEsol calculations of a employed exact exchange mixing $\alpha = 0.25$. Our HSEsol- and LDA-calculated lattice parameters are summarised in Table 6.1. We observe good overall agreement between our calculated lattice parameters and literature values, with agreement to within 1% in all cases. We note, in general, a slight underestimation of the calculated lattice parameters in comparison to experimental literature values. This is a consequence of lattice expansion associated either with measurements having been performed at non-zero temperature, due to the contribution of the zero-point anharmonic lattice energy [79]. Our DFT calculations are carried out at zero temperature and do not account for these contributions. The errors in calculated lattice parameters and the contribution of the zero-point anharmonic lattice energy has been studied by Schimka et al. [79], who found that the HSEsol XC functional yields the smallest deviation from experiment amongst conventionally employed DFT XC functionals. Our HSEsol-calculated a deviate by $\leq 1\%$ from experimental measurements, and we note that a zero-point anharmonic energy correction could further improve the accuracy of these results [79]. Our HSEsol-calculated lattice parameters being larger than those calculated in the LDA is consistent with previous calculations and benchmarking of DFT XC functionals [201].

6.2.2 Elastic parameters

Considering harmonic elasticity, the elastic energy of a material with arbitrary crystal structure is given, using Voigt notation, by

$$E = \frac{\Omega}{2} \sum_{i=1}^{6} \sum_{j=1}^{6} C_{ij} \epsilon_i \epsilon_j \,, \tag{6.9}$$

where $\Omega = |\mathbf{a}_1 \cdot (\mathbf{a}_2 \times \mathbf{a}_3)|$ is the unit cell volume, C_{ij} are the elastic moduli, and ϵ_i are the components of the strain tensor. We note that, in Voigt notation $\epsilon_1 = \epsilon_{xx}$, $\epsilon_2 = \epsilon_{yy}$, $\epsilon_3 = \epsilon_{zz}$, $\epsilon_4 = 2\epsilon_{yz}$, $\epsilon_5 = 2\epsilon_{xz}$ and $\epsilon_6 = 2\epsilon_{xy}$. The elastic energy can be described in terms of components σ_i of the stress tensor produced by an applied strain ϵ_j

$$\sigma_i = \frac{1}{\Omega} \frac{\partial E}{\partial \epsilon_i} = \sum_{j=1}^{6} C_{ij} \epsilon_j \,, \tag{6.10}$$

which is the generalised form of Hooke's law. Combining Eqs. (6.9) and (6.10), we can write the elastic crystal energy as

$$E = \frac{\Omega}{2} \sum_i \sigma_i \epsilon_i \,. \tag{6.11}$$

The elastic moduli can then be computed either by taking second derivatives of the elastic energy with respect to strain, or by taking first derivatives of the lattice stress with respect to strain, yielding

$$C_{ij} = \frac{1}{\Omega} \left(\frac{\partial^2 E}{\partial \epsilon_i \partial \epsilon_j} \right) \Bigg|_{\epsilon_i = 0} = \left(\frac{\partial \sigma_i}{\partial \epsilon_j} \right) \Bigg|_{\epsilon_i = 0} . \tag{6.12}$$

By applying strains of selected symmetry – so-called strain branches that impose lattice deformations with specific symmetries – to the unit cell and calculating the resultant stress, we can use Eq. (6.12) to calculate the elastic moduli C_{ij}. For the zinc-blende compounds of interest in this work, this includes the elastic moduli C_{11}, C_{12} and C_{44} in addition to the bulk modulus B_0. Eq. (6.12) shows two approaches to compute the elastic moduli, via the first derivative of the stress, or second derivative of the energy. We compute the elastic moduli via computation of the first derivative of the stress. This approach has previously been shown to be more robust than a determination based on the second derivative of the energy with respect to strain, in terms of the plane-wave cut-off energies and **k**-point grid densities required to achieve convergence [202]. C_{11} and C_{12} are calculated via the application of a strain branch $(\epsilon_1, \epsilon_2, \epsilon_3, \epsilon_4, \epsilon_5, \epsilon_6) = (\epsilon, 0, 0, 0, 0, 0)$. The bulk modulus B_0 is calculated via the application of a $(\epsilon, \epsilon, \epsilon, 0, 0, 0)$ strain branch, while C_{44} is calculated via the application of a $(0, 0, 0, \epsilon, \epsilon, \epsilon)$ strain branch. The Kleinman parameter ζ is also calculated from the application of the same strain branch as for C_{44}. This represents application of a homogeneous shear from which we can extract ζ by using Eqs. (6.7) and (6.8) in conjunction with the calculated displacement of the cation (group-III) and anion (group-V) sublattices in the unit cell, after allowing internal relaxation in response to the applied shear. For all strain branches, calculations are performed for $|\epsilon| \leq 2\%$, for which the relationship between elastic moduli and stress is linear. For consistency with the calculation of the equilbirum lattice parameter a, the HSEsol calculations of C_{ij} employed $\alpha = 0.25$. Our explicitly calculated bulk modulus B_0 validates the relationship $B_0 = (C_{11} + 2C_{12})/3$ for the zinc-blence structure, without reference to the calculated C_{11} and C_{12}. Our calculated C_{ij} in Table 6.1 again display typical trends, with the HSEsol values being larger than those calculated in the LDA. We note good overall agreement with literature data. The tendency of the DFT-calculated C_{ij} to slightly overestimate experiment is, in part, attributable to our calculated equilibrium lattice parameters a being slightly lower than experimental values. Previous benchmarking of local, semi-local and hybrid XC functionals vs. experiment for the elastic moduli of a range of semiconductors has shown that the HSE

hybrid functional provides higher accuracy than the LDA [201]. This, in addition to the previously discussed work of Schimka et al. [79], provides confidence in our calculated elastic moduli. We therefore recommend the use of the HSEsol-calculated values in further calculations.

6.3 Electronic band structure

In this Section we present our analysis of the electronic band structure of (Al,Ga,In)P. We detail our procedure for calculating the electronic band structure, and validate our calculations in the context of existing experimental measurements.

6.3.1 Fitting to the fundamental energy gap

To calculate electronic band structure for (Al,Ga,In)P we treat the exact exchange mixing α (Becke-Roussel mixing c) as an empirical parameter in the HSEsol (TB-mBJ) calculations. Rather than tuning the XC functional to fit the direct band gap [185], we instead fit α and c to the fundamental (lowest-energy) band gap. This is motivated by the fact that the direct band gap can be challenging to identify in an indirect-gap material while the fundamental band gap is, whether direct or indirect, readily accessible to several classes of spectroscopic measurement. In practice, this means that the fundamental band gap can generally be determined with a high degree of accuracy, while higher energy band gaps have larger associated uncertainties. This indirect-gap fitting has successfully been applied to analyse electronic structure evolution in $(Si,Ge)_{1-x}Sn_x$ alloys [190, 191, 203], and it was also employed by Ziembicki et al. [204] in their recent analysis of wurtzite-structured III-V compounds. We note that fitting to one part of the band structure can have negative implications for the description of other parts. As we will describe below, this fitting procedure can effectively describe band edge parameters and offers improved description of the band edge electronic structure compared to fitting to the direct band gap in indirect band gap materials [185]. Our HSEsol (TB-mBJ) band structure calculations use the HSEsol-calculated (LDA-calculated) equilibrium lattice parameter a. For AlP and GaP we fit α and c to the well-known, low-temperature fundamental (indirect) X_{6c}-Γ_{8v} band gaps of 2.52 and 2.35 eV respectively [44]. This yields $\alpha = 0.363$ and $c = 1.218$ for AlP, and $\alpha = 0.314$ and $c = 1.193$ for GaP. For InP we fit α and c to the direct Γ_{6c}-Γ_{8v} low-temperature band gap of 1.424 eV [44], yielding $\alpha = 0.273$ and $c = 1.166$.

The resulting HSEsol (TB-mBJ) band structures and density of states (DOS) are respectively shown in Figs. 6.1, 6.2 and 6.3 using solid (dashed) lines. The TB-mBJ bands demonstrate systematic underestimation of energetic band widths vs. HSEsol. This reflects the known tendency of the TB-mBJ exchange potential to overestimate effective masses [77]. For AlP, the HSEsol and TB-mBJ calculations indicate X-L-Γ ordering of the CB valley minima, in agreement with

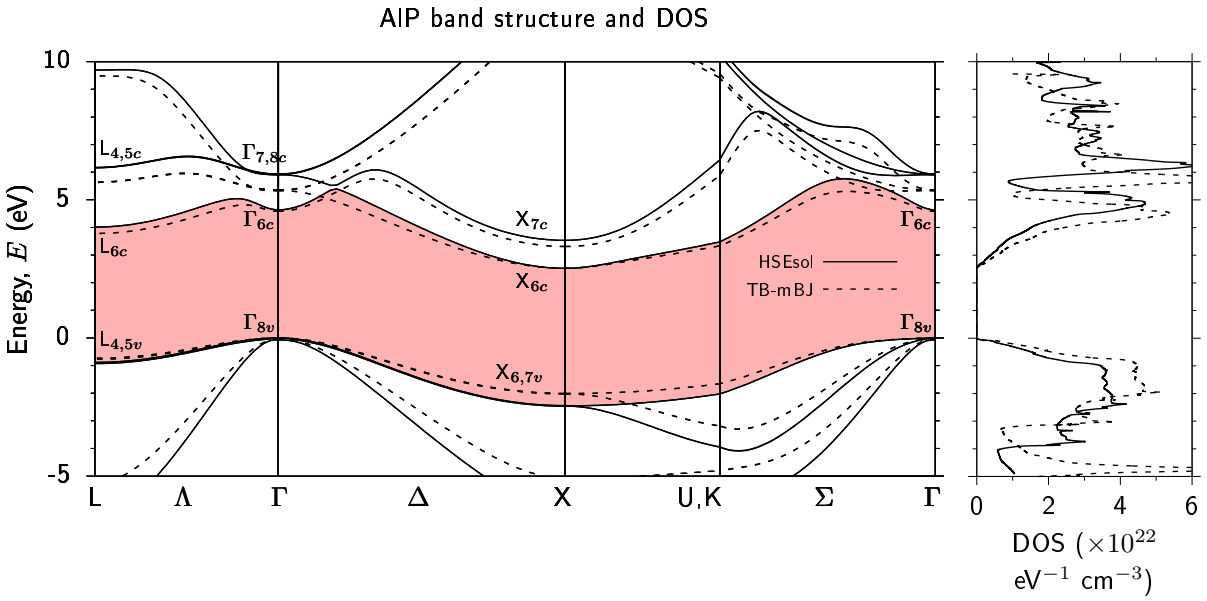


FIGURE 6.1: DFT-calculated band structure (left panel) and density of states (DOS; right panel) of AlP, calculated using the HSEsol (solid lines) and TB-mBJ (dashed lines) XC functionals. The exact exchange mixing in the HSEsol calculation ($\alpha = 0.363$), and the Becke-Roussel mixing in the TB-mBJ calculation ($c = 1.218$), were adjusted to fit to the experimental zero-temperature fundamental (indirect) X_{6c}-Γ_{8v} band gap of 2.52 eV [44]. The zero of energy is set at the valence band maximum.

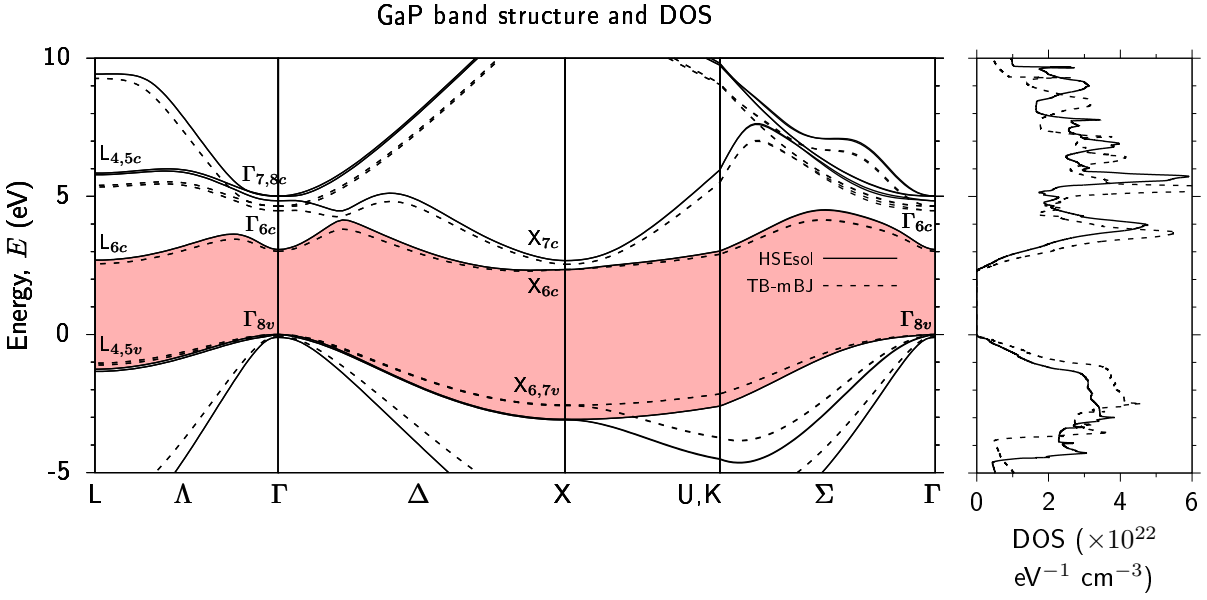


FIGURE 6.2: DFT-calculated band structure (left panel) and density of states (DOS; right panel) of GaP, calculated using the HSEsol (solid lines) and TB-mBJ (dashed lines) XC functionals. The exact exchange mixing in the HSEsol calculation ($\alpha = 0.314$), and the Becke-Roussel mixing in the TB-mBJ calculation ($c = 1.193$), were adjusted to fit to the experimental zero-temperature fundamental (indirect) X_{6c}-Γ_{8v} band gap of 2.35 eV [44]. The zero of energy is set at the valence band maximum.

GW [184] and HSE [185] calculations, but contrary to the X-Γ-L ordering identified in other studies [182]. For GaP, our calculations indicate X-L-Γ ordering of the CB valley minima, consistent with previous literature [44, 184, 185]. For InP, our calculations indicate Γ-L-X ordering,

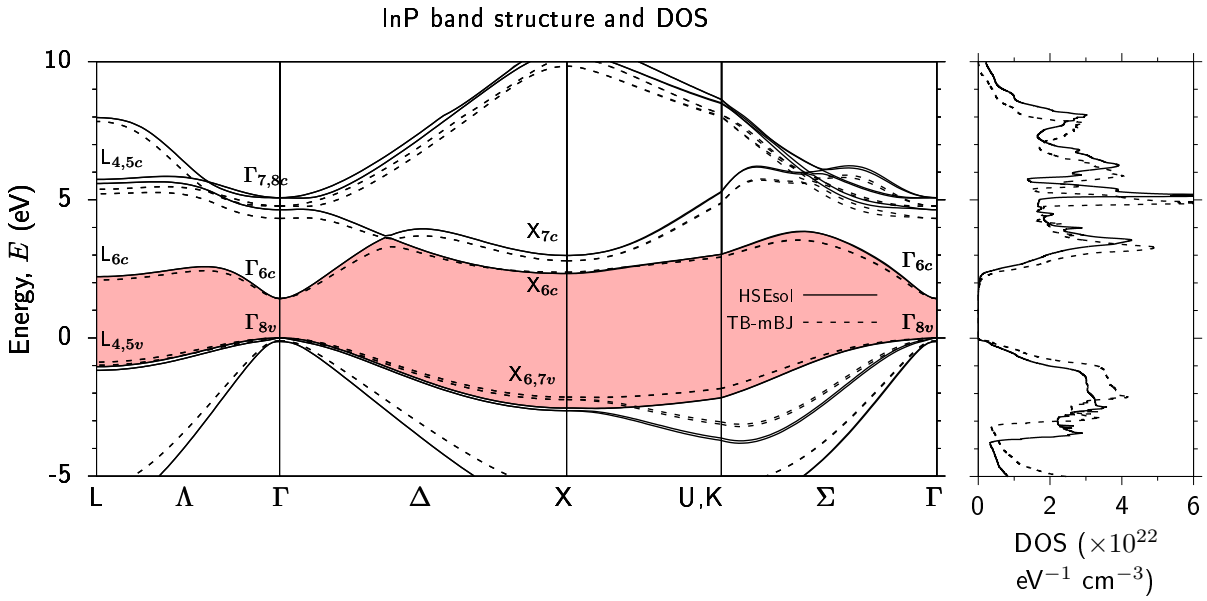


FIGURE 6.3: DFT-calculated band structure (left panel) and density of states (DOS; right panel) of InP, calculated using the HSEsol (solid lines) and TB-mBJ (dashed lines) XC functionals. The exact exchange mixing in the HSEsol calculation ($\alpha = 0.273$), and the Becke-Roussel mixing in the TB-mBJ calculation ($c = 1.166$), were adjusted to fit to the experimental zero-temperature fundamental (direct) Γ_{6c}-Γ_{8v} band gap of 1.424 eV [44]. The zero of energy is set at the valence band maximum.

consistent with GW [184] and HSE [185] calculations. Our calculations provide clarity for the disputed CB valley minima ordering in AlP (cf. Sec. 6.1), consistent with recent theoretical investigations [184, 185].

6.3.2 The direct band gap of AlP: reconciling theory and experiment

Having examined the CB valley minima ordering and energetic band widths of our calculated HSEsol and TB-mBJ electronic band structures for (Al,Ga,In)P, before further investigation of the electronic band parameters we first examine our AlP band structure via direct comparison to experimental measurements. As discussed in Sec. 6.1 the band structure, and band parameters, of (Ga,In)P are generally better understood and agreed upon than those of AlP [44]. For AlP, there exist significant spreads in literature values of several key band parameters including, critically, large discrepancies between reported values of the direct Γ_{6c}-Γ_{8v} band gap. Given these uncertainties, we now perform rigorous benchmarking of our HSEsol-calculated AlP band structure via comparison with literature experimental data.

In AlP, there exist significant discrepancies between the 3.63 eV low-temperature direct Γ_{6c}-Γ_{8v} band gap recommended by Vurgaftman et al. [44] and those predicted via state-of-the-art GW [184] or HSE-DFT [185] calculations. GW and HSE-DFT calculations suggest that the Γ_{6c}-Γ_{8v} band gap is $\gtrsim 0.5$ eV larger than that recommended in Ref. [44]. The original source of the 3.63 eV value recommended by Vurgaftman et al. is the photoluminescence excitation (PLE)

measurement of Monemar [205], in which the measured spectrum displayed a weak "shoulder" at 3.63 eV that was attributed to the Γ_{6c}-Γ_{8v} band gap. When presenting their recommended parameters in Ref. [44], Vurgaftman et al. issued a caveat that little was known about the AlP band structure, and that Ref. [205] was the sole experimental report of the Γ_{6c}-Γ_{8v} band gap. Despite this clear caveat, the value 3.63 eV has proliferated in subsequent literature, likely driven by the reliability of the recommended parameters for better-studied III-V compounds that have established Ref. [44] as a canonical reference.

We compared critical points in the HSEsol-calculated band structure to the spectroscopic ellipsometry (SE) data of Ref. [182]. Measurement of the dielectric function $\epsilon(\hbar\omega)$ via SE constitutes a valuable technique to analyse critical points in the band structure, particularly at high energies where it is challenging to produce optical excitation in wide-gap semiconductors. Taking the second derivative of the measured $\epsilon(\hbar\omega)$ with respect to photon energy $\hbar\omega$ yields a differential spectrum with high sensitivity to critical points in the band structure [206, 207]. This approach was applied by Hwang et al. in Ref. [182], who assigned inter-band optical transition energies at the Γ-, L- and X-points via fitting to the $\mathrm{d}^2\epsilon(\hbar\omega)/\mathrm{d}(\hbar\omega)^2$ spectrum obtained by numerically differentiating the measured $\epsilon(\hbar\omega)$ data. To validate our HSEsol band structure we also fit to the experimental $\mathrm{d}^2\epsilon(\hbar\omega)/\mathrm{d}(\hbar\omega)^2$ data of Ref. [182] employing, for consistency, the same excitonic ($n = -1$) lineshape [182, 208, 209]

$$\frac{\mathrm{d}^2\epsilon}{\mathrm{d}(\hbar\omega)^2} = \sum_j \frac{n(n-1)\,A_j\,e^{i\phi_j}}{(\hbar\omega - E_j + i\Gamma_j)^{2-n}}\,, \tag{6.13}$$

where E_j, A_j, ϕ_j and Γ_j are, respectively, the energy, amplitude, phase and linewidth associated with the jth critical point [182]. We write the complex-valued dielectric function as $\epsilon(\hbar\omega) = \epsilon_1(\hbar\omega) + i\,\epsilon_2(\hbar\omega)$, such that $\epsilon_1(\hbar\omega) = \mathrm{Re}\{\epsilon(\hbar\omega)\}$. In Eq. (6.13), $n = (D-2)/2$ where D is the dimensionality of the critical point [209]. The choice $n = -1$ corresponds to a discrete excitonic transition ($D = 0$), which was employed for AlP in Ref. [182] based on recommendations from earlier analyses [209, 210].

To assess the accuracy of the HSEsol band structure we employ Eq. (6.13) to perform a constrained fit to the real part of $\mathrm{d}^2\epsilon/\mathrm{d}(\hbar\omega)^2$ computed from the experimental SE data of Ref. [182]. The fit is constrained by extracting the critical point energies E_j from the HSEsol-calculated band structure, which are then kept fixed during a non-linear least squares (Levenberg-Marquardt) fit to Eq. (6.13). With the critical point energies kept fixed, during the fit the amplitude A_j, phase ϕ_j and linewidth Γ_j associated with each critical point are allowed to vary. In the energy range for which experimental $\mathrm{d}^2\epsilon_1/\mathrm{d}(\hbar\omega)^2$ data are provided in Ref. [182], we identify five critical points ($j = 1, \ldots, 5$) in the HSEsol band structure. These are, in order of increasing energy: $E_0 = E(\Gamma_{6c}) - E(\Gamma_{8v})$, $E_1 = E(\mathrm{L}_{6c}) - E(\mathrm{L}_{5v})$, $E_2 = E(\mathrm{X}_{6c}) - E(\mathrm{X}_{7v})$, $E_0' = E(\Gamma_{7c}) - E(\Gamma_{8v})$, and $E_2' = E(\mathrm{X}_{7c}) - E(\mathrm{X}_{7v})$. The optical activity of these transitions

was confirmed by computing their associated inter-band optical matrix elements, all of which were found to be non-zero.

Before performing the fit, the HSEsol-calculated values of the critical point energies E_j must first be adjusted to account for the SE measurements of Ref. [182] having been performed at room temperature. We employ the Varshni parameters of Ref. [44] to redshift our HSEsol-calculated critical point energies, yielding suitable E_j values for use in Eq. (6.13). At temperature $T = 300$ K this gives $E_0 = 4.561$ eV, $E_1 = 4.868$ eV, $E_2 = 4.940$ eV, $E_0' = 5.824$ eV, and $E_2' = 5.952$ eV. These critical point energies at the Γ-point (E_0 and E_0'), L-point (E_1), and X-point (E_2 and E_2') have respectively been redshifted by 77, 32 and 32 meV vs. their calculated low-temperature values. Figure 6.4 compares the resulting constrained fit to Eq. (6.13) (solid line) to the experimental $\mathrm{d}^2\epsilon_1/\mathrm{d}(\hbar\omega)^2$ SE data of Ref. [182] (open circles). This constrained fit provides an accurate description of the experimental SE data. As described above, Hwang et al. assigned $E_0 = 3.681$ eV for the Γ_{6c}-Γ_{8v} band gap, despite the absence of a corresponding feature in the SE data [182]. Our assignment of critical point energies in Fig. 6.4 revises that of Ref. [182] as: $E_1 \to E_0$, $E_2 \to E_1/E_2$, and $E_0' \to E_0'/E_2'$. Consistent with Ref. [182], we find that the weak features close to 4.2 and 5.3 eV in the experimental data do not correspond to clear optical transitions in the bulk band structure, and are likely attributable to native defects and/or unintentional dopants.

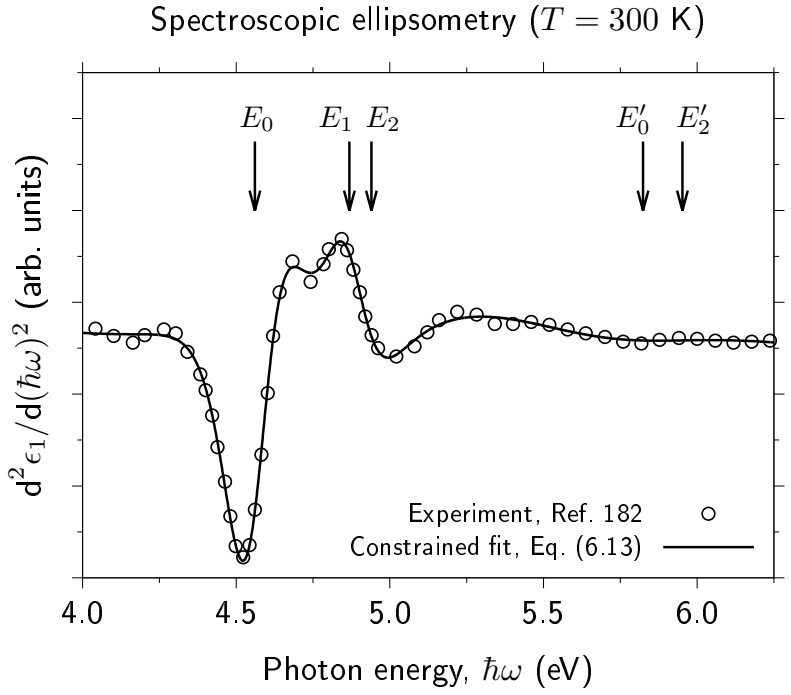


FIGURE 6.4: Second derivative with respect to photon energy $\hbar\omega$ of the real part ϵ_1 of the dielectric function of AlP, computed from the measured spectroscopic ellipsometry data of Ref. [182] (open circles), and calculated via a constrained fit (solid line) employing Eq. (6.13) with fixed critical point energies E_j ($j = 1, \ldots, 5$; vertical arrows) obtained from the HSEsol-calculated AlP band structure (cf. Fig. 6.1).

Notably, our calculated E_0 corresponds to a sharp, prominent feature in the SE data, which is consistent with (i) the high optical matrix element associated with the Γ_{6c}-Γ_{8v} transition (cf. Kane parameter E_P in Table 6.3), and (ii) the appearance of the E_0 transition in SE measurements for other semiconductors [207]. We assert that this constitutes sufficient evidence to ascribe a revised value of 4.639 eV to the zero-temperature Γ_{6c}-Γ_{8v} band gap, an increase of 1.009 eV compared to the value originally proposed by Monemar [205] and subsequently recommended by Vurgaftman et al. [44]. This comparison reconciles theory and experiment, reducing the uncertainty caused by the significant spread in reported values of this key band parameter over the past several decades. Our revision of the direct band gap corresponds to an ≈ 1 eV increase in the energy difference between the direct Γ_{6c} and indirect X_{6c} CB minima suggesting, e.g., a more rapid direct- to indirect-gap transition with increasing Al composition x in $Al_xIn_{1-x}P$ alloys. It is also likely to impact on the value of other parameters that depend on the direct energy gap.

Literature quasiparticle [211], GW [184] and HSE-DFT [185] calculations corroborate the likelihood of a larger Γ_{6c}-Γ_{8v} band gap. The quasiparticle calculations of Zhu and Louie [211], and GW calculations of Wing et al. [184] respectively predicted $E(\Gamma_{6c})$-$E(\Gamma_{8v}) = 4.38$ eV and 4.25 eV. These are lower than the observed feature at ≈ 4.6 eV in the SE data of Ref. [182], an underestimation that can be expected since those calculations underestimate the Γ_{6c}-Γ_{8v} band gap of some III-V semiconductors (e.g. underestimating the well-known GaAs direct band gap by 0.30 eV and 0.57 eV in Refs. [211] and [184] respectively). In their HSE-DFT analysis Bastos et al. [185] employed the exact exchange mixing α as an empirical parameter, which they fit to the direct band gap of 3.63 eV recommended by Vurgaftman et al. [44]. The resulting best-fit $\alpha = 0.127$ is anomalously lower than that obtained for all other III-(P,As,Sb) compounds, which had $\alpha \gtrsim 0.22$ [185]. Using the HSE06 XC functional ($\alpha = 0.25$) Bastos et al. predicted $E(\Gamma_{6c})$-$E(\Gamma_{8v}) = 4.153$ eV.

To summarise, the SE measurements of Hwang et al. [182] displayed no evidence of an optical transition close to 3.6 eV. A clear feature was visible close to 4.6 eV in the SE data, having an appearance qualitatively consistent with the Γ_{6c}-Γ_{8v} (E_0) transition in other semiconductors [207]. The authors of Ref. [182] ascribed a value of 3.681 eV to the Γ_{6c}-Γ_{8v} band gap, despite their measurements not indicating the presence of an optical transition at that energy. The excitation energies employed in the PLE measurements of Ref. [205] were restricted to ≤ 4.1 eV, which precluded probing optical transitions having energies > 4.1 eV. As such, we expect that the direct Γ_{6c}-Γ_{8v} band gap was not visible in the PLE measurements reported by Monemar due to the range of excitation energies employed. Most recently Vurgaftman et al. revised their recommended Γ_{6c}-Γ_{8v} band gap from 3.63 eV to 3.99 eV [178]. Taken together, these observations indicated the possibility that the Γ_{6c}-Γ_{8v} band gap in AlP is significantly larger than previously assumed. We have demonstrated that reinterpretation of the SE data of Ref. [182] is consistent with the zero-temperature direct band gap $E(\Gamma_{6c})$-$E(\Gamma_{8v}) = 4.639$ eV obtained

from our HSEsol-calculated band structure. With our calculated AlP band structure validated via comparison to experimental SE measurements, we now undertake a full re-evaluation of the (Al,Ga,In)P electronic band parameters.

6.4 Unstrained electronic band parameters

In this Section we present our calculated unstrained electronic band parameters for (Al,Ga,In)P. We provide analysis of the direct and indirect band gaps, effective masses, and the inter-band Kane parameter. We also investigate the robustness of our calculated parameters for use in 8-band $\mathbf{k} \cdot \mathbf{p}$ calculations. To do this, we demonstrate the ellipticity of our parameter set and the renormalised inverse CB effective mass s_c (cf. Sec. 4.2.1).

6.4.1 Direct and indirect band gaps

As demonstrated in Sec. 6.3.2, our calculations suggest an increase of $\approx$ 1 eV to the AlP direct Γ_{6c}-Γ_{8v} band gap recommended by Vurgaftman et al. [44]. Having been validated via comparison to experimental SE measurements, our calculations predict, at zero temperature, $E(\Gamma_{6c})$-$E(\Gamma_{8v})$ = 4.639 eV. We now examine the direct band gaps in GaP and InP, and the indirect band gaps in (Al,Ga,In)P. Our calculated direct and indirect band gaps, and valence band (VB) spin-orbit (SO) splitting energies, are shown in Table 6.2.

For GaP, our calculation of the direct Γ_{6c}-Γ_{8v} band gap revises the value recommended by Vurgaftman et al. [44] upwards by $\approx$ 190 meV. This is consistent with recent HSE-DFT calculations by Bastos et al. [185], which suggest an upward revision of $\approx$ 50 meV to the value recommended by Vurgaftman et al. The HSE-DFT calculations of Bastos et al. fit α to the direct gap, rather than following our approach of fitting to the fundamental band gap. As a result, Bastos et al. employed $\alpha = 0.283$, which is 10% smaller than our calculated α. Since the calculated band gap in a HSE(sol) calculation increases monotonically with increasing α the increase in the direct Γ_{6c}-Γ_{8v} band gap predicted by Bastos et al. is underestimated in comparison with our calculations. We note that recent GW calculations suggest a reduction to the value recommended by Vurgaftman et al. by $\approx$ 300 meV [184]. Earlier theoretical [180, 212] and experimental work [213, 214] suggests values consistent with that recommended by Vurgaftman et al.

InP is a direct band gap material. As such, the direct Γ_{6c}-Γ_{8v} band gap is readily measurable and its value is therefore well established in the literature. As described in Sec. 6.3.1, in our calculations we fit to the direct band gap of 1.424 eV recommended by Vurgaftman et al. [44]. This recommended value is in good agreement with GW calculations [184] and early empirical band structure [180] and empirical pseudopotential [212] calculations.

TABLE 6.2: DFT-calculated direct (Γ_{6c}-Γ_{8v}) and indirect (X_{6c}-Γ_{8v} and L_{6c}-Γ_{8v}) band gaps, and valence band spin-orbit splitting energy Δ_{SO} for AlP, GaP and InP. HSEsol- and TB-mBJ-calculated results are respectively denoted by a dagger (†) and an asterisk (∗). The exact exchange mixing α (Becke-Roussel mixing c) is $\alpha = 0.363$ ($c = 1.218$) for AlP, $\alpha = 0.314$ ($c = 1.193$) for GaP, and $\alpha = 0.274$ ($c = 1.165$) for InP.

	AlP		GaP		InP	
Parameter	This work	Reference	This work	Reference	This work	Reference
$E_g(\Gamma_{6c}$-$\Gamma_{8v})$ (eV)	$4.639^{\dagger}$	3.63^{a}	$3.075^{\dagger}$	2.886^{a}	$1.424^{\dagger}$	1.424^{a}
	4.582^{*}	4.25^{b}	3.010^{*}	2.895^{d}	1.423^{*}	1.422^{e}
		4.38^{c}		2.915^{e}		
$E_g(X_{6c}$-$\Gamma_{8v})$ (eV)	$2.520^{\dagger}$	2.52^{a}	$2.350^{\dagger}$	2.35^{a}	$2.330^{\dagger}$	2.384^{a}
	2.520^{*}	2.50^{b}	2.350^{*}	2.36^{d}	2.381^{*}	2.39^{d}
		2.59^{c}		2.38^{f}		2.35^{f}
		2.51^{d}				
$E_g(L_{6c}$-$\Gamma_{8v})$ (eV)	$4.015^{\dagger}$	3.57^{a}	$2.690^{\dagger}$	2.72^{a}	$2.218^{\dagger}$	2.014^{a}
	3.780^{*}	3.90^{c}	2.559^{*}		2.098^{*}	
		4.00^{g}				
Δ_{SO} (eV)	$0.067^{\dagger}$	0.07^{a}	$0.104^{\dagger}$	0.08^{a}	$0.128^{\dagger}$	0.108^{a}
	0.055^{*}	0.06^{d}	0.084^{*}	0.093^{e}	0.104^{*}	0.111^{e}

[a]Recommended by Vurgaftman et al., see Ref. [44] for details
Theory: [b]Ref. [184], [c]Ref. [211], [e]Ref. [185], [f]Ref. [180]
Experiment: [d]Ref. [200]

Considering the indirect band gaps, we recall that for AlP and GaP our DFT calculations were fit to the fundamental $E_g(X_{6c}$-$\Gamma_{8v})$ band gap known from experiment. We now examine the $E_g(L_{6c}$-$\Gamma_{8v})$ band gap in comparison to available literature data. Beginning with AlP, the value of 3.57 eV recommended in Ref. [44] is from an early empirical band structure calculation [180], while the higher 3.90 eV is from the quasiparticle GW calculation by Zhu and Louie [211]. Our calculated values straddle the latter, with our HSEsol (TB-mBJ) calculated L_{6c}-X_{6c} valley splitting being $\approx$ 180 meV higher (50 meV lower) than that predicted by Zhu and Louie. For GaP, our HSEsol calculated $E_g(L_{6c}$-$\Gamma_{8v})$ is in good agreement with the recommendation by Vurgaftman et al. [44]. We note that these values are in good quantitative agreement – to within $\approx$ 10 meV – with previous empirical linear combination of atomic orbitals [180] and empirical pseudopotential [212] calculations.

For InP we fit to the direct $E_g(\Gamma_{6c}$-$\Gamma_{8v})$ band gap. As such, we will now examine both the $E_g(X_{6c}$-$\Gamma_{8v})$ and $E_g(L_{6c}$-$\Gamma_{8v})$ indirect band gaps. Firstly, analysing the $E_g(X_{6c}$-$\Gamma_{8v})$ band gap, we note excellent quantitative agreement with the value 2.384 eV recommended by Vurgaftman et al. [44], with our HSEsol calculated value being within $\approx$ 5 meV. We note that early empirical calculations [180, 212] suggested values 200 - 300 meV larger than our calculations, and the recommendation of Vurgaftman et al. Secondly, examining $E_g(L_{6c}$-$\Gamma_{8v})$, our HSEsol calculations suggest an $\approx$ 200 meV increase vs. the value recommended by Vurgaftman et al. This is consistent with other HSE-DFT calculations which employ a similar exact exchange mixing α

for InP [185], and is also consistent with an early empirical pseudopotential calculation that shows good quantitative agreement with our calculated $E_g(\mathrm{L}_{6c}\text{-}\Gamma_{8v})$ [212].

We will now briefly discuss the spin-orbit splitting Δ_{SO} and the CB valley splittings in (Al,Ga,In)P. The spin-orbit splitting Δ_{SO} can be difficult to determine directly in experiment, due to the weak spin-orbit coupling in III-P compounds, making Δ_{SO} challenging to distinguish in spectroscopic measurements. Our calculations are in excellent agreement with the recommendations of Ref. [44], and those from other HSE-DFT calculations [185]. Secondly, we examine the CB valley minima splittings in InP. It was noted by Vurgaftman et al. [44] that there were uncertainties in the energies of the X- and L-valley CB minima. Our HSEsol calculations predict that the X-valley CB minima lie 0.906 eV above the Γ-valley, within 6% of the recommended values of 0.96 eV of Vurgaftman et al. [44]. Our HSEsol calculations predict that the L-valley CB minima lie 0.794 eV above the Γ-valley. This result suggests an increase of 32% to the recommendation of Vurgaftman et al. [44]. We note, that Ref. [44] also provided a range for the Γ_{6c}-L_{6c} CB valley splitting of 0.4 - 0.7 eV. Our revised value suggests an increase to the upper bound of this range by 13%. Our suggested minor revisions to these aspects of the description of the InP electronic structure are consistent with other HSE-DFT calculations [185].

6.4.2 Effective masses and Luttinger parameters

Our calculated (relative) effective masses and Luttinger parameters are shown in Table 6.3. In Ref. [44] Vurgaftman et al. noted a lack of experimental effective mass data for AlP. Their recommended $m^*_{\mathrm{CB}}(\Gamma_{6c}) = 0.22$ and $m^*_{\mathrm{SO}}(\Gamma_{7v}) = 0.30$ for the zone-center CB and SO VB edge (relative) effective masses were calculated ab initio by Krijn [215]. Our HSEsol-calculated Γ_{6c} CB (Γ_{7v} SO) effective mass is slightly lower (higher) than that predicted by Krijn. Comparing to the HSE calculations of Bastos et al. [185], our HSEsol-calculated Γ_{6c} CB effective mass is in close agreement, while our HSEsol-calculated Γ_{7v} SO effective mass is $\approx 10\%$ lower. The Luttinger parameters γ_1, γ_2 and γ_3 can be computed analytically from a choice of three heavy-hole (HH) and light-hole (LH) VB edge effective masses [44]. We employ the HH and LH effective masses along [001] to fix γ_1 and γ_2, and the HH effective mass along [111] to fix γ_3. The Luttinger parameters can then be computed as [44]

$$\gamma_1 = \frac{1}{2}\left[\left(\frac{1}{m^*_{\mathrm{LH}}}\right)^{[001]} + \left(\frac{1}{m^*_{\mathrm{HH}}}\right)^{[001]}\right], \tag{6.14}$$

$$\gamma_2 = \frac{1}{4}\left[\left(\frac{1}{m^*_{\mathrm{LH}}}\right)^{[001]} - \left(\frac{1}{m^*_{\mathrm{HH}}}\right)^{[001]}\right], \tag{6.15}$$

$$\gamma_3 = \frac{1}{4}\left[\left(\frac{1}{m^*_{\mathrm{LH}}}\right)^{[001]} + \left(\frac{1}{m^*_{\mathrm{HH}}}\right)^{[001]} - 2\left(\frac{1}{m^*_{\mathrm{HH}}}\right)^{[111]}\right]. \tag{6.16}$$

We note that our Luttinger parameters, computed analytically in this manner, are close to those obtained from numerical fitting to the HSE-calculated VB structure by Bastos et al. [185].

Few data are available for the effective masses of the zone-edge X- and L-point CB valleys. Our HSEsol-calculated longitudinal X-point effective mass $m^*_{\mathrm{CB},\parallel}(\mathrm{X}_{6c})$ is significantly lower than that calculated ab initio by Huang and Ching [180], and than that inferred via fitting to photoluminescence data by Issiki et al. [216]. However, we note that the X-point CB DOS effective mass per valley, $m^*_{\mathrm{DOS}} = [m^*_{\parallel}(m^*_{\perp})^2]^{1/3}$, obtained from our HSEsol-calculated effective masses is within 20% of the best-fit value of Issiki et al. [216]. To our knowledge, our calculated L-point CB edge effective masses, $m^*_{\mathrm{CB},\parallel}(\mathrm{L}_{6c})$ and $m^*_{\mathrm{CB},\perp}(\mathrm{L}_{6c})$, are the first for AlP. Our predicted L-point DOS effective mass per valley is close to that of the X valley, with the L-point DOS effective mass per valley exceeding that at the X point by 8%.

For GaP and InP, there exist a larger number of experimental and theoretical investigations of the effective masses [44]. First, we compare our calculated $m^*_{\mathrm{CB}}(\Gamma_{6c})$ and $m^*_{\mathrm{SO}}(\Gamma_{7v})$ effective masses to HSE-DFT calculations [185] and the recommended values of Vurgaftman et al. [44]. Our calculations are in close agreement with these literature results. Our analytically calculated γ_1, γ_2 and γ_3, as in AlP, are in very good agreement with those obtained from fitting to HSE-DFT electronic structure calculations [185].

In Ref. [44] Vurgaftman et al. noted factors complicating the measurement and evaluation of the X-valley CB effective masses in GaP. Vurgaftman et al. noted a resulting large spread in reported values, due to the presence of a "camel back" dispersion of the lowest CB near the X-point [44]. This is consistent with our HSEsol- and TB-mBJ-calculated GaP band structures, where the minimum in this CB valley does not lie precisely at the X-point. To compute our X-point effective masses we perform additional DFT calculations slightly away from the X-point, extracting the longitudinal and transverse effective masses at $\mathbf{k} = \frac{2\pi}{a}(0.884, 0, 0)$ in the HSEsol calculation, and $\mathbf{k} = \frac{2\pi}{a}(0.855, 0, 0)$ in the TB-mBJ calculation. Both our HSEsol- and TB-mBJ-calculated GaP $m^*_{\mathrm{CB},\parallel}(\mathrm{X}_{6c})$ effective masses are in good agreement with the 30-band $\mathbf{k}\cdot\mathbf{p}$ calculations of Fraj et al. [218]. Our calculated $m^*_{\mathrm{CB},\parallel}(\mathrm{X}_{6c})$ effective masses for GaP provide much greater certainty than the range of values originally recommended by Vurgaftman et al. [44]. We note that these effective masses do not follow the typical trend of TB-mBJ-calculated effective masses being larger than those calculated using HSEsol. Our calculated $m^*_{\mathrm{CB},\perp}(\mathrm{X}_{6c})$ effective masses for GaP are within the range recommended by Vurgaftman et al. [44], and find good agreement with the calculations of Fraj et al. [218]. In Ref. [44] Vurgaftman et al. originally recommended X-point InP effective masses on the basis of only an X-valley DOS effective mass. This recommendation was later revised in Ref. [178], citing 40-band $\mathbf{k}\cdot\mathbf{p}$ results by Saidi et al. [217], with a lack of further available literature data. Our calculated InP $m^*_{\mathrm{CB},\parallel}(\mathrm{X}_{6c})$ effective masses see a large discrepancy between those calculated using HSEsol and TB-mBJ. Our HSEsol-calculated InP $m^*_{\mathrm{CB},\parallel}(\mathrm{X}_{6c})$ effective mass is in better agreement with that of Saidi et

TABLE 6.3: DFT-calculated zone-centre CB edge effective mass $m^*_{\mathrm{CB}}(\Gamma_{6c})$, zone-centre VB Luttinger parameters γ_i, SO VB edge effective mass $m^*_{\mathrm{SO}}(\Gamma_{7v})$, and longitudinal ($\|$) and transverse ($\perp$) X- and L-point CB edge effective masses for AlP, GaP and InP. HSEsol- and TB-mBJ-calculated results are respectively denoted by a dagger ($\dagger$) and an asterisk ($*$). The exact exchange mixing α (Becke-Roussel mixing c) is $\alpha = 0.363$ ($c = 1.218$) for AlP, $\alpha = 0.314$ ($c = 1.193$) for GaP, and $\alpha = 0.274$ ($c = 1.165$) for InP.

	AlP		GaP		InP	
Parameter	This work	Reference	This work	Reference	This work	Reference
$m^*_{\mathrm{CB}}(\Gamma_{6c})$ (m_0)	$0.192^{\dagger}$	0.22^{a}	$0.137^{\dagger}$	0.13^{a}	$0.085^{\dagger}$	0.068^{a}
	0.242^{*}	0.197^{b}	0.175^{*}	0.150^{b}	0.106^{*}	0.084^{a}
						0.092^{b}
γ_1	$2.97^{\dagger}$	3.35^{a}	$4.43^{\dagger}$	4.05^{a}	$5.61^{\dagger}$	5.08^{a}
	2.31^{*}	2.85^{b}	3.51^{*}	4.20^{b}	4.96^{*}	5.33^{b}
γ_2	$0.48^{\dagger}$	0.71^{a}	$0.78^{\dagger}$	0.49^{a}	$1.55^{\dagger}$	1.60^{a}
	0.36^{*}	0.54^{b}	0.60^{*}	0.87^{b}	1.40^{*}	1.58^{b}
γ_3	$1.09^{\dagger}$	1.23^{a}	$1.62^{\dagger}$	2.93^{a}	$2.27^{\dagger}$	2.10^{a}
	0.84^{*}	1.11^{b}	1.27^{*}	1.58^{b}	2.02^{*}	2.20^{b}
$m^*_{\mathrm{SO}}(\Gamma_{7v})$ (m_0)	$0.318^{\dagger}$	0.30^{a}	$0.219^{\dagger}$	0.25^{a}	$0.175^{\dagger}$	0.21^{a}
	0.412^{*}	0.355^{b}	0.275^{*}	0.243^{b}	0.212^{*}	0.199^{b}
$m^*_{\mathrm{CB},\|}(\mathrm{X}_{6c})$ (m_0)	$0.704^{\dagger}$	2.680^{a}	$1.316^{\dagger}$	2.0^{a}	$1.625^{\dagger}$	1.35^{d}
	0.853^{*}	3.670^{c}	1.070^{*}	7.0^{a}	2.988^{*}	
				0.672^{c}		
				1.2^{e}		
$m^*_{\mathrm{CB},\perp}(\mathrm{X}_{6c})$ (m_0)	$0.234^{\dagger}$	0.155^{a}	$0.223^{\dagger}$	0.19^{a}	$0.243^{\dagger}$	0.275^{d}
	0.281^{*}	0.212^{c}	0.257^{*}	0.275^{a}	0.276^{*}	
				0.193^{c}		
				0.25^{e}		
$m^*_{\mathrm{CB},\|}(\mathrm{L}_{6c})$ (m_0)	$1.571^{\dagger}$		$1.655^{\dagger}$	1.2^{a}	$1.967^{\dagger}$	1.82^{d}
	1.714^{*}		1.748^{*}	2.0^{e}	2.062^{*}	
$m^*_{\mathrm{CB},\perp}(\mathrm{L}_{6c})$ (m_0)	$0.176^{\dagger}$		$0.137^{\dagger}$	0.15^{a}	$0.141^{\dagger}$	0.132^{d}
	0.216^{*}		0.164^{*}	0.253^{e}	0.163^{*}	

[a]Recommended by Vurgaftman et al., see Ref. [44] for details
Theory: [b]Ref. [185], [c]Ref. [180], [d]Ref. [217], [e]Ref. [218]

al. [217]. As we will discuss below, HSEsol-calculated effective masses typically provide the most accurate description of semiconductor effective masses. We therefore place greater confidence in our HSEsol-calculated value in this case, while acknowledging further literature data would provide greater clarity regarding this material parameter. Our InP $m^*_{\mathrm{CB},\perp}(\mathrm{X}_{6c})$ effective masses are in good agreement with those calculated by Saidi et al. [217]. In GaP and InP, while there are some studies of the L-point effective masses, there are fewer results available than for those at the X-point. The original recommendations of Vurgaftman et al. in Ref. [44] cited experimental studies, while this was later revised in Ref. [178] again citing the $\mathbf{k}\cdot\mathbf{p}$ results of Saidi et al. [217] for InP, and Fraj et al. [218] for GaP. Our calculated GaP $m^*_{\mathrm{CB},\|}(\mathrm{L}_{6c})$ effective masses lie within between the original recommendation of Vurfgaftman et al. and that of Fraj et al. Our GaP $m^*_{\mathrm{CB},\perp}(\mathrm{L}_{6c})$ effective masses find better agreement with the recommendation of

Vurgaftman et al. than that of Fraj et al., with our calculations straddling the recommendation of Vurgaftman et al. For InP we note that both our $m^*_{\mathrm{CB},\parallel}(\mathrm{L}_{6c})$ and $m^*_{\mathrm{CB},\perp}(\mathrm{L}_{6c})$ effective masses are in good agreement with the calculations of Saidi et al.

In line with the known tendency of the TB-mBJ exchange potential to overestimate effective masses [77], we note that our TB-mBJ-calculated Luttinger parameters – which depend on the inverse of the zone-centre VB edge effective masses (cf. Eqs. (6.14) - (6.16)) – are lower than those computed using HSEsol-calculated effective masses, noting the exception in our calculated GaP $m^*_{\mathrm{CB},\parallel}(\mathrm{X}_{6c})$ effective masses. Our results emphasise that careful benchmarking should be undertaken when analysing TB-mBJ band structures, since differences in valley splittings and band edge effective masses can create significant changes in the band edge DOS, particularly in materials possessing multiple valleys lying close in energy. We note that the work of Laurien et al. [78] involved rigorous benchmarking of XC functionals for effective mass calculations, resulting in the recommendation that HSEsol XC functionals produce the most accurate prediction of semiconductor effective masses.

6.4.3 Kane parameter and ellipticity

The semi-local nature of the HSEsol XC functional and TB-mBJ exchange potential modifies the commutation relation between the Kohn-Sham Hamiltonian and the position operator [219]. This, and the improper normalisation of the PAW pseudo-wave-functions, preclude direct application of the gradient operator, $\widehat{\mathbf{p}} = -i\hbar\nabla$, to compute momentum matrix elements [220]. Our Kane parameters E_P are obtained via explicit evaluation of the inter-band momentum matrix elements in the PAW formalism [220], and are presented in Table 6.4. Comparing our HSEsol-calculated E_P for AlP to that obtained by Bastos et al. [185] via numerical fitting of an 8-band $\mathbf{k}\cdot\mathbf{p}$ Hamiltonian to their HSE band structure, we note good quantitative agreement. Comparing our explicitly calculated E_P for GaP and InP those obtained via numerical fitting of an 8-band $\mathbf{k}\cdot\mathbf{p}$ Hamiltonian to HSE-calculated bands by Bastos et al. [185], we do not see the same close agreement as in AlP. We note that this is a consequence of the choice of Bastos et al. to fit the exact exchange mixing in their calculations to the direct band gap recommended by Vurgaftman et al. [44] which, as discussed in Sec. 6.3.2, underestimates the true direct band gap by ≈ 1 eV. Comparing to the range of values recommended in Ref. [44] by Vurgaftman et al., our calculations lie near, for GaP, or within, for InP, these ranges. We obtain a significantly lower value of E_P in our TB-mBJ calculation. This underestimation of momentum matrix elements by the TB-mBJ exchange potential underlies the method's overestimation of effective masses (cf. Sec. 6.4.2) [78].

In Table 6.4 we also present the renormalised inverse zone-center CB effective mass s_c, calculated using Eq. (4.1), and related to Kane's parameter F via $s_c = 1 + 2F$ [44]. As described in

TABLE 6.4: DFT-calculated Kane parameter E_P and renormalised inverse zone-centre CB effective mass s_c for AlP, GaP and InP. HSEsol- and TB-mBJ-calculated results are respectively denoted by a dagger (†) and an asterisk (∗). The exact exchange mixing α (Becke-Roussel mixing c) is $\alpha = 0.363$ ($c = 1.218$) for AlP, $\alpha = 0.314$ ($c = 1.193$) for GaP, and $\alpha = 0.274$ ($c = 1.165$) for InP.

	AlP		GaP		InP	
Parameter	This work	Reference	This work	Reference	This work	Reference
E_P (eV)	$21.23^{\dagger}$	17.7^{a}	$21.53^{\dagger}$	22.2^{a}	$16.86^{\dagger}$	16.6^{a}
	15.68^{*}	22.1^{b}	16.29^{*}	31.4^{a}	13.12^{*}	20.7^{a}
				25.2^{b}		18.3^{b}
s_c	$0.65^{\dagger}$	-0.30^{a}	$0.37^{\dagger}$	-3.09^{a}	$0.25^{\dagger}$	-1.62^{a}
	0.72^{*}		0.35^{*}		0.42^{*}	

[a]Recommended by Vurgaftman et al., see Ref. [44] for details
Theory: [b]Ref. [185]

Chapter 4, having $s_c < 0$ can, at large wave vector $|\mathbf{k}|$ in the widely-employed 8-band $\mathbf{k}\cdot\mathbf{p}$ Hamiltonian [52], produce unphysical states lying energetically within the band gap due to downward bending of the lowest-energy CB [128]. As demonstrated in Chapter 4 and Appendix A, even in the absence of downward bending of the CB, a negative value of s_c can additionally give rise to spurious solutions in heterostructure calculations via bulk states possessing complex-valued wave vector [58]. This highlights the importance of s_c for heterostructure calculations. From our DFT calculations we obtain $s_c > 0$, ensuring no downward bending of the CB in AlP, GaP or InP. This also guarantees $s_c + 1 > 0$, satisfying one of the conditions that ensure ellipticity of the 8-band Hamiltonian [129, 221]. In addition to this condition, the 8-band Hamiltonian is elliptic provided [129, 221]

$$\gamma_1 + 4\gamma_2 + 6\gamma_3 > \frac{2E_P}{E_g}\,, \tag{6.17}$$

$$\gamma_1 + 4\gamma_2 + 3\gamma_3 > \frac{3E_P}{2E_g}\,, \tag{6.18}$$

$$\gamma_1 - 2\gamma_2 + 3\gamma_3 > \frac{E_P}{2E_g}\,, \tag{6.19}$$

$$\gamma_1 - 2\gamma_2 - 3\gamma_3 > -\frac{E_P}{2E_g}\,, \tag{6.20}$$

all of which are satisfied by our HSEsol- and TB-mBJ-calculated band parameters. Tables 6.2, 6.3 and 6.4 thus provide a robust set of 8-band $\mathbf{k}\cdot\mathbf{p}$ parameters for (Al,Ga,In)P, with the

ellipticity of the Hamiltonian expected to mitigate the appearance of spurious solutions in heterostructure calculations [129].

6.5 Strained electronic band parameters

In this Section, having extracted a robust set of parameters for unstrained III-P semiconductors, we investigate the strain dependence of the band structure. This strain dependence is encapsulated by the band edge deformation potential or, equivalently for hydrostatic strain, the band gap pressure coefficients. We now predict the band edge deformation potentials and hydrostatic band gap pressure coefficients for (Al,Ga,In)P.

6.5.1 Band edge deformation potentials

Shifts in the band energies of semiconductors under applied strain can be described using deformation potential theory [222]. These changes in the electronic structure are a result of the change in volume (hydrostatic) and shape (axial or shear) of the unit cell under applied strain, where symmetry-reducing axial or shear strains can lift the degeneracy of the zone-centred VB edge HH and LH states [160, 222]. We compute the band edge deformation potentials via strained HSEsol and TB-mBJ band structures. As in Sec. 6.2, we apply strain branches, denoted in Voigt notation, to the unit cell. In the derivation of the bulk 8-band $\mathbf{k}\cdot\mathbf{p}$ Hamiltonian described in Eq. (2.25), the expansion of terms depending on strain can be included [45]. For an [001]-pseudomorphic strain in the absence of spin-orbit coupling, such that $\epsilon_1 = \epsilon_2$ and $\epsilon_3 = -2C_{12}\epsilon_1/C_{11}$, the strain dependent CB and HH and LH VB edge energies can be rewritten in terms of strain as [13, 45, 215, 222]

$$E^{\epsilon}_{\mathrm{CB}} = E_{\mathrm{CB}} + a_c(\epsilon_1+\epsilon_2+\epsilon_3)\,, \tag{6.21}$$

$$E^{\epsilon}_{\mathrm{HH}} = E_{\mathrm{HH}} + a_v(\epsilon_1+\epsilon_2+\epsilon_3) - \frac{b}{2}(\epsilon_1+\epsilon_2-2\epsilon_3)\,, \tag{6.22}$$

$$E^{\epsilon}_{\mathrm{LH}} = E_{\mathrm{LH}} + a_v(\epsilon_1+\epsilon_2+\epsilon_3) + b(\epsilon_1+\epsilon_2-2\epsilon_3)\,, \tag{6.23}$$

where E_{CB}, E_{HH} and E_{LH} are, respectively, the CB and HH, LH and SO VB edge energies in the absence of strain (cf. Eq. (2.25)), a_c and a_v are the CB and VB edge hydrostatic deformation potentials, and b is the VB edge axial deformation potential. With application of the $(\epsilon,\epsilon,\epsilon,0,0,0)$ strain branch Eqs. (6.21) and (6.22) reduce to

$$E^{\epsilon}_{\mathrm{CB}} = E_{\mathrm{CB}} + 3a_c\epsilon\,, \tag{6.24}$$

$$E^{\epsilon}_{\mathrm{HH}} = E_{\mathrm{HH}} + 3a_v\epsilon\,. \tag{6.25}$$

Using Eqs. (6.24) and (6.25) we can compute the change in band gap as

$$\Delta E_g(\Gamma_{6c}\text{-}\Gamma_{8v}) = -3a_g\epsilon = -a_g\mathrm{Tr}(\epsilon)\,, \tag{6.26}$$

where a_g is the hydrostatic band gap deformation potential and $\mathrm{Tr}(\epsilon) = \epsilon_1 + \epsilon_2 + \epsilon_3$ is the trace of the strain tensor.

To obtain the VB edge axial and shear deformation potentials, b and d, the application of appropriate strain branches can reduce the 8-band $\mathbf{k}\cdot\mathbf{p}$ strain Hamiltonian to a block-diagonalised form, from which expressions for b and d can be obtained in terms of the strained band edge energies. To compute b we apply the trace-free biaxial strain $(\epsilon, \epsilon, -2\epsilon, 0, 0, 0)$. Taking the zero of energy at the unstrained VB maximum, and in the absence of SO coupling, we obtain eigenvalues E_g, $-6b\epsilon$ and two of $3b\epsilon$. Using these band edge energies we compute the LH-HH splitting as

$$\Delta E_{\text{HH-LH}} = 9b\epsilon\,. \tag{6.27}$$

We can then compute the VB axial deformation potential b by fitting to the zone-centre HH-LH splitting vs. ϵ using Eq. (6.27). To obtain d we apply the shear strain $(0, 0, 0, 0, 0, 2\epsilon)$. The application of this strain branch, again taking the zero of energy at the unstrained VB maximum and in the absence of SO coupling, provides eigenvalues E_g, $\pm\sqrt{3}d\epsilon$ and 0. Using these band edge energies we compute

$$\Delta E_{\text{HH-LH}} = 2\sqrt{3}d\epsilon\,. \tag{6.28}$$

The VB edge shear deformation potential d can then be computed by fitting to the zone-centre HH-LH splitting vs. ϵ using Eq. (6.28). Shearing the unit cell produces an internal strain which, akin to calculating C_{44}, mandates internal relaxation of the ionic coordinates (cf. Sec. 6.2). Calculations are performed for $|\epsilon| \leq 2\%$, for which these relationships behave linearly. For the HSEsol (TB-mBJ) deformation potential calculations, for consistency with our calculation of the elastic properties, internal relaxation of the ionic positions in response to an applied macroscopic strain was performed using the HSEsol (LDA) XC functional.

In general, the deformation potentials of III-P materials have undergone limited investigation, resulting in a lack of reference values in the literature [45]. The zone-centre hydrostatic band gap deformation potential a_g values reported in literature for InP display large uncertainty [223–227]. In AlP, there have been no experimental investigations of a_g, with significant uncertainty in the limited set of published theoretical results [196, 228]. Additionally, previous recommendations of d for AlP have been based on the values available for GaP [44]. Given this lack of published information and certainty in the band edge deformation potentials of III-P compounds, we now undertake a rigorous calculation of these parameters.

We present our calculated band edge deformation potentials in Table 6.5. Previous theoretical analysis has produced a spread of predicted values for the band edge deformation potentials of AlP. Our TB-mBJ-calculated $a_g = -8.56$ eV is in quantitative agreement with the LDA calculation of Wei and Zunger [196], and close to that predicted by Van de Walle [228]. Noting that the LDA tends to underestimate the magnitude of a_g, Wei and Zunger employed an external potential to correct the band gap underestimation in their LDA calculation, resulting in $a_g = -9.52$ eV [196]. This is in close quantitative agreement with our HSEsol prediction. In GaP and InP, we note that our TB-mBJ-calculated a_g is also in close quantitative agreement

TABLE 6.5: DFT-calculated hydrostatic band gap, uniaxial and shear deformation potentials a_g, b and d and hydrostatic pressure coefficients $\mathrm{d}E_g/\mathrm{d}P$ for AlP, GaP and InP. HSEsol- and TB-mBJ-calculated results are respectively denoted by a dagger (†) and an asterisk (∗). The exact exchange mixing α (Becke-Roussel mixing c) is $\alpha = 0.363$ ($c = 1.218$) for AlP, $\alpha = 0.314$ ($c = 1.193$) for GaP, and $\alpha = 0.274$ ($c = 1.165$) for InP.

	AlP		GaP		InP	
Parameter	This work	Reference	This work	Reference	This work	Reference
$a_g = a_c - a_v$ (eV)	$-9.43^{\dagger}$	-8.7^{a}	$-9.50^{\dagger}$	-9.9^{a}	$-6.39^{\dagger}$	-6.6^{a}
	-8.56^{*}	-9.52^{b}	-8.72^{*}	-8.83^{b}	-5.92^{*}	-5.93^{b}
		-8.5^{b}		-7.99^{b}		-5.30^{b}
		-8.70^{c}		-9.35^{c}		-5.95^{c}
b (eV)	$-1.72^{\dagger}$	-1.5^{a}	$-2.06^{\dagger}$	-1.6^{a}	$-1.70^{\dagger}$	-2.0^{a}
	-1.82^{*}	-1.0^{c}	-2.01^{*}	-1.5^{c}	-1.61^{*}	-1.6^{c}
		-2.3^{d}		-2.3^{d}		-1.8^{d}
d (eV)	$-5.30^{\dagger}$	-4.6^{a}	$-5.27^{\dagger}$	-4.6^{a}	$-4.26^{\dagger}$	-5.0^{a}
	-5.23^{*}		-4.93^{*}		-3.95^{*}	
$\frac{\mathrm{d}E_g}{\mathrm{d}P}(\Gamma_{6c}\text{-}\Gamma_{8v})$	$10.04^{\dagger}$	9.40^{b}	$9.72^{\dagger}$	8.90^{b}	$8.27^{\dagger}$	7.40^{b}
(meV kbar^{-1})	9.48^{*}	11.1^{b}	9.46^{*}	10.0^{b}	8.14^{*}	8.4^{b}
$\frac{\mathrm{d}E_g}{\mathrm{d}P}(\mathrm{X}_{6c}\text{-}\Gamma_{8v})$	$-1.96^{\dagger}$	-2.06^{b}	$-2.05^{\dagger}$	-2.20^{b}	$-1.93^{\dagger}$	-1.40^{b}
(meV kbar^{-1})	-2.43^{*}	-1.60^{b}	-2.53^{*}	-1.40^{b}	-2.42^{*}	-2.26^{b}
$\frac{\mathrm{d}E_g}{\mathrm{d}P}(\mathrm{L}_{6c}\text{-}\Gamma_{8v})$	$4.62^{\dagger}$	4.17^{b}	$3.88^{\dagger}$	3.30^{b}	$4.01^{\dagger}$	3.14^{b}
(meV kbar^{-1})	3.81^{*}	5.10^{b}	3.41^{*}	4.30^{b}	3.71^{*}	4.20^{b}

[a]Recommended by Vurgaftman et al., see Ref. [44] for details
Theory: [b]Ref. [196], [d]Ref. [229]
Experiment: [c]Ref. [200]

with the corrected-LDA predictions of Wei and Zunger [196]. Our HSEsol-calculated a_g for GaP and InP demonstrate good quantitative agreement with the original recommendations of Vurgaftman et al. The uniaxial deformation potential b is less studied [45]. For AlP, Vurgaftman et al. recommended $b = -1.50$ eV as the average of the values -1.40 and -1.60 eV respectively proposed by O'Reilly [230] and by Krijn [215]. Our calculated values of b for AlP are slightly larger in magnitude, lying between the tight-binding estimations of O'Reilly [230] and Blacha et al. [229]. Our calculated b for GaP and InP are larger in magnitude than the recommendation of Vurgaftman et al., lying between the values proposed by Ritter et al. [200] and Blacha et al. [229]. To our knowledge, there have been no first-principles calculations of the shear deformation potential d for AlP. Citing a lack of data, Vurgaftman et al. [44] recommended $d = -4.6$ eV for AlP, equal to their recommended value for GaP. In both GaP and InP there also exists a lack of theoretical or experimental data for d [44]. Our HSEsol- and TB-mBJ-calculated values of d are in close agreement for each of AlP, GaP and InP, providing certainty regarding this little-studied parameter.

6.5.2 Pressure coefficients

Using the calculated direct Γ_{6c}-Γ_{8v}, and indirect X_{6c}-Γ_{8v} and L_{6c}-Γ_{8v}, hydrostatic band gap deformation potentials a_g we compute the pressure coefficients as [196]

$$\frac{\mathrm{d}E_g}{\mathrm{d}P} = -\frac{a_g}{B_0}\,, \tag{6.29}$$

where B_0 is the bulk modulus (cf. Sec. 6.2). We compare our calculated pressure coefficients for (Al,Ga,In)P to the LDA and corrected-LDA calculations of Wei and Zunger [196] in Table 6.5. The calculated pressure coefficients follow trends common to other III-V semiconductors. First, the Γ_{6c}-Γ_{8v} and L_{6c}-Γ_{8v} band gaps admit $\mathrm{d}E_g/\mathrm{d}P > 0$, with the pressure coefficient associated with the Γ_{6c}-Γ_{8v} band gap being 2-3 times larger in magnitude than that associated with the L_{6c}-Γ_{8v} band gap. Second, the X_{6c}-Γ_{8v} band gap admits $\mathrm{d}E_g/\mathrm{d}P < 0$, with magnitude approximately one-half of that associated with the L_{6c}-Γ_{8v} band gap. For the direct Γ_{6c}-Γ_{8v} hydrostatic deformation potential, the band gap correction scheme applied by Wei and Zunger also acts to increase $\mathrm{d}E_g/\mathrm{d}P$ for the X_{6c}-Γ_{8v} and L_{6c}-Γ_{8v} band gaps. We note a similar trend between our HSEsol and TB-mBJ calculations, with the former yielding increased $\mathrm{d}E_g/\mathrm{d}P$. We note that in all cases our HSEsol-calculated pressure coefficients lie within the range suggested by the LDA and corrected-LDA calculations of Wei and Zunger.

6.6 Valence band offsets

In a heterostructure, the band offsets are critical to determine the nature of carrier confinement [44, 231]. In this Section we present our DFT-calculated unstrained VBOs. These parameters can be combined with the natural (unstrained) bulk band parameters and band edge deformation potentials to provide a complete and consistent set of parameters upon which to base analysis of III-P heterostructures.

To compute the unstrained VBO slab calculations were performed, which are used to determine the alignment of the average electrostatic (Hartree) potential to the vacuum. An unstrained VBO can be extracted reliably from a SL calculation if the two materials are approximately lattice-matched (e.g. AlP/GaP), but otherwise introduces strain if there exists a lattice mismatch between the materials (e.g. AlP/InP or GaP/InP). We therefore use slab calculations to obtain unstrained VBOs. Using the average electrostatic potential energy obtained from a bulk band structure calculation then allows to align the bulk band edge energies to the vacuum, and hence to determine the natural VBO between different materials. We begin by using a slab calculation to determine the difference in energy between the average electrostatic (Hartree) potential and the vacuum. Considering a supercell in which we define a Cartesian coordinate system whose z axis is perpendicular to the slab surface, the planar-average electrostatic potential along the slab is computed as [231]

$$\overline{V}(z) = \frac{1}{S}\int_S V(\mathbf{r})\,\mathrm{d}x\,\mathrm{d}y \tag{6.30}$$

where S is the area of the slab in the (x, y) plane, and $V(\mathbf{r})$ is the DFT-calculated Hartree potential. To determine the average electrostatic potential energy within the slab, Eq. (6.30) is then macroscopically averaged as [231]

$$\overline{\overline{V}} = \frac{1}{L}\int_{-L/2}^{L/2} \overline{V}(z)\,\mathrm{d}z\,, \tag{6.31}$$

where L is the unit cell length along z. This calculation therefore provides an energy difference in reference to the vacuum. Using bulk HSE band structure calculations, Weston et al. [231] demonstrated that performing this averaging procedure in the GGA produces minor quantitative difference in VBO compared to far more computationally expensive calculations in which the potential averaging is performed via HSE. We therefore employed the Perdew-Burke-Ernzerhof XC functional for solids (PBEsol), in 32-atom [110]-oriented slab supercells having > 3 nm vacuum regions. The TB-mBJ exchange potential is not appropriate for slab vacuum calculations. In the presence of an extended vacuum region the average of $|\nabla n|/n$, where n is the electron charge density, becomes singular and has no meaning (cf. Sec. 3.2.1). The TB-mBJ potential

TABLE 6.6: DFT-calculated valence band offsets (VBOs) for AlP, GaP and InP. HSEsol- and TB-mBJ-calculated results are respectively denoted by a dagger (†) and an asterisk (∗). The exact exchange mixing α (Becke-Roussel mixing c) is $\alpha = 0.363$ ($c = 1.218$) for AlP, $\alpha = 0.314$ ($c = 1.193$) for GaP, and $\alpha = 0.274$ ($c = 1.165$) for InP. Following Ref. [44] the VBO is the natural (unstrained) VBO given relative to the VB maximum of InSb.

	AlP		GaP		InP	
Parameter	This work	Reference	This work	Reference	This work	Reference
VBO (eV)	$-1.925^{\dagger}$	-1.74^{a}	$-1.270^{\dagger}$	-1.27^{a}	$-1.137^{\dagger}$	-0.94^{a}
	-1.694^{*}	-2.07^{b}	-1.152^{*}	-1.33^{b}	-1.052^{*}	-0.88^{b}
		-1.72^{c}		-1.18^{c}		-1.05^{c}
		-2.00^{d}		-1.31^{d}		-0.95^{d}
		-2.12^{e}		-1.59^{e}		-1.12^{e}

[a]Recommended by Vurgaftman et al., see Ref. [44] for details
Theory: [b]Ref. [233], [c]Ref. [234], [d]Ref. [228], [e]Ref. [235]

is dependent on this quantity, meaning TB-mBJ slab vacuum calculations are not possible. The TB-mBJ VBOs are therefore, as in the case of the HSEsol-calculated VBOs, computed by aligning the TB-mBJ bulk band structure to the PBE-calculated electrostatic average in vacuum. The **k**-point grid for BZ integration was downsampled to $1 \times 11 \times 7$. Electrostatic potential averaging via Eqs. (6.30) and (6.31) was implemented using VASPKIT [232].

We then perform bulk band structure calculations (cf. Sec. 6.3) to obtain band energies, and a reference between the VB maximum and the average electrostatic potential in bulk. With the VB maximum energy then known relative to the vacuum in the two materials "A" and "B", their bulk bands can be aligned on a single energy scale and the VBO between two materials, denoted by A and B, is computed as

$$\mathrm{VBO} = \Delta E_v^B - \Delta E_v^A + \Delta\overline{\overline{V}}\,, \tag{6.32}$$

where ΔE_v^A (ΔE_v^B) is the energy of the VB maximum relative to the average electrostatic potential in material A (B), and $\Delta\overline{\overline{V}}$ is the difference in the average electrostatic potential energy between materials A and B. The determination of $\Delta\overline{\overline{V}}$ from the DFT slab calculations is illustrated in Fig. 6.5.

We employed both HSEsol- and TB-mBJ-calculated bulk band structures to compute the VBO (cf. Table 6.6). Vurgaftman et al. [44] provide natural VBOs, on an energy scale with the zero of energy set to lie at the InSb VB maximum – i.e. they provide unstrained VBOs with respect to InSb. We adopt this convention for comparative purposes, where the large lattice mismatch between (Al,Ga,In)P and InSb precludes the use of SL calculations.

The calculated VBOs for AlP and GaP straddle the recommended value of Vurgaftman et al. [44], with the TB-mBJ calculation deviating by < 50 and < 120 meV respectively. Our

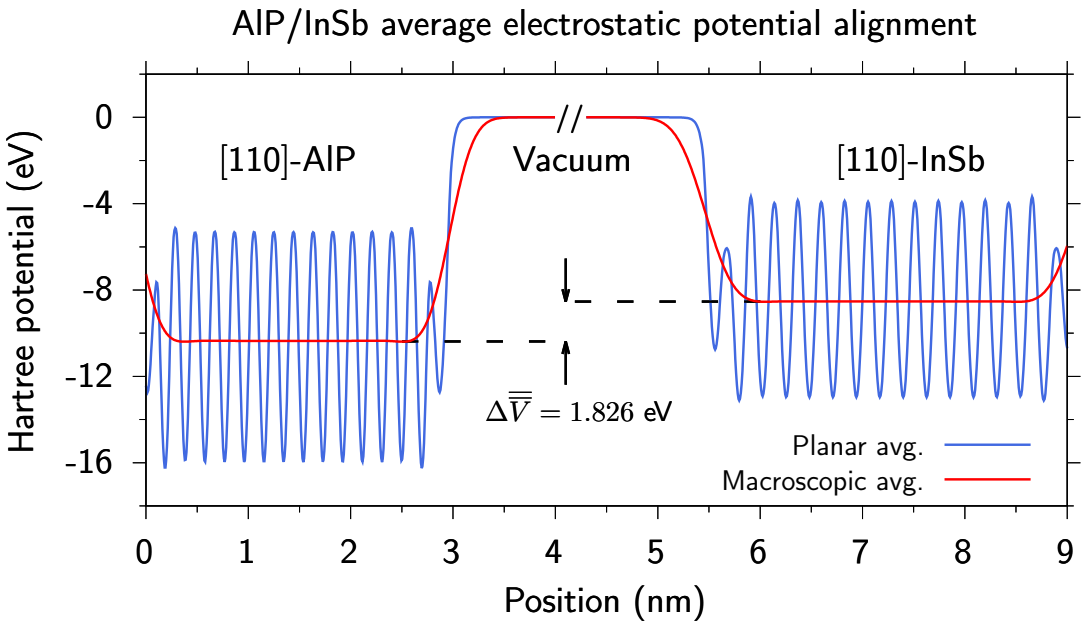


FIGURE 6.5: Schematic illustration of the alignment of the average electrostatic (Hartree) potential $\overline{\overline{V}}$ between [110]-oriented AlP (left) and InSb (right) slabs. Solid blue and red lines respectively show the planar and macroscopic averages $\overline{V}(z)$ and $\overline{\overline{V}}$ calculated using Eqs. (6.30) and (6.31). The vacuum energy is aligned in each slab, shown here by setting the zero of energy at the vacuum level, allowing extraction of $\Delta\overline{\overline{V}}$ between the two materials.

HSEsol-calculated AlP/InSb VBO places the AlP VB maximum 185 meV lower in energy than recommended by Vurgaftman et al. [44]. Our HSEsol-calculated GaP VBO is in exact agreement with the recommendation of Vurgaftman et al. [44]. The HSEsol- and TB-mBJ-calculated InP VBO place the VB maximum $\approx$ 200 and 110 meV lower in energy than the recommendation of Vurgaftman et al. [44], respectively. The larger HSEsol-calculated AlP and GaP VBOs are in close agreement with other predicted VBOs from the literature, including the model solid theory calculations by Van de Walle [228] and by Qteish and Needs [233], and the heterojunction DFT calculations of Li et al. [235]. Our TB-mBJ-calculated VBOs are in good agreement with those computed by Hinuma et al. [234], who combined HSE slab calculations with GW-corrected bulk band edge energies. We note that our HSEsol-calculated AlP and GaP VBOs lie within the range of literature values provided in Table 6.6, while the HSEsol-calculated InP VBO lies outside the range suggested in literature. The DFT-calculated and literature VBOs in Table 6.6 can be used to compute the GaP/AlP, InP/AlP and InP/GaP VBOs. Our calculations predict, on average, a decrease in the magnitude of these VBOs. We note that both our HSEsol- and TB-mBJ-calculated InP/GaP VBOs suggest a decrease in the magnitude of the VBO by 260 - 370 meV, where a notable exception is the prediction of Hinuma et al. [234] which is strong agreement with our DFT-calculated results.

6.7 Conclusions

In summary, we presented a theoretical re-evaluation of the electronic band structure of (Al,Ga,In)P based on first-principles calculations. Literature analysis revealed significant uncertainties in key band parameters, notably a decades-old discrepancy regarding the direct band gap of AlP. Other key uncertainties include the ordering of the X-, Γ- and L-point CB valley minima in AlP, in addition to the values of the band edge effective masses, and band edge deformation potentials. By treating the exact exchange (Becke-Roussel) mixing as an empirical parameter in HSEsol (TB-mBJ) DFT calculations, we demonstrated that fitting to the known fundamental band gap, which can be direct or indirect, produces a reliable description of the band edge electronic structure. This approach produces a direct band gap in AlP that is ≈ 1 eV larger than has generally been assumed in the literature, reconciling this long-standing discrepancy which has proliferated in the literature as a result of a lack of detailed investigation. To validate this significant revision to the direct band gap of AlP, we extracted critical point energies from the HSEsol-calculated band structure and demonstrated that employing these energies in a constrained fit to experimental SE data accounts accurately for the observed optical transitions. Having validated our HSEsol-calculated band structure, we computed an updated set of elastic and band parameters for (Al,Ga,In)P. These parameters have been calculated consistently based on a single underlying lattice parameter and band structure for each III-P compound rather than the disparate combinations of theoretical and experimental parameters that have been assembled ad hoc to construct previous III-P parameter sets. Our calculated band parameters are in good quantitative agreement with those from beyond-DFT (many-body) electronic structure calculations. Multiple benchmark studies of structural, elastic and electronic properties suggest that HSEsol delivers – in the context of DFT calculations – state-of-the-art accuracy, and so it is recommended that the HSEsol parameters provided in this Chapter are employed in heterostructure calculations. However, supercell DFT calculations are much more efficiently performed using the TB-mBJ exchange potential, but incur a reduction in accuracy of the description of some band parameters. The LDA and TB-mBJ parameters constitute an appropriate starting point for many of these types of calculations. The HSE-calculated parameters presented here – several of which have been computed for the first time – constitute an improved basis from which to develop predictive analysis of III-P heterostructures, a platform that continues to attract interest for classical and quantum photonics applications.

Chapter 7

Summary, conclusions and outlook

7.1 Summary and conclusions

This Thesis has presented the results of a theoretical investigation of the electronic and optical properties of III-V superlattices (SLs) for mid-infrared (mid-IR) emission and detection, and the determination of robust electronic band parameters for III-P semiconductors from first-principles. For the former, this involved extending plane-wave based multi-band $\mathbf{k} \cdot \mathbf{p}$ heterostructure calculations to include the miniband dispersion along the growth direction, and detailed benchmarking to ensure accurate and reliable predictive simulations. Analysis of the electronic structure allowed to elucidate the origins of trends in radiative recombination in unstrained broken-gap SLs, and optical absorption in strain-balanced type-II SLs. High-throughput calculations enabled key trends in optoelectronic properties to be identified and quantified, allowing to develop guidelines for epitaxial growth of optimised III-V SLs for applications as high-performance mid-IR emitters and detectors. Following this, literature investigation highlighted the lack of reliable and consistent values for several key electronic band parameters in III-P materials, which are crucial to enable predictive simulations for III-P heterostructures. To address this issue, first principles calculations based on state-of-the-art DFT approaches were performed to produce a set of reliable parameters for AlP, GaP and InP.

Chapter 4 presented an analysis of radiative recombination in InAs/GaSb SLs for mid-IR light-emitting diode (LED) and laser applications. We established a robust computational framework based on multi-band $\mathbf{k} \cdot \mathbf{p}$ calculations to compute the full $\mathbf{k}$-dependent SL band dispersion and eigenstates. In doing this, we elucidated the origin of so-called spurious solutions in the calculated SL electronic properties, via analysis of the bulk complex band structure. Employing a simple renormalisation of the bulk inter-band momentum matrix element – encapsulated by the Kane parameter E_P – we demonstrated the ability to reliably mitigate the impact of these

spurious solutions in heterostructure calculations. Our analysis, validated via comparison to experimental EL measurements, showed that the occupation by electrons and holes of miniband states possessing non-zero wave vector along the growth direction acts to decrease the temperature dependence of the SE peak energy compared to that of the fundamental zone-centre SL band gap. Considering InAs/GaSb SLs having equal InAs and GaSb layer thicknesses, we quantified the impact of miniband formation on the SE rate and radiative recombination coefficient B. Our calculations revealed the important roles played by (i) electron and hole localisation within individual layers of the SL, (ii) carrier occupation of miniband states, and (iii) the strong dependence of the inter-band optical matrix elements on the miniband wave vector q. We demonstrated that the interplay between these factors allow for high optical matrix elements, despite the presence of type-II-like (spatially indirect) carrier confinement, and hence for B values that are large relative to those typically associated with type-II structures. Analysis of the SL electronic structure identified that the electron (hole) minibands being strongly (weakly) dispersive resulted in a significant mismatch in the ranges of miniband wave vector q across which electron and hole states are occupied. This mismatch in electron and hole miniband occupancy – whereby electrons occupy states over a significantly reduced range of q vs. holes – combined with the requirement to conserve crystal momentum during electron-hole recombination, prevents holes close to the SL Brillouin zone edge from undergoing radiative recombination. Thus, miniband formation decreases both the magnitude of B and its dependence on temperature. Having undertaken this detailed interrogation of the properties of InAs/GaSb SLs having equal layer thicknesses, we then performed a systematic analysis of SLs having unequal layer thicknesses. We demonstrated that for shorter wavelengths B is maximised in InAs/GaSb SLs in which the InAs layer thickness is close to equal to the GaSb layer thickness. For longer wavelengths B is maximised for InAs layer thickness $\approx$ 1.5 – 2 $\times$ the GaSb layer thickness. We also identified that B decreases rapidly if the InAs layer thickness is reduced below that of GaSb. To summarise, for emission between 3 and 7 μm, InAs/GaSb SLs should have InAs layer thickness greater than or equal to that of the GaSb layer, with the relative thickness increasing from 1 at 3 μm to 2 at 7 μm to maximise the radiative recombination rate at fixed carrier injection.

Chapter 5 presented an analysis of optical absorption in InAs/$InAs_{1-x}Sb_x$ strain-balanced SLs (SBSLs) for mid-IR photodetectors operating in the 3 - 5 μm wavelength range. We extended the computational framework employed in Chapter 4 to compute the optical absorption. By enforcing fixed cut-off wavelength λ_{cut} (= 5, 5.5 and 6 μm), in addition to strain-balancing with respect to a GaSb substrate, we systematically identified SBSLs having Sb composition x = 18 - 40%. The upper end of this Sb composition range poses challenges for epitaxial growth, due to the presence of large in-plane compressive strain and the requirement for low layer thicknesses in order to maintain the required cut-off wavelength. Using the calculated SL electronic structure and eigenstates we computed the band-to-band optical absorption spectrum for each identified

SBSL, revealing the ability to engineer an increase in optical absorption in the 3 - 5 μm range with increasing Sb composition x. To provide an appropriate figure of merit to enable SBSL optimisation for photodetection, the calculated SBSL absorption spectra were employed in a model calculation of the internal quantum efficiency (IQE) associated with photodetection of 3 - 5 μm radiation from an ambient blackbody source. At fixed Sb composition and SBSL absorber thickness, we demonstrated the potential to increase the IQE in the 3 - 5 μm spectral range by designing structures to have longer λ_{cut}. With increasing Sb composition x, we predict a significant enhancement of the IQE up to $x = 30\%$, independent of λ_{cut}. Our calculations reveal minimal additional enhancement in IQE for $x > 30\%$. Interrogation of the electronic structure evolution vs. Sb composition x allowed to identify that this trend derives from a competition between the joint density of states and optical matrix elements, which respectively decrease and increase with increasing x. The increase in the latter was found to be sufficient to drive a net increase of the IQE. Our calculations predict minimal enhancement for cut-off wavelengths longer than 5.5 μm.

Chapter 6 presented an analysis of the electronic band parameters of the III-P compounds AlP, GaP and InP. Interrogation of theoretical and experimental data from the literature revealed significant uncertainties in key electronic band parameters for III-P semiconductors. Key uncertainties in these parameters included the direct band gap in AlP, the energy ordering of the CB valley minima in AlP and InP, the band edge effective masses, and the band edge deformation potentials. By treating the exact exchange (Becke-Roussel) mixing as an empirical parameter in HSEsol (TB-mBJ) DFT calculations, we demonstrated that fitting to the known fundamental (lowest energy) band gap, reliably accesible via experimental measurement, produces a reliable description of the band edge electronic structure. This fundamental band gap is indirect in AlP and GaP, and direct in InP. Based on a detailed reevaluation of literature data, including a constrained fit to ellipsometry data based on our DFT calculations, we revise the direct band gap of AlP to a value ≈ 1 eV larger than generally assumed. Our reevaluation of the AlP band structure reconciles theory and experiment, and revises a decades old underestimation of the direct band gap that has proliferated in the literature due to a lack of additional analysis. Based on a systematic suite of DFT calculations, we extracted a robust and consistent set of electronic band parameters for AlP, GaP and InP, many of which have now been computed explicitly for the first time. Furthermore, our calculated band parameters are in good quantitative agreement with those from beyond-DFT (many-body) electronic structure calculations and, where available, experimental measurements.

7.2 Outlook

The calculational framework that has been established to treat radiative recombination and optical absorption in SL heterostructures is generally applicable to systems whose constituent

material bulk band structures can be well described via a multi-band $\mathbf{k} \cdot \mathbf{p}$ Hamiltonian. To further develop quantitative in silico design of SL emitters, like the InAs/GaSb SLs investigated in this work, further analysis is required to enable quantitative prediction of the IQE. In particular, this will require accurate computation of the Auger-Meitner recombination coefficient C, which quantifies the rate of three-carrier non-radiative recombination processes. This is due to the importance of this non-radiative recombination process as a critical efficiency-limiting loss mechanism in long-wavelength emitters [6, 108, 109]. Our SL simulation framework allows to reliably compute $\mathbf{k}$-dependent SL eigenstates, thereby providing the basis for accurate evaluation of the matrix elements associated with Coulomb scattering, and hence to evaluate the Auger-Meitner recombination rate.

In the case of absorbers, like the InAs/$InAs_{1-x}Sb_x$ SBSLs investigated in this work, our systematic analysis focused on the active region of photodetector devices. There exist several strategies to improve the performance of mid-IR photodetectors based on these structures. One strategy is the inclusion of thin $Al_xGa_{1-x}Sb$ electron-blocking layers which can, for example, reduce dark currents [11]. Our established calculational framework can be readily extended to analyse and optimise the electronic and optical properties of such structures. Additionally, there is further scope for work using the calculated SBSL electronic structure to develop quantitative calculations of device-specific figures of merit [172]. While our analysis provided insight into underlying trends in the optical absorption of SBSLs, the optimisation of specific device figures of merit may be of interest for ongoing experimental research. This type of work is likely to be of significant value in supporting the design of SL-based detectors in industry for real-world applications.

Having established a robust parameter set for III-P semiconductors, a clear next step would be to apply these parameters to $\mathbf{k} \cdot \mathbf{p}$-based calculations to predict accurate electronic and optical properties for visible-wavelength III-P heterostructures. This could include analysis and optimisation of pseudomorphic and metamorphic III-P quantum wells (QWs) and quantum dots (QDs) for application in LEDs and lasers, particularly in the challenging orange/amber (580 - 620 nm) spectral range, in addition to exploration of the electronic structure of coupled GaInP QDs as hosts of Wigner crystallisation for quantum computing applications [42, 43, 236]. The plane-wave multi-band $\mathbf{k}\cdot\mathbf{p}$ framework established in this work can be applied directly to analyse III-P QWs and can also, once implemented in three dimensions, be applied to perform predictive simulations of III-P QDs [237]. The bowing parameters in AlP alloys are usually assumed to be close to zero [44, 45]. This was based on the historical value for the AlP direct band gap and measurements of the experimental band gap of alloys $Al_xGa_yIn_{1-x-y}P$ alloys grown on GaAs with close to 50% In composition. First instance reevaluation of the AlP alloy bowing parameters can be done using the alloy experimental measurements with new end-point values. Explicit calculation of the bowing parameters in III-P heterostructures using DFT-based methods would

provide clarity and further enhance the accuracy of bowing parameters, enhancing predictive capabilities of future III-P heterostructure simulations. GaInP alloys, and hence GaInP QDs, are subject to CuPt-ordering [238]. Empirical atomistic analysis is required in order to accurately describe the impacts of this short-range ordering on electronic structure. Our DFT calculations can underpin this type of analysis in III-P heterostructures. Firstly, our DFT-calculated structural and elastic properties allow to parametrise empirical interatomic potentials [239], which can underpin atomistic relaxation and strain field calculations for heterostructures. Secondly, our DFT-calculated band structures and band edge deformation potentials provide the information required to parametrise empirical pseudopotential or tight-binding models, which can then underpin atomistic electronic structure calculations for heterostructures [240].

Appendix A

Considerations for 8-band $\mathbf{k} \cdot \mathbf{p}$ plane wave calculations

In this Appendix, the results presented in Chapters 4 and 5 are supplemented with further detailed analysis of key considerations for plane wave multi-band $\mathbf{k} \cdot \mathbf{p}$ calculations. In Sec. A.1, we begin by discussing the presence and mitigation of spurious solutions. We provide additional detail on the renormalisation of the Kane parameter E_P (cf. Sec. 4.2.1), the impact of spurious solutions on calculated electronic band structure, and the extent to which spurious solutions can be mitigated. In Sec. A.2, we analyse the evolution of the envelope functions in InAs/GaSb superlattices (SLs) with miniband wave vector q in our 8-band $\mathbf{k} \cdot \mathbf{p}$ plane wave calculations.

A.1 Presence and mitigation of spurious solutions

Spurious solutions are non-physical solutions of the multi-band $\mathbf{k}\cdot\mathbf{p}$ envelope function (Schrödinger) equations, which can affect the validity of results and provide an inaccurate physical description of heterostructure electronic properties [55, 123, 128]. When applying $\mathbf{k} \cdot \mathbf{p}$ methods and the plane wave expansion method (PWEM) care must be taken to minimise, or if possible, remove the deleterious effect of spurious solutions. As described in Sec. 4.2.1, initial test calculations for InAs/GaSb SLs produced band structures displaying spurious solutions. The emergence of these spurious solutions was observed for basis sets containing relatively low numbers of plane waves, indicating that careful consideration is required in the choice of plane wave basis set size. For a choice of M, $2M + 1$ is the total number of plane waves in the basis set (cf. Sec. 2.2). When comparing the $e1$-$h1$ peak emission wavelength to experimental measurements it was noted that, despite careful selection of M, further efforts were mandated to ensure confidence in the accuracy of our calculations. In the majority of well established parameter sets, for several III-V semiconductors, for the 8-band $\mathbf{k} \cdot \mathbf{p}$ Hamiltonian we see

$$\frac{1}{m_c^*} < \frac{E_P}{3}\left(\frac{2}{E_g} + \frac{1}{E_g + \Delta_{\mathrm{SO}}}\right). \tag{A.1}$$

This gives $s_c < 0$ (cf. Eq. (4.1)), which is the case due to the large magnitude of the Kane parameter E_P. This causes downward bending of the lowest-energy conduction band (CB) at large real wave vector $k = |\mathbf{k}|$, which can produce non-physical states lying energetically within the band gap. In the PWEM k_z is sampled via the discrete wave vectors G_m, with $|m| \leq M$, which for large M can sample non-physical large-k_z bulk states and pollute the results of heterostructure calculations with spurious solutions [55, 123, 128]. As discussed in Sec. 4.2.1, we found that following Foreman's prescription of imposing $s_c = 0$ by renormalising the Kane parameter E_P rectified this issue [128]. However, while this established approach worked to mitigate the impact of spurious solutions in our SL calculations, further analysis revealed that the origin of the spurious solutions was not related to states at large real k_z lying energetically within the band gap. Rather it was the presence of a spurious band having complex-valued wave vector in the bulk band structure. As such, we undertook an analytical analysis of a representative 2-band (Kane) Hamiltonian to identify the origin of the spurious band "SB" identified in Fig. 4.1(a), and to demonstrate why imposing $s_c = 0$ mitigates its impact in the numerical calculations.

Following this renormalisation, we note that it is not possible to conclude that the impact of spurious solutions on the SL electronic structure calculated using the 8-band $\mathbf{k}\cdot\mathbf{p}$ Hamiltonian have been removed entirely. We therefore present an analytical analysis to demonstrate explicitly that imposing $s_c = 0$ mitigates the influence of these spurious solutions in our numerical calculations. Firstly, we note that setting $s_c = 0$ allows for a discontinuity to occur at an InAs/GaSb interface in amplitude of the CB Bloch component of the envelope function [128]. Omitting the spin-split-off (SO) band by setting the valence band (VB) spin-orbit splitting Δ_{SO} equal to zero allows us to reduce $H_{3\times3}$ of Eq. (4.2) to a 2-band (Kane) Hamiltonian for the CB and light-hole (LH) states

$$H_{2\times2}(k_z) = \begin{pmatrix} E_c + ak_z^2 & Pk_z \\ Pk_z & E_v - bk_z^2 \end{pmatrix} \begin{matrix} |\frac{1}{2};+\frac{1}{2}\rangle \\ |\frac{3}{2};+\frac{1}{2}\rangle \end{matrix}, \tag{A.2}$$

where $a = \frac{\hbar^2 s_c}{2m_0}$ and $b = \frac{\hbar^2}{2m_0}(\gamma_1 + 4\gamma_2)$. We can use Eq. (A.2) to understand the origin of the aforementioned discontinuity in the envelope function, which gives rise to the step-like behaviour of the $e1$ probability density observed in Fig. 4.3. We do so by diagonalising Eq. (A.2) for small values of a (equivalent to small values of s_c) and then analyse the evolution of the eigenstates as $a \to 0$. Evaluating the determinant $|H_{2\times2} - E\,I| = 0$, where I is the 2×2 identity matrix, produces a quartic characteristic equation in k_z, for which the solutions at small a are

$$k_{z,\pm}^2(E) \approx \frac{-\left(P^2 + b\left(E_c - E\right)\right) \pm \sqrt{\left(P^2 + b\left(E_c - E\right)\right)^2 - 4ab\left(E_c - E\right)\left(E - E_v\right)}}{2ab}\,. \tag{A.3}$$

In addition to the usual Kane solution $k_{z,+}^2$, which describes the evanescent band linking the VB and CB edges [241], we also obtain a second solution $k_{z,-}^2$ whose value at small a can be approximated as

$$\kappa_-^2(E) \equiv -k_{z,-}^2(E) \approx \frac{P^2 + b\left(E_c - E\right)}{ab}\,, \tag{A.4}$$

with $\kappa_-^2 \to \infty$ as $a \to 0$. The corresponding eigenstates of $H_{2\times2}$ approach $|\psi_\pm\rangle = e^{\pm\kappa_+ z}|\frac{1}{2};+\frac{1}{2}\rangle$ as $a \to 0$, where $|\frac{1}{2};+\frac{1}{2}\rangle$ is the $k_z = 0$ CB Bloch (basis) state [52]. To calculate allowed bound eigenstates in a heterostructure grown along the z direction, we replace $k_z \to -i\frac{\mathrm{d}}{\mathrm{d}z}$ in Eq. (A.2) [133]. Writing this quantised Hamiltonian as

$$\widehat{H}\psi = A\,\frac{\mathrm{d}^2\psi}{\mathrm{d}z^2} + B\,\frac{\mathrm{d}\psi}{\mathrm{d}z} + C\psi\,, \tag{A.5}$$

then the allowed solutions must satisfy the boundary conditions that both ψ and $A\,\frac{\mathrm{d}\psi}{\mathrm{d}z} + \frac{1}{2}B\psi$ are continuous [133], where

$$A = \begin{pmatrix} -a & 0 \\ 0 & b \end{pmatrix},\; B = \begin{pmatrix} 0 & iP \\ -iP & 0 \end{pmatrix},\; \text{and}\;\; C = \begin{pmatrix} E_c & 0 \\ 0 & E_v \end{pmatrix}, \tag{A.6}$$

are the respective coefficient matrices of Eq. (A.2) for terms that are quadratic in k_z, linear in k_z, and independent of k_z.

These boundary conditions appear to mandate that the CB component of ψ must always be continuous. However, the term $A\,\frac{\mathrm{d}\psi}{\mathrm{d}z}$ can allow for a jump discontinuity in the amplitude of ψ as $a \to 0$. For $E \approx E_c$ we have $\frac{\mathrm{d}\psi_-}{\mathrm{d}z} \approx \pm\frac{P}{\sqrt{ab}}\psi_-$, so that the CB component of $A\,\frac{\mathrm{d}\psi}{\mathrm{d}z}$ can then vary as $-a\,\frac{\mathrm{d}\psi_-}{\mathrm{d}z} \approx \mp P\sqrt{\frac{a}{b}}\,\psi_-$, which vanishes as $a \to 0$. This behaviour, discussed by Foreman in the $a = 0$ limit [128], accounts for the observed discontinuities in the $e1$ envelope function at InAs/GaSb interfaces in the full 8-band calculations (cf. Fig. 4.3).

We note that our calculated InAs and GaSb bulk complex band structures, using renormalised parameters with the Kane parameter E_P having been reduced such that $s_c = 0$ (cf. Fig. 4.1(b)), are in good quantitative agreement with the results of atomistic tight-binding calculations over the same ranges of energy and wave vector [242]. States from outside of these ranges of energy and wave vector also contribute, albeit less strongly, to the determination of the variation of

the electron envelope function with position in a full atomistic calculation. However, as described in Chapter 4, our renormalised 8-band $\mathbf{k}\cdot\mathbf{p}$ calculations capture the key features of the envelope functions and inter-band optical matrix elements observed in the full atomistic SL calculations of, e.g., Refs. [92] and [131]. This demonstrates that the impact of spurious solutions is sufficiently mitigated to validate our $\mathbf{k}\cdot\mathbf{p}$ calculations of the InAs/GaSb SL electronic structure. We then use these calculations as a platform to predict and analyse radiative recombination in broken-gap InAs/GaSb SLs (cf. Chapter 4) and, following this, optical absorption in InAs/InAs$_{1-x}$Sb$_x$ SBSLs (cf. Chapter 5).

A.2 Envelope function evolution along minibands in InAs/GaSb superlattices

In this Section we analyse the evolution vs. miniband wave vector q of the envelope functions of InAs/GaSb SLs having equal InAs and GaSb layer thicknesses. In Sec. 4.4.1 we noted that the optical (momentum) matrix element between the $\mathbf{k}_{\|}=0$ $e1$ and $h1$ SL eigenstates goes to zero as q is varied from zero to $\frac{\pi}{L}$ (cf. Fig. 4.5(a)). In Chapter 4 we noted that this behaviour was a consequence of the introduction of a relative phase shift between the $e1$ and $h1$ envelope functions as both minibands are traversed in q. To demonstrate this explicitly, we present here the calculated Bloch components of the $e1$ and $h1$ envelope functions at both $q=0$ and $\frac{\pi}{L}$. We recall that the heavy-hole (HH) band is decoupled at $\mathbf{k}_{\|}=0$, which can be seen in the 8-band Hamiltonian matrix of Eq. (2.25) by setting $k_x=k_y=0$. As such, the $e1$ eigenstate at $\mathbf{k}_{\|}=0$ consists of an admixture of CB, LH and SO Bloch character only, while the $h1$ eigenstate is purely HH-like.

The results of these calculations are summarised in Fig. A.1, which shows the aforementioned non-zero envelope function Bloch components at $q=0$ (top row) and $q=\frac{\pi}{L}$ (bottom row) for a single SL period. Panels (a), (b) and (c) in the top row, and panels (e), (f) and (g) in the bottom row, respectively show the CB, LH and SO Bloch components of the $e1$ eigenstate. Panels (d) and (h) show the HH component of the $h1$ eigenstate at $q=0$ and $\frac{\pi}{L}$, respectively.

Considering first the Bloch components of the $e1$ eigenstate, at $q=0$ the CB (LH and SO) component is purely real and even (imaginary and odd) about the centre of the InAs layer – shaded region – at $z=0$, and remains so as q changes from zero to $\frac{\pi}{L}$. For the $h1$ state, we observe changing phase and parity between $q=0$ and $\frac{\pi}{L}$, with the HH Bloch component changing from being purely real and even about the centre of the InAs layer at $q=0$ to purely real and odd about the centre of the InAs layer at $q=\frac{\pi}{L}$. This directly demonstrates that varying q from zero to $\frac{\pi}{L}$ introduces a difference in parity between the $e1$ and $h1$ SL eigenstates at $\mathbf{k}_{\|}=0$. This results in the $e1$ and $h1$ eigenstates having equal (opposite) parity at $q=0$ ($q=\frac{\pi}{L}$) which, combined with the respective s- and p-like symmetry of the CB and HH Bloch

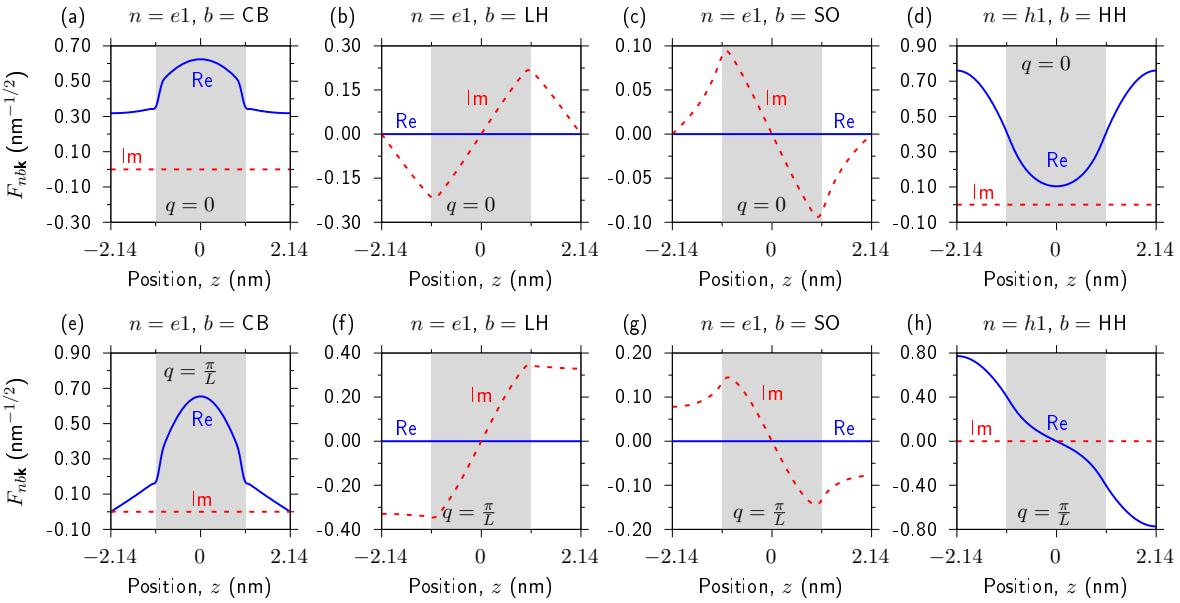


FIGURE A.1: Top row: real (solid blue lines) and imaginary (dashed red lines) parts of the $q = 0$ envelope function Bloch components $F_{nb\mathbf{k}}(z)$ for the $\mathbf{k}_{\parallel} = 0$ $e1$ and $h1$ eigenstates of the exemplar equal layer thickness InAs/GaSb SL considered in Sec. 4.3 (having SL period $L = 2t = 4.28$ nm). (a) CB component of $e1$, (b) LH component of $e1$, (c) SO component of $e1$, and (d) HH component of $h1$. Bottom row: as in the top row, but for $q = \frac{\pi}{L}$. Shaded (unshaded) regions denote the electron-confining InAs (hole-confining GaSb) layers.

basis states $|\frac{1}{2};\pm\frac{1}{2}\rangle$ and $|\frac{3}{2};\pm\frac{3}{2}\rangle$, gives rise to the calculated reduction of the $\mathbf{k}_{\parallel} = 0$ $e1$-$h1$ inter-band optical matrix element to zero at the SL Brillouin zone edge (cf. Fig. 4.5(a)).

We note that the fact that this change in parity appears restricted to the $h1$ eigenstate in Fig. A.1 is a consequence of the specific choice of calculational supercell employed in our analysis. Here, we have utilised a supercell $z \in [-\frac{L}{2}, \frac{L}{2}]$ which is centred about the centre of the electron-confining InAs layer. Changing to, for example, a supercell with $z = 0$ set at the centre of the hole-confining GaSb layer instead produces a change in the phase and parity of the $e1$ eigenstate as q varies from zero to $\frac{\pi}{L}$, with the parity of the $h1$ eigenstate then remaining fixed. This has been confirmed via test calculations and emphasises that it is the *difference* in parity between the $e1$ and $h1$ eigenstates that determines their inter-band optical matrix element, irrespective of a given choice of calculational supercell.

Appendix B

Interface softening in the plane wave expansion method

In this Appendix, the procedure outlined in Chapter 4 to address the emergence of the Gibbs phenomenon in calculated superlattice (SL) envelope functions is supplemented with further detail. We present the procedure for applying interface softening to an arbitrary multi-quantum well heterostructure, which in Chapters 4 and 5 is applied to InAs/GaSb SLs and strain-balanced InAs/$InAs_{1-x}Sb_x$ SLs respectively.

We consider an arbitrary multi-quantum well heterostructure comprised of a total of N_l material layers. The spatial variation $P(z)$ of a generic material parameter P along the growth direction z is given by

$$P(z) = \sum_{l=1}^{N_l} P_l \chi_l(z)\,, \tag{B.1}$$

where P_l is the value of P in the material comprising of the l^{th} layer of the heterostructure, and $\chi_l(z)$ is the characteristic function associated with the l^{th} layer of the heterostructure (cf. Sec. 4.3.1). Assuming "hard" – i.e. spatially abrupt – interfaces between layers, each layer is taken to lie in the range $z_l \leq z \leq z_{l+1}$, with $\chi_l(z)$ then defined to have value $= 1$ within the layer and $= 0$ otherwise. We can therefore write

$$\chi_l(z) = \theta\left(z - z_l\right) - \theta\left(z - z_{l+1}\right)\,, \tag{B.2}$$

where θ is the Heaviside step function.

We emphasise that Eq. (B.2) describes spatially abrupt interfaces between layers in the heterostructure, such that $P(z)$ is a piecewise continuous function of position z. To "soften" this interface – e.g. to simulate non-abrupt interfaces in realistic heterostructures, by emulating intermixing between material layers – we can convolute $\chi_l(z)$ with a Gaussian distribution

$$g(z) = \frac{1}{\sigma\sqrt{2\pi}} \exp\left(-\frac{z^2}{2\sigma^2}\right) , \tag{B.3}$$

to obtain the "softened" layer characteristic function

$$\begin{aligned}(\chi_l * g)(z) &= \int_{-\infty}^{+\infty} \chi_l(z) g(z-t) \mathrm{d}t = \frac{1}{\sigma\sqrt{2\pi}} \int_{z_j}^{z_{j+1}} \exp\left(-\frac{(z-t)^2}{2\sigma^2}\right) \mathrm{d}t \\ &= \frac{1}{2}\left[\mathrm{erf}\left(\frac{z-z_j}{\sqrt{2}\sigma}\right) - \mathrm{erf}\left(\frac{z-z_{j+1}}{\sqrt{2}\sigma}\right)\right] ,\end{aligned} \tag{B.4}$$

where erf is the error function.

In the plane wave expansion method, geometric information is encapsulated via the Fourier transforms $\tilde{\chi}_l(G)$ of the layer characteristic functions (cf. Sec. 2.2). To compute the Fourier transform of the "softened" layer characteristic function of Eq. (B.4), we exploit the convolution theorem

$$\mathcal{F}\left\{(\chi_l * g)(z)\right\}(G) = \tilde{\chi}_l(G)\tilde{g}(G) = \tilde{\chi}_l(G) \exp\left(-\frac{G^2\sigma^2}{2}\right) , \tag{B.5}$$

where $\tilde{g}(G) = \exp\left(-\frac{\sigma^2 G^2}{2}\right)$ is the Fourier transform of Eq. (B.3). This therefore allows the Fourier transform of the "softened" layer characteristic function to be obtained by simple multiplication of its "hard" equivalent $\tilde{\chi}_l(G)$. We now provide an example of the implementation of this technique in Fig. B.1.

In Fig. B.1 we show the calculated $e1$ probability density, and associated conduction band offsets and energy of the $e1$ state, for an exemplar InAs/GaSb SL having equal InAs and GaSb layer thickness (cf. Sec. 4.3.1) (a) with, and (b) without interface softening. In these calculations $M = 25$ ($2M + 1 = 51$). This calculation does not attempt to treat intermixing effects, but instead to introduce minimal softening that mitigates the Gibbs phenomenon. These calculations, and those of Chapters 4 and 5 use $\sigma = 0.075$ nm. Comparing Figs. B.1(a) and B.1(b), demonstrates that this small standard deviation for the Gaussian distribution is sufficient to address the emergence of the Gibbs phenomenon, while producing minimal change in the energy of the bound eigenstate (< 2 meV at $z = 0$). Therefore, the implementation of this interface softening mitigates the oscillations in the probability density generated by the Gibbs phenomenon, while not meaninfully impacting the SL eigenstates in any other manner.

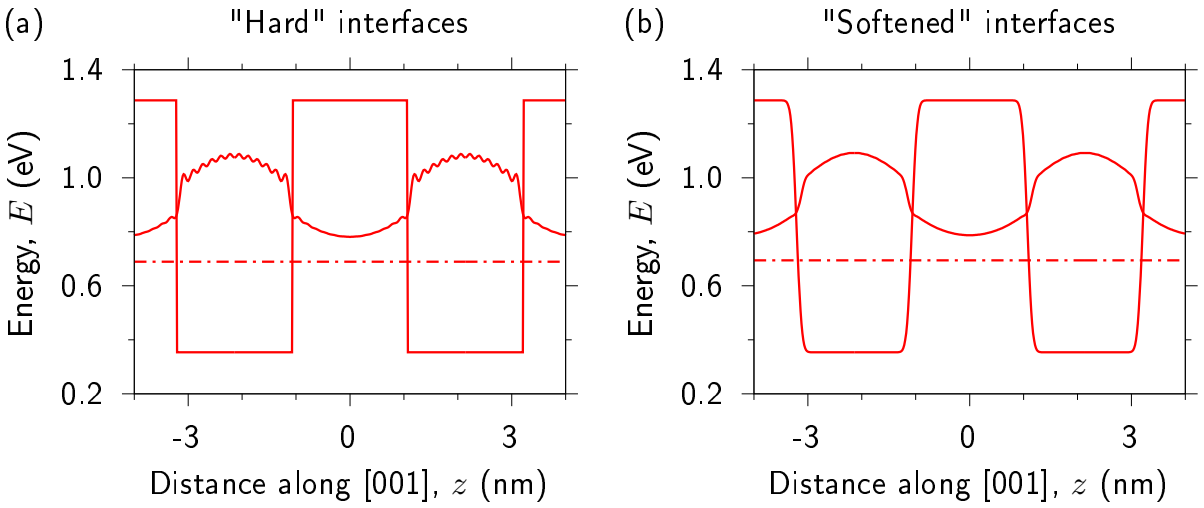


FIGURE B.1: (a) With no interface softening implemented – i.e. "hard" interfaces – calculated conduction band (solid red line) offsets, illustrated for two periods of a InAs/GaSb SL having equal InAs and GaSb layer thickness $t = 2.14$ nm (SL period $L = 4.28$ nm), and total number of plane waves $2M + 1 = 51$ ($M = 25$). The dash-dotted red line denotes the energy of the lowest energy bound electron state $e1$. The $e1$ probability density is shown using a solid red line, shifted so that the zero of probability density lies at the $e1$ energy. (b) Same as in (a) with interface softening implemented – i.e. "softened" interfaces.

Bibliography

[1] D. Popa and F. Udrea, "Towards integrated mid-infrared gas sensors," Sensors **19**, 2076 (2019).

[2] A. Krier, ed., "Mid-Infrared Semiconductor Optoelectronics" (Springer, London, 2006).

[3] I. K. Ilev and R. W. Wayant, "Mid-Infrared Biomedical Applications" (Springer, London, 2006).

[4] E. Tournié and A. N. Baranov, "Mid-infrared semiconductor lasers: a review," Semicond. Semimet. **86**, 183 (2012).

[5] J. Wang, L. Zheng, X. Niu, C. Zheng, Y. Wang, and F. K. Tittel, "Mid-infrared absorption-spectroscopy-based carbon dioxide sensor network in greenhouse agriculture: development and deployment," Appl. Opt. **55**, 7029 (2016).

[6] D. O. Alshahrani, M. Kesaria, E. A. Anyebe, V. Srivastava, and D. L. Huffaker, "Emerging type-II superlattices of InAs/InAsSb and InAs/GaSb for mid-wavelength infrared photodetectors," Adv. Photonics Res. **3**, 2100094 (2021).

[7] P. Wang, H. Xia, Q. Li, F. Wang, L. Zhang, T. Li, P. Martyniuk, A. Rogalski, and W. Hu, "Sensing infrared photons at room temperature: from bulk materials to atomic layers," Small **15**, 1904396 (2019).

[8] C. A. Broderick, W. Xiong, S. J. Sweeney, E. P. O'Reilly, and J. M. Rorison, "Theory and design of $In_xGa_{1-x}As_{1-y}Bi_y$ mid-infrared semiconductor lasers: type-I quantum wells for emission beyond 3 μm on InP substrates," Semicond. Sci. Technol. **33**, 094007 (2018).

[9] M. S. Vitiello, G. Scalari, B. Williams, and P. D. Natale, "Quantum cascade lasers: 20 years of challenges," Opt. Express **23**, 5167 (2015).

[10] M. Razeghi, Q. Y. Lu, N. Bandyopadhyay, W. Zhou, D. Heydari, Y. Bai, and S. Slivken, "Quantum cascade lasers: from tool to product," Appl. Opt. **23**, 8462 (2015).

[11] E. Delli, V. Letka, P. D. Hodgson, E. Repiso, J. P. Hayton, A. P. Craig, Q. Lu, R. Beanland, A. Krier, A. R. J. Marshall, et al., "Mid-Infrared InAs/InAsSb superlattice nBn photodetector monolithically integrated onto silicon," ACS Photonics **6**, 538 (2019).

[12] H. Sakaki, L. L. Chang, G. A. Sai-Halasz, C. A. Chang, and L. Esaki, "Two-dimensional electronic structure in InAs-GaSb superlattices," Solid State Commun. **26**, 589 (1978).

[13] S. L. Chuang, "Physics of Photonic Devices" (Wiley, New Jersey, 2009).

[14] B. Roul, M. Kumar, M. K. Rajpalke, T. N. Bhat, and S. B. Krupanidhi, "Binary group III-nitride based heterostructures: band offsets and transport properties," J. Phys. D: Appl. Phys. **48**, 423001 (2015).

[15] H. Kroemer, "The 6.1 Å family (InAs, GaSb, AlSb) and its heterostructures: a selective review," Physica E **20**, 196 (2004).

[16] Y. Zhou, Q. Li, X. Chai, Z. Xu, J. Chen, A. Krier, and L. He, "InAs/GaSb superlattice interband cascade light emitting diodes with high output power and high wall-plug efficiency," Appl. Phys. Lett. **114**, 253507 (2019).

[17] H. Mohseni and M. Razeghi, "High-performance InAs/GaSb superlattice photodiodes for the very long wavelength infrared range," Appl. Phys. Lett. **78**, 2107 (2001).

[18] Y. Wei, A. Hood, H. Yau, A. Gin, and M. Razeghi, "Uncooled operation of type-II InAs/-GaSb superlattice photodiodes in the midwavelength infrared range," Appl. Phys. Lett. **86**, 233106 (2005).

[19] Y. Zhang, W. Ma, Y. Cao, J. Huang, Y. Wei, K. Cui, and J. Shao, "Long wavelength infrared InAs/GaSb superlattice photodetectors with InSb-like and mixed interfaces," IEEE J. Quantum Electron. **47**, 1475 (2011).

[20] E. Delli, P. D. Hodgson, M. Bentley, E. Repiso, A. P. Craig, Q. Lu, R. Beanland, A. R. J. Marshall, A. Krier, and P. J. Carrington, "Mid-infrared type-II InAs/InAsSb quantum wells integrated on silicon," Appl. Phys. Lett. **117**, 131103 (2020).

[21] E. H. Steenbergen, B. C. Connelly, G. D. Metcalfe, H. Shen, M. Wraback, D. Lubyshev, Y. Qiu, J. M. Fastenau, A. W. K. Liu, S. Elhamri, et al., "Significantly improved minority carrier lifetime observed in a long-wavelength infrared III-V type-II superlattice comprised of InAs/InAsSb," Appl. Phys. Lett. **99**, 251110 (2011).

[22] E. H. Steenbergen, K. Nunna, L. Ouyang, B. Ullrich, D. L. Huffaker, D. J. Smith, and Y.-H. Zhang, "Strain-balanced InAs/$InAs_{1-x}Sb_x$ type-II superlattices grown by molecular beam epitaxy on GaSb substrates," J. Vac. Sci. Technol. B **30**, 02B107 (2012).

[23] B. V. Olson, E. A. Shaner, J. K. Kim, J. F. Klem, S. D. Hawkins, L. M. Murray, J. P. Prineas, M. E. Flatté, and T. F. Boggess, "Time-resolved optical measurements of minority carrier recombination in a mid-wave infrared InAsSb alloy and InAs/InAsSb superlattice," Appl. Phys. Lett. **101**, 092109 (2012).

[24] A. Bader, F. Rothmayr, N. Khan, F. Jabeen, J. Koeth, S. Höfling, and F. Hartmann, "Interband cascade infrared photodetectors based on Ga-free InAs/InAsSb superlattice absorbers," Appl. Phys. Lett. **121**, 041104 (2022).

[25] D. Lackner, M. Steger, M. L. W. Thewalt, O. J. Pitts, Y. T. Cherng, S. P. Watkins, E. Plis, and S. Krishna, "InAs/InAsSb strain balanced superlattices for optical detectors: material properties and energy band simulations," J. Appl. Phys. **111**, 034507 (2012).

[26] P. T. Webster, N. A. Riordan, S. Liu, E. H. Steenbergen, R. A. Synowicki, Y.-H. Zhang, and S. R. Johnson, "Absorption properties of type-II InAs/InAsSb superlattices measured by spectroscopic ellipsometry," Appl. Phys. Lett. **106**, 061907 (2015).

[27] T. Manyk, K. Michalczewski, K. Murawski, K. Grodecki, J. Rutkowski, and P. Martyniuk, "Electronic band structure of InAs/InAsSb type-II superlattice for HOT LWIR detectors," Results Phys. **11**, 1119 (2018).

[28] D. Z. Ting, A. Khoshakhlagh, A. Soibel, and S. D. Gunapala, "Long wavelength InAs/InAsSb infrared superlattice challenges: a theoretical investigation," J. Electron. Mater. **49**, 6936 (2020).

[29] J. Petticrew, Y. Ji, I. S. Han, B. White, A. Evirgen, J.-L. Reverchon, M. Hopkinson, C. H. Tan, and J. S. Ng, "Characterisation, modelling and design of cut-off wavelength of InGaAs/GaAsSb type-II superlattice photodiodes," Semicond. Sci. Technol. **38**, 025002 (2023).

[30] F. A. Kish and R. M. Fletcher, "AlGaInP light-emitting diodes," Semicond. Semimet. **48**, 149 (1997).

[31] K. Kobayashi, S. Kawata, A. Gomyo, I. Hino, and T. Suzuki, "Room-temperature CW operation of AlGaInP double-heterostructure visible lasers," Electron. Lett. **21**, 931 (1985).

[32] R. S. Geels, D. F. Welch, D. R. Scifres, D. P. Bour, D. W. Treat, and R. D. Bringans, "High power, low threshold, single mode 630 nm laser diodes," Electron. Lett. **28**, 1810 (1992).

[33] G. Walter, N. Holonyak, Jr., J. H. Ryou, and R. D. Dupuis, "Room-temperature continuous photopumped laser operation of coupled InP quantum dot and InGaP quantum well InP–InGaP–In(AlGa)P–InAlP heterostructures," Appl. Phys. Lett. **79**, 1956 (2001).

[34] J. H. Ryou, R. D. Dupuis, G. Walter, D. A. Kellogg, N. Holonyak, Jr., D. T. Mathes, R. Hull, C. V. Reddy, and V. Narayanamurti, "Photopumped red-emitting $InP/In_{0.5}Al_{0.3}Ga_{0.2}P$ self-assembled quantum dot heterostructure lasers grown by metalorganic chemical vapor deposition," Appl. Phys. Lett. **78**, 4091 (2001).

[35] Z. Huang, M. Zimmer, S. Hepp, M. Jetter, and P. Michler, "Optical gain and lasing properties of InP/AlGaInP quantum-dot laser diode emitting at 660 nm," IEEE J. Quantum Electron. **55**, 2000307 (2019).

[36] J.-T. Oh, S.-Y. Lee, Y.-T. Moon, J. H. Moon, S. Park, K. Y. Hong, K. Y. Song, C. Oh, J.-I. Shim, H.-H. Jeong, et al., "Light output performance of red AlGaInP-based light emitting diodes with different chip geometries and structures," Opt. Express **26**, 11194 (2018).

[37] S. Han, C. Xu, H. Li, S. Liu, H. Xu, Y. Zhu, A. Fang, and X. Wang, "AlGaInP-based Micro-LED array with enhanced optoelectrical properties," Opt. Mater. **114**, 110860 (2021).

[38] B. O. Jung, W. Lee, J. Kim, M. Choi, H.-Y. Shin, M. Joo, S. Jung, Y.-H. Choi, and M. J. Kim, "Enhancement in external quantum efficiency of AlGaInP red μ-LED using chemical solution treatment process," Sci. Rep. **11**, 4535 (2021).

[39] P. Dhingra, P. Su, B. D. Li, R. D. Hool, A. J. Muhowski, M. Kim, D. Wasserman, J. Dallesasse, and M. L. Lee, "Low-threshold InP quantum dot and InGaP quantum well visible lasers on silicon (001)," Optica **8**, 1495 (2021).

[40] P. Dhingra, S. Fan, Y. Sun, R. D. Hool, B. Eng, and M. L. Lee, "InP quantum dots for dislocation-tolerant, visible light emitters on Si," Appl. Phys. Lett. **117**, 181102 (2020).

[41] T.-Y. Chang, H. Kim, W. A. Hubbard, K. M. Azizur-Rahman, J. J. Ju, J.-H. Kim, W.-J. Lee, and D. Huffaker, "InAsP quantum dot-embedded InP nanowires toward silicon photonic applications," ACS Appl. Mater. Interfaces **14**, 12488 (2022).

[42] A. M. Mintairov, J. Kapaldo, J. L. Merz, S. Rouvimov, D. V. Lebedev, N. A. Kalyuzhnyy, S. A. Mintairov, K. G. Belyaev, M. V. Rakhlin, A. A. Toropov, et al., "Control of Wigner localization and electron cavity effects in near-field emission spectra of In(Ga)P/GaInP quantum-dot structures," Phys. Rev. B **97**, 195443 (2018).

[43] A. M. Mintairov, D. V. Lebedev, N. Bert, K. G. Belyaev, V. N. Nevedomskiy, M. V. Rakhlin, A. A. Toropov, A. S. Vlasov, A. Gocalinska, G. Juska, et al., "Atomic ordering and bond relaxation in optical spectra of self-organized InP/$GaInP_2$ Wigner molecule structures," Appl. Phys. Lett. **115**, 202104 (2019).

[44] I. Vurgaftman and J. R. Meyer, "Band parameters for III–V compound semiconductors and their alloys," J. Appl. Phys. **89**, 5815 (2001).

[45] S. Bogusevschi, Ph.D. thesis, "Theory and optimisation of metamorphic photonic devices", University College Cork, Ireland (2018).

[46] E. Repiso, C. A. Broderick, M. de la Mata, R. Arkani, Q. Lu, A. R. J. Marshall, S. I. Molina, E. P. O'Reilly, P. J. Carrington, and A. Krier, "Optical properties of metamorphic type-I $InAs_{1-x}Sb_x/Al_yIn_{1-y}As$ quantum wells grown on GaAs for the mid-infrared spectral range," J. Phys. D: Appl. Phys. **52**, 465102 (2019).

[47] E. P. O'Reilly, "Quantum Theory of Solids" (Taylor and Francis, London, 2002).

[48] P. Yu and M. Cardona, "Fundamentals of Semiconductors: Physics and Materials Properties" (Springer-Verlag, Berlin Heidelberg, 2010).

[49] P.-O. Löwdin, "A note on the quantum-mechanical perturbation theory," J. Chem. Phys. **19**, 1396 (1951).

[50] R. Willardson and A. Beer, "Semiconductors and Semimetals" (Elsevier Science, Amsterdam, 1977).

[51] A. B. Cohen and G. E. Marques, "Electronic structure of zinc-blende-structure semiconductor heterostructures," Phys. Rev. B **41**, 10608 (1990).

[52] T. B. Bahder, "Eight-band $\mathbf{k}\cdot\mathbf{p}$ model of strained zinc-blende crystals," Phys. Rev. B **41**, 11992 (1990).

[53] S. Tomic, E. P. O'Reilly, and R. Fehse, "Theoretical and experimental analysis of 1.3 μm InGaAsN/GaAs lasers," IEEE J. Sel. Topics Quantum Electron. **9**, 253507 (2003).

[54] M. Altarelli, U. Ekenberg, and A. Fasolino, "Calculations of hole subbands in semiconductor quantum wells and superlattices," Phys. Rev. B **32**, 5138 (1985).

[55] C. A. Broderick, Ph.D. thesis, "Theory of the electronic and optical properties of dilute bismide alloys", University College Cork, Ireland (2015).

[56] S. B. Healy and E. P. O'Reilly, "Influence of electrostatic confinement on optical gain in GaInNAs quantum-well lasers," IEEE J. Quantum Electron. **42**, 608 (2006).

[57] C. Murphy, E. P. O'Reilly, and C. A. Broderick, "Efficient multi-band $\mathbf{k}\cdot\mathbf{p}$ calculations of superlattice electronic and optical properties using plane waves," Proc. Numerical Simulation of Optoelectronic Devices (NUSOD), 137 (2021).

[58] C. Murphy, E. P. O'Reilly, and C. A. Broderick, "Theory and optimisation of radiative recombination in broken-gap InAs/GaSb superlattices," J. Phys. D: Appl. Phys. **57**, 035103 (2024).

[59] M. Erhardt and T. Koprucki, eds., "Multi-Band Effective Mass Approximations: Advanced Mathematical Models and Numerical Techniques" (Springer, London, 2014).

[60] A. T. Meney, B. Gonul, and E. P. O'Reilly, "Evaluation of various approximations used in the envelope-function method," Phys. Rev. B **50**, 10893 (1994).

[61] F. Szmulowicz, "Derivation of a general expression for the momentum matrix elements within the envelope-function approximation," Phys. Rev. B **51**, 1613 (1995).

[62] "Vienna Ab initio Simulation Package (VASP),", http://www.vasp.at.

[63] G. Kresse and J. Furthmüller, "Efficient iterative schemes for ab initio total-energy calculations using a plane-wave basis set," Phys. Rev. B **54**, 11169 (1996).

[64] R. M. Martin, "Electronic Structure: Basic Theory and Practical Methods" (Cambridge University Press, Cambridge, 2004).

[65] P. Hohenberg and W. Kohn, "Inhomogenous electron gas," Phys. Rev. **136**, B864 (1964).

[66] W. Kohn and L. J. Sham, "Self-consistent equations including exchange and correlation effects," Phys. Rev. **140**, A1133 (1965).

[67] M. A. Caro, Ph.D. thesis, "Theory of elasticity and electric polarization effects in the group-III nitrides", University College Cork, Ireland (2013).

[68] M. Born and R. Oppenheimer, "Zur quantentheorie der molekeln," Annalen der Physik **389**, 457 (1927).

[69] L. H. Thomas, "The calculation of atomic fields," Math. Proc. Cambridge Philos. Soc. **23**, 542 (1927).

[70] E. Fermi, "Un metodo statistico per la determinazione di alcune prioretà dell'atome," Rend. Accad. Naz. Lincei **6**, 32 (1927).

[71] J. P. Perdew and Y. Wang, "Accurate and simple analytic representation of the electron-gas correlation energy," Phys. Rev. B **45**, 13244 (1992).

[72] J. P. Perdew and A. Zunger, "Self-interaction correction to density-functional approximations for many-electron systems," Phys. Rev. B **23**, 5048 (1981).

[73] F. Tran and P. Blaha, "Accurate band gaps of semiconductors and insulators with a semilocal exchange-correlation potential," Phys. Rev. Lett. **102**, 226401 (2009).

[74] J. P. Perdew, K. Burke, and M. Ernzerhof, "Generalized gradient approximation made simple," Phys. Rev. Lett. **77**, 3865 (1997).

[75] A. D. Becke and R. R. Johnson, "A simple effective potential for exchange," J. Chem. Phys. **124**, 221101 (2006).

[76] A. D. Becke and M. R. Roussel, "Exchange holes in inhomogeneous systems: A coordinate-space model," Phys. Rev. A **39**, 3761 (1989).

[77] Y.-S. Kim, M. Marsman, G. Kresse, F. Tran, and P. Blaha, "Towards efficient band structure and effective mass calculations for III-V direct band-gap semiconductors," Phys. Rev. B **82**, 205212 (2010).

[78] M. Laurien and O. Rubel, "Benchmarking exchange-correlation potentials with the mstar60 dataset: importance of the nonlocal exchange potential for effective mass calculations in semiconductors," Phys. Rev. B. **106**, 045204 (2022).

[79] L. Schimka, J. Harl, and G. Kresse, "Improved hybrid functional for solids: The HSEsol functional," J. Chem. Phys. **134**, 024116 (2011).

[80] A. Seidl, A. Görling, P. Vogl, J. A. Majewski, and M. Levy, "Generalized Kohn-Sham schemes and the band-gap problem," Phys. Rev. B **53**, 3764 (1996).

[81] J. Heyd, G. E. Scuzeria, and M. Ernzerhof, "Hybrid functionals based on a screened Coulomb potential," J. Chem. Phys. **118**, 8207 (2003).

[82] J. P. Perdew, A. Ruzsinszky, G. I. Csonka, O. A. Vydrov, G. E. Scuseria, L. A. Constantin, X. Zhou, and K. Burke, "Restoring the density-gradient expansion for exchange in solids and surfaces," Phys. Rev. Lett. **100**, 136406 (2008).

[83] G. I. Csonka, J. P. Perdew, A. Ruzsinszky, P. H. Philipsen, H. T. Pier, S. Lebègue, J. Paier, O. A. Vydrov, and J. G. Ángyán, "Assessing the performance of recent density functionals for bulk solids," Phys. Rev. B **79**, 155107 (2009).

[84] P. E. Blöchl, "Projector augmented-wave method," Phys. Rev. B **50**, 17953 (1994).

[85] V. Fiorentini, M. Methfessel, and M. Scheffler, "Electronic and structural properties of GaN by the full-potential linear muffin-tin orbitals method: the role of *d* electrons," Phys. Rev. B **47**, 13353 (1993).

[86] G. Kresse and D. Joubert, "From ultrasoft pseudopotentials to the projector augmented-wave method," Phys. Rev. B **59**, 1758 (1999).

[87] C.-L. Fu and K.-M. Ho, "First-principles calculation of the equilibrium ground-state properties of transition metals: applications to Nb and Mo," Phys. Rev. B **28**, 5480 (1983).

[88] J. Ihm, P. K. Lam, and M. L. Cohen, "Electronic structure of the [001] InAs-GaSb superlattice," Phys. Rev. B **20**, 4120 (1979).

[89] G. Grosso, S. Moroni, and G. P. Parravicini, "Electronic structure of the InAs-GaSb superlattice studied by the renormalization method," Phys. Rev. B **40**, 12328 (1989).

[90] Y. Wei and M. Razeghi, "Modeling of type-II InAs/GaSb superlattices using an empirical tight-binding method and interface engineering," Phys. Rev. B **69**, 085316 (2004).

[91] R. N. Mir and W. R. Frensley, "Electrical design of InAs-Sb/GaSb superlattices for optical detectors using full bandstructure sp^3s^* tight-binding method and Bloch boundary conditions," J. Appl. Phys. **114**, 153706 (2013).

[92] T. Kato and S. Souma, "sp^3s^* tight-binding calculation of band edges and effective masses of InAs/GaSb superlattices with different interface structures," Superlattice Microstruct. **122**, 492 (2018).

[93] A. Sawamura, J. Otsuka, T. Kato, T. Kotani, and S. Souma, "Nearest-neighbor $sp^3d^5s^*$ tight-binding parameters based on the hybrid quasi-particle self-consistent GW method verified by modeling of type-II superlattices," Opt. Mater. Express **8**, 1569 (2018).

[94] G. Bastard, "Superlattice band structure in the envelope-function approximation," Phys. Rev. B **24**, 5693 (1981).

[95] G. Bastard, "Theoretical investigations of superlattice band structure in the envelope-function approximation," Phys. Rev. B **25**, 7584 (1982).

[96] M. Altarelli, "Electronic structure and semiconductor-semimetal transition in InAs-GaSb superlattices," Phys. Rev. B **28**, 842 (1983).

[97] N. F. Johnson, H. Ehrenreich, P. M. Hui, and P. M. Young, "Electronic and optical properties of III-V and II-VI semiconductor superlattices," Phys. Rev. B **41**, 3655 (1990).

[98] J. Wang and Y. Zhang, "Band-gap corrected density functional theory calculations for InAs/GaSb type II superlattices," J. Appl. Phys. **116**, 214301 (2014).

[99] J. Otsuka, T. Kato, H. Sakakibara, and T. Kotani, "Band structures for short-period $(\mathrm{InAs})_n(\mathrm{GaSb})_n$ superlattices calculated by the quasiparticle self-consistent GW method," Jpn. J. Appl. Phys. **56**, 021201 (2017).

[100] T. Garwood, N. A. Modine, and S. Krishna, "Electronic structure modeling of InAs/-GaSb superlattices with hybrid density functional theory," Infrared Phys. Technol. **81**, 27 (2017).

[101] Z. Taghipour, E. Shojaee, and S. Krishna, "Many-body perturbation theory study of type-II InAs/GaSb superlattices within the GW approximation," J. Phys.: Condens. Matter **30**, 325701 (2018).

[102] S. Yang, D. Dardzinski, A. Hwang, D. I. Pikulin, G. W. Winkler, and N. Marom, "First-principles feasibility assessment of a topological insulator at the InAs/GaSb interface," Phys. Rev. Materials **5**, 084204 (2021).

[103] C. Liu, T. L. Hughes, X.-L. Qi, K. Wang, and S.-C. Zhang, "Quantum spin Hall effect in inverted type-II semiconductors," Phys. Rev. Lett. **100**, 236601 (2008).

[104] I. Knez, R.-R. Du, and G. Sullivan, "Evidence for helical edge modes in inverted InAs/-GaSb quantum wells," Phys. Rev. Lett. **107**, 136603 (2011).

[105] F. Qu, A. J. A. Beukman, S. Nadj-Perge, M. Wimmer, B.-M. Nguyen, W. Yi, J. Thorp, M. Sokolich, A. A. Kiselev, M. J. Manfra, et al., "Electric and magnetic tuning between the trivial and topological phases in InAs/GaSb double quantum wells," Phys. Rev. Lett. **115**, 036803 (2015).

[106] V. S. Pribiag, A. J. A. Beukman, F. Qu, M. C. Cassidy, C. Charpentier, W. Wegscheider, and L. P. Kouwenhoven, "Edge-mode superconductivity in a two-dimensional topological insulator," Nature Nanotech. **10**, 593 (2015).

[107] A. Krier, E. Repiso, F. Al-Saymari, P. J. Carrington, A. R. J. Marshall, L. Qi, S. E. Krier, K. J. Lulla, M. Steer, C. MacGregor, et al., "Mid-Infrared Optoelectronics: Materials, Devices and Applications, Chapter 2: Mid-Infrared Light-Emitting Diodes" (Woodhead, Sawston, 2020).

[108] S. D. Sifferman, H. P. Nair, R. Salas, N. T. Sheehan, S. J. Maddox, A. M. Crook, and S. R. Bank, "Highly strained mid-infrared type-I diode lasers on GaSb," IEEE J. Sel. Topics Quantum Electron. **21**, 1 (2015).

[109] T. D. Eales, I. P. Marko, B. A. Ikyo, A. R. Adams, S. Arafin, S. Sprengel, M. C. Amann, and S. J. Sweeney, "Wavelength dependence of efficiency limiting mechanisms in type-I mid-infrared GaInAsSb/GaSb lasers," IEEE J. Sel. Topics Quantum Electron. **23**, 1 (2017).

[110] J. R. Meyer, C. A. Hoffman, F. J. Bartoli, and L. R. Ram-Mohan, "Type-II quantum-well lasers for the mid-wavelength infrared," Appl. Phys. Lett. **67**, 757 (1995).

[111] R. J. Ricker, S. R. Provence, D. T. Norton, T. F. Boggess, Jr., and J. P. Prineas, "Broad-band mid-infrared superlattice light-emitting diodes," J. Appl. Phys. **121**, 185701 (2017).

[112] J. R. Meyer, C. L. Canedy, M. Kim, C. S. Kim, C. D. Merritt, W. W. Bewley, and I. Vurgaftman, "Comparison of Auger coefficients in type I and type II quantum well midwave infrared lasers," IEEE J. Quantum Electron. **57**, 2500110 (2021).

[113] E. Tournié, L. M. Bartolome, M. R. Calvo, Z. Loghmari, D. A. Díaz-Thomas, R. Teissier, A. N. Baranov, L. Cerutti, and J.-B. Rodriguez, "Mid-infrared III–V semiconductor lasers epitaxially grown on Si substrates," Light: Sci. Appl. **11**, 165 (2022).

[114] G. G. Zegrya and A. D. Andreev, "Mechanism of suppression of Auger recombination processes in type-II heterostructures," Appl. Phys. Lett. **67**, 2681 (1995).

[115] A. J. Muhowski, A. M. Muellerleile, J. T. Olesberg, and J. P. Prineas, "Internal quantum efficiency measurements in InAs/GaSb superlattices for midinfrared emitters," J. Appl. Phys. **126**, 243101 (2019).

[116] A. J. Muhowski, A. M. Muellerleile, J. T. Olesberg, and J. P. Prineas, "Internal quantum efficiency in 6.1 Å superlattices of 77% for mid-wave infrared emitters," Appl. Phys. Lett. **117**, 061101 (2020).

[117] E. J. Koerperick, J. T. Olesberg, J. L. Hicks, J. P. Prineas, and T. F. Boggess, "High-power MWIR cascaded InAs-GaSb superlattice LEDs," IEEE J. Quantum Electron. **45**, 849 (2009).

[118] E. J. Koerperick, D. T. Norton, J. T. Olesberg, B. V. Olson, J. P. Prineas, and T. F. Boggess, "Cascaded superlattice InAs/GaSb light-emitting diodes for operation in the long-wave infrared," IEEE J. Quantum Electron. **47**, 50 (2011).

[119] S. R. Provence, R. Ricker, Y. Aytac, T. F. Boggess, and J. P. Prineas, "High power cascaded mid-infrared InAs/GaSb light emitting diodes on mismatched GaAs," J. Appl. Phys. **118**, 123108 (2015).

[120] C. H. Grein, M. E. Flatté, J. T. Olesberg, S. A. Anson, L. Zhang, and T. F. Boggess, "Auger recombination in narrow-gap semiconductor superlattices incorporating antimony," J. Appl. Phys. **92**, 7311 (2002).

[121] E. P. O'Reilly and A. R. Adams, "Band-structure engineering in strained semiconductor lasers," IEEE J. Quantum Electron. **30**, 366 (1994).

[122] S. J. Sweeney, T. D. Eales, and A. R. Adams, "The impact of strained layers on current and emerging semiconductor laser systems," J. Appl. Phys. **125**, 082538 (2019).

[123] M. J. Godfrey and M. A. Malik, "Boundary conditions and spurious solutions in envelope-function theory," Phys. Rev. B **53**, 16504 (1996).

[124] M. Schlüter, G. Martinez, and M. L. Cohen, "Pressure and temperature dependence of electronic energy levels in PbSe and PbTe," Phys. Rev. B **12**, 650 (1975).

[125] P. B. Allen and M. Cardona, "Theory of the temperature dependence of the direct gap of germanium," Phys. Rev. B **23**, 1495 (1981).

[126] D. Schneider, C. Brink, G. Irmer, and P. Verma, "Effective mass and bandstructure of n-InAs from magnetophonon resonance and Raman scattering at temperatures between $T = 64$ and 360 K," Physica B **256-258**, 625 (1998).

[127] L. L. Li, W. Xu, and F. M. Peeters, "Intrinsic optical anisotropy of [001]-grown short-period InAs/GaSb superlattices," Phys. Rev. B **82**, 235422 (2010).

[128] B. A. Foreman, "Elimination of spurious solutions from eight-band $\mathbf{k}\cdot\mathbf{p}$ theory," Phys. Rev. B **56**, R12748 (1997).

[129] R. G. Veprek, S. Steiger, and B. Witzigmann, "Ellipticity and the spurious solution problem of $\mathbf{k}\cdot\mathbf{p}$ envelope equations," Phys. Rev. B **76**, 165320 (2007).

[130] Y.-C. Chang and J. N. Schulman, "Complex band structures of crystalline solids: an eigenvalue method," Phys. Rev. B **25**, 3975 (1982).

[131] Y.-C. Chang and J. N. Schulman, "Interband optical transitions in GaAs/$Ga_{1-x}Al_xAs$ and InAs/GaSb superlattices," Phys. Rev. B **31**, 2069 (1985).

[132] H. Carrillo-Nuñez, M. Luisier, and A. Schenk, "Analysis of InAs-Si heterojunction nanowire tunnel FETs: extreme confinement vs. bulk," Solid State Electron. **113**, 61 (2015).

[133] B. Chen, M. Lazzouni, and L. R. Ram-Mohan, "Diagonal representation for the transfer-matrix method for obtaining electronic energy levels in layered semiconductor heterostructures," Phys. Rev. B **45**, 1204 (1992).

[134] H. M. Dong, L. L. Li, W. Xu, and K. Han, "Effect of microscopic interface asymmetry on optical properties of short-period InAs/GaSb type-II superlattices," Thin Solid Films **589**, 388 (2015).

[135] U. Rössler and J. Kainz, "Microscopic interface asymmetry and spin-splitting of electron subbands in semiconductor quantum structures," Solid State Commun. **121**, 313 (2002).

[136] E. Burstein, "Anomalous optical absorption limit in InSb," Phys. Rev. **93**, 632 (1954).

[137] T. S. Moss, "The interpretation of the properties of indium antimonide," Proc. Phys. Soc. **67**, 775 (1954).

[138] G. Lasher and F. Stern, "Spontaneous and stimulated recombination radiation in semiconductors," Phys. Rev. **133**, A553 (1964).

[139] S. Wu, Y. Cao, S. Tomic, and F. Ishikawa, "The optical gain and radiative current density of GaInNAs/GaAs/AlGaAs separate confinement heterostructure quantum well lasers," J. Appl. Phys. **107**, 013107 (2010).

[140] W. J. Fan, M. F. Li, T. C. Chong, and J. B. Xia, "Valence hole subbands and optical gain spectra of GaN/$Ga_{1-x}Al_xN$ strained quantum wells," J. Appl. Phys. **80**, 3471 (1996).

[141] I. P. Marko, C. A. Broderick, S. R. Jin, P. Ludewig, W. Stolz, K. Volz, J. M. Rorison, E. P. O'Reilly, and S. J. Sweeney, "Optical gain in GaAsBi/GaAs quantum well diode lasers," Sci. Rep. **6**, 28863 (2016).

[142] Y. P. Varshni, "Temperature dependence of the energy gap in semiconductors," Physica **34**, 149 (1967).

[143] B. Klein, E. Plis, M. N. Kutty, N. Gautam, A. Albrecht, S. Myers, and S. Krishna, "Varshni parameters for InAs/GaSb strained layer superlattice infrared photodetectors," J. Phys. D: Appl. Phys. **44**, 075102 (2011).

[144] M. Stone and P. Goldbart, "Mathematics for Physics: A Guided Tour for Graduate Students" (Cambridge University Press, Cambridge, 2012).

[145] E. P. O'Reilly, K. C. Heasman, A. R. Adams, and G. P. Witchlow, "Calculations of the threshold current and temperature sensitivity of Al(GaIn)As strained quantum well laser operating at 1.55 μm," Superlatt. Micro. **3**, 99 (1987).

[146] A. Ghiti, E. P. O'Reilly, and A. R. Adams, "Improved dynamics and linewidth enhancement factor in strained-layer lasers," Elec. Lett. **25**, 821 (1989).

[147] A. Haug, "Relations between the T_0 values of bulk and quantum-well GaAs," Appl. Phys. B **44**, 151 (1987).

[148] J. Hader, S. C. Liebscher, J. V. Moloney, and S. W. Koch, "Intrinsic carrier losses in tellurium due to radiative and Auger recombinations," Appl. Phys. Lett. **121**, 192103 (2022).

[149] A. Ghiti, M. Silver, and E. P. O'Reilly, "Low threshold current and high differential gain in ideal tensile- and compressive-strained quantum-well lasers," J. Appl. Phys. **71**, 4626 (1992).

[150] C. Downs and T. E. Vandervelde, "Progress in infrared photodetectors since 2000," Sensors **13**, 5054 (2013).

[151] M. Razeghi and B.-M. Nguyen, "Advances in mid-infrared detection and imaging: a key issues review," Rep. Prog. Phys. **77**, 082401 (2014).

[152] M. Bouschet, V. Arounassalame, A. Ramiandrasoa, I. Ribet-Mohamed, J.-P. Perezer, N. Péré-Laperne, and P. Christol, "Temperature dependence study of electric and electro-optical performances of midwave infrared Ga-free T2SL barrier photodetector," Appl. Sci. **12**, 10358 (2022).

[153] Y. Aytac, B. V. Olson, J. K. Kim, E. A. Shaner, S. D. Hawkins, J. F. Klem, J. T. Olesberg, M. E. Flatté, and T. F. Boggess, "Bandgap and temperature dependence of Auger recombination in InAs/InAsSb type-II superlattices," J. Appl. Phys. **119**, 215705 (2016).

[154] D. Wu, J. Li, A. Dehzangi, and M. Razeghi, "Mid-wavelength infrared high operating temperature pBn photodetectors based on type-II InAs/InAsSb superlattice," AIP Adv. **10**, 025018 (2020).

[155] D. Wu, J. Li, A. Dehzangi, and M. Razeghi, "High performance InAs/InAsSb Type-II superlattice mid-wavelength infrared photodetectors with double barrier," Infrared Phys. Technol. **109**, 103439 (2020).

[156] Y. Livneh, P. C. Klipstein, O. Klin, N. Snapi, S. Grossman, A. Glozman, and E. Weiss, "**k**·**p** model for the energy dispersions and absorption spectra of InAs/GaSb type-II superlattices," Phys. Rev. B **86**, 235311 (2012).

[157] P. C. Klipstein, Y. Livneh, A. Glozman, S. Grossman, O. Klin, N. Snapi, and E. Weiss, "Modeling InAs/GaSb and InAs/InAsSb superlattice infrared detectors," J. Electron. Mater. **43**, 2984 (2014).

[158] N. J. Ekins-Daukes, K. Kawaguchi, and J. Zhang, "Strain-balanced criteria for multiple quantum well structures and its signature in x-ray rocking curves," Cryst. Growth Des. **2**, 287 (2002).

[159] L. D. Landau, L. P. Pitaevskii, A. M. Kosevich, and E. Lifshitz, "Theory of Elasticity" (Elsevier, Oxford, 1986).

[160] C. O'Donnell, Ph.D. thesis, "Germanium tin for use in semimetal electronics", University College Cork, Ireland (2021).

[161] C. A. Broderick, S. R. Jin, I. P. Marko, K. Hild, P. Ludewig, Z. L. Bushell, W. Stolz, J. M. Rorison, E. P. O'Reilly, K. Volz, et al., "$GaAs_{1-x}Bi_x/GaN_yAs_{1-y}$ type-II quantum wells: novel strain-balanced heterostructures for GaAs-based near- and mid-infrared photonics," Sci. Rep. **7**, 46371 (2017).

[162] J. Liang and M. Razeghi, "Handbook of Infra-red Detection Technologies, Chapter 4: GaInAs(P) based QWIPs on GaAs, InP and Si Substrates for Focal Plane Arrays" (Elsevier Science, Amsterdam, 2002).

[163] Y. Zhou, Z. Li, X. Zhou, J. Zhou, Y. Zheng, L. Li, N. Li, P. Chen, X. Cheng, and W. Lu, "Cut-off wavelength manipulation of pixel-level plasmonic microcavity for long wavelength infrared detection," Appl. Phys. Lett. **114**, 061104 (2019).

[164] M. S. Milosavljevic, P. T. Webster, and S. R. Johnson, "Impact of unintentional Sb in the tensile InAs layer of strain-balanced type-II InAs/InAsSb superlattices grown on GaSb by molecular beam epitaxy," J. Appl. Phys. **134**, 053103 (2023).

[165] E. P. O'Reilly, "Valence band engineering in strained-layer structures," Semicond. Sci. Technol. **4**, 121 (1989).

[166] J. H. van der Merwe, "Structure of epitaxial crystal interfaces," Surface Science **31**, 198 (1972).

[167] P. Voisin, "Heterostructures of lattice mismatched semiconductors: fundamental aspects and device perspectives," Proc. SPIE **861**, 88 (1988).

[168] E. A. Fitzgerald, "Dislocations in strained-layer epitaxy: theory, experiment and applications," Mat. Sci. Rep. **7**, 87 (1991).

[169] S. Tomić and E. P. O'Reilly, "Optimization of material parameters in 1.3-μm InGaAsN-GaAs lasers," IEEE Phot. Tech. Lett. **15**, 6 (2003).

[170] M. Bouschet, V. Arounassalame, A. Ramiandrasoa, J.-P. Perez, N. Péré-Laperne, I. Ribet-Mohamed, and P. Christol, "Electro-optical performance and anisotropic transport study of a Ga-free type-II superlattice barrier structure," Opto-Electron. Rev. **31**, e144549 (2023).

[171] G. Krizman, F. Carosella, J. Bermejo-Ortiz, A. Philippe, J. B. Rodriguez, J.-P. Perez, P. Christol, L.-A. de Vaulchier, and Y. Guldner, "Magneto-spectroscopy investigation of InAs/InAsSb superlattices for midwave infrared detection," J. Appl. Phys. **130**, 055704 (2021).

[172] P. G. Datskos and N. V. Lavrik, "Encyclopedia of Optical and Photonic Engineering, Volume I: Detectors: Figures of Merit" (CRC Press, Florida, 2016).

[173] J. Nelson, "The Physics of Solar Cells" (Imperial College Press, London, 2003).

[174] R. Magri and A. Zunger, "Effects of interficial atomic segregation and intermixing on the electronic properties of InAs/GaSb superlattices," Phys. Rev. B **65**, 165302 (2002).

[175] G. C. Osbourn, "Electronic properties of strained-layer superlattices," J. Vac. Sci. Technol. B **1**, 379 (1983).

[176] J. Ihm, "Effects of the layer thickness on the electronic character in GaAs-AlAs superlattices," Appl. Phys. Lett. **50**, 1068 (1987).

[177] F. M. Peeters, A. Mathulis, M. Helm, T. Fromherz, and W. Hilber, "Oscillator strength and sum rule for intersubband transitions in a superlattice," Phys. Rev. B **48**, 12008 (1993).

[178] I. Vurgaftman, M. P. Lumb, and J. R. Meyer, "Bands and Photons in III-V Semiconductor Quantum Structures" (Oxford University Press, Oxford, 2020).

[179] A. Onton and R. J. Chicotka, "Conduction Bands in $In_{1-x}Al_xP$," J. Appl. Phys. **41**, 4205 (1970).

[180] M.-Z. Huang and W. Y. Ching, "A minimal basis semi-ab initio approach to the band structures of semiconductors," J. Phys. and Chem. Sol. **46**, 977 (1985).

[181] C. K. Williams, T. H. Glisson, J. R. Hauser, and M. A. Littlejohn, "Energy bandgap and lattice constant contours of iii-v quaternary alloys of the form $A_xB_yC_zD$ or $AB_xC_yD_z$," J. Electron. Mater. **7**, 639 (1978).

[182] S. Y. Hwang, T. J. Kim, Y. W. Jung, N. S. Barange, H. G. Park, J. Y. Kim, Y. R. Kang, Y. D. Kim, S. H. Shin, J. D. Song, et al., "Dielectric function and critical points of AlP determined by spectroscopic ellipsometry," J. Alloys Compd. **587**, 361 (2014).

[183] D. J. Stukel and R. N. Euwema, "Electronic Band Structure and Related Properties of Cubic AlP," Phys. Rev. **186**, 754 (1969).

[184] D. Wing, J. B. Haber, R. Noff, B. Barker, D. A. Egger, A. Ramasubramaniam, S. G. Louie, J. B. Neaton, and L. Kronik, "Comparing time-dependent density functional theory with many-body perturbation theory for semiconductors: screened range-separated hybrids and the GW plus Bethe-Salpeter approach," Phys. Rev. Mat. **3**, 064603 (2019).

[185] C. M. O. Bastos, F. P. Sabino, G. M. Sipahi, and J. L. F. Da Silva, "A comprehensive study of g-factors, elastic, structural and electronic properties of III-V semiconductors using hybrid-density functional theory," J. Appl. Phys. **123**, 065702 (2018).

[186] A. T. Meney, D. Prins, A. F. Phillips, A. F. Sly, E. P. O'Reilly, D. Dunstan, A. R. Adams, and A. Valster, "Determination of the band structure of disordered AlGaInP and its influence on visible-laser characteristics," IEEE J. Sel. Topics Quantum Electron. **1**, 697 (1995).

[187] D. J. Mowbray, O. P. Kowalski, M. Hopkinson, M. S. Skolnick, and J. P. R. David, "Electronic band structure of AlGaInP grown by solid-source molecular-beam epitaxy," Appl. Phys. Lett. **65**, 213 (1994).

[188] P. Borlido, J. Schmidt, and A. W. Huran, "Exchange-correlation functionals for band gaps of solids: benchmark, reparametrization and machine learning," Comput. Mater. **6**, 96 (2020).

[189] M. P. Polak, P. Scharoch, and R. Kudrawiec, "The electronic band structure of $Ge_{1-x}Sn_x$ in the full composition range: indirect, direct, and inverted gaps regimes, band offsets, and the Burstein–Moss effect," J. Phys. D: Appl. Phys. **50**, 195103 (2017).

[190] E. J. O'Halloran, C. A. Broderick, D. S. P. Tanner, S. Schulz, and E. P. O'Reilly, "Comparison of first principles and semi-empirical models of the structural and electronic properties of $Ge_{1-x}Sn_s$ alloys," Opt. Quantum Electron. **51**, 314 (2019).

[191] P. M. Pearce, C. A. Broderick, M. P. Nielsen, A. D. Johnson, and N. J. Ekins-Daukes, "Electronic and optical properties of $Si_xGe_{1-x-y}Sn_y$ alloys lattice-matched to Ge," Phys. Rev. Materials **6**, 015402 (2022).

[192] P. N. Keating, "Effect of invariance requirements on the elastic strain energy of crystals with application to the diamond structure," Phys. Rev. **145**, 637 (1966).

[193] L. Kleinman, "Deformation potentials in silicon. I. Uniaxial strain," Phys. Rev. **128**, 2614 (1962).

[194] D. S. P. Tanner, M. A. Caro, S. Schulz, and E. P. O'Reilly, "Hybrid functional study of nonlinear elasticity and internal strain in zinc-blende III-V materials," Phys. Rev. Materials **3**, 013604 (2019).

[195] S. Q. Wang and H. Q. Ye, "Plane-wave pseudopotential study on mechanical and electronic properties for IV and III-V crystalline phases with zinc-blende structure," Phys. Rev. B **66**, 235111 (2002).

[196] S.-H. Wei and A. Zunger, "Predicted band-gap pressure coefficients of all diamond and zinc-blende semiconductors: chemical trends," Phys. Rev. B **60**, 5404 (1999).

[197] D. S. P. Tanner, Ph.D. thesis, "A study of the elastic and electronic properties of III-nitride semiconductors", University College Cork, Ireland (2017).

[198] V. N. Bessolov, S. G. Konnikov, V. E. Umanskii, and Y. P. Yakovlev, "Lattice-constant of $Al_xGa_{1-x}P$," Fiz. Tverd. Tela **24**, 1528 (1982).

[199] S. Adachi, "Properties of Semiconductor Alloys: Group-IV, III-V and II-VI Semiconductors" (John Wiley & Sons, Ltd, 2009).

[200] T. M. Ritter, B. A. Weinstein, R. E. Viturro, and D. P. Bour, "Energy level alignments in strained-layer GaInP/AlGaInP laser diodes: model solid theory analysis of pressure-photoluminescence experiements," phys. stat. sol. (b) **211**, 869 (1998).

[201] M. Råsander and M. A. Moram, "On the accuracy of commonly used density functional approximations in determining the elastic constants of insulators and semiconductors," J. Chem. Phys. **143**, 144104 (2015).

[202] M. A. Caro, S. Schulz, and E. P. O'Reilly, "Comparison of stress and total energy methods for calculation of elastic properties of semiconductors," J. Phys.: Condens. Matter **25**, 025803 (2013).

[203] C. O'Donnell, A. Sanchez-Soares, C. A. Broderick, and J. C. Greer, "Impact of stoichiometry and strain on $Ge_{1x}Sn_x$ alloys from first principles calculations," J. Phys. D: Appl. Phys. **54**, 245103 (2021).

[204] J. Ziembicki, P. Scharoch, M. P. Polak, M. Wiśniewski, and R. Kudrawiec, "Band parameters of group III–V semiconductors in wurtzite structure," J. Appl. Phys. **132**, 225701 (2022).

[205] B. Monemar, "Fundamental energy gaps of AlAs and AlP from photoluminescence excitation spectra," Phys. Rev. B **8**, 5711 (1973).

[206] V. R. D'Costa, C. S. Cook, J. Menéndez, J. Tolle, J. Kouvetakis, and S. Zollner, "Transferability of optical bowing parameters between binary and ternary group-IV alloys," Solid State Commun. **138**, 309 (2006).

[207] P. M. Pearce, S. W. Ong, A. D. Johnson, E. S. Tok, and N. J. Ekins-Daukes, "Compositional dependence of direct transition energies in $Si_xGe_{1xy}Sn_y$ alloys lattice-matched to Ge/GaAs," arXiv:2203.08605v1 (2022).

[208] D. E. Aspnes, "Third-derivative modulation spectroscopy with low-field electroreflectance," Surf. Sci. **37**, 418 (1973).

[209] H. Lee, M. V. Klein, D. E. Aspnes, C. P. Kuo, M. Peanasky, and M. G. Craford, "Optical study of $(Al_xGa_{1-x})_{0.5}In_{0.5}P$/GaAs semiconductor alloys by spectroscopic ellipsometry," J. Appl. Phys. **73**, 400 (1993).

[210] P. Lautenschlager, M. Garriga, L. Vina, and M. Cardona, "Temperature dependence of the dielectric function and interband critical points in silicon," Phys. Rev. B. **36**, 4821 (1987).

[211] X. Zhu and S. G. Louie, "Quasiparticle band structure of thirteen semiconductors and insulators," Phys. Rev. B **43**, 14142 (1991).

[212] J. R. Chelikowsky and M. L. Cohen, "Nonlocal pseudopotential claculations for the electronic structure of eleven diamond and zinc-blende semiconductors," Phys. Rev. B **14**, 556 (1976).

[213] P. J. Dean, G. Kaminsky, and R. B. Zetterstrom, "Intrinsic optical absorption of gallium phosphide between 2.33 and 3.12 eV," J. Appl. Phys. **38**, 3551 (1967).

[214] R. Zallen and W. Paul, "Band structure of gallium phosphide from optical experiments at high pressure," Phys. Rev. **134**, A1628 (1964).

[215] M. P. C. M. Krijn, "Heterojunection band offsets and effective masses in III-V quaternary alloys," Semicond. Sci. Technol. **6**, 27 (1991).

[216] F. Issiki, S. Fukatsu, and Y. Shiraki, "Efficient luminescence from AlP/GaP neighboring confinement structure with AlGaP barrier layers," Appl. Phys. Lett. **67**, 1048 (1995).

[217] I. Saïdi, S. Ben Radhia, and K. Boujdaria, "Band parameters of GaAs, InAs, InP and InSb in the 40-band $\mathbf{k} \cdot \mathbf{p}$ model," J. Appl. Phys. **107**, 043701 (2010).

[218] N. Fraj, I. Saïdi, S. Ben Radhia, and K. Boujdaria, "Band structures of AlAs, GaP, and SiGe alloys: a 30 $\mathbf{k} \cdot \mathbf{p}$ model," J. Appl. Phys. **102**, 053703 (2007).

[219] A. F. Starace, "Length and velocity formulas in approximate oscillator-strength calculations," Phys. Rev. A **3**, 1242 (1971).

[220] M. Gajdoš, K. Hummer, G. Kresse, J. Furthmüller, and F. Bechstedt, "Linear optical properties in the projector-augmented wave methodology," Phys. Rev. B **73**, 045112 (2006).

[221] D. Sytnyk and R. Melnik, "The Luttinger-Kohn theory for multiband Hamiltonians: a revision of ellipticity requirements," arXiv:1808.06988v1 (2018).

[222] G. L. Bir and G. E. Pikus, "Symmetry and strain-induced effects in semiconductors" (Wiley, New York, 1974).

[223] H. Müller, R. Trommer, M. Cardona, and P. Vogl, "Pressure dependence of the direct absorption edge of InP," Phys. Rev. B **21**, 4879 (1980).

[224] C. S. Menoni and I. L. Spain, "Equation of state of InP to 19 GPa," Phys. Rev. B **35**, 7520 (1987).

[225] D. D. Nolte, W. Walukiewicz, and E. E. Haller, "Band-edge hydrostatic deformation potentials in III-V semiconductors," Phys. Rev. Lett. **59**, 501 (1987).

[226] J. Camassel, P. Merle, L. Bayo, and H. Mathieu, "Deformation potentials of the fundamental exciton spectrum of InP," Phys. Rev. B **22**, 2020 (1980).

[227] T. Kobayashi, K. Aoki, and K. Yamamoto, "Pressure dependence of optical absorption in InP at 77 K," Physica B+C **139-140**, 537 (1986).

[228] C. G. Van de Walle, "Band lineups and deformation potentials in the model-solid theory," Phys. Rev. B **39**, 1871 (1989).

[229] A. Blacha, H. Presting, and M. Cardona, "Deformation potentials of $\mathbf{k} = 0$ states of tetrahedral semiconductors," Phys. Status Solidi B **126**, 11 (1984).

[230] E. P. O'Reilly, "Axial-strain effects on superlattice band structures," Semicond. Sci. Technol. **1**, 128 (1986).

[231] L. Weston, H. Tailor, K. Krishnaswamy, L. Bjaalie, and C. G. Van de Walle, "Accurate and efficient band-offset calculations from density functional theory," Comput. Mater. Sci. **151**, 174 (2018).

[232] V. Wang, N. Xu, J. C. Liu, G. Tang, and W. T. Geng, "VASPKIT: a user-friendly interface facilitating high-throughput computing and analysis using VASP code," Comput. Phys. Commun. **267**, 108033 (2021).

[233] A. Qteish and R. J. Needs, "Improved model-solid-theory calculations for valence-band offsets at semiconductor-semiconductor interfaces," Phys. Rev. B **45**, 1317 (1992).

[234] Y. Hinuma, A. Grüneis, G. Kresse, and F. Oba, "Band alignment of semiconductors from density-functional theory and many-body perturbation theory," Phys. Rev. B **90**, 155405 (2014).

[235] Y.-H. Li, A. Walsh, S. Chen, W.-J. Yin, J.-H. Yang, J. Li, J. L. F. Da Silva, X. G. Gong, and S.-H. Wei, "Revised ab initio natural band offsets of all group IV, II-VI and III-V semiconductors," Appl. Phys. Lett. **94**, 212109 (2009).

[236] K. Jauregui, W. Häusler, and B. Kramer, "Wigner molecules in nanostructures," Europhys. Lett. **24**, 581 (1993).

[237] T. Murphy, C. A. Broderick, E. P. O'Reilly, and F. H. Peters, "Theory of lateral field electro-absorption modulation in quantum dot heterostructures," SPIE **PC12415**, PC1241505 (2023).

[238] A. Pescaglini, A. Gocalinska, S. Bogusevschi, S. T. Moroni, G. Juska, E. E. Mura, J. Justice, B. Corbett, E. P. O'Reilly, and E. Pelucchi, "Three-dimensional self-assembled columnar arrays of AlInP quantum Wires for polarized micrometer-sized amber light emitting diodes," ACS Photonics **5**, 1318 (2018).

[239] D. S. P. Tanner, M. A. Caro, S. Schulz, and E. P. O'Reilly, "Fully analytic valence force field model for the elastic and inner elastic properties of diamond and zincblende crystals," Phys. Rev. B **100**, 094112 (2019).

[240] C. A. Broderick, E. P. O'Reilly, and S. Schulz, "Perspective: theory and simulation of highly mismatched semiconductor alloys using the tight-binding method," J. Appl. Phys. **135**, 100902 (2024).

[241] S. Das, C. A. Broderick, and E. P. O'Reilly, "Impact of band-anticrossing on band-to-band tunneling in highly-mismatched semiconductor alloys," Phys. Rev. Applied **17**, 014029 (2022).

[242] J. N. Schulman and Y. C. Chang, "Band mixing in semiconductor superlattices," Phys. Rev. B **31**, 2056 (1985).